JOURNAL OF APPLIED PHYSICS

Vol. 31, No. 10 October, 1960

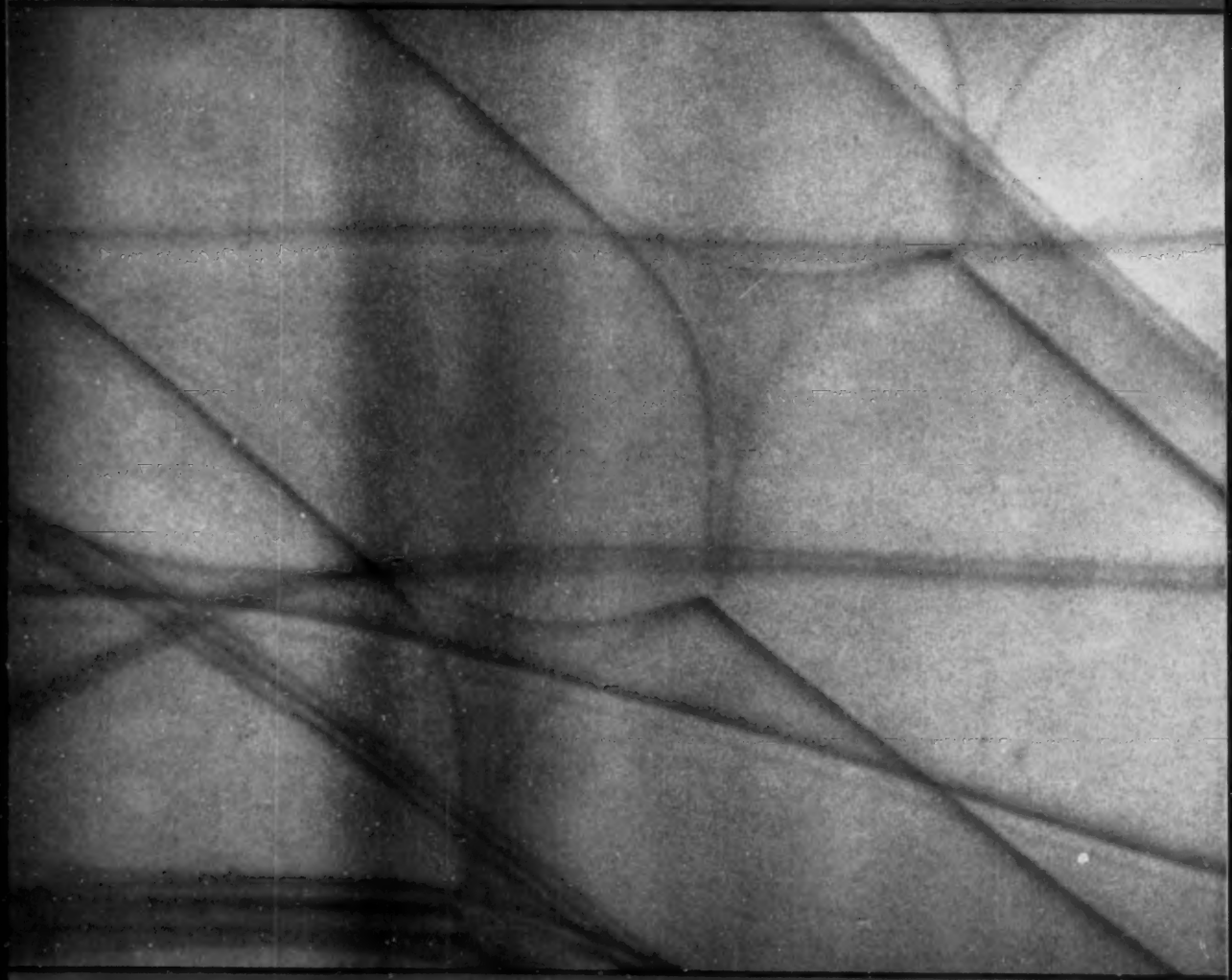

Extended Dislocation Nodes in Graphite.
See Page 1830.

the five keys to TIME MICROSCOPY

These photo instruments cover the ranges from 200 to 4.3 million frames per second, and up to 9 millimeters per microsecond sweeping-image rates. In their various ways, they provide access to magnified segments of time for quantitative analysis of high-speed events throughout science and industry.

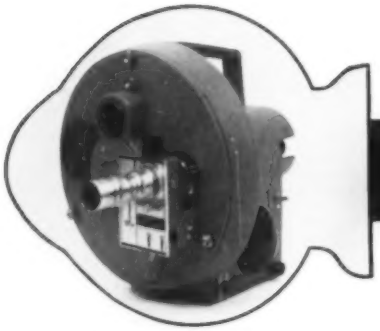

Dynafax Continuous-Writing Framing Camera

For object speeds from 100 to 2,000 meters per second at 0.1 magnification. No synchronization necessary. Produces 224 16-mm frames on 35-mm film. Rates, 200 to 26,000 pps.

Model 189 Synchronized Framing Camera

For object speeds from 500 to 25,000 meters per second at 0.1 magnification. Twenty-five 35-mm frames. Rate, to 4.3 million per second.

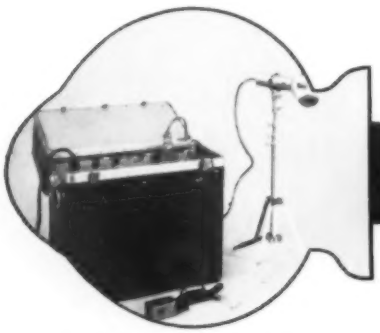

Model 357 Electronic Flash Unit

One-million beam candlepower of cold light in square pulses provides uniform illumination of high-speed sequences over adjustable time ranges of 8.6, 11.15, 14.85, and 22.35 milliseconds.

Model 192 Continuous-Writing Framing Camera

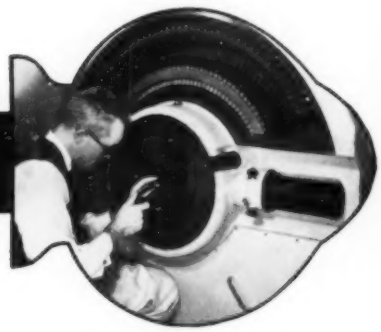

For object speeds from 1,000 to 13,000 meters per second at 0.1 magnification. No synchronization necessary. Eighty 35-mm frames. Rates to 1.4 million per second.

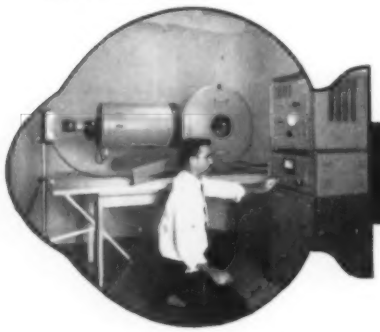

Model 339 Continuous-Writing Streak Camera

New camera produces uninterrupted streak image on 50-in strip of 35-mm film. Incorporating a 2600-rps distortionless beryllium mirror, unit has writing rates to 9-mm per microsecond with writing time 145 microsec.

Professional opportunities exist in the Instrument, Missile Products, and Research & Development Divisions of the company. You are invited to send a resume to the personnel manager.

Beckman & Whitley

SAN CARLOS 8 • CALIFORNIA • U.S.A.

JOURNAL OF APPLIED PHYSICS

Vol. 31, No. 10 OCTOBER, 1960

In This Issue

Domains in Thin Magnetic Films Observed by Electron Microscopy . . . Harrison W. Fuller and Murray E. Hale 1699

Longitudinal Wave Propagation in Stretched Polymers . . . Peter Mason 1706

Cathode of an Arc in Xenon . . . John E. White 1709

Density of a Thorium Monolayer for Maximum Thermionic Emission . . . W. E. Danforth and D. L. Goldwater 1715

Anomalous Barrier Capacitance in *p-n* Junctions of InSb . . . C. A. Lee and G. Kaminsky 1717

Growth of Cesium Chloride Crystals from Solution and Melt . . . P. Avakian and A. Smakula 1720

Propagation Constants for Electromagnetic Waves in Weakly Ionized, Dry Air . . . A. V. Phelps 1723

Effects of Internal Oxidation and Heat Treatment on the Electrical Resistivity of Dilute CuMn, CuFe, and CuCo Alloys . . . C. A. Domenicali and E. L. Christenson 1730

Improved Method of Growing CdS Crystals from the Vapor Phase . . . P. D. Fochs 1733

Note on Evaporation . . . S. A. Zwick 1735

Aperture Fields in the Diffraction by a Slit . . . Hwei-Piao Hsu 1742

Grain-Boundary Photoresponse . . . W. W. Lindemann and R. K. Mueller 1746

Surface Space-Charge Calculations for Semiconductors . . . D. R. Frankl 1752

Oblique-Incidence Anisotropy in Evaporated Permalloy Films . . . D. O. Smith, M. S. Cohen, and G. P. Weiss 1755

Ordering in the Intermediate Phases TiFe, TiCo, and TiNi . . . Paul Pietrokowsky and Frank G. Youngkin 1763

On a Complex Recrystallization Texture in 3% Silicon Iron . . . C. G. Dunn and C. J. McHargue 1767

Hall Field Relaxation in Semiconductors at High Frequency . . . Keith S. Champlin 1770

Fast Neutron Bombardment of Germanium and Silicon Esaki Diodes . . . J. W. Easley and R. R. Blair 1772

Interaction between High-Power Microwave Losses and Magnetic Flux Reversal . . . E. M. Gyorgy and F. B. Hagedorn 1775

On the Strength of Glass in Water Vapor . . . F. R. L. Schoening 1779

Study of Irradiation Effects and the H^2+H^2 Buildup in Tantalum . . . A. F. Gabrysh, H. Eyring, M. E. Wadsworth, G. S. Baker, and T. Ree 1785

Anomalous Surface Channels on Silicon *p-n* Junctions . . . Raymond Solomon 1791

Effect of Thermal History on the Dislocation Substructure near the Surfaces of a Lithium Fluoride Crystal . . . J. M. Schultz and J. Washburn 1800

Anisotropy of the Magnetic Susceptibility of Gallium . . . Titus Pankey, Jr. 1802

Measurements of the Dielectric Constant of $BaTiO_3$ Single Crystals in the Paraelectric Region at X Band . . . A. Lurio and E. Stern 1805

Experimental Determination of Stresses Generated by an Electric Detonator . . . John S. Rinehart and William C. McClain 1809

Electron Sheet Beam Focusing with Tape Ladder Lines . . . William E. Waters 1814

Metal Precipitates in Silicon *p-n* Junctions . . . A. Goetzberger and W. Shockley 1821

Letters to the Editor:

On the Temperature of an Object Irradiated with Electrons . . . S. Yamaguchi 1825

Determination of Dose Rates from Beta Transmission Currents . . . Arthur Bradley 1826

Oscillations in Germanium with an Applied Pulsed Electric Field . . . M. Cardona and W. Ruppel 1826

Direct Replica Technique for Copper . . . J. O. Stiegler and T. S. Noggle 1827

Generation of Millimeter Waves by the Electron Beam of a Microtron . . . E. Brannen, H. Froelich, and T. W. W. Stewart 1829

Research Reports . . . 1829

Books Reviewed . . . 1829

Books Received . . . 1830

Announcements . . . 1830

Cover Photograph . . . 1830

Proceedings of the Electron Microscope Society of America . . . 1831

JOURNAL OF APPLIED PHYSICS

A journal of general physics and its applications to other sciences and to industry

Published by the

American Institute of Physics

GOVERNING BOARD

Members

Ralph A. Sawyer, *Chairman*
James G. Baker
R. H. Bolt
W. R. Brode
Harvey Brooks
Dirk Brouwer
J. W. Buchta
Vernet E. Eaton
J. H. Elliott
Herbert A. Erf
S. A. Goudsmit
W. W. Havens, Jr.
Winston E. Kock
R. Bruce Lindsay
H. V. Neher
C. J. Overbeck
G. E. Pake
Ray Pepinsky
F. W. Sears
Frederick Seitz
John Strong
George E. Uhlenbeck
M. E. Warga
Victor F. Weisskopf
W. R. Willets

ADMINISTRATION

Elmer Hutchisson
Director

Wallace Waterfall
Secretary and Treasurer

Henry A. Barton
Administrative Consultant

W. C. Kelly
Director of Education

Eugene H. Kone
Director of Public Relations

Hugh C. Wolfe
Director of Publications

Kathryn Setze
Assistant Treasurer

Norma Frankel
Publications Editor

Sistina Greco
Circulation Manager

Edward Tober
Manager, Production and Distribution

Theodore Vorburger
Advertising Manager

Emily Wolf
Manager, Special Services

Editor
James A. Krumhansl

Assistant Editor
Ethel McMillan

Editorial Board

J. H. Crawford
Arthur Kantrowitz
A. F. Kip
J. E. Goldman
J. L. Tuck
C. A. Wert
Herman A. Haus
C. Lester Hogan
R. S. Rivlin

THE JOURNAL OF APPLIED PHYSICS is devoted to general physics and its applications to other sciences, to engineering, and to industry. Previous to 1937, this journal was called PHYSICS.

The JOURNAL OF APPLIED PHYSICS welcomes articles of two distinct kinds: (1) Descriptions of new results in experimental or theoretical physics which are of general interest to physicists. The author should explain his contribution in such a way that a physicist or engineer in another field of specialization can appreciate its objectives and essential features. (2) Critical reviews of particular areas of physics or surveys of extensive investigations at a single laboratory. Authors contemplating writing such should correspond with the Editor before they begin writing.

The JOURNAL OF APPLIED PHYSICS welcomes Letters to the Editor which are short [approximately four (4) typewritten pages] communications without abstracts. Timeliness, briefness, and degree of current importance of the subject matter will be of primary concern in the publication of Letters. Letters should not be looked upon as partial publication or announcement of more comprehensive work, but rather self-contained presentations in themselves.

Manuscripts should be submitted to the Editor, J. H. Crawford, Solid State Division, Oak Ridge National Laboratory, Oak Ridge, Tennessee. Authors should read the "Information for Contributors," facing page 1 of the January issue, before writing articles or letters. The *Style Manual* of the American Institute of Physics is also helpful to writers preparing manuscripts for journals published by the American Institute of Physics. It can be obtained for $1.00 from the American Institute of Physics, 335 East 45 Street, New York 17, New York.

Corrected proofs and all correspondence concerning papers in the process of publication should be addressed to the Publication Manager, American Institute of Physics, 335 East 45 Street, New York 17, New York.

Subscriptions, renewals, and orders for back numbers should be addressed to the American Institute of Physics, 335 East 45 Street, New York 17, New York.

Subscription Price	U.S. and Canada	Elsewhere
To members of member organizations of the American Institute of Physics and Affiliated Societies ..	$12.00	$13.00
To all others	14.00	16.00

Back Number Prices

Yearly back number rate when complete year is available: $17.00.
Single copies: $1.75 each (exception: March, 1958—$3.00 each).

Changes of address should be sent to the American Institute of Physics.

Advertising rates supplied on request. Orders, advertising copy, and cuts should be sent to the American Institute of Physics.

The Journal of Applied Physics is published monthly at Prince and Lemon Streets, Lancaster, Pennsylvania.
Second-class postage paid at Lancaster, Pa.

IN TOUCH WITH NEW WORLDS

Another project of IBM Applied Scientists: helping solve Einstein's Two-Body Problem

Helping to increase man's understanding and control of reality is a job of IBM Applied Science Representatives. Project by project, through unique and creative applications of data processing, they are changing the worlds of engineering, the sciences, and business.

IBM Applied Scientists are even helping illuminate the fundamental mysteries of space and matter. They are working with mathematicians in an attempt to solve Einstein's field equations for the Two-Body Problem, using an IBM computer.

Others are working on industrial process control, linear and non-linear programming, operations research, and design analysis. The variety of projects is limitless.

You may play an important part in this challenging profession. There are openings in many cities for men and women with advanced degrees in engineering, mathematics, or a physical science, or a degree in one of these areas plus a Master's in business administration or experience in programming.

For a confidential interview, please call any IBM Branch Office or one of these Regional Managers of Applied Science:

L. M. Fulton
IBM Corporation
425 Park Avenue
New York 22, N.Y.

R. W. DeSio
IBM Corporation
618 S. Michigan Ave.
Chicago 5, Ill.

L. C. Hubbard
IBM Corporation
3424 Wilshire Blvd.
Los Angeles 5, Calif.

DATA PROCESSING DIVISION **IBM.**®

A NEW STANDARD OF EXCELLENCE

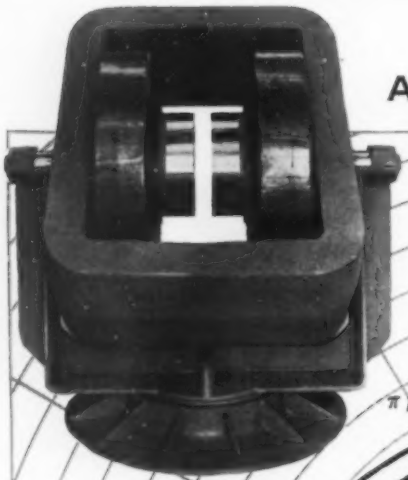

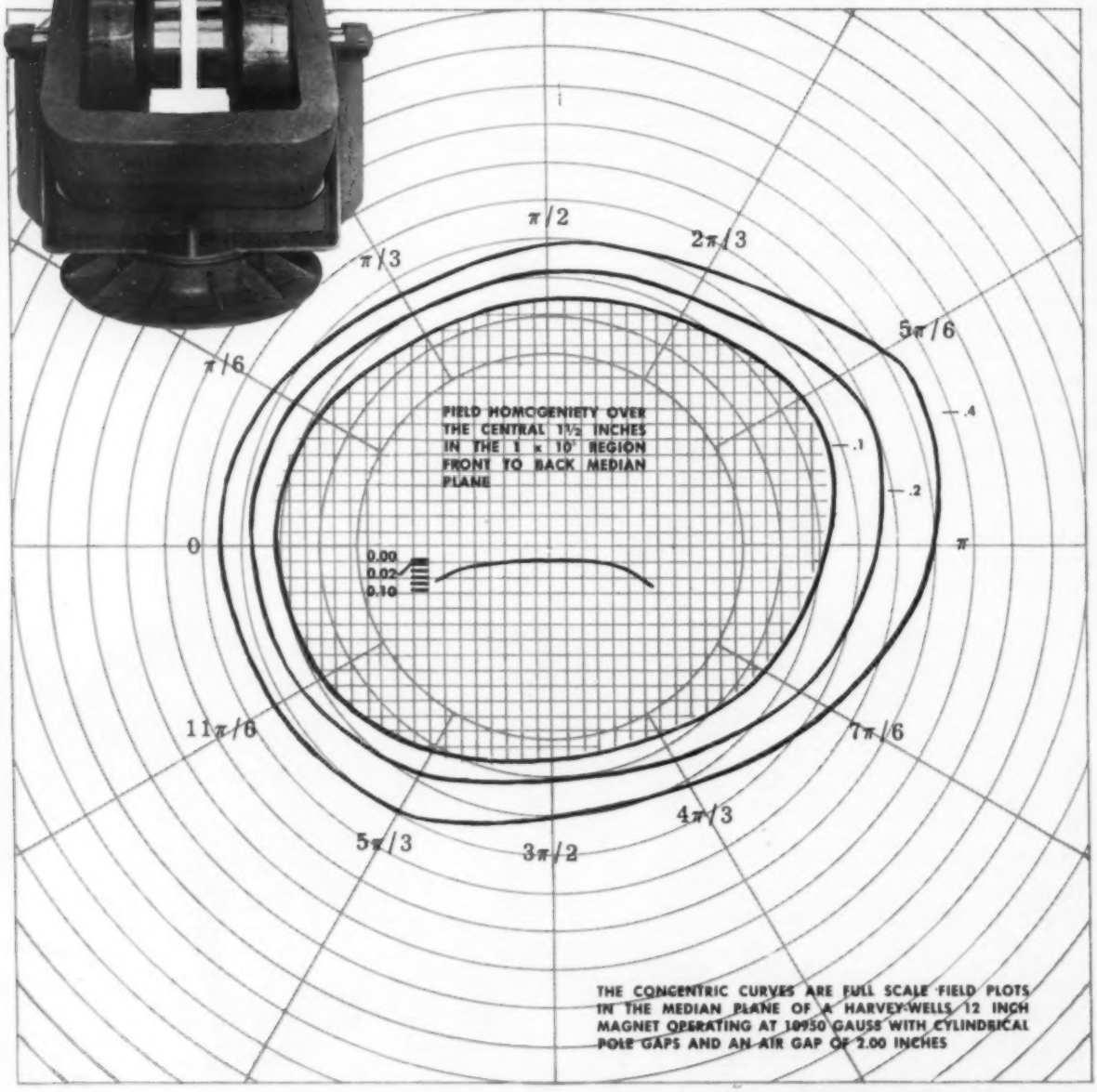

The concentric curves and specifications shown above are indicative of the performance parameters of the new Harvey-Wells Model L-128 Electromagnet. A magnet development program, staffed with specialists in metallurgy, magnet design and solid state research applications, together with consultants of recognized stature, has produced this member of a new family of electromagnets, designed with the end user in mind and which afford greater flexibility and ease of operation.

A cast yoke for increased mechanical rigidity and field homogeniety and a continuously regulated power supply are but two of the advanced features of the Model L-128. Full specifications and performance details will be sent promptly upon request.

For specifications write to

HARVEY-WELLS ELECTRONICS, INC.
14 HURON DRIVE
EAST NATICK INDUSTRIAL PARK
NATICK, MASSACHUSETTS
CE 5-7370 OL 3-7380

HW

NMR GAUSSMETER
NMR FIELD CONTROL
LABORATORY ELECTROMAGNETS AND POWER SUPPLIES
CONTRACT MAGNETS AND POWER SUPPLIES

FIRST PHONE CALL VIA MAN-MADE SATELLITE!

"Project Echo" satellite went into a near-perfect circular orbit 1000 miles high, circling the earth once every two hours. Its orbital path covered all parts of the U. S.

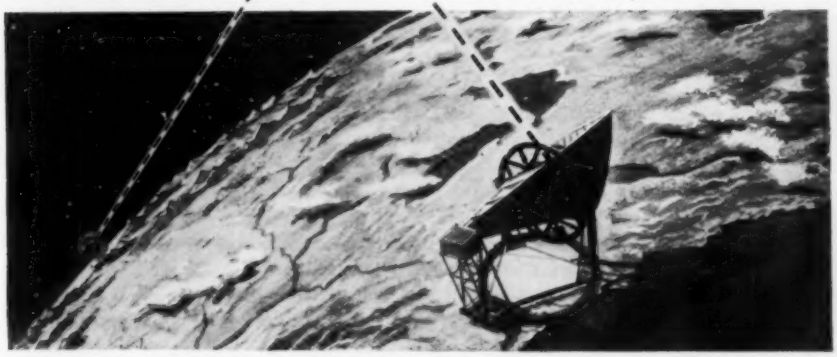

BELL TELEPHONE LABORATORIES BOUNCES VOICE OFF SPHERE PLACED IN ORBIT A THOUSAND MILES ABOVE THE EARTH

Think of watching a royal wedding in Europe by live TV, or telephoning to Calcutta—*via outer-space satellites!* Once a mere dream, this idea is now a giant step closer to reality.

Bell Telephone Laboratories recently took the step by successfully bouncing a phone call between its Holmdel, N. J., test site and the Jet Propulsion Laboratory of the National Aeronautics and Space Administration (NASA) in Goldstone, California. The reflector was a 100-foot sphere of aluminized plastic orbiting the earth 1000 miles up.

Dramatic application of telephone science

Sponsored by NASA, this dramatic experiment—known as "Project Echo"—relied heavily on telephone science for its fulfillment . . .

- The Delta rocket which carried the satellite into space was steered into a precise orbit by the Bell Laboratories Command Guidance System. This is the same system which recently guided the remarkable Tiros I weather satellite into its near-perfect circular orbit.
- To pick up the signals, a special horn-reflector antenna was used. Previously perfected by Bell Laboratories for microwave radio relay, it is virtually immune to common radio "noise" interference. The amplifier—also a Laboratories development—was a traveling wave "maser" with very low noise susceptibility. The signals were still further protected from noise by a special FM receiving technique invented at Bell Laboratories.

"Project Echo" foreshadows the day when numerous man-made satellites might be in orbit all around the earth, acting as 24-hour-a-day relay stations for TV programs and phone calls between all nations.

This experiment shows how Bell Laboratories, as part of the Bell System, is working to advance space communication. Just as we pioneered in world-wide telephone service by radio and cable, so we are pioneering now in using outer space to improve communications on earth. It's part of our job, and we are a long way toward the goal.

BELL TELEPHONE LABORATORIES
World Center of Communications
Research and Development

How Do You Meet a Challenge?

Delco Radio is doing it with TALENT and RESOURCES

We feel the challenge of new concepts in electronics and Solid State Physics can only be met by an intelligent application of outstanding abilities and resources.

To meet this challenge, Delco—over the years—has built up over one million square feet of modern manufacturing, laboratory and office facilities. Newest in the Delco complex is a 125,000 sq. ft. engineering and research facility now under construction in Kokomo, Ind., and scheduled for completion in 1961. In addition, Delco has available the extensive services of the General Motors Technical Center and field test facilities.

But physical resources are only half the answer. It took bold, imaginative talent to lead Delco to its present respected position in the electronics industry. Likewise, the challenge of the future requires a constant infusion of new ideas and new talent.

To maintain and further expand leadership in these areas, we are conducting aggressive programs in semiconductor device development and new materials research. This activity has created unusual opportunities for those who qualify. Specifically, we are vitally interested in ambitious men with experience and TALENT in the following areas:

SEMICONDUCTOR DEVICE DEVELOPMENT

We need men with experience in the techniques of semiconductor device development including alloying and diffusion.

We need a man with experience in the chemistry of semiconductor devices.

We need a man with experience in semiconductor materials to lead a program on metallurgical research of new semiconductor materials.

We need a man with experience in semiconductor device encapsulation.

PROCESS ENGINEERING

We need several men for production set-up and trouble shooting.

EQUIPMENT DEVELOPMENT

We need men to develop automatic and semi-automatic fabrication equipment.

We're eager to find experienced personnel with a desire for a stimulating challenge and the abilities to fulfill this challenge. Responsible positions are available for those who qualify.

If you're interested in becoming a member of our Delco—GM team of outstanding scientists and engineers, send your resume today to the attention of Mr. Carl Longshore, Supervisor Salaried Employment.

DELCO RADIO
DEPENDABILITY
RELIABILITY

Division of General Motors · Kokomo, Indiana

3 *good ways to make dc measurements*

KEITHLEY ELECTROMETERS have up to 64 voltage, resistance and current ranges

1 Model 610A, 64 ranges

The line-operated 610A is a refinement of the popular 610, covering virtually every dc laboratory test. It measures nine voltage ranges from 0.01 to 100 volts full scale with 2% accuracy, current from three amperes to 1 x 10^{-13} ampere full scale, and resistance from 10 ohms to 10^{14} ohms full scale. The 610A also serves as a useful dc pre-amplifier with precise gains to 1000 and outputs for driving scopes and recorders. Input resistance is variable from one ohm to over 10^{14} ohms. The instrument checks its own resistance standards. Zero drift is within two millivolts per hour. **$480.00**

2 Model 600A, 54 ranges

This portable instrument is a battery-operated counterpart of the 610A. Its ranges cover 10 mv to 10 volts, 3 amperes to 10^{-13} ampere, and 10^{4} to 10^{13} ohms full scale. Like the 610A, it has selectable input resistance, a dc to 100 cps bandwidth, and output sufficient to drive recorders directly. Battery life is 500 hours; condition may be checked on the panel meter. **$380.00**

Three accessory probes and test shield are available to facilitate measurements and extend voltage ranges to 30 kv (Model 610A) or 10 kv (Model 600A).

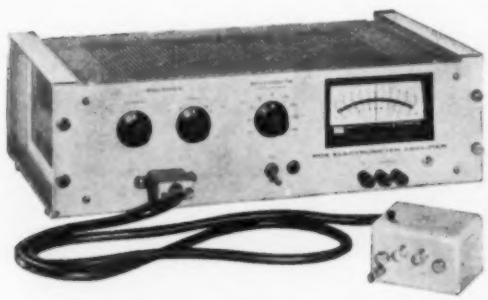

3 Model 603, differential input

This instrument is a wide-band dc amplifier, with an extremely high input impedance, high voltage and current sensitivity, and a remote differential input. Its separate input head permits measurements up to 24 feet from the amplifier. The 603 has nine ranges from 2.5 to 1000 mv, with precise gains up to 4000, and a 10-volt output at 10 ma. Bandwidth is dc to 10 kc on the 2.5 mv range, rising to 30 kc on the 1000 mv range. **$650.00**

KEITHLEY INSTRUMENTS, INC.
12415 EUCLID AVENUE CLEVELAND 6, OHIO

Experimental Physicists – MS & PhD

COLLISION STUDIES IN PLASMA PHYSICS

...Part of a broad program in radio physics attracting scientists to SYLVANIA

ARL
Applied Research Laboratory

New effectiveness for communication and detection systems in natural and man-made environments may result from current Sylvania efforts in the field of plasma physics.

In the Radio Physics Department of the Applied Research Laboratory, investigators are studying a variety of wave propagation and scattering techniques in ionized gases and conducting fluids. Of particular promise are experimental developments in microwave diagnostics of ionized gas flow.

Through microwave heating, inelastic collisions are being induced between free electrons in ionized air. To measure collision frequency, the fractional energy loss G per collision must be known. New experiments will measure the temperature dependence of G in the afterglow of a DC discharge in ionized air. Small shock tube environments are also being explored.

Additional programs involve electromagnetic phenomena associated with solar flares and aurora, propagation in non-uniform media, and formulation of a new microscopic electrodynamics theory of the ionosphere.

The Applied Research Laboratory's studies in radio physics offer important opportunities to advance your professional reputation in a genuine scientific environment. Qualified physicists will be invited to meet the manager of the Radio Physics Department to discuss programs in progress and the opportunities for initiating original studies.

Please write in confidence to Dr. Leonard Sheingold, Director, Applied Research Laboratory

Waltham Laboratories / **SYLVANIA ELECTRONIC SYSTEMS**
A Division of

SYLVANIA
Subsidiary of GENERAL TELEPHONE & ELECTRONICS

100 First Avenue—Room 10-B—Waltham 54, Massachusetts

SOLID STATE ELECTRONICS

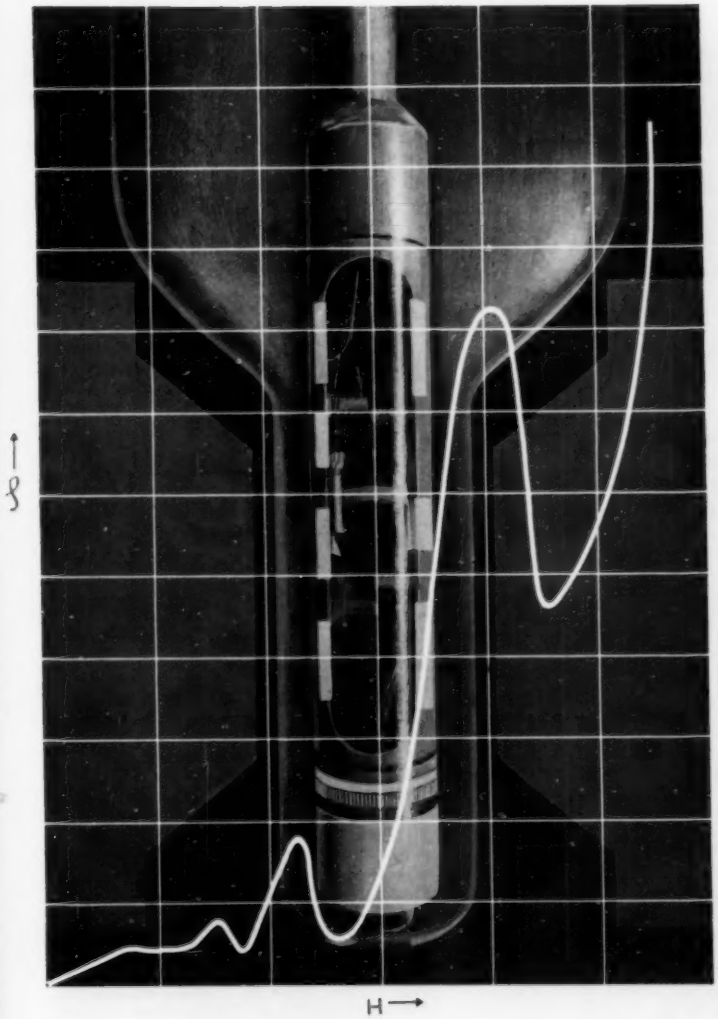

Observation of oscillatory behavior of magneto-resistance in semiconductors at low temperatures. This study of Landau levels in conduction or valence bands provides band structure information necessary to an understanding of transport properties.

At Lockheed Missiles and Space Division, solid state electronics encompasses a wide range of activities. Solid state physics concerns itself with theoretical and experimental work in the areas of paramagnetic resonance studies in solids; ferromagnetics and ferroelectrics; transport processes in solids; infrared spectroscopy; microwave properties of solids; radiation effects in semiconductors; crystal growth; and other related topics.

In solid state devices, the basic work applies to thermoelectric and radiant energy conversion; evaluation of environmental effects; and the study of new components based on ferrites, ferroelectrics, thin films, semiconductors, intermetallic compounds and other solid state materials.

Research in solid state circuits relates to circuit aspects of novel solid state components and systems, such as in microsystem electronics and in lumistor circuitry; and to unconventional uses of existing solid state devices.

Engineers and Scientists: Programs at Lockheed Missiles and Space Division reach far into the future and deal with unknown and challenging environments. If you are experienced in one of the above areas, or in related work, you are invited to join a company with an outstanding record of achievement and make an important individual contribution to your country's scientific progress. Write: Research and Development Staff, Dept. J-32, 962 W. El Camino Real, Sunnyvale, California. U.S. citizenship or existing Department of Defense industrial security clearance required.

Lockheed
MISSILES AND SPACE DIVISION

Systems Manager for the Navy POLARIS FBM; the Air Force AGENA Satellite in the DISCOVERER, MIDAS and SAMOS Programs

SUNNYVALE, PALO ALTO, VAN NUYS, SANTA CRUZ, SANTA MARIA, CALIFORNIA · CAPE CANAVERAL, FLORIDA · HAWAII

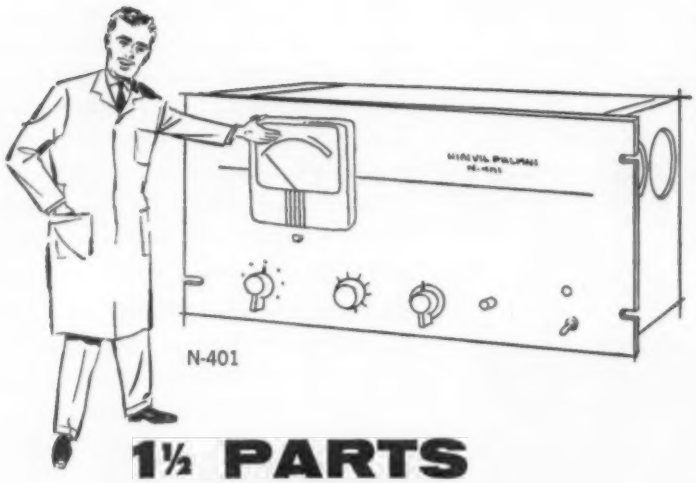

N-401

1½ PARTS PER MILLION LONG TERM STABILITY*

In Hamner's N-401 High Voltage Power Supply, stability is unexcelled, yet its measurement for the purpose of laying down specifications posed a great problem. The measurement was made by a leading university noted for their precision measurements of atomic constants by X-ray methods. The results obtained indicated a basic long term stability of *approximately 1½ parts per million per day — actually more stable than batteries. In the experiment, resistances used to attenuate the N-401's output had been aged and their values studied for over 50 years. Temperature was held constant to within .05°C.

Voltage:	500-1800 V, dual polarity
Current:	0-5 ma
Noise and Ripple:	Less than 1 mv rms at full output

The N-401 has been designed for use in scintillation and proportional counting systems, where other systems' components offer the same degree of stability.

Some of Hamner's other instruments are described at the right. Each instrument has been designed to operate as an independent unit or in a system with other Hamner instruments.

Hamner

Hamner Electronics Co., Inc.

Department 10AP, P. O. Box 531, Princeton, New Jersey
PEnnington 7-1320

N-357 ULTRA LOW-NOISE PREAMPLIFIER

This unit has been designed especially for use with Solid State Detectors. The performance of this instrument is unexcelled in providing a high S/N ratio.

Gain:	100
Risetime:	0.25 μs
Input Capacity:	Approx. 20 mmf
Equivalent Input Noise:	20 μv peak to peak
Output Pulse Shape:	negative, noise to 2.5 volts, 7 μs RC decay
Output Impedance:	100 ohms

The preamplifier incorporates an adjustable bias supply for the solid state detector. Pulse shaping has been selected for optimum S/N ratio and to match the input requirements of Hamner's N-300 series amplifiers. The latter units will also provide suitable B+ and filament voltages for the N-357.

The N-357 is available from stock.

Automatic Data Handling with High-Speed Scaler and Crystal-Controlled Electronic Timer

Operating Modes

- **Preset Count:** 15 settings from 10 to 500,000 counts.
- **Preset Time:** 15 settings from 0.1 to 50,000 seconds.
- **Combined Preset Time & Count:** Any of the time or count settings may be used simultaneously with the system stopping when the first preset event occurs.
- **Data Print-Out:** Both scaler and timer provide "staircase" outputs. Time, counts, or both may be printed out or code punched on cards or tape.
- **Automatic Recycling:** The system will recycle automatically, if desired, following occurrence of a preset event and data print-out. In this case, print-out can be cumulative or destructive. Both print-out and automatic recycling can be used in any mode of operation.

These units are not only highly flexible but are also of the fine research quality typical of all Hamner Instruments. Scaler and Timer may be used together to provide the operational modes listed above. They may also be used independently.

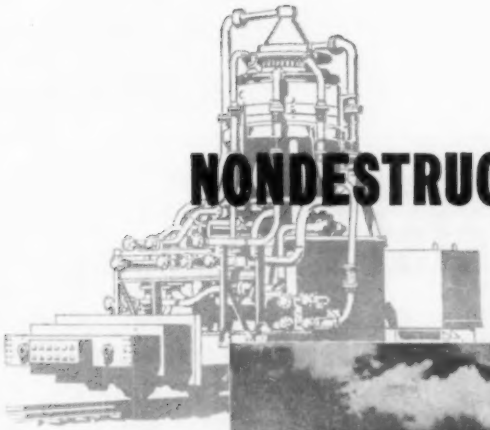

NONDESTRUCTIVE TESTING

an important aspect of scientific progress at Los Alamos

In an attractive scientific, geographical, and climatic environment, nondestructive testing at Los Alamos utilizes an impressive array of equipment and involves a broad variety of problems, materials, and techniques.

Los Alamos representatives, registered at the Ben Franklin Hotel, attending the Philadelphia meetings of the Society for Nondestructive Testing, will be happy to talk with interested Physicists, Metallurgists, Physical Chemists and Engineers. Specialized experience desirable but not mandatory.

If more convenient, write to
Director of Personnel, Division 60-98

los alamos
scientific laboratory
OF THE UNIVERSITY OF CALIFORNIA
LOS ALAMOS, NEW MEXICO

Solid State Physicists ...an invitation to consider

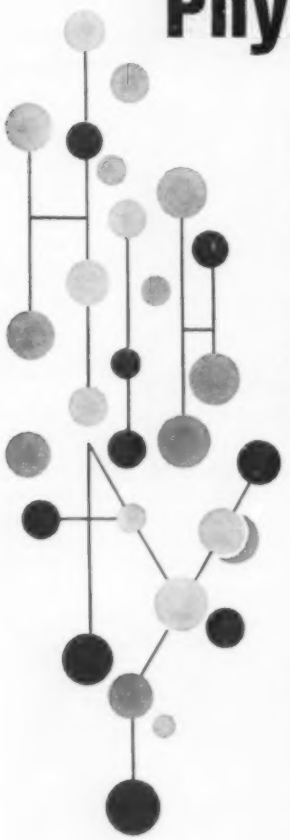

THEORETICAL AND EXPERIMENTAL INVESTIGATIONS

at the Research Division of

STROMBERG-CARLSON

Physicists enjoy the freedom of an academic environment at Stromberg-Carlson's Research Division. Programs are of sufficient breadth as to allow the investigator wide latitude in choice of research.

A sampling of the areas under exploration involves these studies:

- ...relation of various crystal structures to spin levels
- ...interaction between lattice vibrations and microwaves
- ...methods and techniques for preparing semiconductor materials
- ...electrical properties of semiconductor materials
- ...charge transport in semiconducting films and switching mechanism in magnetic films

Research in the commencement stage or proposed for the immediate future involves:

- ...theory of many-particle interaction
- ...defect solid state
- ...nucleation and growth of crystals
- ...cryogenics, emphasizing thermal and electrical properties of matter near absolute zero

If you would like to discuss your field of interest with the head of this research group, write informally to Mr. Maurice Downey. Background at the doctoral level or equivalent is prerequisite to a staff appointment.

STROMBERG-CARLSON

A DIVISION OF **GENERAL DYNAMICS**

1488 N. Goodman St., Rochester 3, New York

many new developments

INCREASE PERFORMANCE, RUGGEDNESS, RELIABILITY

CRL manipulators... as obedient as your hand

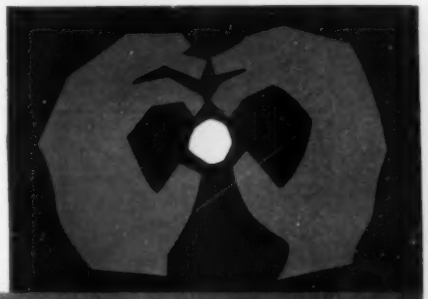

Central Research Laboratories brings you important refinements in lateral rotation, azimuth assembly, wrist joint, tong, handle, roller mounts, load hook, and booting. Each is the result of CRL's continuing program to give you the finest in master-slave manipulators . . . manipulators which duplicate the natural motions of the operators' hand. Many of these improved features can be added to manipulators already in service. This program of improvement without obsolescence plus CRL's policy of immediate shipment on spare parts insures continued customer satisfaction.

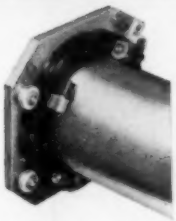

Improved *roller mount:* More rugged, more serviceable, less wear on through tube.

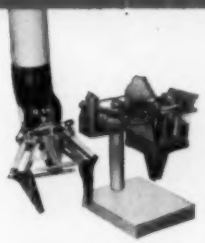

Improved *wrist joint, tong,* and *tong jig:* Greater protection of gears, more rugged, easier interchange.

Improved *handle:* More rugged, more satisfactory control of separation indexing and squeeze motion lock.

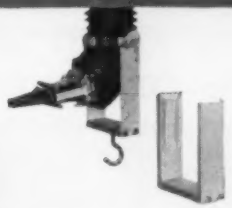

Improved *booting* and *load hook: Partial or* complete booting possible, load hook fits on booted or unbooted arm.

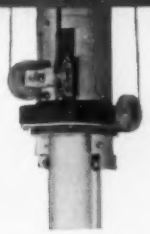

Improved *azimuth assembly:* Eliminates exposed rollers, provides greater "Z" motion or shorter collapsed length.

for thru-wall installation

CRL MODEL 8

Thru-wall installation for intermediate to high-level shielding. Separation indexing and lateral rotation keeps operator close to window with full visibility over large area. Easy to relocate —one man with a light crane can remove and relocate in less than five minutes.

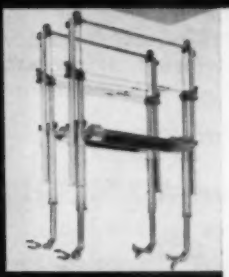

for over-wall installation

CRL MODEL 4

General purpose — for installation over a barrier wall or through ceiling opening of protective enclosure.

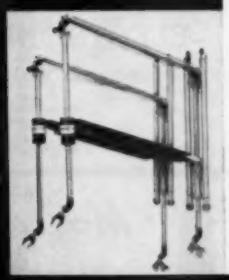

for restricted-space installation

CRL MODEL 7

Space saving, light weight — for use in "junior caves" or over thin walls where minimum clearance and easy portability are important factors.

Central Research Manipulators from basic Argonne National Laboratory designs

write today for complete information to:

Central Research
laboratories, inc.
Red Wing, Minnesota, Dept. 302

Timely McGRAW-HILL Books

Ready now . . .

Middleton—AN INTRODUCTION TO STATISTICAL COMMUNICATION

By David Middleton, Consulting Physicist. *International Series in Pure and Applied Physics.* 900 pages, $25

Collin—FIELD THEORY OF GUIDED WAVES

By Robert E. Collin, Case Institute of Technology. *McGraw-Hill Electrical and Electronic Engineering Series.* 591 pages.

Yeh and Abrams—PRINCIPLES OF MECHANICS OF SOLIDS AND FLUIDS, Volume I.

By Hsuan Yeh, University of Pennsylvania, and Joel I. Abrams, Yale University. *McGraw-Hill Series in Engineering Sciences.* 396 pages, $8.95

Chernov—WAVE PROPAGATION IN A RANDOM MEDIUM

By L. A. Chernov, U.S.S.R. Translated by Richard A. Silverman, New York University. 176 pages, $7.50

Ready in January . . .

Harrington—TIME-HARMONIC ELECTROMAGNETIC FIELDS

By Roger V. Harrington, Syracuse University.

Langmuir—ELECTRONIC FIELDS AND WAVES

By Robert V. Langmuir, California Institute of Technology.

Send for copies on approval

McGraw-Hill
BOOK COMPANY, INC.
330 West 42nd Street New York 36, N.Y.

New CERAMELEX® 1011... A piezoelectric element with the temperature range required for ultrasonic cleaning uses

Designers and manufacturers of ultrasonic microphones, phono cartridges, IF transformers, sonic devices, delay lines and ultrasonic cleaning devices rely on CERAMELEX piezoelectrics for efficient energy conversion.

Barium titanate, first artificially polarized* by Erie Resistor, is the base material of CERAMELEX. This precision-produced material has qualities not found in the conventional single crystal piezoelectrics:

Variety of sizes and shapes . . . ceramic composition allows molding and pressing.

Wide temperature range . . . recommended continuous operation 125°C.

Efficient performance . . . higher degree of energy conversion than possible with natural crystals.

You're invited to contact Department **302** of Erie Technical Ceramics for literature and information regarding further capabilities, tolerances and availability of Erie CERAMELEX products.

*U.S. Patent 2,486,560

NOMINAL CHARACTERISTICS OF CERAMELEX® BODIES

	Ceramelex 1005	Ceramelex 1006	Ceramelex 1007*	Ceramelex 1009	Ceramelex 1011
Density gm/cc	5.6	5.5	5.4	5.6	5.35
Young's Modulus X 10^{10} Newton/m^2	10.2	11.5	10.1	11.0	11.2
Dielectric Constant	1800	1200	1200	1400	700
Diss. Factor %	0.8	0.9	2.5	0.8	0.65
Radial Coup. Coeff, k_r	.33	.31	.37	.32	0.27
k_{31}	0.20	0.18	0.22	0.19	0.16
k_{33}	.47	.48	.55	.52	0.51
$d_{31} \times 10^{-12}$ m/v	−77	−56	−71	−62	−38
$d_{33} \times 10^{-12}$ m/v	180	148	177	168	120
$g_{31} \times 10^{-3}$ v.m./New.	−4.9	−5.2	−6.7	−5.1	−6.1
$g_{33} \times 10^{-3}$ v.m./New.	11.5	13.7	16.7	13.8	19.3
Frequency Constant (fc) cyc. m	1440	1560	1465	1500	1540
Aging %/decade	2	1	4	1½	½
Maximum Temperature °C	100	100	45	110	125
*Phono Pick-up units only					

Write for Erie Bulletin 454, which gives complete technical data on CERAMELEX.

ERIE

TECHNICAL CERAMICS DIVISION

State College, Pa.

ERIE RESISTOR CORPORATION

MATCHED PERFORMANCE · HIGH VACUUM

Welch Duo-Seal® Mechanical and Diffusion Pump Assembly

GUARANTEED VACUUM–0.001 Micron
(0.000 001 mm Hg)

CAPACITY AT 0.1 MICRON–600 Liters Per Minute

No. 1392 Patent No. 2337849

EACH ELEMENT WITH TWO-STAGE CONSTRUCTION

WATER-COOLED OR AIR-COOLED MODELS

- **CONVENIENT**
- **PORTABLE**
- **QUIET RUNNING**

$300.00
Complete with Motor

This is an unusually convenient portable diffusion-pump unit, employing a two-stage mechanical pump and an unbreakable, all-metal diffusion pump. The two components are properly matched as to performance and together will produce a vacuum of better than 10^{-6} mm without the use of cold traps. Complete with oil for both pumping elements.

Other combinations are available with speeds of 120 to 6000 liters per min at 0.1 micron. We will gladly submit full details describing the best combination for your particular application

1392. MECHANICAL AND DIFFUSION PUMP, Water-Cooled
For 115 Volts, 60 Cycles, A.C. **Each, $300.00**

1392A. MECHANICAL AND DIFFUSION PUMP, Air Cooled.
For 115 Volts, 60 Cycles, A.C. **Each, $300.00**

For attached Belt Guard, add $15.00 to above prices.

1391. DIFFUSION PUMP, Only, Water Cooled, With Octoil. **Each, $160.00**

1394. DIFFUSION PUMP, Only, Air Cooled, With Octoil. **Each, $160.00**

1393. MOUNTING PARTS.
For mounting No. 1391 or No. 1394 Diffusion Pump on base of mechanical pump. **Set, $3.00**

W. M. WELCH SCIENTIFIC COMPANY
DIVISION OF W. M. WELCH MANUFACTURING COMPANY
ESTABLISHED 1880
1515 Sedgwick Street, Dept. C-1 Chicago 10, Illinois U. S. A.

Manufacturers of Scientific Instruments and Laboratory Apparatus

REMEMBER THE AMERICAN VACUUM SOCIETY SYMPOSIUM—OCTOBER 12–14

Journal
of
Applied Physics

Volume 31, Number 10 October, 1960

Domains in Thin Magnetic Films Observed by Electron Microscopy*

HARRISON W. FULLER AND MURRAY E. HALE
Computer Products Division, Laboratory for Electronics, Inc., Boston, Massachusetts
(Received April 18, 1960)

A new method for observing full domains in thin magnetic films by electron microscopy is described. Observations are made with standard transmission instruments utilizing an off-centered objective aperture diaphragm as a knife edge. The method has the high-resolution advantage that the microscope is focused on the specimen during domain observations. Limitations of the method and comparisons with the previously reported defocusing technique are presented. Applications to the interpretation of complex domain patterns and cross-tie walls are demonstrated. The observations were made with electrostatic-focusing microscopes, the AEG-Zeiss and Trüb-Täuber instruments, which allow the use of full objective power without influencing the magnetization distribution of low coercive force films. A second method using a knife edge is proposed that would potentially permit a simple measurement of the detailed magnetization distribution of a domain wall in a thin film.

INTRODUCTION

A MEANS for observing domain walls in a thin magnetic film has been demonstrated that utilizes a standard transmission electron microscope in a defocused mode of operation.[1] The defocusing method for viewing domain walls has been analyzed using a simple model for the deflection of electrons passing through the magnetization of a thin-film specimen, and the results have been shown to be in quantitative agreement with experimental observations.[2] The electron microscope defocusing method has been shown to be of value in the investigation of thin-film magnetics[2] as an adjunct to the Kerr and Faraday magneto-optic methods[3,4] and to the Bitter[5] or powder-pattern method[6] of viewing the magnetization distribution in thin films.

In the analysis of the defocusing method of observation an electron passing through the thin-film specimen was assumed to be deflected by a force

$$\mathbf{F}=-(4\pi e/c)(\mathbf{v}\times\mathbf{M}), \tag{1}$$

where $\mathbf{v}$ is the electron velocity in the direction of the optical axis (z axis), and $\mathbf{M}$ is the magnetization of the specimen (in the xy plane). The deflecting force was assumed to act only during the transit of the electron through the thickness of the magnetic material, and to be uninfluenced by demagnetizing fields. The latter assumption is not applicable in general, but applies in many simple but important cases. The resulting angular deflections in the x and y directions, neglecting normal scattering mechanisms, were found to be

$$\begin{aligned}\phi_x(x,y)&=-\Phi M_y/M_s,\\ \phi_y(x,y)&=\Phi M_x/M_s,\\ \Phi&=(4\pi\tau M_s/c)(e/2Vm_0)^{\frac{1}{2}}[1+(eV/2m_0c^2)]^{-\frac{1}{2}}.\end{aligned} \tag{2}$$

In Eq. (2) M_x and M_y are the components of magnetization in the plane of the film at point x,y. M_s is the saturation magnetization, and Φ represents the maximum total angle of deflection including a relativistic correction factor [cf. Eq. (5) of reference 2]. The specimen thickness is τ, V is the accelerating potential of the instrument, and m_0 is the electronic rest mass. The electron intensity distribution at an X,Y observation plane below the specimen plane was found in

* This work was supported in part by the Bell Helicopter Corporation, and through contracts by the U. S. Office of Naval Research, Information Systems Branch, and by the U. S. Air Force Cambridge Research Center, Air Research and Development Command.

[1] M. E. Hale, H. W. Fuller, and H. Rubinstein, J. Appl. Phys. **30**, 789 (1959).
[2] H. W. Fuller and M. E. Hale, J. Appl. Phys. **31**, 238 (1960).
[3] C. A. Fowler, Jr., and E. M. Fryer, Phys. Rev. **100**, 746 (1955).
[4] M. E. Hale, *1958 Fifth National Symposium on Vacuum Technology Transactions* (Pergamon Press, New York, 1959), p. 212.
[5] F. Bitter, Phys. Rev. **38**, 1903 (1931).
[6] H. J. Williams and R. C. Sherwood, J. Appl. Phys. **28**, 553 (1957).

Copyright © 1960 by the American Institute of Physics.

terms of parametric equations in x and y:

$$I(X,Y)=I_0\left|\left(1+z\frac{\partial\phi_x}{\partial x}\right)\left(1+z\frac{\partial\phi_y}{\partial y}\right)-z^2\frac{\partial\phi_y}{\partial x}\frac{\partial\phi_x}{\partial y}\right|^{-1} \tag{3}$$

$$X=x+z\phi_x,$$

$$Y=y+z\phi_y.$$

In Eq. (3) I_0 is the (uniform) electron beam intensity at the specimen plane, and z (*positive*) is the *defocusing distance* of the observation plane *below* the specimen plane.

Note from Eq. (3) that the formation of an image at the observation plane due to the magnetization of the specimen depends on defocusing, i.e., on making $z\neq 0$, for otherwise all electrons deflected by the specimen that are within the (symmetrical) angular aperture of the objective are returned to the correct image point in the image plane. This requirement imposes the disadvantage that the normal structural details of the film are not in focus, though in practice an in-focus micrograph can be obtained separately. The present paper, by contrast, discusses methods of viewing the magnetization of a thin film at instrumental focus through the use of a knife edge positioned appropriately in the optical system to intercept a portion of the electron beam.

The electron microscope observations so far reported[1,2] were obtained with a magnetic instrument (Philips EM75B). High magnification and resolution defocusing observations require operating the objective under nearly normal focused conditions, and such observations with a magnetic instrument frequently cannot be made because of the influence of the field of a magnetic objective lens on the specimen. Some exploratory work was accordingly carried out with the AEG-Zeiss and Trüb-Täuber electrostatic instruments.[7] It was in the course of this work that a practical method of viewing domains at focus was discovered, and the micrographs of the paper were obtained with these instruments.

METHOD OF OBSERVATION

The method used with the AEG-Zeiss and Trüb-Täuber instruments produces full-domain intensity contrast at instrumental focus. The microscope is adjusted by focusing the (full-power) objective on the thin-film specimen and manipulating the centering controls of the objective aperture diaphragm, which is in the back focal plane of the objective, so that an edge of the diaphragm used as a knife edge intercepts the electrons that have passed through domains of one magnetization direction, but not those that have passed through others. There is a reduction of electron intensity in the final image plane for the domains affected by the knife edge, giving an intensity contrast between domains of differing magnetization direction. The technique is reminiscent of the Foucault knife-edge test used for observing the figure of optical mirrors,[8] and appears to be identical to the method used by Boersch and Raith.[9]

The method is explained in greater detail by considering that for an ideal lens, parallel beams converge at a point in the back focal plane that is off-axis by a distance proportional to the angle between the parallel beams and the optical axis.[10] The geometry is shown in Fig. 1 where the incoming parallel beams make an angle ϕ with the optical axis, and converge at a point P in the back focal plane. F_1 and F_2 are the focal points that determine the position of the focal planes. H_1 and H_2 are the principal points defining the position of the principal planes of the lens as shown in the figure. The point P is located by the standard construction shown in Fig. 1 using the incoming beam that passes through F_1. It is seen that

$$PF_2=F_1H_1\tan\phi\doteq f\phi,\phi\ll 1, \tag{4}$$

where f is the focal length of the lens.

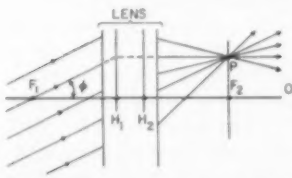

FIG. 1. Geometry for the focusing of parallel rays by an ideal lens.

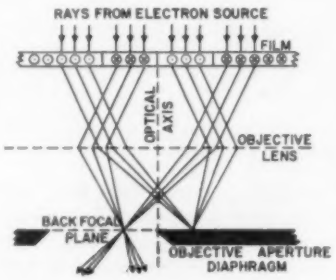

FIG. 2. Interception of deflected rays from one set of like-oriented domains by off-centered objective aperture diaphragm.

Figure 2 shows how the above consideration of parallel-ray focusing applies to the method of viewing full domains in an electron microscope. The nearly parallel rays making up the electron beam travel parallel to the optical axis of the microscope and enter the domain-bearing film. The electrons undergo a deflection due to the Lorentz force in passing through the film, [Eq.(1)]. The angle of deflection has a magnitude Φ[Eq. (2)]

[7] For descriptions of the AEG-Zeiss and Trüb-Täuber instruments see H. Schluge, Zeiss-Werk-Z. **2**, 105 (1954), and M. Gribi, M. Thürkaus, W. Villiger, and L. Wegmann, Optik **16**, 65 (1959).

[8] J. Strong, *Procedures in Experimental Physics* (Prentice-Hall, Inc., Englewood Cliffs, New Jersey, 1938).

[9] H. Boersch and H. Raith, Paper J6, Meeting of the German Electron Microscope Society, Freiburg, Germany, October 21, 1959.

[10] C. E. Hall, *Introduction to Electron Microscopy* (McGraw-Hill Book Company, Inc., New York, 1953), p. 44.

for the case shown in Fig. 2, and the direction of deflection depends on the direction of magnetization in the domain. Similarly directed domains deflect electrons passing through them in the identical direction. For domains with magnetization pointing into the paper, the associated electrons are accordingly caused by the objective lens to converge to a point at the back focal plane and to the left of the optical axis, while for domains with magnetization pointing out of the paper, the associated electrons converge at a point symmetrically to the right of the optical axis.

Note that a (large magnification) objective lens, still referring to Fig. 2, is arranged with the specimen plane slightly above the front focal plane. The focused image then appears a considerable distance below the back focal plane, that distance being approximately mf, with

FIG. 3. Full-domain contrast by "Foucault" method of observation using AEG-Zeiss. Film is Fe-Ni and micrograph is 20μ wide. Aperture diaphragm edge was moved into optical axis from lower right (from 110°).

f the focal length and m the magnification. If the (circular) objective aperture diaphragm in Fig. 2 were centered, therefore, all the rays from both sets of domains would pass through the diaphragm and be focused to the correct points in the image plane in spite of the magnetic domain deflections, as long as the deflections are within the angular aperture of the lens. A centered diaphragm thus results in no intensity contrast between oppositely directed domains. When the diaphragm is off-centered as in Fig. 2, however, the electrons from domains whose magnetization is directed out of the paper are intercepted by the diaphragm edge and do not arrive at the image plane. These domains accordingly appear dark in the image, while the oppositely directed domains appear bright.

Figure 3 shows a micrograph obtained by the above-described "Foucault" method using the AEG-Zeiss

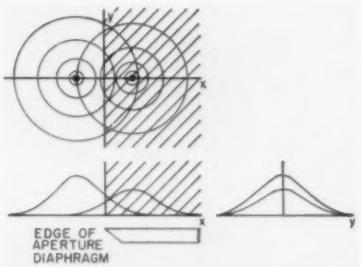

FIG. 4. Electron intensity distribution at back focal plane for random scattering in addition to magnetic deflections, and effect of off-centered aperture diaphragm.

instrument. The diaphragm edge, serving as a knife edge, was brought toward the optical axis from the lower right side, a direction approximately perpendicular to the domain wall as in Fig. 2. Note in Fig. 3 that some intensity and fine detail remain in the image of the dark domains that would not be expected from the idealized ray paths of Fig. 2. The most significant factor contributing to this reduced contrast is the normal random scattering of electrons that occurs in addition to the coherent magnetic deflections. The deflection angle of Eq. (2) is in the order of $\Phi \sim 10^{-4}$ rad, and the normal small-angle scattering (within the objective aperture), which is predominantly due to inelastic collisions, is also in the order of 10^{-4} rad.[11]

The superposition of random scattering on magnetic deflections means that the two points of electron convergence in the back focal plane in Fig. 2 must be replaced by two radially symmetrical distributions centered on the two previous points. This is illustrated in the three-view diagram of Fig. 4, where the bell-shaped electron intensity distribution at the back focal plane is indicated, and where it is assumed, by the unequal heights of the two intensity lobes, that the total area of domains whose electrons are intercepted is less than the total area of the antiparallel domains. It is seen from Fig. 4 that because of random scattering, a certain fraction $r<\frac{1}{2}$ of the electrons in the intercepted lobe pass through the objective aperture diaphragm and are correctly focused to image the "dark" domains, while the same fraction $r<\frac{1}{2}$ of the electrons in the nonintercepted lobe are lost from the image of the "bright" domains. The intensity contrast between the two sets of domains is thus $(1-r)/r>1$.

Other contributions to a reduction in domain contrast through broadening of the electron distribution of individual lobes at the back focal plane are the angular aperture of the electron source, and objective aberrations. If the aperture diaphragm edge is not accurately in the back focal plane a further reduction in domain contrast results, together with a general nonuniformity of average intensity over the image plane.

The aperture diaphragm edge is drawn as a straight

[11] See footnote reference 10, p. 234.

FIG. 5. Same specimen as in Fig. 3, but with aperture diaphragm edge moved into optical axis from lower left (from 200°).

edge in the xy-plane view of Fig. 4, when actually the diaphragm opening is circular. This approximation is justified in the present case, since from Eq. (4) the separation between lobe centers at the back focal plane is $2\Phi f = 2(10^{-4})(0.6) \doteq 10^{-4}$ cm, while the diameter of the diaphragm opening was 50 μ.

Note in the micrograph of Fig. 3 that several bright spots due to holes in the film have assumed a semicircular shape with an off-centered aperture diaphragm, while with a centered diaphragm the holes are circular. The semicircular spots were found to "point" in the direction from which the diaphragm edge was moved toward the optical axis. The effect was explained[12] as a deformation of the Fresnel fringes around a hole as a result of unsymmetrically cutting away a portion of the subsidiary maxima of the intensity distribution in the focal plane. The effect is a potential limitation to the resolution that can be obtained in "Foucault" observations of domains, even though the image is a focused one for this method. The effect might be reduced by utilizing a knife edge in the back focal plane of a projector lens.

FIG. 6. Same specimen as in Fig. 3, but with aperture diaphragm edge moved into optical axis from top (from 340°).

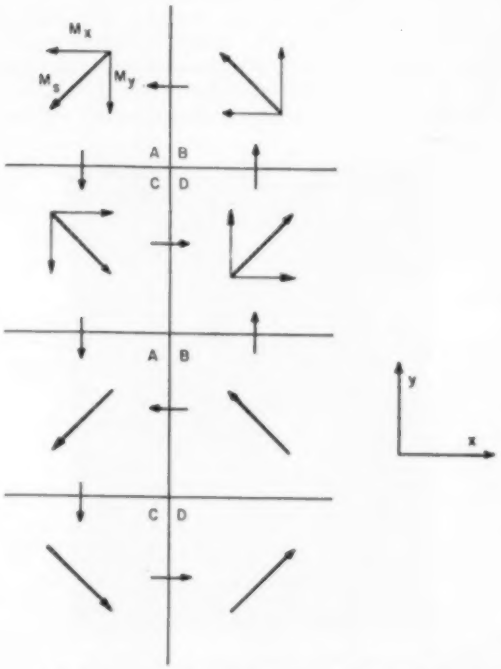

FIG. 7. Simplified domain configuration illustrating the observations of Figs. 3, 5, and 6.

OBSERVATION OF COMPLEX DOMAINS BY "FOUCAULT" METHOD

The AEG-Zeiss instrument was used to observe complicated domain configurations in an Fe-Ni film in which the magnetization direction assumed not one of two but one of several directions in the film. Figures 3, 5, and 6 are a sequence of micrographs for exactly the the same region of the Fe-Ni film, observed by "Foucault" method. The only difference in conditions between the micrographs is the direction from which the aperture diaphragm edge is brought to the optical axis. From the three figures it is apparent that two distinct "families" of domains exist in the film. The light wall in Fig. 5 that runs upward from left to right appears

[12] W. Weitsch, Carl Zeiss Works, Oberkochen, Germany (private communication). Dr. Weitsch has demonstrated the occurrence of similar patterns about holes in a nonmagnetic film.

because of a slight inadvertent defocusing of the instrument. The walls visible in the left-hand domain of Fig. 3 similarly result from this defocusing, which is not necessary to the "Foucault" observations.

Figure 7 is a simplified magnetization distribution that will be used to explain the observations made in Figs. 3, 5, and 6. The configuration of Fig. 7 is seen to consist of domains whose magnetizations are oriented in one of four directions along 45° lines of the x,y coordinate system. Films in which this multiplicity of magnetization direction occurs are frequently found, and are identified with low uniaxial anisotropy. The walls are 90° Néel walls indicated by the small arrows, with Bloch regions at the intersections between walls. The angular deflection of electrons in passing through

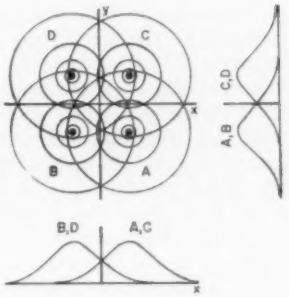

FIG. 8. Electron intensity distribution at back focal plane of objective lens for domain configuration of Fig. 7.

the magnetization of a domain is, from Eq. (2),

$$\phi = -\mathbf{x}_1\Phi(M_y/M_s)+\mathbf{y}_1\Phi(M_x/M_s). \qquad (5)$$

When the effects of random scattering are superimposed

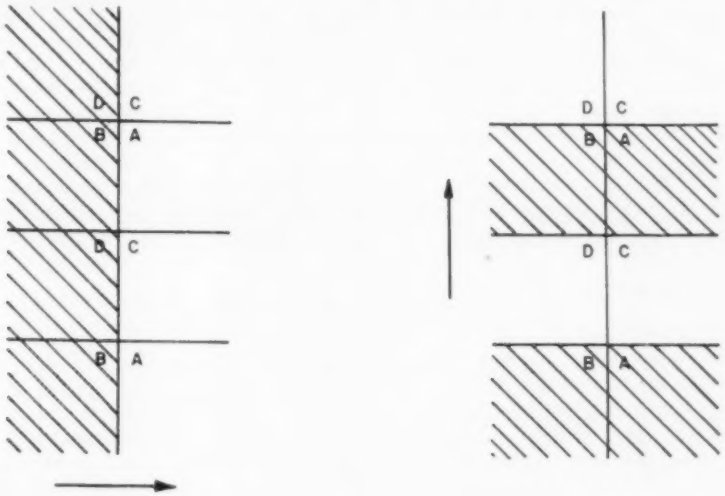

FIG. 9. Intensity contrasts of domain images obtained by "Foucault" method. The arrow in each case indicates the direction from which the aperture diaphragm edge is moved into the optical axis.

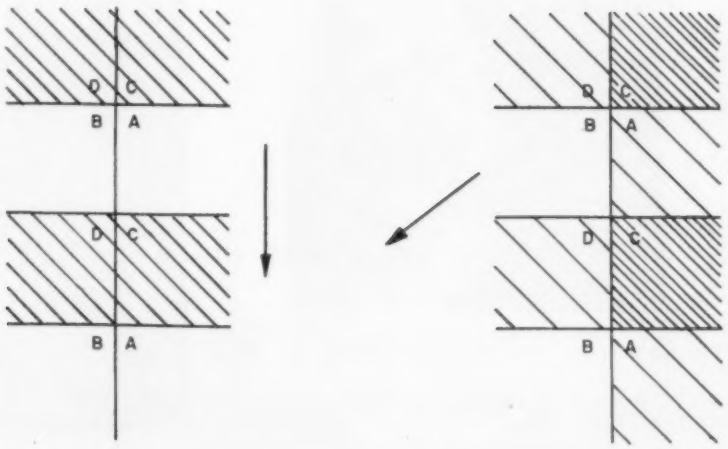

on the magnetic deflections, Eq. (5) gives the electron intensity distribution at the back focal plane of the objective shown in the three-view diagram of Fig. 8, where the four lobes are identified with the domains of Fig. 7 through the labels A, B, C, and D.

By imagining the aperture diaphragm edge to be moved into the optical axis from various directions in Fig. 8, it is possible to derive the intensity distribution at the image plane after the electrons have been focused (cf. Fig. 4). Four such cases are illustrated in Fig. 9, where the arrow indicates the direction in which the edge was moved from a centered position to the optical axis. In the first three cases the relative domain intensities are $r'<\frac{1}{2}$ and $(1-r')$, where r' is somewhat greater than r previously defined because of the angle that the domain magnetization direction makes with respect to the intercepting edge. In the last case, the relative intensities of domains B are $1-r$, those of domains A and D are $\frac{1}{2}$, and those of domains C are r.

Figure 10 shows a complex multidirectional domain pattern in a 90/10 Fe-Ni film viewed by the "Foucault" method using the Trüb-Täuber instrument. The high contrast and structure-revealing resolution are noteworthy in this micrograph. The Trüb-Täuber instrument, unlike the AEG-Zeiss microscope, possesses a condenser lens that can be overfocused to obtain a small source angular aperture, which may account for the enhanced contrast.

Figures 11 and 12 are micrographs of cross-tie walls in a Permalloy film (20 ohms/square) viewed by the "Foucault" method on the AEG-Zeiss electrostatic microscope. The figures differ in the direction from which the edge of the objective aperture diaphragm is brought to the optical axis. The observations, when interpreted according to the preceding discussion, yield a magnetization distribution that is fully consistent with the Huber, Smith, and Goodenough[13] model.

FIG. 10. Domains in 90/10 Fe-Ni film observed on Trüb-Täuber microscope using the "Foucault" method. Micrograph is 100 μ wide.

[13] E. E. Huber, Jr., D. O. Smith, and J. B. Goodenough, J. Appl. Phys. **29**, 294 (1958).

DOMAIN WALL MAGNETIZATION DISTRIBUTION AT FOCUS

An alternative way to utilize a knife edge in an electron microscope for measuring the detailed magnetization distribution of a domain wall is here proposed. The method has the potential advantages of high resolution, since the specimen is focused, and of simplicity in deriving the magnetization distribution from the experimental data, in contrast to the defocusing method [cf. Eqs. (30) and (31) of footnote reference 2].

In this method an adjustable knife edge is positioned a small distance z beneath the center of a convergent wall in a thin film, as shown in Fig. 13. The opaque knife edge is placed parallel to the wall, below the position where overlap of the convergent beam takes place. The edge in this case is seen to intercept the dotted rays and so exclude them from the image. The lens in Fig. 13 is shown with a magnification of unity for simplicity. The focused image will accordingly have the intensity distribution sketched at the bottom of Fig. 13. If the edge is now moved vertically upward, a measurement of the wall-magnetization distribution can be obtained by recording the width x_0 of the light and dark bands of the focused intensity pattern vs the vertical edge position z. The value of x_0 is determined by the condition $X=0$ at plane z, so that from Eq. (3),

$$X=x_0+z\phi_x(x_0)=0, \tag{6}$$

assuming that ϕ_x is a function of x alone (wall parallel to the y axis). From Eq. (2), therefore,

$$M_y(x_0)=(M_s/\Phi)[x_0(z)/z]. \tag{7}$$

The delicacy of adjustment required to carry out this measurement probably makes the measurement impractical at the objective, but an equivalent procedure carried out below the magnified objective image may prove feasible.

FIG. 11. Cross-tie walls in Permalloy film viewed by "Foucault" method with AEG-Zeiss instrument. Aperture diaphragm edge moved into optical axis from 70° direction. Micrograph is 65 μ wide.

FIG. 12. Same specimen as in Fig. 11, but with aperture diaphragm edge moved into optical axis from 140° direction.

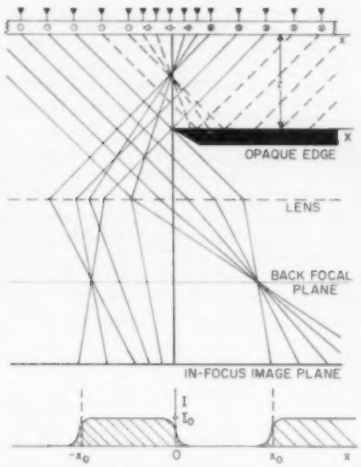

FIG. 13. Proposed in-focus method for measurement of magnetization distribution of a simple (convergent) domain wall using knife edge.

An alternative measurement is possible by fixing z at a value sufficiently large to guarantee overlap of the (convergent) electron beam, then sliding the edge position in the x direction. Again calling the coordinate in the edge plane X, measurements can be made of the X position of the edge vs the positions x_0 of the two edges of the intensity plateau in the focused image. With the experimental data $X(x_0)$, Eqs. (3) and (2) give

$$M_y(x_0) = -(M_s/\Phi)[X(x_0)/z - x_0/z]. \tag{8}$$

An observation of the expected intensity plateau in the focused image (Fig. 13) was attempted with the AEG-Zeiss instrument using a selector diaphragm located 180 mm below the objective and 100 mm above the projector. The correct image was not obtained, probably due to an apparent roughness of the diaphragm edge that was the result of electrostatic charge on the diaphragm.

ACKNOWLEDGMENTS

The authors wish to thank H. Rubinstein for helpful discussions, and to acknowledge the assistance of other members of the Applied Physics Group of the Computer Products Division at Laboratory for Electronics, Inc.

The observations using the AEG-Zeiss instrument were made at the Electron Microscope Laboratory of the Carl Zeiss Works in Oberkochen, Germany, with the kind permission of Dr. H. Mahl and Dr. H. Schluge and with the invaluable assistance of Dr. W. Weitsch, all of that Laboratory.

The observations using the Trüb-Täuber instrument were made at the Electron Microscope Laboratory of the Trüb-Täuber Company in Zurich, Switzerland, with the permission and assistance of Dr. L. Wegmann and M. Gribi.

Longitudinal Wave Propagation in Stretched Polymers

PETER MASON
The British Rubber Producers' Research Association, Welwyn Garden City, Herts, England
(Received October 29, 1959; and in final form May 16, 1960)

The wave equation is derived for the propagation of longitudinal waves along a stretched filament of a highly elastic material. It is found that the tension in the filament reduces the effective modulus by twice the product of Poisson's ratio and the tensile traction, leaving the internal viscosity term unchanged. This result is illustrated by measurements of continuous 1 kcps wave propagation in natural rubber at 50°C, where the damping is small ($\tan\delta<0.1$). An alternative derivation is given for the purely elastic case of zero damping without restriction upon the amplitude.

The "equilibrium" or "static" Young's modulus is obtained for extensions up to about 600% from the slope of the equilibrium stress-strain curve and used to predict the corresponding wave velocities from the wave equation for zero damping. The predicted velocities are slightly higher—by up to about 10%—than the measured velocities. It is shown that the deviations could arise from differences in rate of strain between the wave-propagation and the stress-strain measurements. At the higher extensions the rubber is very hysteretic for large deformations, and the Young's modulus governing the small-amplitude wave propagation is shown to relate substantially to the *loading* branch of the stress-strain curve.

APART from the general acoustical interest in the propagation of longitudinal wavesa long rods or filaments, this subject has been particularly utilized in recent years as a technique for studying the dynamic behavior of polymers.[1–6] Originally the aim was to measure the dynamic properties substantially in the unstrained state so that the usual wave equation was applicable, viz.,

$$\rho(\partial^2\xi/\partial t^2)=E(\partial^2\xi/\partial x^2)+f(\partial^3\xi/\partial x^2\partial t), \tag{1}$$

where ξ is the displacement, ρ the density, E Young's modulus, and f the coefficient of normal viscous traction. Since E and f are defined for vanishingly small strains, it is immaterial whether they are referred to the original or to the strained cross section.

Subsequently, however, the method has been used for stretched filaments, for example, to examine the effects of continuous drawing[7] or to study the strain dependence of the dynamic properties.[8] It is then necessary to derive the wave equation for a uniform filament of the polymer stretched to a mean extension ratio λ at an equilibrium tensile traction σ in which λ is the ratio of the stretched to the unstretched length and σ is the tension divided by the *actual* cross section.

THE EQUATION OF MOTION

In Fig. 1 it can be seen that an element originally of length dx/λ is stretched to a length dx which becomes $dx[1+(\partial\xi/\partial x)]$ when the stretched filament is given a small displacement. Thus the strain at the displaced position $(x+\xi)$ *with reference to the equilibrium stretched state* is $\partial\xi/\partial x$. If E and f are now also taken with reference to the equilibrium stretched state, the traction across the left-hand section of the element caused by the displacement will consist of an elastic component $E\partial\xi/\partial x$ and a viscous component $f\partial^2\xi/\partial x\partial t$. Hence the total traction across this section is given by

$$\sigma_{\text{tot}}=\sigma+E(\partial\xi/\partial x)+f(\partial^2\xi/\partial x\partial t). \tag{2}$$

If the density and cross-sectional area of the element in the equilibrium stretched state are ρ and A, respectively, the mass of the element is $\rho A dx$, and the equation of motion is obtained as

$$\rho A dx(\partial^2\xi/\partial t^2)=[\partial(\sigma_{\text{tot}}A)/\partial x]dx[1+(\partial\xi/\partial x)]. \tag{3}$$

The change in cross-sectional area with strain may be expressed in terms of ν, the Poisson's ratio in the stretched state, by

$$\partial A/\partial x=-2\nu A\partial^2\xi/\partial x^2.$$

On combining this with (2) and (3) the equation of motion becomes

$$\rho\frac{\partial^2\xi}{\partial t^2}=\left\{\left(E\frac{\partial^2\xi}{\partial x^2}+f\frac{\partial^3\xi}{\partial x^2\partial t}\right)-2\nu\frac{\partial^2\xi}{\partial x^2}\left(\sigma+E\frac{\partial\xi}{\partial x}+f\frac{\partial^2\xi}{\partial x\partial t}\right)\right\}\left(1+\frac{\partial\xi}{\partial x}\right),$$

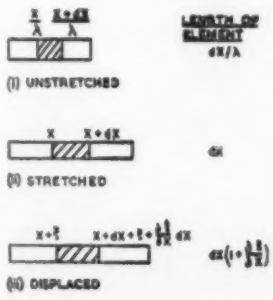

FIG. 1. Strain in a stretched filament.

[1] J. W. Ballou and S. Silverman, J. Acoust. Soc. Am. **16**, 113 (1944).
[2] A. W. Nolle, J. Acoust. Soc. Am. **19**, 194 (1947).
[3] A. W. Nolle, J. Appl. Phys. **19**, 753 (1948).
[4] K. W. Hillier, Proc. Phys. Soc. (London) **B62**, 701 (1949).
[5] R. S. Witte, B. A. Mrowca, and E. Guth, J. Appl. Phys. **20**, 481 (1949).
[6] W. Bismuth, Proceedings of the Third International Congress on Acoustics, Stuttgart, 1959.
[7] K. W. Hillier and H. Kolsky, Proc. Phys. Soc. (London) **B62**, 111 (1949).
[8] P. Mason, J. Appl. Polymer Sci. **1**, 63 (1959).

which, on rearranging and neglecting $\partial\xi/\partial x$ in relation to unity, gives

$$\rho\frac{\partial^2\xi}{\partial t^2}=(E-2\nu\sigma)\frac{\partial^2\xi}{\partial x^2}+f\frac{\partial^3\xi}{\partial x^2\partial t}. \tag{4}$$

The comparison of Eq. (4) with Eq. (1) shows that the tension in the filament reduces the effective dynamic modulus by the amount $2\nu\sigma$ and leaves the internal viscosity term unchanged. Coulson[9] considered the case of undamped propagation in bars where the extension follows Hooke's Law, and found that the effect of tension was to increase the velocity of propagation by the factor λ. By taking $f=0$ and $\sigma=E(\lambda-1)$ in Eq. (4), it can be shown that the ratio of velocities in the stretched and unstretched states is $\{\lambda[1-2\nu(\lambda-1)]\times[\lambda-2\nu(\lambda-1)\}^{\frac{1}{2}}$. With $\nu=0$, (the case considered by Coulson) this ratio reduces to λ; with $\nu=\frac{1}{4}$, it becomes $\lambda^{\frac{1}{2}}$; and for $\nu=\frac{1}{2}$, it is unity so that the propagation velocity in incompressible materials is unaltered by strains within the Hookean region.

CONTINUOUS WAVE PROPAGATION

If the steady-state propagation of small sinusoidal waves is now considered by inserting the condition $\xi=\xi_0\exp\{-\alpha x+\omega(t-x/c)\}$ into (4), the components of the complex Young's modulus ($E^*=E'+iE''$, with $E'=E$ and $E''=\omega f$) are obtained in terms of the propagation constants c (velocity) and α (attenuation) as

$$\left.\begin{aligned}E'&=\rho c^2\frac{1-\beta^2}{(1+\beta^2)^2}+2\nu\sigma\\ E''&=\rho c^2\frac{2\beta}{(1+\beta^2)^2}\end{aligned}\right\}, \tag{5}$$

where $\beta=(\alpha c/\omega)$, $\omega/2\pi$ being the frequency of the vibration. An illustration of the application of these relations is given by Fig. 2. This shows the variation with extension of E', the real part of the dynamic Young's modulus, for natural rubber at 50°C. The values of E' were calculated from the propagation constants of 1 kcps longitudinal waves in stretched rubber filaments using the first of Eq. (5); details of the experimental technique used to measure the propagation constants have been given elsewhere.[10] Now at 50°C and 1 kcps, natural rubber is relatively soft and the term $2\nu\sigma$ (here, equal to σ) may account for a considerable proportion of the modulus E'. The values of E' obtained by the conventional relations for unstrained material (i.e., Eqs. (5) with $\omega=0$) are thus lower than the true values. For the present example the "apparent" values of E', as shown by the open circles in Fig. 2, may be as little as one-half the corresponding values of E'. As E'' is unaffected by the tension, the apparent values of damping (i.e., E''/E' or $\tan\delta$) would be as much as double the true values obtained from Eqs. (5).

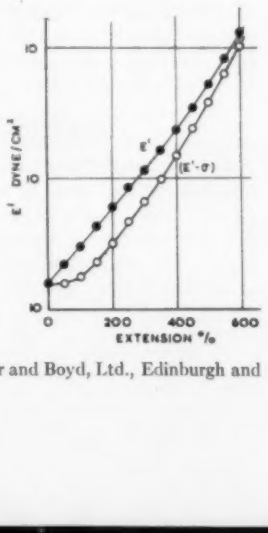

FIG. 2. Variation in E' with extension for natural rubber at 50°C and 1 kcps. ● represents E'; ○ represents $(E'-\sigma)$.

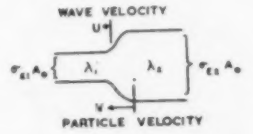

FIG. 3. Propagation along a stretched filament.

PROPAGATION IN THE ABSENCE OF DAMPING

It may be remarked that for perfectly elastic materials the propagation velocity can be deduced from considerations of momentum and continuity. Thus consider a perfectly elastic, incompressible filament initially of cross-sectional area A_0, stretched to an extension ratio λ_1. Suppose that one end is suddenly displaced so that a stress wave is propagated with velocity u along the filament, the particle velocity being v at the rear of the wave where the new extension ratio is λ_2. This situation is illustrated by Fig. 3. Then if σ_s is the "nominal" or "engineering" stress, i.e., the tensile force divided by the unstrained cross-sectional area, the net force acting on the material involved in the wave is $(\sigma_{s1}-\sigma_{s2})A_0$. In unit time the volume of material accelerated from rest to velocity v is $(A_0/\lambda_1)u$ so that the increase in momentum is $\rho u(A_0/\lambda_1)v$. On equating this to the net force, the result is

$$(\sigma_{s1}-\sigma_{s2})\cdot A_0=\rho u(A_0/\lambda_1)v. \tag{6}$$

For continuity, the increase in volume of material at λ_2 must equal the decrease in volume of material at λ_1, so that

$$(A_0/\lambda_1)u=A_0/\lambda_2(u-v). \tag{7}$$

Elimination of v from (6) and (7) then yields

$$u^2=\lambda^2{}_1(\sigma_{s1}-\sigma_{s2})/\rho(\lambda_1-\lambda_2). \tag{8}$$

The argument so far is based solely on the existence of an undispersed wave without any restriction upon its

[9] C. A. Coulson, *Waves* (Oliver and Boyd, Ltd., Edinburgh and London, 1955) 7th ed., p. 54.

[10] P. Mason, in "The Physical Properties of Polymers" (Society of Chemical Industry, London, 1959) Monograph No. 5, p. 262.

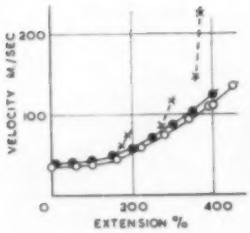

FIG. 4. Velocity of elastic waves in stretched natural rubber at 50°C. ● 1 kcps wave propagation; ○ derived from loading curve; ✕ (with broken line) derived from unloading curve.

amplitude. For infinitesimal displacements, Eq. (8) gives the wave velocity c in the form

$$c=\lambda[1/\rho\cdot d\sigma_s/d\lambda]^{\frac{1}{2}}. \tag{9}$$

As the Young's modulus E for small displacements about a mean extension λ is given by $E=\lambda d\sigma/d\lambda$, and as $\sigma_s=\sigma/\lambda$, the following is obtained:

$$d\sigma_s/d\lambda=1/\lambda^2[E-\sigma].$$

Combining this with Eq. (9) leads to

$$E=\rho c^2+\sigma, \tag{10}$$

which is identical with the real part of the modulus given by Eqs. (5) for zero damping, i.e., for $\beta=0$.

An experimental test of Eq. (9) has been obtained from observations of the velocity of small sinusoidal waves in stretched strips of natural rubber for which the "equilibrium" stress-strain curve in simple extension had been measured. At 50°C and 1 kcps the damping of the rubber was very low, with β varying between about 0.02 and 0.08 over the extension range, and the corresponding loss factor ($\tan\delta=E''/E'$) between about 0.05 and 0.10. Under these conditions the modulus given by Eq. (10) was within 1% of that given by Eq. (5). As there was so little dispersion, Eq. (9) was used to calculate the velocities of propagation at different extensions from the corresponding slopes $d\sigma_s/d\lambda$ of the equilibrium stress-strain curve; the resulting values are shown by the filled circles in Fig. 4 for comparison with the measured values indicated by the open circles. The predicted and measured velocities are seen to agree within about 10% over the extension range examined. Part of the divergence may be due to differences between the test specimens, even though these were cut from the same rubber sheet. A small systematic departure would also be expected in view of the finite, though small, degree of damping, owing to differences in rate of strain between the wave propagation and the equilibrium stress-strain measurements.

THE EFFECTS OF STRAIN-RATE AND HYSTERESIS

To examine the effects of rate of strain more closely, an effective stress-strain curve was derived from the wave-propagation measurements by integrating Eq. (9). Thus,

$$\sigma_s=\rho\int_1^\lambda \frac{c^2}{\lambda^2}d\lambda.$$

The resulting curve is shown in Fig. 5 together with the equilibrium relation obtained by direct loading with weights and two dynamic stress-strain curves obtained from tensometer measurements. It is evident that the deviations in Fig. 4 could be accounted for by differences in rate.

Another possible reason for such deviations, first suggested by Mullins,[11] is that the effective dynamic stiffness at any point on the stress-strain curve is that given by the branch of the stress-strain curve obtained in *unloading* from that point, rather than that corresponding to the complete loading curve. Thus the wave-propagation velocity could be greatly affected by large-strain hysteresis of a material even though the hysteresis loss in small-strain cycles is negligible. Natural rubber under the present conditions is just

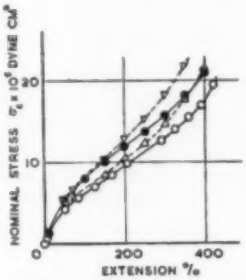

FIG. 5. Stress-strain curves for natural rubber at 50°C. ● derived from 1 kcps wave velocities; ○ "equilibrium" stress-strain curve; △ loading curve at 0.2% sec^{-1}; ▽ loading curve at 2000% sec^{-1}.

such a material, the large-strain hysteresis arising from strain-induced crystallization. Unloading curves from 190%, 300%, and 390% extension were therefore obtained at rates of approximately 100% sec^{-1}; the velocities derived from these results are indicated in Fig. 4. It can be seen that the observed wave-propagation velocities lie between the equilibrium loading values and the unloading values. However, the wave velocities are much closer to the loading than to the unloading data, and it would appear that for small periodic disturbances the governing modulus is essentially that corresponding to the stress-strain curve obtained in loading at the appropriate rate.

ACKNOWLEDGMENTS

The author wishes to thank Sir Geoffrey Taylor for drawing his attention to the dynamical derivation of Eq. (9) and Dr. H. W. Greensmith for providing the dynamic-tensometer measurements of the stress-strain curves. This work forms part of the research program of the Board of the British Rubber Producers' Research Association.

[11] L. Mullins, Trans. Inst. Rubber Ind. **26**, 27 (1950).

Cathode of an Arc in Xenon

JOHN E. WHITE
General Electric Lamp Research Laboratory, Cleveland, Ohio
(Received May 2, 1960; and in final form June 1, 1960)

Energy balance, space charge, and thermionic equations have been combined to provide a description of the mechanism of the cathode in an ac arc, and the quantities required for solution determined experimentally. The experiments were carried out on barium-activated electrodes in xenon at 1.4 atm and extended over a range of 25–75 amps rms. The work function was found to be 1.77 v at zero-field and reduced to 1.67 v under Schottky effect of the space charge field. The work function did not change with current, but the Richardson-Dushman A fell, as the current was raised, to a value of approximately 0.1 at the highest load. The cathode fall varied with phase angle and showed a maximum of 1.2 v at maximum current. The component of current at the cathode carried by ions reduced from 12% to 6% as the load increased.

I. INTRODUCTION

NO generally accepted method has been developed for determination of the thermionic constants of a cathode in a gas discharge. This is because the ion component of the cathode current is generally unknown, and because of other complexities, such as the suspicion that the thermionic "constants" are actually functions of the current in the discharge.

Recent studies of cathodes in fluorescent-lamp-type discharges[1–4] and in discharges at higher pressure[5,6] have contributed to the general understanding but have not produced agreement as to emission mechanisms. Thus Kühl[3] finds pure thermionic emission, with negligible ion component of current at the cathode, adequate to explain even the concentrated, spot-type discharge in the fluorescent lamp. Cayless, on the other hand, finds thermionic emission more than a factor of 10 too low[1] to explain the fluorescent-lamp cathode even before the high-current density spot mode sets in.

These examples from the literature are cited to emphasize the fact that understanding the performance of a hot cathode in a gas involves much more than the determination of work function and substitution into the Richardson-Dushman equation. Cayless[1] cites 7 mechanisms which may be important in the fluorescent-lamp cathode, not to mention autoelectronic emission, important at higher currents.[5]

The investigation to be presented here uses a method different from those described elsewhere and so produces independent results. It has been applied to an arc in xenon at 1.4-atm pressure, in a lamp designed to operate at nearly 100 amp rms.[7] The method seems to reveal facts not generally available for cathodes in gas, such as the value of the Richardson-Dushman A, and the fraction of current at the cathode carried by positive ions. These facts are obtained at the cost of certain assumptions which must not be overlooked. For example, the positive ion fraction is assumed constant through the ac cycle. The validity of assumptions made has been checked by calculation or experiment as far as possible. But it must not be supposed that the assumptions applied here will be equally valid for other cathodes.

One of the restrictive conditions of this study concerns the discharge "mode." When the discharge concentrates into a spot or several of them on the cathode, analysis by the method used here is difficult. Experimentally, when the arc burned in a spot mode the arc drop was about 4 v higher than when the current distributed evenly over the cathode ("diffuse mode"). The electrode temperature was much higher during spot mode operation. It was found possible to eliminate the spot mode permanently in these lamps by proper cathode activation.

A condition which simplified calculations in this work, but which might not apply to some other electrode arrangement, is the fact that electrode heat transfer by conduction and convection is negligible. This turns out to be true because of the low-thermal conductivity of xenon and the convection-minimizing effect of the concentric anode and lamp envelope. Numerically, under a condition where 141 w is radiated from an electrode, 2 w is carried away by conduction and ½ w by convection.

II. ASSUMPTIONS AND EQUATIONS

As indicated above, the object of analysis is the cathode of an ac arc in xenon. The heat necessary for thermionic emission is supplied by the arc itself. The operating pressure is 1.4 atm. Thermal and radiation properties of such arcs have been studied extensively in Germany, which is the justification for taking Schirmer's[8] value of 7300°K as the plasma temperature. It is an equilibrium temperature of atoms, ions, and electrons, and varies little over the range of currents considered because the density of ions is an exponential function of plasma temperature. This temperature T

[1] M. A. Cayless, Brit. J. Appl. Phys. **8**, 331 (1957).
[2] M. A. Cayless, J. Electronics and Control **4**, 237 (1958).
[3] B. Kühl, Tech. Wiss. Abhandl. Osram-Ges. **7**, 73 (1958).
[4] J. F. Waymouth, Sylvania Technologist **13**, (1960).
[5] A. Bauer, Tech. Wiss. Abhandl. Osram-Ges. **7**, 38 (1958).
[6] A. Bauer and P. Schulz, Z. Physik **139**, 197 (1954).
[7] A. Lompe, Lichttechnik **10**, 108 (1958).
[8] H. Schirmer, Z. Physik **156**, 55 (1959).

enters as a relatively small factor in the electrode energy balance.

During the anode half-cycle of the electrode under study, heat is transferred to it primarily by electrons. There is also a contribution by conduction and radiation from the arc, which is w/cm^2 averaged over the cycle, and is delivered to an area A_1. The total energy to the electrode during the time $t/2$ of the half-cycle as anode is, then,

$$\{wA_1+I[2(kT/e)+\varphi_0]\}t/2,$$

which reduces to average power when divided by the period t of the ac wave:

$$W_a=\tfrac{1}{2}wA_1+\tfrac{1}{2}I[2(kT/e)+\varphi_0]. \quad (1)$$

In these expressions, I is the average of the arc current over $\frac{1}{2}$ cycle; k is the Boltzmann constant; e is the electronic charge; and φ_0 is the work function of the region of the anode which collects electrons. Note that the anode fall of potential, if any, does not enter Eq. (1) explicitly but serves only to raise the electron temperature.

While the electrode is cathode, the electrons emitted produce a cooling effect. But the ions carry thermal energy and neutralization energy, analogous to the electron terms of the opposite half-cycle, and energy acquired in the cathode fall V_k as well. Aside from the fact that the ion free path is of the order of the cathode fall space, the large charge-exchange cross section for Xe^+ ions in Xe makes it logical to expect essentially full transfer of the energy acquired by ions in the cathode fall to the cathode.[9] Accordingly, the energy delivered to the electrode during the cathode half-cycle is

$$(wA_1+I\{[1-f][(2kT/e)+V_k+\varphi_+]-\varphi f\})t/2,$$

in which f is the fraction of the current at the cathode carried by electrons, φ_+ is the neutralization energy per ion, and φ is the work function of the cathode-emitting surface.

Dividing the expression for energy by t gives W_c, the average power delivered to the electrode by its operation as cathode:

$$W_c=\tfrac{1}{2}wA_1+\tfrac{1}{2}I\{[1-f][(2kT/e)+V_k+\varphi_+]-\varphi f\}. \quad (2)$$

Since the ions are neutralized at the same surface from which electrons are emitted, and since the latent heat of vaporization of Xe atoms from the cathode is negligible,

$$\varphi_+=V_i-\varphi, \quad (3)$$

where V_i is the ionization potential of xenon.

The total power W dissipated from the electrode in full-wave operation is the sum of the power components delivered to it from its operation as anode and its operation as cathode:

$$W=W_a+W_c. \quad (4)$$

It must now be recognized that φ_0, the work function during the anode half-cycle, may not be the same as φ, the work function of the emitting cathode. On defining the difference between these as $\Delta\varphi$,

$$\Delta\varphi=\varphi_0-\varphi. \quad (5)$$

By solving Eq. (1)–(5) for f, one obtains

$$f=\frac{[(4kT/e)+V_k+V_i+\Delta\varphi]-(2/I)(W-wA)}{(2kT/e)+V_k+V_i}. \quad (6)$$

If the emission is purely thermionic, the electron current density at the cathode is given by the Richardson-Dushman equation

$$j_-=AT_c^2\exp(-\varphi e/kT_c), \quad (7)$$

where T_c is the temperature of the emitting surface.

Ultimate justification for neglecting all electron emission processes other than thermionic lies in the self-consistency of the results, but some explanation of $\Delta\varphi$ is in order.

It will be seen later that the cathodes used have an emitting surface of the thin-film type, to which barium complexes are dispensed by evaporation and surface diffusion.[10] Such thin films (in final operating condition constituted of perhaps less than complete monolayer coverage) obey Schottky's work-function reduction relation fairly well. Therefore, $\Delta\varphi$, given by Schottky's equation[11] is

$$\Delta\varphi=3.79\times10^{-4}E^{\frac{1}{2}}\text{ v}, \quad (8)$$

where E is the effective field at the surface of the cathode in v/cm. E is, of course, greater than the field produced by space charge E_0 because of surface roughness and patch effect. I have assumed

$$E=\gamma E_0, \quad (9)$$

where γ is taken as 2.81, a value deduced from data of footnote reference 5.

Since γ enters all equations only through $\Delta\varphi$, which is proportional to the square root of γ, and since $\Delta\varphi$ turns out to be only about 0.1 v and small compared to the work function it modifies, further refinement of γ is not justifiable here. But in the case of thick-layer oxide cathodes, even relation (8) should be avoided.

The field produced at the cathode by space charge E_0 is derived from the relation between cathode drop V_k and the thickness of the cathode fall space d, which is

$$V_k^2=32\pi/9[(j_+/\mu_+)-(j_-/\mu_-)]d^2, \quad (10)$$

[9] H. S. W. Massey and E. H. S. Burhop, *Electronic and Ionic Impact Phenomena* (Oxford University Press, New York, 1952), p. 546.

[10] The bulk emission material was barium thorate, kindly provided by Dr. Speros [cf. D. M. Speros, J. Electrochem. Soc. **106**, 791 (1959)].

[11] Stroboscopic observation reveals that in these arcs, the current burns to the same electrode region in anode and cathode half-cycles.

where j_+ and μ_+ are positive ion-current density and mobility in Gaussian units, and j_-, μ_- are the corresponding quantities for electrons. Converting (10) to practical units and neglecting j_-/μ_- gives

$$d^3 = 0.995 \times 10^{-13}(\mu_+/j_+)V_k^2, \tag{11}$$

with units of cm, v, cm/vsec, and amp/cm². Equation (11) is given by Cayless[1] without neglecting j_-/μ_-.

Differentiation of (10) gives the field produced at the cathode by space charge

$$E_0 = \tfrac{3}{4}V_k/d. \tag{12}$$

The total current density j is the sum of its components,

$$j = j_+ + j_-, \tag{13}$$

while the definition of f is expressed as

$$f = j_-/j. \tag{14}$$

If the average electrode temperature is T_r, the power dissipated from it is

$$W = BT_r^4, \tag{15}$$

where B is determined by geometry and material.

The power which must be dissipated as a result of energy accumulated during the anode portion of the cycle may be measured by operating at half-wave and measuring T_a, the temperature of the anode:

$$W_a = BT_a^4. \tag{16}$$

The circuit in which these lamps have been studied does not give strictly sine-wave currents. It has been established that

$$I_m = 1.596I_r, \tag{17}$$

where I_m is the peak current and I_r the full-wave rms current. Half-wave rms current is

$$I_a = I_r/\sqrt{2}, \tag{18}$$

which does not enter our other equations.

The current average over $\frac{1}{2}$ cycle is

$$I = 0.987I_r \tag{19}$$

for the experimental circuit.

Current densities of particular interest are those at maximum current

$$I_m = jA_2, \tag{20}$$

where A_2 is the thermionically emitting area of the cathode.

On considering the quantities of interest and the equations available to determine them, we note the following:

Quantities assumed: T, γ.
Calculated to reasonable accuracy: B, A_1, A_2.
Measured: w, I, T_c, T_r, T_a, I_m, V_k.
Unknown: W_a, φ_0, f, W_c, φ_+, φ, W, $\Delta\varphi$, j_-, j_+, j, A, E_0, E, and d (15 unknowns).

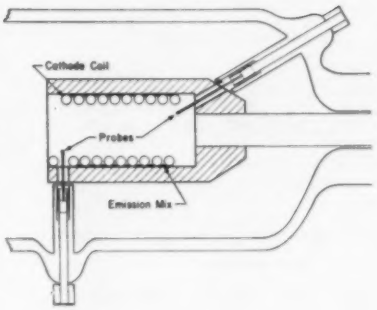

FIG. 1. Electrode with probes.

Independent equations: 1, 2, 3, 4, 5, 7, 8, 9, 11, 12, 13, 14, 15, 16, and 20 (15 equations).

III. DETERMINATION OF PARAMETERS AND CONSTANTS

Proceeding in the tabulation of constants above to the second group, the radiation coefficient B is easily dealt with. With reference to Fig. 1, all electrodes were designed as shown there except that not all had probes and one had peepholes (to be discussed later). B is determined from the Jones-Langmuir total emissivity of tungsten times the peripheral area of the electrode body, plus the blackbody emissivity of the open-electrode end. Since the material emissivity varies slightly with temperature, B also varies slightly; its value was calculated separately for each temperature.

As mentioned earlier, emission mix is dispensed in a thin layer onto the cathode coil as the arc burns. The coil is 50-mil tungsten wire, fit snugly against the electrode body. One electrode was made with two peepholes 60 mils in diameter, aimed between the first and second turns of the coil, and between the last two turns of the coil. Visual observation through these peepholes established that the arc burned to the last turn of the coil. From this, A_2 was taken as $\frac{3}{4}$ the peripheral area of the coil (up to $\frac{1}{4}$ being shielded by contact with the electrode body), which was 7.55 cm² for lamp X-5.

In operation, these arcs burn stably parallel to the axis of the quartz envelope and spaced about 3 mm from it, up to a short distance from the electrode. Here, the arc contracts and enters the electrode cavity. With electrodes spaced at 20 cm and the plasma diameter determined photographically, total power input to the lamp minus electrode dissipation, divided by the peripheral area of the positive column plasma, gives w, the power dissipated/square centimeter to electrically insulated objects in the plasma. The plasma density varies linearly from the mouth of the electrode to zero at the end of the coil such that w heats the end of the electrode and an average of half the envelope of the coil inner diameter. This area, by which w is multiplied in Eq. (1), has the value $A_1 = 2.46$ cm².

We then proceed to find the other quantities: I is determined from meter readings of I_r and Eq. (19).

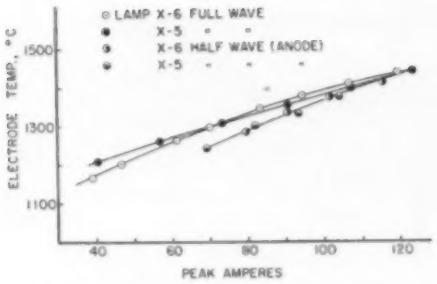

FIG. 2. Full- and half-wave electrode temperatures.

The coefficient 0.987 was determined by graphical integration.

All temperatures T_r, T_o, and T_c were measured with an optical pyrometer sighted at the region of interest and focused with the arc on, and a quick determination made after opening the arc circuit. The pyrometer filament had to be set to a value where a match was expected and the match confirmed after arc extinction. Electrode temperatures, full- and half-wave, are shown for two lamps in Fig. 2. The temperatures were corrected for spectral emissivity and envelope absorption.

Peak current I_m, against which temperatures have been plotted to permit a common reference for full- and half-wave operation, is related to the meter reading by Eq. (17). This was established by oscilloscope calibration and a manganic shunt.

To complete our data, only the cathode drop V_k remains to be measured. Bauer and Schulz,[6] in studying a dc discharge in xenon at 25 atm, determined the sum of the cathode and anode drops by varying electrode spacing and extrapolating to zero. Another procedure permitted them to divide the total loss between electrodes and decide upon a value for the cathode drop. In this paper, however, I have avoided use of the moving electrode technique in determining V_k because it is questionable whether the same potential exists between two points of an arc when one of them marks an electrode and when the space is free. At pressures of the order of 1 mm Hg, Karelina and Klarfeld[12]

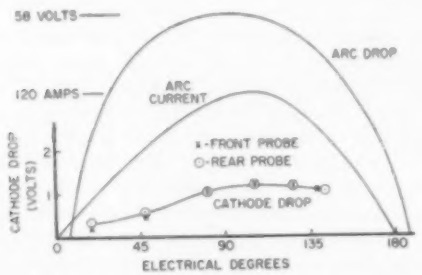

FIG. 3. Variation of arc current, arc drop, and cathode fall with time, at 75 amp rms.

[12] N. A. Karelina and B. N. Klarfeld, J. Tech. Phys. (U.S.S.R.) 18, 1235 (1948).

showed great distortion of local voltages by approaching electrodes, and although the effect is less at higher pressures, it seems worth avoiding if possible. For this reason, a probe technique was developed to measure V_k. The method would overburden this paper if described here; it will be discussed in a separate paper.

The variation of V_k with phase, as determined by probe measurements, is shown in Fig. 3. The current-weighted average of V_k from these data is 1.00 v; the max value is 1.20 v.

It should be noted here that the probe measurements may be in some error from contact potential difference. Since the probes are of tungsten, like the cathode coil, and exposed to the same evaporating emission material (barium complexes) as is the cathode, CPD should be at a minimum.

IV. SOLUTION AND RESULTS

If one accept the assumption mentioned earlier of $T=7300°K$, $2kT/e=1.26$ v and we have at hand everything needed to solve Eq. (1) for φ_0. The results are given in Table I.

TABLE I. Computation of zero-field work function from Eq. (1).

Lamp no.	I Peak amp	I ½ cycle av amp	$2W_o$ w	w w/cm	wA_1 w	φ_0 v
X-5	104.2	64.4	244.2	19.7	48.4	1.78
X-5	93.9	58.1	215.2	17.0	41.8	1.73
X-5	82.1	50.8	192.0	14.21	35.0	1.83
X-5	69.4	42.9	161.0	11.40	28.05	1.83
X-6	79.8	49.4	184.0	14.84	36.55	1.73
X-6	90.6	56.1	214.0	17.60	43.3	1.78
X-6	101.6	62.9	241.0	20.60	50.6	1.77
X-6	115.9	71.6	273.2	24.60	60.5	1.72
					Av	1.77

There does not appear to be a systematic variation of work function with current or between lamps, so further calculations will be based upon the average value of φ_0 from Table I, or 1.77 v.

Simultaneous solution of the remaining equations runs into analytical difficulties because of the exponential in (7). But a few trials show that a value of 0.1 v for $\Delta\varphi$ is reasonable, so this value is substituted into (6) for the calculation of f. Using $4kT/e=2.52$ v, $V_k=1.00$ v, $V_i=12.1$ v (for xenon), and $\Delta\varphi=0.1$ v in Eq. (6) gives the values of f recorded in Table II. The positive ion-current density is calculated from these values of f, and j_+ is inserted into (11) to determine d, the cathode fall-space thickness. For this calculation, the value of V_k is taken as 1.2 v, since reference is to the moment of maximum current. A positive ion mobility of 2.22 cm²/vsec is appropriate to our conditions, converted from the data of Chanin and Biondi.[13] The values of V_k and d, with Eq. (9) and (12),

[13] L. B. Loeb, *Basic Processes of Gaseous Electronics* (University of California Press, Berkeley, 1955), p. 92.

TABLE II. Variation of characteristic quantities with peak arc current. (First four rows for lamp X-5; remaining data for X-6).

I_m Peak amp	j Peak cathode amp/cm²	$(1-f)$ Fraction of cathode current by + ions	j_+ Positive ion current density, amp/cm²	d Thickness of cathode fall space cm×10⁻⁵	E Effective field at cathode v/cm×10⁴	$\Delta\varphi$ Reduction of work function by Schottky effect, v	j_- Electron current density at cathode, amp/cm²	T_c Temp. of cathode coil, °K
104.2	13.80	0.074	1.01	6.80	7.44	0.103	12.79	1846
93.9	12.43	0.084	1.05	6.73	7.51	0.104	11.38	1805
82.1	10.90	0.101	1.10	6.61	7.64	0.105	9.80	1760
69.4	9.20	0.124	1.14	6.55	7.71	0.105	8.06	1709
79.8	11.73	0.100	1.17	6.48	7.79	0.106	10.56	1778
90.6	13.32	0.090	1.20	6.44	7.85	0.106	12.12	1834
101.6	14.92	0.075	1.17	6.48	7.80	0.106	13.75	1882
115.9	17.02	0.061	1.03	6.64	7.62	0.105	15.99	1932

determine the effective field at the cathode surface E. This field, in turn, reduces the work function of the cathode according to Eq. (8). The calculations described in this paragraph give results collected in Table II.

It is seen from Table II that the original assumption of 0.1 v for $\Delta\varphi$ is correct. Furthermore, when the arc current is reduced, the percent of the total current carried by ions increases to keep the cathode emitting despite reduced temperature. Thus j_+ changes relatively little with arc current. And, since $\Delta\varphi$ is proportional to $(j_+)^{1/6}$, $\Delta\varphi$ remains almost constant over a considerable range of arc current.

The variation of electron current fraction is presented as a function of arc current in Fig. 4.

Since $\Delta\varphi$ and φ_0 are both constant, the thermionic work function is constant for all loads at $1.77-0.10=1.67$ v.

The last parameter of our system of equations, the Richardson-Dushman A, can now be calculated from Eq. (7). For convenience in making this calculation, the cathode temperature T_c and the emitted electron current density j_- have been included in Table II.

Values of A are plotted as a function of arc current in Fig. 5.

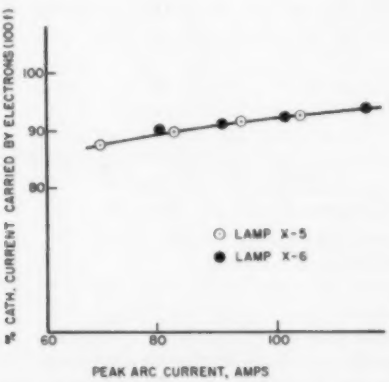

FIG. 4. % of cathode current carried by electrons.

V. DISCUSSION

The results for φ and A seem reasonable. If they are compared with those listed by Wright in his survey paper,[14] he is found to quote 1.6 v as φ and 1.5 amp/(cm² deg²) as A for barium on tungsten. Rather than argue that our A might approach his at low currents, it seems more logical to recognize that we probably do not have a single monolayer of Ba on W, but that various components of the emission mixture must exist on the surface during operation. In fact our values of A all lie between the two curves given by Reimann (Fig. 31)[15] for $W(O-Ba)_x$ and for $W(Ba-O)_x$, respectively. So our emission mechanism is adequate to explain the facts, and makes it unnecessary to call upon other processes.

Low cathode drops like the values reported here are not often encountered in the literature. But they are also not unknown.[16] As Langmuir pointed out in his early studies of thermionic cathodes in gas, a cathode drop must perform or contribute to the function of producing the ions needed to maintain the space charge

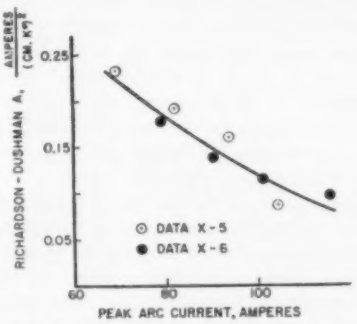

FIG. 5. Variation of the thermionic emission coefficient with arc current.

[14] D. A. Wright, Proc. Inst. Elec. Engrs. (London) **100**, III, 125 (1953).

[15] A. L. Reimann, *Thermionic Emission* (John Wiley & Sons, Inc., New York, 1934).

[16] L. Malter, E. O. Johnson, and W. M. Webster, RCA Rev. **12**, 415 (1951).

sheath. In a relatively high-pressure arc like the one studied here, individual electrons need not be accelerated to voltages required for ionization, in their passage through the cathode fall. Instead, the power input through the cathode fall serves to maintain the plasma temperature at the value needed for thermal ionization. A rough calculation shows that for our case the intra-electrode plasma energy balance is reasonably supported by a 1-v cathode fall.

The positive ion functions, of heating the cathode and aiding emission of electrons by producing a space charge field, provide an interesting regulatory action on the arc. The understanding of the numbers involved here is important in understanding practical problems such as blackening of lamps near the cathode. In the experiments described here, when the ion current rose and the discharge transferred into a "spot mode," the arc drop rose, the electrode got hotter, and bulb blackening occurred quickly.

VI. SUMMARY

The energy balance method employed here for determining thermionic parameters avoids the pitfall of measuring a "constant" at one current and employing it to interpret results at currents an order of magnitude or so higher. But it must be recognized that there is enough uncertainty in determination of some of the parameters, as pointed out in Secs. II and III, that more work will be required before precision indices can be stated for the results obtained.

It is interesting that such a high-current arc at relatively high pressure operates in a purely thermionic mode. This is not inconsistent with some of the very old experiments on refractory cathodes, but does not fit into the pattern of investigations within the last few years. That about 10% of the cathode current is carried by ions suggests added caution in assuming negligible ion current in thermionic discharges.

The results show that as arc current is reduced, the ion current component must rise to support the emission. It is to be expected that after the current is reduced beyond a certain point, the arc will actually transfer to a cathode spot mode, with attendant greater ion current component, larger arc drop, and higher electrode heating for a given arc current.

In consideration of the well-known great change of thermionic constants from vacuum to gas conditions and with operating temperature,[1,4] the variation of the Richardson-Dushman A over a factor of two in the range studied is not surprising. The essential constancy of zero-field work function at about 1.8 v is probably fortuitous.

Schottky reduction of the work function turns out to be small: the 0.1 v obtained almost relegates this effect to a second-order phenomenon under the conditions studied.

The low cathode drop of about 1.0 v is not inconsistent with the presence of a well-activated, low work-function cathode and a geometry favoring conservation of energy in the cavity plasma.

ACKNOWLEDGMENTS

I am grateful to J. S. Saby for supporting and encouraging this work. It would have been impossible without the skilled quartz work of Frank Krotine. And I am very thankful to B. T. Barnes, M. A. Easley, and Carl Kenty for helpful criticism and thoughtful discussion and suggestions.

LIST OF SYMBOLS

A = Richardson-Dushman constant, Eq. (7)
A_1 = effective area of anode exposed to w
A_2 = area of electrode emitting thermionically
B = electrode emissivity-area factor, Eq. (15)
d = thickness of cathode fall space
e = electronic charge
E = effective field at cathode surface, Eq. (9)
E_0 = space-charge field before the cathode, Eq. (12)
f = fraction of current at cathode carried by electrons
I = arc current, average over ½ cycle
I_a = arc current, rms value during half-wave operation
I_r = arc current, rms value during full-wave operation
I_m = peak value of arc current
j = instantaneous cathode current density at peak current
j_- = electron component of j
j_+ = ion component of j
k = Boltzmann constant
T = plasma temperature (same for ions, electrons, atoms)
T_a = average temperature of electrode radiating area, in half-wave operation as anode
T_r = average temperature of electrode radiating area during full-cycle operation
T_c = temperature of cathode emitting area
t = period of ac arc current
V_i = ionization potential of gas
V_k = cathode drop
W_a = average power dissipation resulting from the energy taken in during operation as anode
W_c = average power dissipation resulting from the energy taken in during operation as cathode
$W = W_a + W_c$, total power converted to heat at an electrode under full-wave ac operation
w = power per unit area from the full-wave arc to an insulated object in the plasma
γ = roughness factor, Eq. (9)
μ_+ = mobility of positive ions
μ_- = mobility of electrons
φ_0 = work function of electron-collecting surface of anode
φ = work function of cathode emitting area
$\Delta\varphi$ = work function reduction by electrostatic field
φ_+ = energy of neutralization of positive ions at cathode.

Density of a Thorium Monolayer for Maximum Thermionic Emission*

W. E. Danforth and D. L. Goldwater
Bartol Research Foundation of the Franklin Institute, Swarthmore, Pennsylvania

(Received May 16, 1960)

An investigation is described in which a high-sensitivity analytical balance of standard design is used for determination of the surface density of that thorium layer which corresponds to maximum thermionic emission with the thorium-on-tungsten system. Following Brattain and Becker's definition of this value of surface density as one "*f* unit," thorium vapor is allowed to accumulate on a quartz plate until a weighable number of *f* units (about 600) has been deposited. The thorium flux in *f* units per minute is monitored periodically by means of a tungsten filament diode during the course of the deposition. Two polycrystalline specimens of ribbon from the same source have yielded the value of $(4.2\pm0.2)10^{14}$ atoms/cm² as the density for maximum emission. This is to be compared with a value of 5.0×10^{14} atoms/cm² obtained in 1934 on theoretical grounds by Langmuir.

I. INTRODUCTION

STUDIES have been made of the thermionic emission of tungsten as modified by monolayer films of Cs,[1] Th,[2–4] Sr,[5] and Ba.[5] In the cases of Cs and Th, a pronounced maximum is found in the relation between emission and coverage. In the cases of Sr and Ba, Moore and Allison report emission rising to a relatively constant value for a coverage of one monolayer, but did not observe a well-defined maximum.

The question of calibration naturally arises in all of these studies; this was first achieved by J. A. Becker[6] for the case of Cs. When Cs atoms fall upon a hot tungsten filament they become ionized, and by measuring the ion current, the absolute intensity of a flux of Cs atoms can be determined. This complete ionization does not take place in the other three cases so one must resort to other methods of measurements. Moore and Allison[5] achieved calibration for Sr by means of a radioactive isotope and radiation counting. No isotope with really convenient half-life exists in the cases of Ba and Th. The present paper reports a calibration for Th on tungsten which has been carried out by direct weighing.

II. METHOD

Following customary notation the degree of thorium coverage corresponding to maximum emission (whatever may turn out to be its numerical value) is designated as one *f* unit. Since this quantity is presumed to be of the order of one monolayer, it cannot be weighed on a balance. We therefore arrange to form a layer consisting of a large and determinable number of *f* units, so that one then has a number of monolayers large enough to be weighed on a mechanical balance. The weight for a single *f* unit is then immediately calculable.

In the tube shown in Fig. 1 a source of thorium vapor produces a stream of atoms which fall at equal rates on the quartz plate and the ribbon filament. This ribbon was 0.030 in. wide, 0.001 in. thick and 0.625 in. long. The material had been obtained from Kulite Tungsten Company in August, 1959. It was outgassed by holding at 2150°C_B (2680°K) for about an hour. Microscopic examination of the etched surface after removal from the tube showed that recrystallization into a relatively small number of large grains had occurred. The thorium source consisted in a tungsten dish, machined from bar

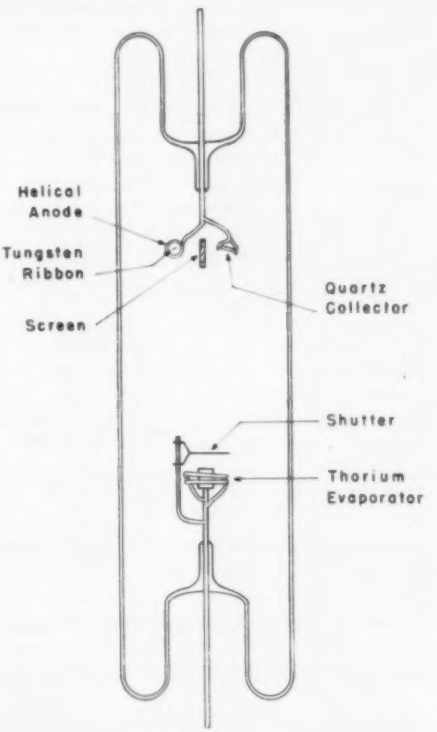

FIG. 1. Tube in which thorium vapor falls at equal rates upon a ribbon filament and a weighable collector.

* This work is supported by the U. S. Air Force Cambridge Research Center.

[1] J. H. DeBoer, *Electron Emission and Adsorption Phenomena* (Cambridge University Press, Cambridge, England, 1936); work of I. Langmuir, J. A. Becker, J. H. DeBoer, *et al.*
[2] I. Langmuir, J. Am. Chem. Soc. **54**, 2798 (1932).
[3] I. Langmuir, J. Franklin Inst. **217**, 543 (1934).
[4] W. H. Brattain and J. A. Becker, Phys. Rev. **43**, 428, 1933.
[5] G. E. Moore and H. W. Allison, J. Chem. Phys. **23**, 1609 (1955).
[6] J. A. Becker, Phys. Rev. **28**, 341 (1926).

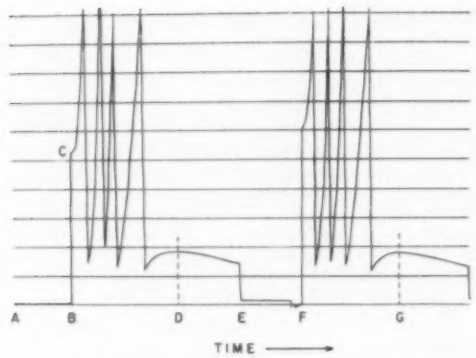

FIG. 2. Section of chart record during deposition of thorium.

stock, containing thorium metal, heated by electron bombardment. All metal parts, press leads, etc. were prefired in a vacuum furnace before being assembled in the tube. A shutter, which was movable by inclining the tube, served to prevent any accumulation of thorium on the quartz collector during processing of the tube. A tantalum plate separated the filament with its helical anode from the quartz collector and prevented thorium which evaporated from the filament during cleaning from being deposited on the collector.

The tube, with attached ion guage, was evacuated with a mercury diffusion pump, and baked at 400°C for 52 hr in its final processing. Counting previous exhaust periods, the total time of baking was 150 hr. The filament, helix, and thorium evaporator were outgassed until the pressure with all parts at operating temperature was about 5×10^{-9} mm. After sealoff, the pressure was somewhat higher but returned to the above value after a period of ion gauge operation, and remained there during conduct of the experiments.

No attempt was made to secure temperature uniformity over the length of the tungsten ribbon; the observations of thermionic emission from the ribbon did not have to be absolute measurements. This is justified by previous work[6] with Cs on tungsten which has shown that the surface density of Cs which corresponds to maximum thermionic emission is independent of temperature as long as evaporation is not taking place. The same is assumed to be true in the present case.

Emission observations were made with constant potential (45 volts) on the helical anode. Maximum current was 1 ma; "saturation" conditions prevailed throughout, but no attempt was made to make "zero field" determinations. It is assumed that, within the accuracy of this study, and for the low values of field concerned, the density for maximum emission is independent of field at the cathode surface. Emission currents were observed and recorded on a strip chart recorder connected to the output of an electronic electrometer.

Figure 2 is a sample of the chart record. At point *A* the source of thorium vapor is turned on and allowed to remain on during the whole course of the run. At point *B* the filament, which was being held at 2100°C_B for cleaning, was allowed to cool quickly to 1100°C_B and the anode voltage turned on. The line segment *BC* corresponds to the "background" current, tungsten emission plus whatever leakage or other spurious current might be present. Immediately after the filament cools (point *B*) accumulation of thorium begins. When sufficient thorium has accumulated to raise the emission above the background, the curve starts upwards. Several changes of scale are made as the emission continues to increase until finally at point *D* it reaches the maximum and starts to decrease. After the curve has passed through the maximum the anode voltage and chart drive are both turned off (point *E*), accumulation of thorium upon the collector being allowed to continue. At some time before the next activation curve is to be taken (usually 2 min prior to this), the filament temperature is raised to 2100°C_B for cleaning. At point *F* the temperature is again lowered to 1100°C_B and the next activation curve is started which attains its maximum at point *G*. If the rate of evaporation of thorium has not changed, the time *FG* will be equal to the previous interval *BD*. Designating by τ the time in minutes corresponding to *BD* or *FG*, the flux of thorium atoms arriving at the filament and also at the collector, expressed in *f* units per minute, is equal to $1/\tau$. The cycle of operations described above was allowed to continue, determinations of the time being about 10 min apart, until approximately 600 *f* units of thorium had accumulated on the collector.

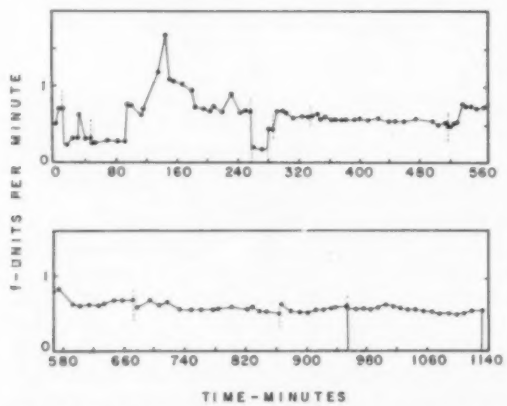

FIG. 3. Flux of thorium atoms in *f* units per minute during deposition. The number of atoms/cm² corresponding to one *f* unit is the quantity being determined.

Figure 3 shows, for the first of the two determinations here reported, the thorium flux in *f* units per minute plotted against time during the period in which the deposit on the collector was accumulating. Integration of curves of this kind, by graphical or numerical methods, yields figures for the total number of *f* units deposited.

III. RESULTS

Numerical results obtained thus far are given in Table I. The two determinations show agreement well within estimated error and lead to the value of 4.2×10^{14} as the thorium density corresponding to maximum thermionic emission for the polycrystalline material which we used.

Although this is, we believe, the first direct experimental determination of this quantity, it is not the first published value. Over 25 years ago Langmuir[2,3] developed his theory of the surface phase which related rate of evaporation to dipole moment of the adsorbed particles and therefore to change of work function. Langmuir found that his theory best explained the evaporation and thermionic data if the value 5.0×10^{14} were used for the density corresponding to maximum emission. Determination of the value of fractional coverage θ at which the maximum occurs would require detailed crystallographic knowledge concerning the specimens; this is not available at the present time. Measurements of the kind here reported using single crystal ribbons are contemplated.

TABLE I.

Run	Number of f units	Weight of deposit (μg)	Area in cm^2	Grams per cm^2 per f unit	Atoms per cm^2 per f unit
1	675	52±2	0.480	$(1.60\pm.06)10^{-7}$	$(4.18\pm.20)10^{14}$
2	611	54±2	0.556	$(1.59\pm.06)10^{-7}$	$(4.15\pm.20)10^{14}$

ACKNOWLEDGMENT

It is a pleasure to acknowledge the skilled assistance of N. A. Hunter.

JOURNAL OF APPLIED PHYSICS VOLUME 31, NUMBER 10 OCTOBER, 1960

Anomalous Barrier Capacitance in p-n Junctions of InSb

C. A. LEE AND G. KAMINSKY
Bell Telephone Laboratories, Murray Hill, New Jersey

(Received May 19, 1960; and in final form June 13, 1960)

Reverse bias transition capacitance measurements on alloy diodes of InSb at 78°K give values a factor of three times those calculated from normal diode theory. This result is in contrast to the reasonable agreement obtained for diodes of germanium and gallium arsenide in a comparable doping range. The experimental techniques are critically reviewed and an attempt made to assess the implications of the results.

A STUDY of alloy p-n junction characteristics in InSb at liquid nitrogen temperatures has been made that shows many of the usual properties of step junctions.[1] Measurements of the reverse bias transition capacitance, however, are a factor ≈3 times the values calculated for these step junctions using conventional diode theory.[2] In contrast, we observe reasonable agreement ($\lesssim40\%$) between measurement and calculation for alloy diodes of germanium and gallium arsenide. In view of the unusual nature of this result, many experimental details were checked in an effort to find a suitable explanation.

The diodes were fabricated by evaporating a fairly heavy film of cadmium (1–2 μ) and alloying this film in a reducing atmosphere at a temperature between 350 and 400°C. The total time of the alloy cycle was about 30 sec. The crystal orientation of the base material was typically (111), although other orientations were tried without affecting the results. Subsequent to alloying, the excess cadmium was removed and areas of the regrowth layer of 10^{-5} to 10^{-3} cm^2 were then masked and etched. Electrolytic etching was found to etch the regrowth preferentially in such a manner that the junction boundary was clearly delineated. Further, samples were sectioned and etched to ensure that the junctions were planar.

The p-n junctions formed in this manner are asymmetrical step junctions for which the transition capacitance is principally dependent on the uncompensated donor density of the base material and relatively independent of the acceptor density of the alloy regrowth layer. The donor density of the base material was in all cases determined by Hall effect measurements prior to alloying.

The principal question, after one is assured of the correctness of the measurement techniques, is whether an order of magnitude increase in the density of donors has occurred during fabrication. These added impurities, which may possess shallow or deep donor levels, would provide an obvious explanation of the observed excess capacitance.

A first assumption that seems reasonable to make is that the density of impurities which are introduced during alloying should be independent of the donor

[1] C. A. Lee and G. Kaminsky, J. Appl. Phys. **30**, 2021 (1959).
[2] W. Shockley, Bell System Tech. J. **28**, 435 (1949).

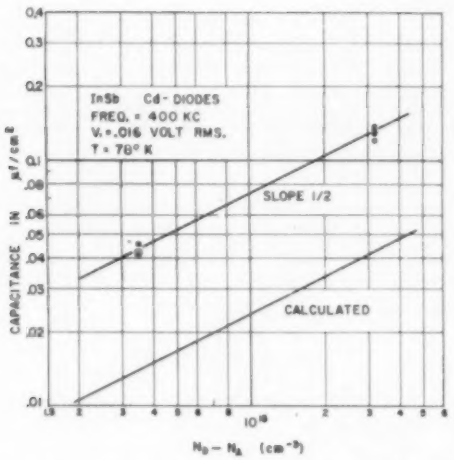

FIG. 1. Capacitance of alloy p-n junctions of InSb as a function of impurity concentration of the base material at zero bias.

density of the base material. In Fig. 1 are shown measurements of the capacitance at zero bias for two crystals differing by an order of magnitude in the excess donor density. The measured capacitance varies with the square root of the excess donor density, as one would expect if no other impurities were introduced into the base material during alloying. The calculated variation of capacitance per unit area, shown in Fig. 1, was obtained from the relation

$$C/A=[q(N_d-N_a)\epsilon/2\Delta\Psi]^{\frac{1}{2}}, \tag{1}$$

where (N_d-N_a) is the excess donor density of the base material, the dielectric constant $\epsilon=16.7\epsilon_0$,[3] and $\Delta\Psi$ is the "built-in" potential at zero bias (taken to be 0.2 v). The discrepancy between measurement and calculation, as mentioned before, is approximately a factor of three.

A second consideration against the introduction of impurities during alloying is the manner in which these "excess" impurities may be introduced into the base material. Diffusion from the liquidus during alloying should produce a steep gradient of these impurities in the immediate neighborhood of the junction. A plot of the inverse square of the capacitance, however, is a very good straight line (see Fig. 2), implying that the distribution of excess donors is constant.

It is conceivable that the diffusion constant of an impurity added during alloying could be of such a magnitude that the resultant gradient of impurities might be too shallow or too steep (i.e., most of the added impurities lie within the space charge region) to be observed by the sort of measurement given in Fig. 2. Further evidence bearing on this circumstance is shown in Fig. 3, where zero bias resistance and capacitance are plotted as a function of the temperature. The relevant features are the very rapid decrease of the transition capacitance at a temperature ($10^2/T\simeq5$) corresponding to the start of intrinsic behavior of the n-type base material, and the exponential decrease of R with increase in temperature. If we assume $\tau_p=10^{-8}$ sec (consistent with the data on p-type InSb of Zitter, Attard, and Strauss[4]) and $N_d-N_a=3.2\times10^{15}$/cm³ as obtained from Hall measurements, we may calculate the variation of R with temperature from the relation

$$R=\frac{kT}{qI_0}=\frac{kT\tau_p^{\frac{1}{2}}}{q^2p_nAD_p^{\frac{1}{2}}}. \tag{2}$$

The saturation current is expressed as a function of the diffusion of holes ($D_p\simeq43$ cm²/v sec), the area of the junction A, and the equilibrium density of holes in the n-type material $[p_n=n_i^2/(N_d-N_a)]$. In spite of the neglect of the temperature variation of D_d and τ_d, reasonable agreement is obtained because of the strong exponential temperature dependence of n_i^2. The agreement between calculation and measurement of R implies the donor density within a diffusion length of the junction is essentially the same as that of the base material before alloying. This agreement is, of course, dependent on the choice of τ_p, but in order to fit R with a donor density ten times the measured value one would require an unreasonably low value of lifetime of 10^{-11} sec. Turning to the behavior of the capacitance with temperature, we observe that the space charge region should collapse entirely when the base material becomes intrinsic, leading to very small values of the capacitance. As mentioned before, the observed capacitance decreases rapidly as the base material becomes intrinsic. We infer, therefore, that the excess donor density within the transition region is not an order of magnitude greater than that of the base material before alloying.

All of the arguments presented, except the one concerning junction resistance as a function of temperature, apply equally well to shallow or deep-lying donors. The presence of deep-lying donors requires special considera-

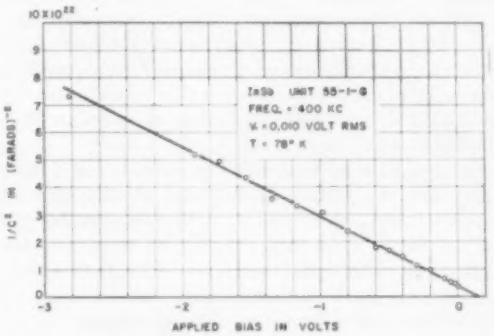

FIG. 2. Reverse bias capacitance of an InSb alloy p-n junction vs applied bias.

[3] F. Oswald and R. Schaade, Z. Naturforsch. **9A**, 611 (1954).

[4] R. N. Zitter, A. J. Strauss, and A. E. Attard, Phys. Rev. **115**, 266 (1959).

tion since an impurity might possess two donor levels, the deeper level becoming ionized only in the transition region of the junction.[5] No deep-lying donor levels were observable, however, in Hall effect measurements as a function of the temperature on both *n*-type and *p*-type crystals grown from the same zone-refined material and having an uncompensated impurity density of $\approx 5\times 10^{14}/\text{cm}^3$.

Remembering that we are assuming the applicability of conventional diode theory and trying to assess the consistency of the presence of "excess" charge, a further consideration against its presence is a calculation of the maximum electric field in the junction at breakdown. The maximum observed breakdown potential of several units has clustered around 8 volts. This observed breakdown may be due to some surface mechanism rather than body breakdown, but the electric field is far in excess of that reported for avalanche breakdown in bulk material.[6-8] It is thought-provoking that in order to sustain a potential across the junction many times the band gap one would require a mean free path for lattice scattering less than the junction width, while in bulk material avalanche excitation across the gap at the fields reported (≈ 200 v/cm) would seem to require a mean free path many times the junction width.

Using the relation

$$E_{\max}=2V_b C/A\epsilon, \tag{3}$$

where V_b is the maximum observed breakdown potential and the other symbols are a defined in Eq. (1), we calculate a maximum electric field of ≈ 200 kv/cm. Since the "Zener" breakdown in germanium has been reported[9] to be ≈ 200 kv/cm, one could expect the similar breakdown mechanism to occur in InSb at 20–30 kv/cm if one applies the analysis of field ionization mechanism given by Keldysh.[10,11] We wish to argue that the discrepancy of these fields makes the presence of the "excess" charge improbable, but one must remember that the idealized problem considered by Keldysh is quite far removed from the "narrow" junction considered here, in spite of the fact that we have used the field ionization limit of a germanium "narrow" junction as a sort of calibration.

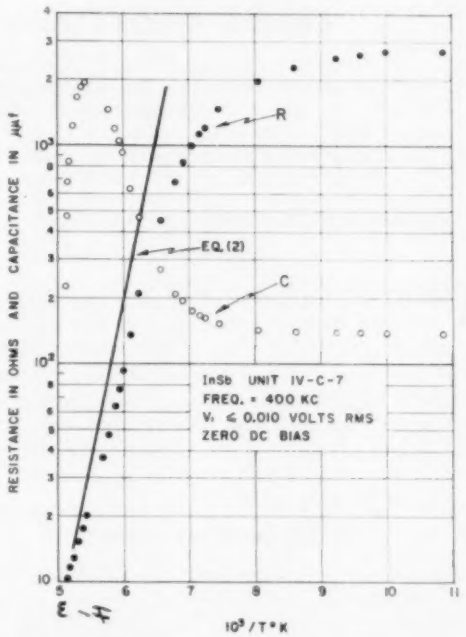

FIG. 3. Resistance and capacitance of an InSb alloy *p-n* junction as a function of temperature at zero bias.

The considerations presented here have involved the application of "normal" diode theory. The experimental justification of using "normal" diode theory and further for considering step junctions has been presented in Figs. 1 and 2. It should be noted that the anomalously high capacitance reported on is also measured at reverse biases for which the junction transition region is an order of magnitude larger than the effective Debye length and for which the transition from neutral to space charge regions should not be a significant part of the total transition region.

It is possible that some subtlety of the approximations in diode theory has been overlooked which make its application here invalid. The data, however, leave little room for doubt that a reconsideration of "diode" theory is necessary for our understanding of these results.[12] If present "diode" theory is applicable, then the only remaining assumption to question is the dielectric constant of the transition region where we have used the value obtained from infrared measurements of Oswald and Schaade.[3,13]

[5] *Note added in proof.*—An impurity possessing a shallow and a deep donor level can only account for an "excess" charge of a factor of two while almost a factor of ten is necessary.

[6] A. C. Prior, J. Electronics and Control **4**, 165 (1958).

[7] M. Glicksman and M. C. Steele, Phys. Rev. **110**, 1204 (1958); M. C. Steele and M. Glicksman, J. Phys. Chem Solids **8**, 242 (1959).

[8] Y. Kanai, J. Phys. Soc. Japan **13**, 967 (1958).

[9] K. B. McAfee, E. J. Ryder, W. Shockley, and M. Sparks, Phys. Rev. **83**, 650 (1951).

[10] L. V. Keldysh, J. Exptl. Theoret. Phys. (U.S.S.R.) **33**(6), 763 (1958); *ibid.*, **34**(7), 665 (1958).

[11] E. O. Kane, J. Phys. Chem. Solids **12**, 181 (1960).

[12] D. A. Kleinman has suggested that carrier generation in the transition region can significantly alter the impedance.

[13] T. S. Moss, S. D. Smith, and T. D. H. Hawkins, Proc. Phys. Soc. (London) **B70**, 776 (1957).

Growth of Cesium Chloride Crystals from Solution and Melt*

P. AVAKIAN AND A. SMAKULA
Laboratory for Insulation Research, Massachusetts Institute of Technology, Cambridge, Massachusetts
(Received May 16, 1960; and in final form June 23, 1960)

Large cesium chloride crystals were obtained from solution only upon addition of urea. These crystals, however, show NH_4^+ impurity. Since CsCl undergoes a phase transition between its melting point and room temperature, normal growing methods from the melt could not be used, but a modified ("double-run") Bridgman method yielded good results.

ALKALI halide crystals can be grown readily from the melt by the Bridgman technique[1] (i.e., by gradual unidirectional cooling of the molten material in a crucible with a conical bottom), except for cesium chloride which undergoes a phase transformation between its melting point and room temperature,[2] generally causing turbidity in the crystals.[3] The purpose of this work was to obtain optically clear crystals of about 1 cm³ for color-center studies.

GROWTH FROM SOLUTION

From solution CsCl grows directly in the simple cubic phase, but the crystallization does not take place readily from a pure aqueous solution.[4] Because of continuous formation of new nuclei, the crystals tend to remain small. The addition of Na_2CO_3,[4] urea,[5,6] Ce^{3+}, Nd^{3+}, or Ba^{2+} [7] promotes the growth of CsCl crystals from water solution. Of these additives, urea (NH_2CONH_2) was selected because its large molecules are unlikely to become incorporated into the crystal lattice.

The apparatus for growing crystals from solution is shown in Fig. 1. A glass container with the solution was immersed in a water bath[8] heated from below with an infrared lamp. The bath temperature was kept uniform by forced water circulation and controlled by means of a specially constructed mercury thermoregulator. The temperature could be kept constant to within ±0.005°C, and could be lowered slowly by forcing a steel plunger into the mercury reservoir (Fig. 2). Crystals could thus

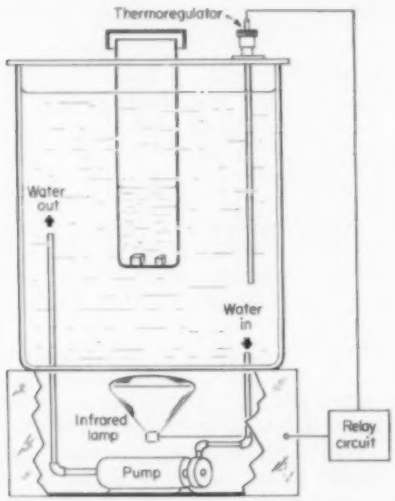

FIG. 1. Apparatus for growing crystals from solution.

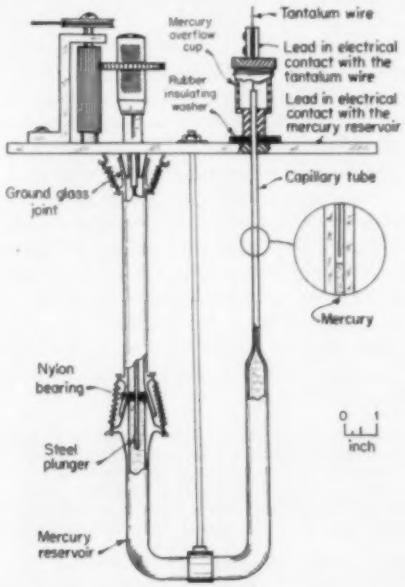

FIG. 2. Mercury thermoregulator for continuous, controlled temperature drop in the infrared bath.

* Sponsored by the Office of Naval Research, the Army Signal Corps, and the Air Force; based on a thesis submitted in partial fulfillment of the requirements for the degree of Doctor of Philosophy in Physics at the Massachusetts Institute of Technology.

[1] A. Smakula, in *Molecular Science and Molecular Engineering*, edited by A. R. von Hippel (Technology Press, Massachusetts Institute of Technology, Cambridge, Massachusetts, and John Wiley & Sons, Inc., New York, 1959), p. 182.

[2] J. W. Menary, A. R. Ubbelohde, and I. Woodward, Proc. Roy. Soc. (London) **A208**, 158 (1951).

[3] E. Jahoda, Sitzber. Akad. Wiss. Wein, Abt. IIa **135**, 675 (1926).

[4] M. Sprockhoff, Neues Jahrb. Mineral. Geol. u. Paläontol., Beilage Bd. **18**, 117 (1904).

[5] P. Wulf and D. Schaller, Z. Krist. **87**, 43 (1934).

[6] P. Wulf and T. F. Anderson, Z. Physik **94**, 28 (1935).

[7] T. Yamamoto, Rikwagaku-Kenkyu-jo Ihô **13**, 1108 (1934); English abstract: Bull. Inst. Phys. Chem. Research (Tokyo), Abstracts **7**, 60 (1934).

[8] Manufactured by Ralph Kaye and Associates, Highland Park, Illinois.

be grown both by the temperature-drop and the evaporation techniques.[9] Crystals up to 7×6×3 mm were obtained within several days with the help of 10% (by weight of CsCl) urea additive (Fig. 3).

The infrared absorption did not show any contamination by either urea or water. However, extraneous bands did appear both in the infrared and ultraviolet regions of the spectrum (Figs. 4 and 5). The infrared bands (Fig. 4, curve a) were correlated to NH_4Cl (Fig. 4, curve c). The NH_4^+ ions resulted from a slight hydrolysis of the urea in solution.[10] Using Wagner and Hornig's value for the absorption coefficient of NH_4Cl,[11] the concentration of NH_4^+ in the crystals was found to be about 0.01%. Upon heating the crystal at 225°C in vacuum for 23 hrs, the infrared absorption decreased markedly (Fig. 4, curve b) but the crystal became hazy. It appears that NH_4^+ and the corresponding number of electrons or anions "evaporate" out of the lattice, leaving vacancies behind. The coagulation of these

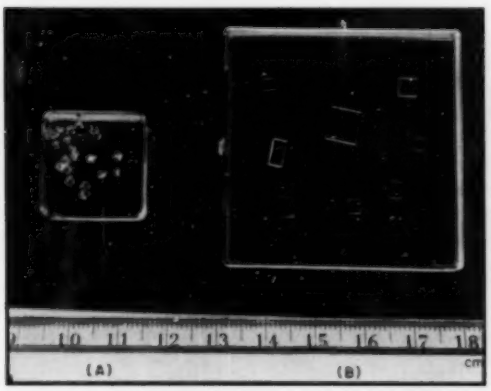

FIG. 3. Cesium chloride crystals grown in several days from (A) pure aqueous solution, (B) aqueous solution with 10% urea additive.

vacancies may be the cause of the haziness in the crystals after heat treatment. The heat treatment also decreased the intensity of the band at 268 mμ, but had no effect on the 244-mμ band. One can assume, therefore, that the former is associated with NH_4^+. The 244-mμ band is caused by some other impurity; it also sometimes appears in crystals grown from the melt. A comparison of the absorption with crystals grown without urea was not possible, because these crystals were too small for optical absorption measurements.

GROWTH FROM THE MELT

Optically clear crystals have been obtained from the melt by a double-run Bridgman technique. Cesium

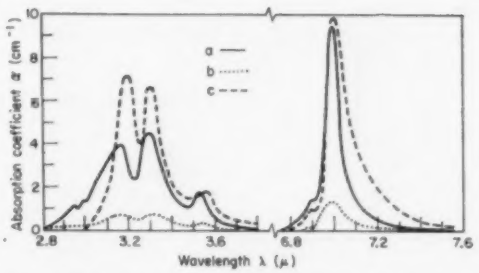

FIG. 4. Infrared absorption spectrum at room temperature (a) of a CsCl crystal grown from water solution with 10% urea additive, (b) the same crystal after heating in vacuum for 23 hrs at 225°C, and (c) of NH_4Cl (after Wagner and Hornig[11]). For curve c the ordinate must be multiplied by 10^1.

chloride powder (cp grade) was first heated in the upper part of a Vycor crucible (Fig. 6) in vacuum for several hours, in order to expel water and possible organic impurities. After reaching 450°C, the crucible was sealed and a hook attached. Upon melting in the Bridgman furnace the CsCl filtered through the platinum mesh plug into the lower section of the crucible. First a face-centered cubic crystal was grown by keeping the upper chamber of the Bridgman furnace at 720°C (melting point of CsCl is 646°C[12]) and the lower chamber at 520°C.

In order to transform this crystal gradually to the low-temperature phase, the temperature of the upper chamber was lowered to about 530°C and the crystal again raised into the upper chamber. Then the lower chamber was set at 330°C (transition temperature of CsCl is 469°C[2]), and the crystal was lowered once more at a rate of 2 mm/hr.

The resultant crystals were transparent but consisted of several large grains. The final crystal could have been either in the low-temperature simple cubic phase or in the improbable high-temperature face-centered cubic phase. The lattice constant of the crystal, as determined

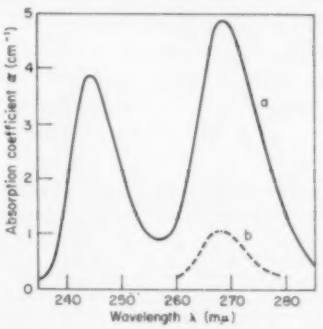

FIG. 5. Ultraviolet absorption spectrum at room temperature (a) of a CsCl crystal grown from water solution with 10% urea additive, and (b) the same crystal at 268 mμ after heating in vacuum for 23 hrs at 225°C.

[9] P. Avakian, Ph.D. thesis, Massachusetts Institute of Technology, 1960.
[10] R. C. Warner, J. Biol. Chem. **142**, 705 (1942).
[11] E. L. Wagner and D. F. Hornig, J. Chem. Phys. **18**, 296 (1950).
[12] F. M. Jaeger, Z. anorg. Chem. **101**, 1 (1917).

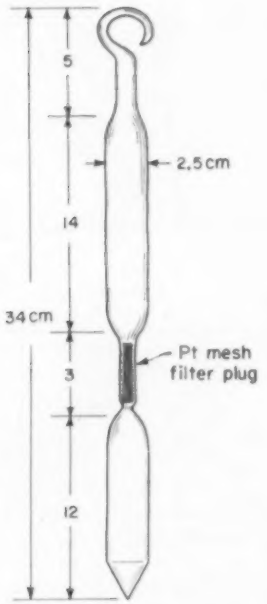

FIG. 6. Vycor crucible for growing crystals from the melt.

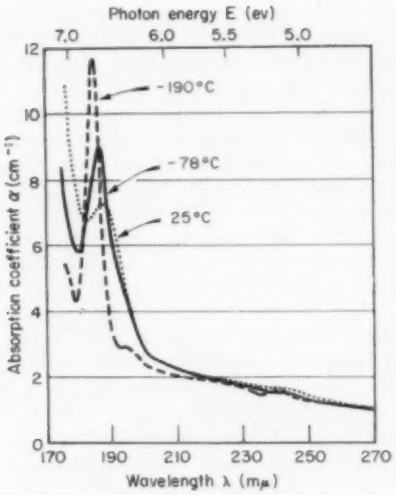

FIG. 7. Ultraviolet absorption of melt-grown CsCl.

by the x-ray oscillation photograph, proved, however, that it was in the low-temperature phase.

Figure 7 shows the optical absorption of crystals grown from the melt. The band of several reciprocal centimeters near the absorption edge is probably caused by an unknown impurity. Since an analogous band did not appear in CsBr and CsI crystals grown in the same type of crucible (Fig. 6), it can be assumed that the band in CsCl is not related to the Vycor crucible nor to the platinum filter plug. A spectrographic analysis of the crystals did not reveal any serious contamination. The absorption edge of CsCl is in the vicinity of 175 mμ.

The transformation of CsCl from the high-temperature face-centered cubic to the low-temperature simple cubic phase involves a sizeable change. The unit cell contracts about 40% along a space-diagonal axis and expands by about 18% perpendicularly to this axis.[8,13] Despite these atomic displacements, the crystal can be transformed in the solid state without shattering (as described previously). The crystals do not appear to have any preferential orientation with respect to the temperature gradient.

ACKNOWLEDGMENT

The authors are indebted to J. Kalnajs, Laboratory for Insulation Research, for his help in constructing the equipment.

[13] P. Avakian, Tech Rept. 149, Laboratory for Insulation Research, MIT, April, 1960.

JOURNAL OF APPLIED PHYSICS VOLUME 31, NUMBER 10 OCTOBER, 1960

Propagation Constants for Electromagnetic Waves in Weakly Ionized, Dry Air*

A. V. PHELPS
Westinghouse Research Laboratories, Pittsburgh, Pennsylvania
(Received May 31, 1960)

Formulas and graphs are given for the calculation of the propagation constants of an electromagnetic wave in weakly ionized, dry air at ionospheric temperatures in the presence of a magnetic field. Experimental studies of electron collision frequencies in nitrogen and oxygen are reviewed and used to obtain the magnitude and energy dependence of the electron collision frequency in air. The equations for the components of the conductivity tensor are developed taking into account the approximately linear dependence of the electron collision frequency on electron energy. Expressions derived on this assumption are found to be accurate except at low temperatures, high pressures, and low frequencies. The errors resulting from the use of an effective value for the energy independent collision frequency in the Appleton-Hartree equations are evaluated. Procedures are given for the calculation of the propagation constants for electromagnetic waves propagated parallel to and perpendicular to the magnetic field. These results are then applied to the derivation of relations required to reanalyze the ionospheric collision frequency measurements reported by Kane. The use of an effective collision frequency is found to lead to errors comparable to the experimental errors in the ionospheric observations.

RECENT laboratory experiments show that the frequency of momentum transfer collisions in air is approximately directly proportional to the electron energy for thermal electrons at ionospheric temperatures. In this paper we shall summarize the results of the laboratory measurements and then show how they can be used to compute the complex propagation constant for a weak electromagnetic wave passing through weakly ionized, dry air. We shall discuss the errors which result when the collision frequency is assumed to be either directly proportional to the electron energy or equal to an "effective" collision frequency which is independent of electron energy. Finally, the results of this analysis are compared with ionospheric observations designed to measure the collision frequency of electrons in the "*D*" layer. The calculations presented in this paper assume the air to be of sea level composition and so are applicable only for altitudes below 90 km.

I. ELECTRON COLLISION FREQUENCIES IN AIR

The frequency of momentum transfer collisions for low-energy electrons in nitrogen has been determined from measurements of the microwave conductivity and the dc mobility as a function of gas temperature. Thus, Phelps, Fundingsland, and Brown[1] show that their measurements of microwave conductivity are consistent with an electron collision frequency, $\nu(u)$, given by the relation, $\nu(u)=1.15\times10^{-7}\mathrm{N}(\mathrm{N}_2)u$ sec^{-1}. Here u is the electron energy in ev and $\mathrm{N}(\mathrm{N}_2)$ is the nitrogen density in molecules/cc. Pack and Phelps[2] show that while the electron mobility measurements[2a] are consistent with a linear variation of the collision frequency with electron energy at the higher energies, the collision frequency at low energies must vary less rapidly than linearly with energy. Theory[3] requires that the electron collision cross section be finite at zero energy, i.e., that the collision frequency vary as $u^{\frac{1}{2}}$ at very low energies. Therefore, the results are given in terms of a two-term approximation to the energy dependence of the collision frequency which is consistent with observations[2] and theory, i.e., $\nu(u)/\mathrm{N}(\mathrm{N}_2)=2.5\times10^{-9}u^{\frac{1}{2}}+1.2\times10^{-7}u$ cm^3/sec. Since ionospheric temperatures correspond to electron energies covering a relatively narrow range of energies, we can obtain reasonable consistency with the observations in the temperature range from 150°–290°K using a collision frequency equal to $\nu(u)=1.33\times10^{7-}uN(N_2)$ sec^{-1}.

Electron collision frequencies in nitrogen at energies somewhat above that of the gas temperature can be estimated from analyses of measurements of electron mobility and of the ratio of the electron diffusion coefficient to the electron mobility. Thus, Huxley[4] has shown that the experimental results are consistent with a collision frequency equal to $\nu(u)/\mathrm{N}(\mathrm{N}_2)=1.16\times10^{-7}u$ cm^3/sec. These results are in very good agreement with the higher energy portion of the data given in the preceding paragraph.

Electron collision frequency determinations at low energies in oxygen are very limited. Shkarofsky, Bach-

* This work was supported in part by the U. S. Air Force Special Weapons Center, the Advanced Research Projects Agency, and the U. S. Office of Naval Research.

[1] A. V. Phelps, O. T. Fundingsland, and S. C. Brown, Phys. Rev. **84**, 559 (1959). See also J. M. Anderson and L. Goldstein, Phys. Rev. **102**, 388 (1956) and D. Formato and A. Gilardini, *Ionization Phenomena in Gases*, edited by N. R. Nilsson (North-Holland Publishing Company, Amsterdam, 1960), Vol. I, p. 99.

[2] J. L. Pack and A. V. Phelps (to be published). For a preliminary report see A. V. Phelps and J. L. Pack, Phys. Rev. Letters **3**, 340 (1959).

[2a] *Note added in proof.*—J. L. Pack has recently remeasured the mobility of thermal electrons in nitrogen using an improved technique. The derived electron collision frequencies are 10–12% larger than those given in this paper. This can be taken into account in Figs. 2–4 and in Eqs. (9) and (12) by using pressures 10% below the actual values.

[3] H. S. W. Massey and E. H. S. Burhop, *Electronic and Ionic Impact Phenomena* (Oxford University Press, New York, 1952), p. 113.

[4] L. G. H. Huxley, J. Atmospheric and Terrest. Phys. **16**, 46 (1959). See also R. W. Crompton, L. G. H. Huxley, and D. J. Sutton, Proc. Roy. Soc. (London) **A218**, 507 (1953).

ynski, and Johnston[5] have reanalyzed the available measurements of mobility and of the ratio of the diffusion coefficient to the mobility for electrons with average energies above the gas temperature. Their derived collision cross sections are consistent with an electron collision frequency given by the relation $\nu(u)/N(O_2) = 4\times10^{-9}u^{\frac{1}{2}}+5\times10^{-8}u$ cm^3/sec for energies between 0.03 and 0.2 ev. For energies below 0.1 ev the relation $\nu(u)=7\times10^{-8}N(O_2)u$ sec^{-1} fits the data to an accuracy of $\pm10\%$. Van Lint *et al.*[6] have measured the microwave conductivity due to thermal electrons in oxygen at low pressures and 300°K. We can obtain an expression for the electron collision frequency which is consistent with their results using the scheme given by Phelps, Fundingsland, and Brown,[1] i.e., we assume that $\nu(u)$ can be written in the form $\nu(u)=au^{j/2}$. If we assume that $j=2$, then the experimental data requires that $\nu(u)=9\times10^{-8}N(O_2)u$ sec^{-1}.

The collision frequency for electrons in air is found by adding collision frequencies in proportion to the oxygen and nitrogen densities. Electron collisions with argon and water molecules are neglected. Our two-term approximation to the collision frequency is $\nu(u)/N = 3\times10^{-9}u^{\frac{1}{2}}+1.1\times10^{-7}u$ cm^3/sec while the one term approximation is $\nu(u)=1.25\times10^{-7}Nu$ sec^{-1}. Here, and for the remainder of the paper, N is the density of air molecules. Because of the simplifications resulting from its use, the one-term approximation to the collision frequency will serve as a basis for subsequent discussion. The more accurate approximation using two terms leads to integrals requiring numerical evaluation and so will be used primarily to indicate the accuracy of the one-term approximation.

It should be kept in mind that these results apply only to weakly ionized, dry air. The effect of electron collisions with ions and water-vapor molecules can be estimated as follows. Anderson and Goldstein[7] have measured average values for the frequency of electron collisions with positive ions. Their results are consistent with a collision frequency given by $\nu_+(u)=2\times10^{-8}N_+u^{-\frac{1}{2}}$ sec^{-1}, where N_+ is the positive ion density. The collision frequency of electrons with negative ions will be the same as for positive ions. In order for the collision frequency for electrons with positive and negative ions to be less than 1% of that for neutral atoms, we require that $(N_++N_-)/N\leq6\times10^{-8}u^{\frac{1}{2}}$. For an average electron energy corresponding to 200°K, this means that we require that $(N_++N_-)/N\leq2\times10^{-9}$. The collision frequency for electrons with water-vapor molecules has been calculated by Altschuler[8] to be $\nu(u)=10^{-7}u^{-\frac{1}{2}}N(H_2O)$. In order that this frequency be less than 1% of that for air we require that $N(H_2O)/N\leq10^{-2}u^{\frac{1}{2}}$. For an average electron energy corresponding to 288°K, this means that $N(H_2O)/N\leq4\times10^{-5}$ compared to a value of 1.6×10^{-2} for air saturated with water vapor at this temperature. Although the water-vapor content of the air decreases rapidly with increasing altitude,[9] this condition probably is not satisfied for altitudes below about 50 km. At 30 km the water content is estimated[9] to be about 3 parts in 10^4.

The rather strong energy dependence of the collision frequencies for air found in the preceding discussion suggests that there may be significant errors in the propagation constants customarily calculated assuming an energy independent collision frequency and using the Appleton-Hartree equations.[10] In the following sections we shall give equations and graphs for the calculation of the propagation constants based on our approximations to the energy dependent collision frequency. We shall compare these results with those obtained using an energy independent collision frequency.

II. COMPONENTS OF CONDUCTIVITY TENSOR

Generalized expressions for the propagation constant can be obtained from the relations given by Jancel and Kahan[11] in terms of components of the conductivity tensor. A number of authors[11–14] have related the components of the conductivity tensor to integrals involving the electron density n, the normalized electron energy distribution function f_0, the frequency of momentum transfer collisions of electrons with gas molecules $\nu(u)$, the angular frequency of the electromagnetic wave ω, and the gyrofrequency $\omega_b=eB/m$, where e and m are the charge and mass of the electron and B is the magnetic field intensity. Thus, when the magnetic field is parallel to the z axis, the conductivity tensor can be written as

$$\begin{vmatrix} \sigma_2 & -\sigma_3 & 0 \\ \sigma_3 & \sigma_2 & 0 \\ 0 & 0 & \sigma_1 \end{vmatrix}, \tag{1}$$

[5] I. P. Shkarofsky, M. P. Bachynski, and T. W. Johnston, RCA Victor Company, Ltd., Research Laboratories, Montreal, Canada, Rept. 7-801 (December 5, 1959, unpublished). See also M. P. Bachynski, T. W. Johnston, and I. P. Shkarofsky, Proc. I. R. E. **48**, 347 (1960).

[6] V. A. J. van Lint, E. G. Wicker, and D. L. Trueblood, Rept. No. TR59-43 (August 31, 1959), General Atomic Division of General Dynamics Corporation, San Diego, California (unpublished).

[7] J. M. Anderson and L. Goldstein, Phys. Rev. **100**, 1037 (1955). For a recent discussion of the theory see M. S. Sodha and Y. P. Varshni, Phys. Rev. **111**, 1203 (1958) and **114**, 717 (1959). We neglect variations due to the logarithmic term.

[8] S. Altschuler, Phys. Rev. **107**, 114 (1957). Experimental measurements are summarized by S. Takeda and A. A. Dougal, J. Appl. Phys. **31**, 412 (1960).

[9] L. E. Miller, J. Geophys. Research **62**, 351 (1957).

[10] See for example, J. A. Ratcliffe, *The Magneto-Ionic Theory and Its Application to the Ionosphere* (Cambridge University Press, Cambridge, England, 1959).

[11] R. Jancel and T. Kahan, J. phys. radium **15**, 696 (1955).

[12] P. Molmud, Phys. Rev. **114**, 29 (1959).

[13] M. Bayet, J. phys. radium **15**, 258 (1954).

[14] See for example, W. P. Allis in *Handbuch der Physik*, edited by S. Flügge (Springer-Verlag, Berlin, 1956), Vol. 21, p. 413. In the limit of $\omega_b=0$ these relations reduce to those of H. Margenau, Phys. Rev. **69**, 508 (1946). Note that the conductivity relations proposed by E. A. Desloge, S. W. Matthysse, and H. Margenau, Phys. Rev. **112**, 1437 (1958) are not applicable to the problems considered in this paper. See footnote reference 2.

where $\mathbf{J}=|\sigma|$, $\mathbf{E}$ is the electric field, and $\mathbf{J}$ is the current density.
Here

$$\sigma_2=\tfrac{1}{2}(\sigma_L+\sigma_R),\quad \sigma_3=(i/2)(\sigma_L-\sigma_R)\quad\text{and}\quad \sigma_1=\sigma_P, \tag{2}$$

where

$$\sigma_P=-\frac{4\pi ne^2}{3m}\int_0^\infty \frac{u^{\frac{1}{2}}}{[\nu(u)+i\omega]}\frac{\partial f_0}{\partial u}du, \tag{3}$$

$$\sigma_L=-\frac{4\pi ne^2}{3m}\int_0^\infty \frac{u^{\frac{1}{2}}}{[\nu(u)+i(\omega+\omega_b)]}\frac{\partial f_0}{\partial u}du, \tag{4}$$

and

$$\sigma_R=-\frac{4\pi ne^2}{3m}\int_0^\infty \frac{u^{\frac{1}{2}}}{[\nu(u)+i(\omega-\omega_b)]}\frac{\partial f_0}{\partial u}du. \tag{5}$$

The preceding definitions show that the only integral we need to evaluate is[12]

$$\sigma=-\frac{4\pi}{3}\frac{ne^2}{m}\int_0^\infty \frac{u^{\frac{1}{2}}}{[\nu(u)+i\Omega]}\frac{\partial f_0}{\partial u}du, \tag{6}$$

where Ω is a generalized angular frequency equal to ω, $\omega+\omega_b$, or $\omega-\omega_b$ when evaluating σ_P, σ_L, or σ_R, respectively. It is convenient to introduce the normalized conductivity components defined by the following equations:

$$A=(m\Omega/ne^2)\,\mathrm{Re}(\sigma)\quad\text{and}\quad B=(m\Omega/ne^2)\,\mathrm{Im}(\sigma).$$

We are interested in situations where the electric field is small enough so that the electrons are in thermal equilibrium with the gas. Therefore, the electron energy distribution function is Maxwellian and is given by

$$f_0=(e/\pi kT)^{\frac{1}{2}}e^{-eu/kT}.$$

On using the approximation that $\nu(u)=au$, Eq. (6) becomes

$$\sigma(\nu_2,\Omega)=\frac{ne^2}{m}\frac{4\pi}{3}\left(\frac{e}{\pi kT}\right)^{\frac{1}{2}}\int_0^\infty \frac{u^{\frac{1}{2}}(au-i\Omega)}{(a^2u^2+\Omega)}e^{-eu/kT}d\left(\frac{eu}{kT}\right)$$

$$=\frac{ne^2}{m\Omega}[(\tfrac{3}{2})\gamma_2^{-1}\mathfrak{C}_{\frac{1}{2}}(1/\gamma_2)-i(1/\gamma_2^2)\mathfrak{C}_{\frac{1}{2}}(1/\gamma_2)]$$

$$=\frac{ne^2}{m\Omega}[A_2-iB_2]. \tag{7}$$

Here $\gamma_2\equiv\nu_2/\Omega=akT/e\Omega$ is a normalized collision frequency and the $\mathfrak{C}_p(x)$ integrals have been evaluated by Dingle, Arnt, and Roy.[15] The solid curves of Fig. 1 show values of $|A_2|$ and B_2 as a function of γ_2. The sign of A is the same as that of Ω such that A/Ω is positive.

At this point it is important to note that our use of the collision frequency $\nu_2=akT/e$ means that we have chosen to express the conductivities in terms of the collision frequency for monoenergetic electrons $\nu(u)$ evaluated at the energy $u=kT/e$. This choice is dictated by the exponent of the Maxwellian velocity distribution. This notation should not be taken to mean that we have averaged the collision frequency over the velocity distribution. The subscript 2, used with ν_2, A_2, and B_2 (and with D_2 and F_2 as defined later), is chosen to remind us that we have used the relation $\nu(u)=au^{j/2}$ with $j=2$ to approximate the collision frequency and to calculate the corresponding A and B functions. Similarly, we will use ν_0, A_0, etc., when the collision frequency is approximated by a constant, i.e., when $j=0$.

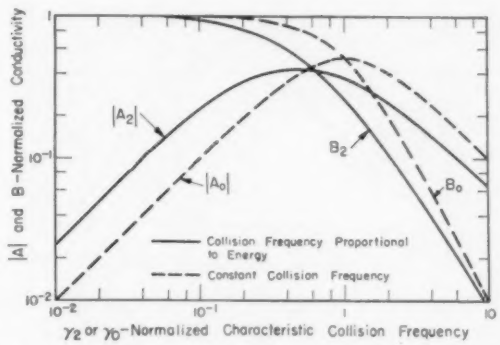

FIG. 1. Normalized conductivity components $|A|$ and B as a function of normalized characteristic collision frequency for the cases of collision frequency proportional to electron energy and independent of electron energy.

In gases for which the electron collision frequency is independent of electron energy, the calculation of the conductivity terms is very simple.[10–14] Thus,

$$A_0=\frac{\Omega\nu_0}{\nu_0^2+\Omega^2}=\frac{\gamma_0}{1+\gamma_0^2}\quad\text{and}\quad B_0=\frac{\Omega^2}{\nu_0^2+\Omega^2}=\frac{1}{1+\gamma_0^2}, \tag{8}$$

where $\gamma_0=\nu_0/\Omega$. The dashed curves of Fig. 1 show $|A_0|$ and B_0 as a function of γ_0. One notes that for small values of γ_0 or γ_2 the two A curves can be made to coincide by sliding the A_0 curve to the left by a factor of 2.5. Thus, if $\nu(u)$ is accurately given by $\nu(u)=au$ so that A is accurately given by A_2 one can also obtain the correct value of A for $\gamma_2\ll1$ by using a value of $\gamma_0=2.5\nu_2/\Omega=2.5akTN/e\Omega$ in Eqs. (8). This possibility has been noted previously by Belcher and Sugden[16] and by Pfister[17] for the case of constant collision cross section and led to the introduction of the concept of an effective collision frequency ν_0 which is used in Eqs. (8) to calculate approximate values of A and B, i.e., A_0 and B_0.

[15] R. B. Dingle, D. Arnt, and S. K. Roy, Appl. Sci. Research **6B**, 155 (1956). The applicability of these integrals was pointed out by P. H. Fang, Phys. Rev. **113**, 13 (1959).

[16] H. Belcher and T. M. Sugden, Proc. Roy. Soc. (London) **A201**, 480 (1950).

[17] W. Pfister, *The Physics of the Ionosphere* (The Physical Society, London, 1955) p. 399. Note, however, that the effective collision frequency at low pressures is $\frac{4}{3}$ times the average value only for a gas with a constant collision cross section. If $\nu=au^{j/2}$ then $\nu_0=(j+3)\bar{\nu}/3$. This result is consistent with the cases discussed in footnote reference 12. It is of interest to note that in our notation the principal values of the dielectric tensor are $1+\sigma_P'$, $1+\sigma_R'$, and $1+\sigma_L'$.

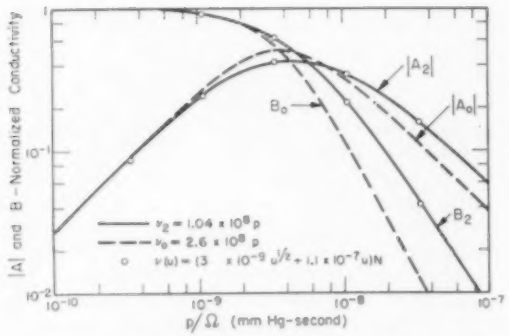

FIG. 2. Normalized conductivity components $|A|$ and B for weakly ionized, dry air as a function of p/Ω. The curves show approximations to the exact values for air and can be used to calculate the principal values of the conductivity tensor σ_P, σ_L, or σ_R by setting Ω equal to ω, $\omega+\omega_b$, or $\omega-\omega_b$, respectively.

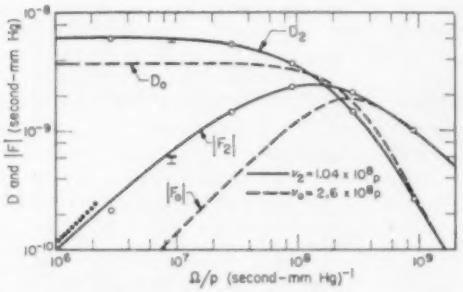

FIG. 3. Normalized conductivity components D and $|F|$ for weakly ionized, dry air as a function of Ω/p. These approximations to the exact values are especially useful for low frequencies, ω and $\omega_b \to 0$, or near the gyrofrequency, $(\omega-\omega_b) \to 0$. The conductivity components σ_P, σ_L, and σ_R are calculated from these curves by setting Ω equal to ω, $\omega+\omega_b$, or $\omega-\omega_b$, respectively. The dotted line shows the asymptotic value of the $|F_2|$ curve.

Effective collision frequencies have been defined for this and other limiting conditions by Molmud.[12] Thus, for $\gamma \gg 1$, the A curves can be made to coincide by sliding the A_0 curve to the left by a factor of 1.5. This means that the effective collision frequency for the computation of A_2 at $\gamma \gg 1$ using Eqs. (8) is the value of $\nu(u)$ for air at $u=3kT/2e$, i.e., $\nu_0=1.5\nu_2$. The calculation of B_2 for $\gamma \ll 1$ and $\gamma \gg 1$ requires effective collision frequencies equal to the actual collision frequency evaluated at $(35/4)^{\frac{1}{2}}kT/e$ and $(4/3)^{\frac{1}{2}}kT/e$, respectively. We, therefore, have four effective collision frequencies to keep in mind and can use them only for the limiting cases of $\gamma \ll 1$ or $\gamma \gg 1$. If we use a single effective collision frequency in Eqs. (8), say $\nu_0=2\nu_2=2akTN/\epsilon$, the resultant values of A_2 are about 20% low for $\gamma \ll 1$, 20% high for $\gamma_0=1$ and 25% low for $\gamma \gg 1$, while the values of B_2 are 10% high for $\gamma_0=0.5$ and 55% low for $\gamma \gg 1$.

For practical calculations of A_2 and B_2 it is convenient to note that because of the linear relation between collision frequency and electron energy the collision frequency at $u=kT/e$ is uniquely determined by the air pressure. Thus,

$$\nu_2=1.25\times10^{-7}kTN/\epsilon=1.04\times10^8 p \text{ sec}^{-1}, \quad (9)$$

where p is the pressure in mm of Hg. The solid curves of Fig. 2 show a plot of A_2 and B_2 as a function of p/Ω calculated using Eqs. (7) and (9). The dashed curves show the values of A_0 and B_0 calculated using Eqs. (8) and an effective collision frequency 15% larger than that obtained by Nicolet[13] from Kane's[19] rocket data, i.e., $\nu_0=2.6\times10^8 p$ sec^{-1} at an average temperature of 225°K. Note that this value is 2.5 times that given by Eq. (9) and so is expected to be most accurate at small values of p/Ω. Figure 2 shows that the differences between A_2 and A_0 and between B_2 and B_0 are less than 20% for $p/\Omega<5\times10^{-9}$ mm Hg-sec, but that the difference between B_2 and B_0 is almost a factor of 4 for very large p/Ω.

The curves shown in Figs. 1 and 2 are particularly suited to the calculation of the real and imaginary components of the conductivity tensor when the angular frequency of the wave and the gyrofrequency are fixed and the gas pressure is varied. However, these curves are somewhat confusing when either ω or ω_b is varied at constant pressure. In this case it is convenient to write the generalized conductivity of Eq. (7) in the form

$$\sigma(\nu_2,\Omega)=(ne^2/m\nu_2)[(\tfrac{1}{2})\mathfrak{C}_{\frac{1}{2}}(1/\gamma_2) - i(1/\gamma_2)\mathfrak{C}_{\frac{1}{2}}(1/\gamma_2)]. \quad (10)$$

Because of the dependence of ν_2 on pressure only, it is convenient to define normalized conductivity components at unit pressure by the relations

$$D=(mp/ne^2)\,\mathrm{Re}(\sigma) \quad \text{and} \quad F=(mp/ne^2)\,\mathrm{Im}(\sigma), \quad (11)$$

so that $D=(p/\Omega)A$, $F=(p/\Omega)B$, and

$$D_2-iF_2=9.6\times10^{-9}[2.5\mathfrak{C}_{\frac{1}{2}}(1/\gamma_2) - i(\gamma_2)^{-1}\mathfrak{C}_{\frac{1}{2}}(1/\gamma_2)]. \quad (12)$$

The solid curves of Fig. 3 show plots of D_2 and $|F_2|$ for air as functions of Ω/p. The sign of F is the same as that of Ω. These curves are especially useful when $\omega-\omega_b$ approaches zero since the 0/0 which appears in the real part of Eq. (7) at $\omega=\omega_b$ becomes a well-defined quantity.

A second feature brought out by the curve for $|F_2|$ in Fig. 3 is the slow approach of the imaginary part of the conductivity to its asymptotic values as $\Omega/p \to 0$, i.e., at cyclotron resonance or for very small magnetic fields and very low frequency or dc electric fields. Examination of the conductivity integrals shows that this behavior results from the first-order zero of the assumed energy dependence of the collision frequency at zero electron energies. The circles of Figs. 2 and 3 show the effect of using the more accurate approximation to the electron collision frequency in air from Sec. I to calculate A, B, D, and F for air. Here we have used the

[18] M. Nicolet, Phys. Fluids **2**, 95 (1959).
[19] J. A. Kane, J. Geophys. Research **64**, 133 (1959).

relation $\nu(u)/N=3\times10^{-9}u^{\frac{1}{2}}+1.1\times10^{-7}u$ cm³/sec and have assumed that the gas temperature is 235°K. The conductivity integrals were evaluated numerically. The effect of varying the air temperature between 140°K and 270°K is shown by the vertical extent of the symbols at $\Omega/p=9.2\times10^{6}$ sec^{-1} mm Hg^{-1} in Fig. 3; the larger values correspond to the higher temperature. The dashed curves show values of D_0 and $|F_0|$ obtained using $\nu_0=2.6\times10^{8}p$ sec^{-1}. Since eD/mp equals the dc electron mobility when $\Omega/p=0$, the different limiting values of D for the different approximations to $\nu(u)$ can be compared directly with measured mobilities. When proper allowance is made for the effects of oxygen, the asymptotic value for the circles agrees with the nitrogen data[2] to within experimental accuracy.

III. CALCULATION OF PROPAGATION CONSTANTS

The generalized propagation constant for an electromagnetic wave in a conducting gas and in the presence of a magnetic field has been evaluated by Jancel and Kahan[11] and has been applied to the present problem by Sen and Wyller.[20] If the electric field is given by

$$E=E_0\exp(i\omega t-ikz), \tag{13}$$

then

$$\left(\frac{k\lambda}{2\pi}\right)^2=\frac{b+d\sin^2\theta\pm(d\sin^2\theta-g\cos^2\theta)^{\frac{1}{2}}}{m+n\sin^2\theta}, \tag{14}$$

where λ is the wavelength of the radiation in free space, θ is the angle between the magnetic field and the direction of propagation, $b=2(1+\sigma_1')(1+\sigma_2')$, $d=(\sigma_2'-\sigma_1')\times(1+\sigma_2')-(\sigma_3')^2$, $g=2\sigma_3'(1+\sigma_1')$, $m=2(1+\sigma_1')$, and $n=2(\sigma_2'-\sigma_1')$. Here $\sigma'=\sigma/i\omega\epsilon_0$ where we use rationalized mks units. In view of the complexity of this general expression[10] and the relative simplicity of the experiments to which we shall apply our results, our discussion is limited to the cases of propagation parallel to and perpendicular to the magnetic field.

(a) Propagation parallel to the magnetic field ($\theta=0$). In this case

$$(k\lambda/2\pi)^2=1+(\sigma_2/i\omega\epsilon_0)\pm(\sigma_3/\omega\epsilon_0). \tag{15}$$

It is customary to call the wave associated with the positive sign in Eq. (15) the ordinary wave. Its propagation constant is given by

$$k_0=\frac{2\pi}{\lambda}\left(1+\frac{\sigma_L}{i\omega\epsilon_0}\right)^{\frac{1}{2}}=\frac{2\pi}{\lambda}\left\{1-\frac{\omega_p^2}{\omega(\omega+\omega_b)}[B(\omega+\omega_b)+iA(\omega+\omega_b)]\right\}^{\frac{1}{2}}, \tag{16}$$

where $\omega_p=(ne^2/m\epsilon_0)^{\frac{1}{2}}$ is the plasma resonance frequency and the notation $A(\omega+\omega_b)$ and $B(\omega+\omega_b)$ is used to indicate that A and B are evaluated with $\Omega=\omega+\omega_b$. As indicated by the σ_L, this wave can be shown to be left circularly polarized about the direction of propagation.[10] The use of the minus sign in Eq. (15) gives the propagation constant for the extraordinary wave k_x which is right circularly polarized. Thus,

$$k_x=\frac{2\pi}{\lambda}\left(1+\frac{\sigma_R}{i\omega\epsilon_0}\right)^{\frac{1}{2}}=\frac{2\pi}{\lambda}\left\{1-\frac{\omega_p^2}{\omega(\omega-\omega_b)}[B(\omega-\omega_b)+iA(\omega-\omega_b)]\right\}^{\frac{1}{2}}. \tag{17}$$

If we write $k=\mu-i\kappa$, then μ is the real part of the refractive index and κ is the absorption coefficient. If we now assume that

$$|\omega_p^2/\omega(\omega-\omega_b)|\ll1,$$

then

$$\mu_{o,x}=(2\pi/\lambda)\left\{1-\frac{[\omega_p^2B(\omega\pm\omega_b)]}{[2\omega(\omega\pm\omega_b)]}\right\} \tag{18}$$

and

$$\kappa_{o,x}=\frac{\pi\omega_p^2A(\omega\pm\omega_b)}{\lambda\omega(\omega\pm\omega_b)}, \tag{19}$$

where the + sign and the o subscript apply to the ordinary wave and the − sign and x subscript apply to the extraordinary wave. Note that the condition $|\omega_p^2/\omega(\omega-\omega_b)|\ll1$ becomes very difficult to satisfy for $\omega\rightarrow\omega_b$.

(b) Propagation perpendicular to the magnetic field ($\theta=90°$). In this limit

$$k_o=\frac{2\pi}{\lambda}\left(1+\frac{\sigma_P}{i\omega\epsilon_0}\right)^{\frac{1}{2}}=\frac{2\pi}{\lambda}\left\{1-\frac{\omega_p^2}{\omega^2}[B(\omega)+iA(\omega)]\right\}^{\frac{1}{2}} \tag{20}$$

and

$$k_x=\frac{2\pi}{\lambda}\left\{1+\frac{i\omega\epsilon_0(\sigma_L+\sigma_R)+2\sigma_R\sigma_L}{i\omega\epsilon_0(2i\omega\epsilon_0+\sigma_R\sigma_L)}\right\}^{\frac{1}{2}}. \tag{21}$$

For $\omega_p^2/\omega^2\ll1$, Eq. (20) shows that the real parts of the dielectric coefficient and the absorption coefficient are given by the expressions

$$\mu_0=(2\pi/\lambda)[1-(\omega_p^2/2\omega^2)B(\omega)]$$

and

$$\kappa_0=(\pi\omega_p^2/\lambda\omega^2)A(\omega). \tag{22}$$

We note that these propagation constants are those obtained in the absence of a magnetic field. Similarly, for $|\omega_p^2/\omega(\omega-\omega_b)|\ll1$, Eq. (21) becomes

$$k_x=(2\pi/\lambda)\{1+[(\sigma_L+\sigma_R)/4i\omega\epsilon_0]\}^{\frac{1}{2}},$$

or

$$\mu_x=\frac{2\pi}{\lambda}\left[1-\frac{\omega_0^2}{4\omega(\omega+\omega_b)}B(\omega+\omega_b)-\frac{\omega_0^2}{4\omega(\omega-\omega_b)}B(\omega-\omega_b)\right], \tag{23}$$

[20] H. K. Sen and A. A. Wyller, Phys. Rev. Letters 4, 355 (1960).

and

$$\kappa_x=\frac{\pi}{2\lambda}\left[\frac{\omega_0^2}{\omega(\omega+\omega_b)}A(\omega+\omega_b)+\frac{\omega_0^2}{\omega(\omega-\omega_b)}A(\omega-\omega_b)\right].$$

Equations (20) and (22) apply to the ordinary wave which is polarized parallel to the magnetic field, while Eqs. (21) and (23) apply to the extraordinary wave which is polarized perpendicular to the magnetic field.

IV. APPLICATIONS OF CALCULATIONS

A recent example of ionospheric studies for which the above relations are useful is the determination by Kane[19] of electron collision frequencies in the "D" layer from radio propagation measurements using rockets. The experimental data are expressed in terms of a quantity Q which is a function of altitude and is defined by the relation

$$Q=\frac{\kappa_x-\kappa_o}{[(2\pi/\lambda)-\mu_x]+1.4[(2\pi/\lambda)-\mu_o]}. \tag{24}$$

For the rocket trajectories used in these experiments the direction of propagation is parallel to the earth's magnetic field. We therefore substitute Eqs. (18) and (19) into Eq. (24) to obtain

$$Q=\frac{(\omega-\omega_b)^{-1}A(\omega-\omega_b)-(\omega+\omega_b)^{-1}A(\omega+\omega_b)}{(\omega-\omega_b)^{-1}B(\omega-\omega_b)+1.4(\omega+\omega_b)^{-1}B(\omega+\omega_b)}$$
$$=\frac{D(\omega-\omega_b)-D(\omega+\omega_b)}{F(\omega-\omega_b)+1.4F(\omega+\omega_b)}. \tag{25}$$

Upon using the approximation that $\nu(u)=au$ for air, the corresponding approximation to Q is given by

$$Q_2=\frac{2.5\nu_2\{\mathfrak{S}_{\frac{1}{2}}[(\omega-\omega_b)/\nu_2]-\mathfrak{S}_{\frac{1}{2}}[(\omega+\omega_b)/\nu_2]\}}{(\omega-\omega_b)\mathfrak{S}_{\frac{1}{2}}[(\omega-\omega_b)/\nu_2]+1.4(\omega+\omega_b)\mathfrak{S}_{\frac{1}{2}}[(\omega+\omega_b)/\nu_2]}. \tag{26}$$

This function is plotted as a function of ν_2/ω in Fig. 2 of footnote reference 1 for a value of ω_b/ω appropriate to Kane's experimental conditions and for values of $\nu_2/\omega<1$. Equation (26) is not useful for $\nu_2/\omega>2$. For $\omega_b^2\ll\omega^2$, Eq. (26) becomes

$$Q_2=\frac{4.17\omega_b}{\nu_2}\frac{\mathfrak{D}_{\frac{1}{2}}(\omega/\nu_2)}{\mathfrak{S}_{\frac{1}{2}}(\omega/\nu_2)}, \tag{27}$$

where $\mathfrak{D}_{\frac{1}{2}}$ is given by Dingle, Arnt, and Roy.[15] For Kane's value of $\omega_b/\omega=0.208$, Eq. (27) gives values[21] of Q which are about 10% low for $\nu_2/\omega<0.05$, correct for $\nu_2/\omega\sim0.25$, and about 4% high for $\nu_2/\omega>1$. However, as was pointed out in footnote reference 2, and is discussed below, the accuracy of these expressions for $\nu_2/\omega\gg1$ may be poor because of errors introduced by departures of the true $\nu(u)$ from the assumed linear variation with u.

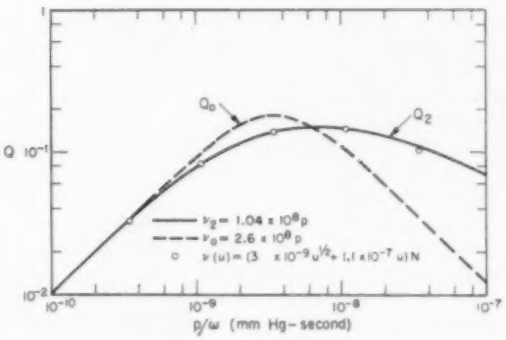

FIG. 4. Kane's Q function vs p/ω for weakly ionized, dry air and for $\omega_b/\omega=0.208$.

The solid curve of Fig. 4 shows a plot of Q_2 as a function of p/ω for Kane's value of $\omega_b/\omega=0.208$ as calculated using Eqs. (9), (26), and (27). The dashed curve shows the approximate Q function, i.e., Q_0 calculated using our effective collision frequency ν_0 in Eqs. (8) for the A and B terms in Eq. (25). The agreement is good for $p/\omega<10^{-9}$ mm Hg-sec. For sufficiently large p/ω, Eq. (27) yields $Q_2=0.315\ (\gamma_2)^{-\frac{1}{2}}$ whereas Eqs. (8) give $Q_0=0.335\ (\gamma_0)^{-1}$. The unusual behavior of Q_2 at large p/ω is caused by the first-order zero in our approximation to $\nu(u)$ and its effect on the quantity $\kappa_x-\kappa_0$ of Eq. (24). If we again assume that $\nu(u)/N=3\times10^{-9}u^{\frac{1}{2}}+1.1\times10^{-7}u$ cm^3/sec and that the gas temperature is 235°K, we obtain the circles shown in Fig. 4. These points lie below the Q_2 curve by an amount which increases with decreasing gas temperature and increasing p/ω. At sufficiently large p/ω or sufficiently low temperatures the circles lie on a curve which is parallel to the Q_0 curve.

The Q functions given in Fig. 4 can be used to calculate the air pressure as a function of altitude from the experimental results given by Kane[19] and then compared with pressures derived from other observations. However, since we are primarily concerned with the Q functions,[22] we shall compare Kane's measured values of Q as a function of altitude with the values computed using

[21] The values given by Eq. (27) should be divided by $(1-\omega_b^2/\omega^2)(1-\omega_b/6\omega)$ for $\gamma_2\to0$ and divided by $(1+\omega_b/6\omega)$ for $\gamma_2\to\infty$. The number 6 is the factor by which the low-frequency signal is multiplied in frequency before comparison with the high-frequency signal. See footnote reference 19.

[22] In this discussion we have compared the Q values rather than the collision frequencies since the apparent agreement or disagreement between derived collision frequencies may depend upon the energy at which the collision frequency is evaluated. Thus, the disagreement between the collision frequencies derived from laboratory experiments shown in Fig. 3 of footnote reference 2 is larger than would be the case if the collision frequencies had been evaluated at a higher value of u than kT/e. This peculiarity results from the fact that the two $\nu(u)$ curves do not have the same energy dependence and so cross at a finite u.

Fig. 4 and the available measurements of pressure.[23] The results are shown in Fig. 5 where the vertical lines indicate the experimental uncertainty assigned to the observations by Kane and the solid and dashed curves are calculated using the Q_2 and Q_0 curves of Fig. 4. We see that for this particular experiment the experimental uncertainties are large enough such that either Q curve gives reasonable agreement with the experimental data. As shown by Nicolet,[15] a better fit between the experimental data and the Q_0 curve is obtained by using a somewhat smaller ν_0 than that used in our analysis.

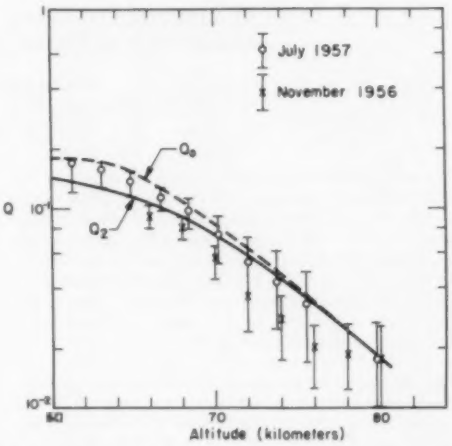

FIG. 5. Kane's Q function vs altitude. The two sets of experimental data are from separate rocket flights during "polar blackouts" on the dates indicated. The smooth curves were calculated assuming that the pressures were the same on the two dates.

V. SUMMARY

The nearly linear variation with energy in the frequency of momentum transfer collisions for electrons in air leads to significant differences between the correct propagation constants for electromagnetic waves in weakly ionized air and the constants calculated on the assumption that the collision frequency is independent of the electron energy. By approximating the electron collision frequency in dry air by a linear function of the electron energy, expressions have been derived for propagation constants in terms of tabulated functions. At temperatures of ionospheric interest these expressions are accurate except for very large values of p/ω. In many ionospheric experiments the experimental uncertainties are large enough so that it is satisfactory to calculate the propagation constants for weakly ionized air using an effective collision frequency in the standard Appleton-Hartree expressions.

The deviations of the conductivity tensor components for air from the values calculated using the linear approximation to the collision frequency at large p/Ω suggests the possibility of using a laboratory measurement of one of these quantities as a means of determining the collision frequency for electrons in air at electron energies below those obtainable by cooling the gas. Laboratory measurements of the temperature dependence of the high frequency or dc mobility of thermal electrons in oxygen would be very useful in order to give a more accurate evaluation of the collision frequency for air.

[23] We have used the pressure vs altitude data given by Nicolet in footnote reference 18 since it is readily available. More recent compilations such as the ARDC model atmosphere of 1959 give pressures which are equal to those of Nicolet at 60 km and about 15% lower for 80 km.

VI. ACKNOWLEDGMENTS

The author wishes to express his appreciation to his associates in the Atomic Physics Group for valuable discussions of this problem.

Effects of Internal Oxidation and Heat Treatment on the Electrical Resistivity of Dilute CuMn, CuFe, and CuCo Alloys

C. A. Domenicali and E. L. Christenson
Honeywell Research Center, Hopkins, Minnesota
(Received May 23, 1960)

This investigation was concerned with the effects of high temperature treatment *in vacuo* or in rarefied oxygen atmospheres upon the effective electrical resistivity of dilute (copper-rich) CuMn, CuFe, and CuCo rods and wires. The CuMn alloys studied most extensively contained between 1 and 12 at. % manganese while the CuFe and CuCo alloys contained between 0.1 and 0.3 at. % iron or cobalt. It was found that the solutes in the CuFe and CuCo wires and rods become rapidly oxidized (internally) during heat treatment for several hours at 990°C in pure oxygen pressures of 0.5 μ or greater, while in 0.05 μ O_2 this oxidation is absent and previously oxidized specimens are reduced. These observations are based on measurements of electrical resistivity, and in the case of CuFe, substantiated by measurements on the magnetization. Heat treatment of these CuFe and CuCo wires and rods near 1000°C for several hours either *in vacuo* (0.1 μ air) or 5 μ O_2 does not appreciably affect the cross-sectional *uniformity* of these specimens. In the case of CuFe alloys, the magnetic behavior demonstrates the virtually complete oxidation of solute to Fe_3O_4 after prolonged anneal in an oxidizing atmosphere. The behavior of the CuMn alloys was found to be more complicated, partly because of the high solute concentrations involved. It was found that wires and rods of CuMn rapidly become nonuniform in solute concentration throughout their cross section when annealed near 1000°C for several hours either in a vacuum (0.1 μ air) or in 5 μ of pure oxygen; this nonuniformity of manganese concentration develops at a considerably higher rate in the 5 μ O_2 atmosphere than in vacuum, and leads to erroneous values of the resistivity and to erroneous curves of resistivity vs temperature for CuMn wires or rods. On the other hand, annealing of such wires for several hours in vacuum at temperatures around 800°C does not appreciably disturb the cross-sectional uniformity. Finally, it is emphasized that the "carrier gas" technique (involving a flow system with small concentrations of oxygen mixed with helium at atmospheric pressure, for example) is entirely unsatisfactory for experiments on internal oxidation, particularly if one wants to know the oxygen partial pressure.

I. INTRODUCTION

IT has long been known from the work of Addicks[1] and others[2] that the electrical conductivity of "technically pure" copper is influenced by the presence of oxygen in the copper. Apparently Heuer[3] was the first to point out that some of the iron impurity in otherwise "pure" copper may be in the form of an oxide (which he considered to be FeO) and will therefore not affect the electrical conductivity of the copper. Smart and Smith[4] have shown from resistance measurements that small amounts of oxygen can completely precipitate iron or cobalt in the form of oxides in copper. Sato[5] investigated the electrical behavior of a copper-manganese alloy which had been rather heavily oxidized (in air?). More recently Pawlek, Viessmann, and Wendt[6] have extensively studied the influence of oxygen on the resistivity of various dilute copper-base alloys. The effect of oxygen on the resistivity of "pure" copper at liquid helium temperatures has been investigated by MacDonald and Pearson,[7] by Redman *et al.*,[8] and by Sekula,[9] who found that the resistance minimum in impure copper can be alternately "introduced" and "removed" by successive heat treatments in reducing and oxidizing atmospheres. However, in all these studies (except in a part of Sato's work) the wire or rod specimens were considered to have uniform solute concentration over the cross section of the specimen. Sato found that heavy oxidation of a Cu+25 at.% Mn alloy, sufficient to grow a rather thick oxide layer, actually changed the sign of the temperature coefficient of resistance; this effect was attributed to the formation of a "pure copper" or manganese-depleted layer at the surface of his rod specimen.

It is clearly important to know whether or not the various typical heat treatments used in the study of metal alloys lead to identical values of electrical parameters such as the electrical resistivity, for example. With this question in mind we have investigated the following aspects of this problem: (a) dependence of effective or "apparent" electrical resistivity of CuMn, CuFe, and CuCo wires on high-temperature treatment (990°C) *in vacuo* (0.1 μ air); (b) same, but for treatment in a rarefied, pure oxygen atmosphere equivalent to several ppm O_2 in an inert "carrier gas" at 1 atm; (c) cross-sectional uniformity of CuMn wires treated for several hours at 800° *in vacuo*; (d) determination of "safe" or critical oxygen partial pressure which may surround CuFe or CuCo alloys without lowering the resistivity because of internal oxidation of solute; (e) identification of Fe_3O_4 in internally oxidized CuFe alloys by magnetic measurements; (f) verification of work of others concerning the reversibility of internal oxidation and reduction of solutes in copper.

II. EXPERIMENTAL RESULTS

In studying aspects (a), (b), and (c) previously mentioned, our method consists simply in measuring

[1] L. Addicks, Trans. AIME **36**, 18 (1906).
[2] F. L. Antiselle, Trans. AIME **64**, 432 (1921).
[3] R. P. Heuer, J. Am. Chem. Soc. **49**, 2711 (1927).
[4] J. S. Smart and A. A. Smith, Trans. AIME **147**, 48 (1942).
[5] T. Sato, J. Phys. Soc. Japan **5**, 287 (1950).
[6] F. Pawlek, K. Viessmann, and H. Wendt, Z. Metallk. **47**, 357 (1956).
[7] D. K. C. MacDonald and W. B. Pearson, Acta Met. **3**, 392, 403 (1955).
[8] J. K. Redman, R. R. Coltman, T. H. Blewitt, and C. E. Klabunde, Bull. Am. Phys. Soc. Ser.II, **4**, (3), 150 (abstract G12) (1959).
[9] S. T. Sekula, Phys. Rev. Letters **3**, 416 (1959).

the resistivity of a wire specimen after a given heat treatment and after each of several heavy etches intended to remove considerable amounts of material from the wire. Thus, when we state that the solute concentration over a wire cross section is uniform, we mean that we find the same value of resistivity for the wire before and after these several reductions in cross-sectional area by heavy etching. The resistance of the wires (of either 0.030-in.×0.030-in. or 0.070-in.×0.070-in. square cross section) was measured by the usual potentiometric probe method. The copper, of nominal purity 99.999%, was obtained from American Smelting and Refining Company; the manganese, iron, and cobalt, of purity 99.99+%, were from Johnson-Matthey. Before making the alloys, the manganese was treated in our laboratory by melting in hydrogen in order to remove the oxide. The alloys were made by melting (accompanied by mechanical shaking) in sealed quartz tubes. The apparatus for heat treatment of the wire specimens is illustrated schematically in Fig. 1; the "vacuum head" or manifold shown is about 4 in. in diam and the 25-mm quartz tube is approximately 3 ft long. The furnace could be slid along the Transite table top to allow cooling of the tube and specimens. The small oxygen pressure was controlled quite satisfactorily by means of three needle valves in series.

A. Copper-Manganese Alloys

We show in Fig. 2 the effective or "apparent" resistivity of Cu+7.55 at.% Mn wire after various treatments. In curve 1 the wire had been annealed 2–3 hrs at 800°C in 0.1 μ vacuum. Subsequent heavy etching of several sections of this wire gave substantially the same resistivity vs temperature curve, and we therefore consider curve 1 as representing the true behavior of copper containing 7.55 at.% Mn. Treatment of a section of this wire for 2 hr at 990°C in 5 μ of pure oxygen[10] appears to "remove" most of the manganese solute, as shown by curve 2. However, this behavior results from the "shorting" effect of a manganese-depleted layer on the wire, as already described by Sato[5] in connection with a very heavily oxidized copper-manganese alloy. After

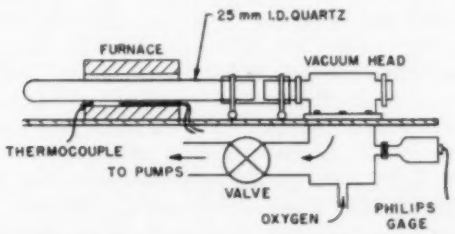

FIG. 1. Schematic diagram of apparatus used for heat treatment of alloy wires in rarefied, pure oxygen atmospheres. The oxygen pressure was controlled by three needle valves in series.

[10] This corresponds to about 7 ppm of oxygen in helium at atmospheric pressure.

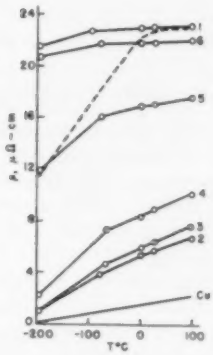

FIG. 2. Effective resistivity vs temperature for a wire (0.030 in.× 0.030 in. square cross section) of Cu+7.55 at. % Mn alloy, after various heat treatments. Curve 1: after 2–3 hrs at 800°C in 0.1 μ vacuum. Curve 2: after 2 hrs at 990°C in 5 μ pure oxygen. Curves 3, 4, 5, and 6: after heavy etching to reduce original cross section area by 8, 20, 35, and 55%, respectively. Dashed curve: data of Otter (footnote reference 11) for a Cu+9.14 at. % Mn wire. Solid curve at bottom: pure copper.

we remove the surface layer by etching, to reduce the cross section area by 8%, we find curve 3. Further etching gives in succession the curve (4) for 20% total reduction, curve (5) for 35% total reduction and curve (6) for 55% total reduction. The dashed line in Fig. 2 represents the results of Otter[11] for a Cu+9.14 at.% Mn wire; the solid curve at the bottom shows the resistivity of pure copper. One suspects that the wires studied by Otter were of nonuniform cross section, unfortunately.

In other experiments on CuMn wires we have performed essentially the same steps as described above, except that the 2-hr treatment at 990°C was carried out in an 0.1 μ vacuum (instead of 5 μ O_2). The results here were the same as in Fig. 2 except that the initial apparent manganese "removal," represented by the drop from curve 1 to curve 2, was not quite so drastic after vacuum treatment (990°C, 2 hr) as after O_2 treatment. (The vacuum treatment reduced the resistivity at −196°C from 22 to 14 μohm-cm.) We attribute this difference to the fact that the rapid formation of manganese oxide on the surface, with an O_2 atmosphere, represents a much more effective "sink" for manganese atoms diffusing outward from the interior of the wire than does the mere evaporation of Mn atoms from the surface. In fact, a CuMn wire which has been treated for 2 hrs at 990°C in 5 μ O_2 acquires such a large radial gradient of Mn concentration that subsequent treatment for 2 hr at 990°C *in vacuo* actually leads to a considerable *recovery* of the resistivity. Apparently this latter treatment smooths out the gradient caused by the oxidation; but this smoothing out is only partly effective because there is at the same time a continuing evaporation of Mn atoms from the outer layers. We have similarly investigated CuMn alloys containing

[11] F. A. Otter, Jr., J. Appl. Phys. **27**, 197 (1956).

between 1 and 12 at.% Mn and have found essentially the same behavior as that described above.

B. Copper-Iron Alloys

In agreement with other recent work,[7–9] we find that the iron impurity resistivity can be "cycled" in and out by alternate oxidation and reduction of the solute. Some of our early experiments of this sort (performed with an apparatus other than that shown in Fig. 1) were done with helium containing 0.045 at.% O_2 as determined by mass-spectrographic analysis. However, in order to determine the critical oxygen pressure required for internal oxidation of the iron solute in copper at 990°C we used pure oxygen atmospheres. (We consider the use of oxygen-bearing gas mixtures to be unsatisfactory for this purpose.) By cycling CuFe wires containing 0.1 or 0.2 at.% Fe through a series of 990°C treatments in pure oxygen atmospheres at various pressures, and observing the corresponding resistivity at −195°C, we find the critical oxygen pressure for the internal oxidation of iron in copper to be between 0.05 and 0.5 μ O_2 (at 990°C). Other observations lead us to believe that for iron this critical pressure is nearer the *lower* end of this range, or 0.05 μ.

These dilute CuFe alloys which have been internally oxidized (either lightly or heavily) can have their entire resistivity restored by treatment *in vacuo* or in an oxygen pressure of no more than 0.05 μ. This recovery of the resistivity proceeds at a considerably slower rate at a given temperature, than the oxidation process.

Magnetic measurements on internally oxidized CuFe rods show that magnetite (Fe_3O_4) is formed by this oxidation, and such rods exhibit the low-temperature "transition" characteristic of polycrystalline, slightly nonstoichiometric magnetite[12] in the region −150° to −180°C. Successive treatment of three different alloy specimens at 1000°C for a total of 42 hr in an oxidizing atmosphere increased the magnetic moments to values which correspond quite closely to the complete conversion of all the iron solute to magnetite. The precipitated oxide has already been identified as magnetite by Rhines[13] by means of x ray diffraction.

To determine whether or not significant evaporation of solute occurs during prolonged heating of CuFe wires at high temperatures, we have used the heavy-etching technique to examine the uniformity of cross section of an 0.2-at.% Fe wire which was heated for nearly 11 hrs at 990°C *in vacuo*. We find no significant "deterioration" of the wire after such treatment. Other specimens of our CuFe wires have been heated to these high temperatures for much longer periods of time with no apparent harmful effects as determined from resistivity measurements. (These latter wires, however, were not examined by the etching technique.)

[12] C. A. Domenicali, Phys. Rev. **78**, 458 (1950).
[13] F. N. Rhines, Trans. AIME **137**, 246 (1940).

C. Copper-Cobalt Alloys

CuCo alloys containing approximately 0.1, 0.2, or 0.3 at.% Co exhibit essentially the same electrical behavior upon internal oxidation as do dilute CuFe alloys; thus the solute resistivity can be cycled in and out by successive reducing and oxidizing treatments. Again using pure oxygen atmospheres, we find that the critical oxygen pressure for internal oxidation of the cobalt solute at 990°C is also between 0.05 and 0.5 μ O_2; in this case, however, other observations lead us to believe that for cobalt this critical pressure is nearer the *upper* end of this range, i.e., 0.5 μ.

We have examined the effect of high temperature treatment on the cross section uniformity of a Cu+0.2 at.% Co wire, and have found no significant deterioration of the wire as indicated by heavy etching. This wire was heated for 3 hr, and later for an additional 5 hr, *in vacuo* at 990°C. After a 39% area reduction (by etching) following the 5-hr treatment, the apparent resistivity remained the same as for all the previous states of the wire.

III. SUMMARY AND CONCLUSIONS

1. Copper-manganese wires to be used for resistivity measurements should not be heated even *in vacuo* to above 800°C. The presence of 5 μ of oxygen at 990°C for as little as 5 or 10 min will ruin these wires. Such improper heat treatment of CuMn wires leaves them with a manganese-depleted layer which shunts the current to such an extent as to give meaningless resistivity data.

2. The apparent electrical resistivity of dilute copper-iron and copper-cobalt alloy wires can be drastically affected by heat treatment around 1000°C for even a few minutes if the atmosphere contains more than 0.5 μ of oxygen. On the other hand, treatment at 1000°C for periods up to at least 10 or 12 hr does not appreciably alter the distribution of solute within the wire cross section and therefore does not alter the measured or "effective" resistivity, provided that the atmosphere contains no more than 0.05 μ partial pressure of O_2.

3. Treatment of dilute CuFe wires (ca. 1 mm diam) at 1000°C in 0.5 μ or more O_2 for 30 or 40 hr will convert essentially all the iron solute into Fe_3O_4. Subsequent treatment in less than 0.05 μ O_2 will reduce the iron oxide, lower the magnetic moment, and increase the resistivity. However, there is not a simple one-to-one correspondence between magnetic moment and resistivity during oxidation and subsequent reduction. The reason for this "hysteresis" is that the magnetic behavior depends on the size of the magnetic particles, and the kinetics of formation of these precipitate particles during oxidation is not the same as the kinetics of their disappearance during subsequent reduction *in vacuo*.

4. We wish to emphasize that if helium carrying a very low concentration of oxygen is passed slowly over a hot alloy wire in which internal oxidation can occur, the oxygen may be taken up very rapidly by the "upstream" end of the wire; thus while the upstream end may be heavily oxidized, the downstream end will be surrounded by a reducing, pure-helium atmosphere. These observations, based on our own experience, lead us to believe that the so-called "carrier gas" technique should be used with caution in internal oxidation work, especially if one wants to know the oxygen partial pressure.

ACKNOWLEDGMENTS

We wish to acknowledge the valuable help and cooperation of Paul Lund, who prepared several of the alloys used in this investigation; and of Kurt Kaiser of the University of Minnesota Physics Department, who made the mass-spectrographic analysis of our helium gas.

JOURNAL OF APPLIED PHYSICS VOLUME 31, NUMBER 10 OCTOBER, 1960

An Improved Method of Growing CdS Crystals from the Vapor Phase

P. D. Fochs
Associated Electrical Industries Research Laboratory, Harlow, Essex, England
(Received April 25, 1960)

The gradual increase in the difference in temperatures of two Kanthal heating elements enables CdS crystals to be grown directly on the inside of a silica tube, remote from one another, instead of on a continuous polycrystalline CdS substrate as happens in most existing methods.

A COMMON but seldom discussed feature of most of the existing methods[1] of growing CdS crystals from the vapor phase is the need to form initially a crystalline substrate on the walls of the furnace tube before the crystals can subsequently grow (in some cases[2] the charge of CdS powder itself acts as the substrate). It frequently happens that this substrate can become quite thick before conditions are favorable for actual crystal growth, particularly if attempts are made to spread the crystal growth over a large area of the tube in order to grow crystals remote from one another. This substrate is wasteful of CdS, but more important is the element of uncertainty it introduces into a run.

Prior[3] has described an elegant method of initiating the formation of a single "seed" of lead selenide, and of subsequently growing a single monocrystal upon it. However, for fundamental work in the fields of photoconductivity and dielectrics, it is an advantage to grow crystals with the required geometry (the thickness is often only a few microns), as well as with the required properties in order to avoid any further mechanical or chemical treatment which is necessary with larger crystals. Accordingly, Prior's method has been modified to grow crystals (without a substrate) under a wide range of experimental conditions, and to make full use of the purification that is possible by fractional sublimation (see later). The method is, in fact, readily adaptable to growing either needle-shaped or thin plate-type crystals.

The furnace used in this process is heated by two Kanthal A1 tubular elements, one of which is designated the *charge* element, and the other, the *crystal* element. The two elements are usually, but not necessarily, set to the same temperature (1000–1100°C) at the beginning of a run. Purified CdS powder is placed at one end of a long sealed silica tube containing either argon or hydrogen sulfide. The tube is placed in the furnace with the CdS in the center of the *charge* element, and extends through the *crystal* element to the outside of the furnace at room temperature. The CdS starts subliming and diffusing along the tube towards the somewhat cooler regions where it becomes supersaturated. Some of this vapor then condenses out starting a crystalline substrate; the remainder diffuses further along the tube toward the cold end (where the saturated vapor pressure becomes progressively lower) so that further condensation is possible, and in fact the crystalline substrate will usually be spread over some 200–300°C. In most existing methods, the temperatures are maintained constant throughout the run so that the substrate thickens up, and when the conditions are favorable, actual crystal growth will occur.

The important difference introduced in the present method is that the temperature of the *crystal* element is reduced very slowly once the temperature distribution in the silica tube has reached equilibrium. This results in the vapor from the charge becoming supersaturated before it reaches the beginning of the substrate, and eventually the degree of supersaturation is sufficient to

[1] D. C. Reynolds and L. C. Greene, J. Appl. Phys. **29**, 559 (1958). (This reference summarizes the various methods of growing CdS crystals from the vapor phase.)
[2] D. C. Reynolds and S. J. Czyzak, Phys. Rev. **79**, 543 (1950).
[3] A. C. Prior, National Research Defence Corporation Bull. **13**, 34 (1958).

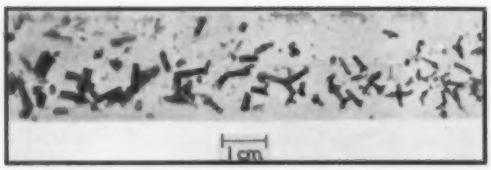

FIG. 1. Needle-shaped CdS crystal growth on the inside surface of a silica tube.

cause some of the vapor to condense on suitable *nucleation* centers. Once this condensation has been initiated, the degree of supersaturation necessary for further growth is lower, so that the vapor preferentially condenses on these seeded sites rather than on the adjacent parts of the silica tube; crystals then grow out from the walls remote from one another. The temperature of the *crystal* element is slowly reduced throughout the run (usually 1–2 days) so that further nucleation continues toward the charge region, and the crystal growth can be extended over a comparatively large part of the tube (Fig. 1).

Runs are usually stopped when about one-third of the charge is left; otherwise if all the charge is used up, the last crystals to grow start re-evaporating and condense on crystals grown earlier in the run. Also undesirable is the condition in which impurities less volatile than the CdS are incorporated to an increasing extent in the last crystals to grow.

The crystals produced by the aforementioned procedure are generally needle-shaped, with many of very regular habit, and are usually larger and of darker color when grown at higher temperatures. Fuller experimental details will be given in a subsequent paper, as the object of this article is to describe the principles involved.

The method works equally well if the *crystal* element is held at a constant temperature and the temperature of the *charge* element slowly raised, or if both the temperature of the *charge* element is slowly raised and the temperature of the *crystal* element is slowly lowered. Also, a flow of gas can be used to speed up the transfer of vapor from the charge resulting in faster crystal growth, which in turn favors the formation of plate-type crystals (Fig. 2). To obtain large plate-type crystals the temperature gradient must be steeper than for needle crystals; and, rather surprisingly, the faster they are grown the fewer striations they incorporate. It is most important to establish a constant temperature distribution throughout the furnace, otherwise the crystals will soon evaporate or become irregular. Also, it appears necessary to exercise very close control over short term fluctuations in temperature (and flow).

The crystals in particular runs have very useful photosensitivities without any further treatment; this is attributed to departures from stoichiometry (cf. Bube and Barton[4]).

It may be noted that the distribution of any impurities in the crystals is different in the present arrangement from that obtained under constant temperature conditions. Impurities more volatile than the CdS come over quickly at the beginning of the run and condense on comparatively cool parts of the silica tube; impurities less volatile than the CdS tend to stay behind in the charge. An important feature of this method is that any one crystal grows for a part of the run, and therefore the impurity content in the crystal depends largely upon when it is grown. This is easily ascertained from the location of the crystal. (In most existing methods, the individual crystals grow throughout the run so that the impurity distribution within the crystals is less uniform).

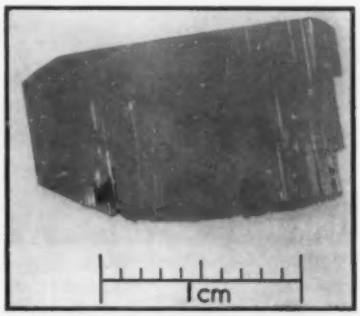

FIG. 2. Plate-type CdS crystal.

ZnS crystals have also been successfully grown by this method, which should, in fact, be suitable for all crystals that can be grown from the vapor phase. In some cases, the addition of a third element to the furnace might be necessary to maintain an adequate partial pressure of the more volatile constituent(s).

ACKNOWLEDGMENTS

The author is indebted to R. Nettleton, B. Lunn, and Mrs. D. A. Batty for the experimental work involved, and to Dr. M. E. Haine, Director of the A. E. I. Research Laboratory, Harlow, for permission to publish this article.

[4] R. H. Bube and L. A. Barton, RCA Rev. **20**, 564 (1959).

Note on Evaporation*

S. A. Zwick
Lawrence Radiation Laboratory, University of California, Livermore, California
(Received April 25, 1960)

A simple kinetic model is employed to investigate nonequilibrium evaporation from a liquid. Molecules are assumed to evaporate into a (one-sided) Maxwellian velocity distribution at the liquid surface. Molecules reaching the surface from the vapor are assumed to form part of an ellipsoidal velocity distribution. Of the molecules approaching the liquid at the interface only the fraction α condenses there; the remainder is taken to undergo specular reflection back into the vapor. By equating physical conditions at the surface with conditions in the vapor, one can relate the vapor pressure to that which would prevail at equilibrium, as a function of the surface accommodation coefficient α and the mean velocity u of the vapor relative to the interface.

I. INTRODUCTION

THE problem of evaporation at a liquid surface has been discussed in papers by Wyllie,[1] Plesset,[2] and Mathews.[3] Using Plesset's expression for the normal vapor current at the surface,

$$J=\bar{u}(\rho_{eq}-\rho_{vap}), \quad \text{with} \quad \bar{u}=\alpha(RT/2\pi M)^{\frac{1}{2}}, \qquad (1)$$

Mathews obtains an approximate formula relating the vapor pressure to the velocity u of the vapor relative to the interface, which may be written in the form

$$p_{eq}/p_{vap}=1+(u/\bar{u}). \qquad (2)$$

In these equations, p_{vap} and ρ_{vap} denote the actual pressure and density of the vapor, in comparison with the equilibrium values p_{eq}, ρ_{eq} at the temperature T of the surface; R is the universal gas constant; M denotes the molecular weight of the vapor; and α is the "surface accommodation coefficient" of the liquid, which measures essentially the fraction of liquid surface available for evaporation or condensation. For a nonpolar liquid α is equal to unity, but for a polar liquid with hydrogen bonding (such as water) α lies between 0 and 1. In the latter case the surface acts as a "bottleneck" to the flow of vapor molecules, and will tend to choke the flow at sufficiently large positive or negative values of u. Thus, in condensation, Eq. (2) formally makes p_{vap} infinite when $u=-\bar{u}$. Mathew's approximation is useful when u is small in comparison with the velocity of sound in the vapor [$c=(\gamma RT/M)^{\frac{1}{2}}$, where γ is the specific heat ratio of the vapor].[3]

In the present note, the evaporation boundary condition for normal vapor flow is derived on the basis of a simple kinetic model. Assumptions regarding the liquid are kept to a minimum, consistent with the problem to be solved. The approximations made imply that the vapor density is small in comparison with that of the liquid, but do not otherwise restrict the relative velocity.

II. MODEL FOR EVAPORATION

To establish a frame of reference, we take the liquid surface to be at rest, and the vapor to be streaming away with mean velocity $\mathbf{u}$ normal to the surface. The model may then be described by the following assumptions:

(i) At equilibrium ($\mathbf{u}=0$), the distribution of molecular velocities within the vapor is everywhere Maxwellian.

(ii) But even away from equilibrium, macroscopic conditions within the vapor are the same at all points.

(iii) The process of evaporation proper (i.e., involving those molecules that pass from the liquid to the gas phase) does not depend on the motion of the vapor.

(iv) Of the molecules of vapor which reach the surface of the liquid, only a fraction α actually condenses there, while the fraction $1-\alpha$ undergoes specular reflection back into the vapor.

(v) The velocity distribution of those vapor molecules at the surface which have a velocity component toward the surface can be estimated in terms of an ellipsoidal distribution.

Assumption (iii) appears to be reasonable so long as the vapor density is small in comparison with that of the liquid, since then the motion of a surface molecule will be determined predominantly by the behavior of its neighbors in the liquid, and only to a slight extent by the relatively rare collisions with a gas molecule. We suppose, in order to construct the model, that the liquid-vapor interface can be treated as a plane, so that the reflection in (iv) will affect only one of the velocity components of a molecule. This assumption of specular reflection has been made for simplicity. It is consistent physically if the vapor at the surface is taken to have vanishing mean velocity components tangential to the surface; in a more complex model, in which motion parallel to the surface might be considered in detail, a better assumption would be that gas molecules reflect diffusely from the interface. Here we may also ignore the question of how far from

* Supported in part by the U. S. Air Force Office of Scientific Research, Combustion Dynamics Division, and in part by the U. S. Atomic Energy Commission.

[1] G. Wyllie, Proc. Roy. Soc. (London) **A197**, 383 (1949).

[2] M. S. Plesset, J. Chem. Phys. **20**, 790 (1952).

[3] W. E. Mathews, "On the Flow of Vapor between Liquid Surfaces," thesis, California Institute of Technology, 1953.

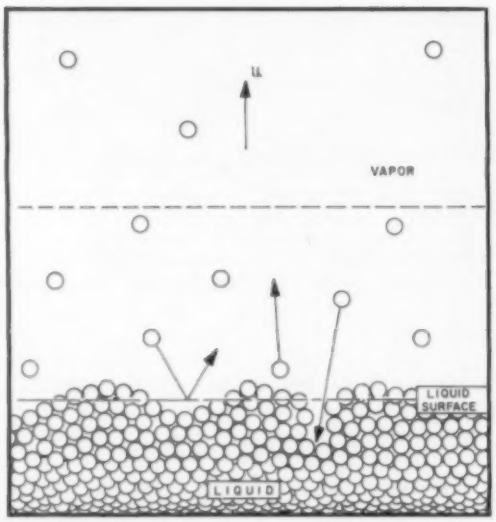

FIG. 1. Diagram depicting the model for evaporation. Molecules reaching the liquid surface from the vapor are assumed either to enter the surface or to undergo specular reflection there. The mean velocity $\mathbf{u}$ of the vapor relative to the surface has only a normal component, taken positive when a net evaporation occurs.

the surface "within the vapor" may be, and take the actual surface zone an undetermined number of collision-mean-free-paths thick. A diagram depicting the model is shown in Fig. 1.

The use of a (one-sided) ellipsoidal velocity distribution for vapor molecules reaching the surface is required primarily in order to satisfy continuity requirements; i.e., a truncated Maxwellian distribution is too restrictive for the problem at hand. Apart from this, the ellipsoidal form is suggested by a collision picture of molecular interactions. As one approaches a surface of velocity discontinuity in the gas, one must find the representative points in velocity space, corresponding to the extreme tail in the velocity distribution for molecules speeding toward the surface, "raining" out and across the distribution, because of collisions with fast molecules appearing from the surface. At the interface, where this raining process is pronounced, the velocity distribution should approximate the ellipsoidal form.

Finally, the model is not intended to account for rotational features of molecules (such as are responsible for the appearance of the accommodation coefficient α), or for effects related to time lags between energy transfer from vibrational to translational or rotational degrees of freedom, light emission upon or following collisions, etc. In using quasi-Maxwellian velocity distributions to describe the vapor, we imply that the vapor may be approximated by a perfect gas.

III. FORMULATION

According to assumptions (i) and (iii) the distribution of velocities of molecules evaporating—which is a (one-sided) Maxwellian distribution when the vapor is at rest relative to the liquid—will be unchanged when relative motion occurs. Thus we take

$$n_{\text{evap}} = A \exp[-(m/2kT)\mathbf{v}^2] \quad (\mathbf{v}\cdot\mathbf{n}>0) \tag{3}$$

to describe the number of molecules/cc/unit volume of velocity space, which are present in the vapor at the interface because of evaporation. In Eq. (3), A is a constant, $\mathbf{v}$ is the molecular velocity under consideration, m represents the mass of a molecule, and k denotes the Boltzmann constant. The unit normal $\mathbf{n}$ to the interface is directed into the vapor.

At equilibrium the distribution in (3) is balanced by a corresponding one-sided distribution from the vapor for $\mathbf{v}\cdot\mathbf{n}<0$, and the net result is isotropic at the surface. Away from equilibrium ($\mathbf{u}\neq 0$) the one-sided distribution (3) would introduce anisotropic effects in the vapor, since it is not symmetrically located (in velocity space) with respect to the center $\mathbf{u}$ of the Maxwellian distribution in the interior of vapor. The latter is given by

$$n_{\text{vap}} = C \exp[-(m/2kT)(\mathbf{v}-\mathbf{u})^2] \quad \text{(for all } \mathbf{v}\text{)}. \tag{4}$$

To compensate for such an effect—so that assumption (ii) may be satisfied—the distribution of velocities for molecules reaching the surface from the vapor must also be anisotropic. It is not difficult to show, however, that a truncated distribution of the type (4) is too restrictive for assumption (ii). We have thus supposed that the velocity distribution of molecules approaching the surface is taken from an ellipsoidal distribution with mean velocity $\mathbf{w}$ different from $\mathbf{u}$.

By an ellipsoidal distribution, we mean one for which the expression $(\mathbf{v}-\mathbf{u})^2$ in Eq. (4) is replaced with a general (positive definite) quadratic form in the velocity components. By symmetry, one principal axis of the quadratic form must be along $\mathbf{n}$, and the other two be parallel to the interface, for the present problem, and the axes in the surface must be equal. Let the component of velocity in the direction normal to the interface be denoted by ζ, and the magnitude of the surface component (the radial component in a cylindrical-coordinate system) by ξ. Then the velocity distribution for molecules approaching the surface may be written

$$n_{\text{appr}} = B \exp\left\{-\left(\frac{s}{u}\right)^2\left[\frac{\xi^2}{a^2}+\frac{(\zeta-w)^2}{b^2}\right]\right\} \quad (\zeta<0), \tag{5}$$

where we have put

$$m/2kT \equiv M/2RT = (s/u)^2. \tag{6}$$

In the same notation,

$$\left.\begin{aligned} n_{\text{evap}} &= A \exp\{-(s/u)^2[\xi^2+\zeta^2]\} \quad (\zeta>0), \\ n_{\text{vap}} &= C \exp\{-(s/u)^2[\xi^2+(\zeta-u)^2]\} \end{aligned}\right\} \tag{7}$$

The parameter s introduced in Eq. (6) has the significance of being the mean flow velocity of the vapor in nondimensional form. For the total distribution function at the surface, one has

$$n_{\text{surf}}(\xi,\zeta)=\begin{cases} n_{\text{appr}}(\xi,\zeta) & (\zeta<0) \\ n_{\text{evap}}(\xi,\zeta)+(1-\alpha)n_{\text{appr}}(\xi,-\zeta) & (\zeta>0) \end{cases} \tag{8}$$

to account for the specular reflection.

Continuity Relations

Assumption (ii) requires that the vapor density at the liquid surface,

$$\rho_{\text{surf}}=\int m n_{\text{surf}}d\omega$$

$$=\int_{\zeta>0} m[n_{\text{evap}}(\zeta)+(1-\alpha)n_{\text{appr}}(-\zeta)]d\omega + \int_{\zeta<0} m n_{\text{appr}}(\zeta)d\omega$$

$$=m\int_0^\infty 2\pi\xi d\xi \int_0^\infty d\zeta\cdot A\exp\left\{-\left(\frac{s}{u}\right)^2[\xi^2+\zeta^2]\right\}$$

$$+(2-\alpha)m\int_0^\infty 2\pi\xi d\xi\int_{-\infty}^0 d\zeta\cdot B \times\exp\left\{-\left(\frac{s}{u}\right)^2\left[\frac{\xi^2}{a^2}+\frac{(\zeta-w)^2}{b^2}\right]\right\},$$

$$=\tfrac{1}{2}\pi m(u/s)^3\{\pi^{\frac{1}{2}}A+2(2-\alpha)Ba^2b\phi_0\},$$

say, must equal the vapor density in the body of the vapor,

$$\rho_{\text{vap}}=\int m n_{\text{vap}}d\omega$$

$$=m\int_0^\infty 2\pi\xi d\xi\int_{-\infty}^\infty d\zeta\cdot C \times\exp\left\{-\left(\frac{s}{u}\right)^2[\xi^2+(\zeta-u)^2]\right\} \tag{9}$$

$$=\tfrac{1}{2}\pi m(u/s)^3\{2\pi^{\frac{1}{2}}C\};$$

whence

$$\pi^{\frac{1}{2}}A+2(2-\alpha)Ba^2b\phi_0=2\pi^{\frac{1}{2}}C. \tag{10}$$

In the integrals above, the symbol $d\omega\equiv 2\pi\xi d\xi d\zeta$ stands for the element of "volume" in velocity space. The functions ϕ_k [of which ϕ_0 appears in Eq. (10)] arising from the integration over ζ will be discussed later. [See Eqs. (17)–(23).]

The net amount of mass/unit area/unit time transported away from the surface of the liquid is given by

$$\int m\zeta\times n_{\text{surf}}d\omega,\equiv\frac{\pi}{2}m\left(\frac{u}{s}\right)^4\{A+2\alpha Ba^2b^2\phi_1\}.$$

This must equal the rate of mass transport across a parallel surface in the vapor

$$\int m\zeta\times n_{\text{vap}}d\omega=\frac{\pi}{2}m\left(\frac{u}{s}\right)^4\{2s\pi^{\frac{1}{2}}C\},$$

so that

$$A+2\alpha Ba^2b^2\phi_1=2s\pi^{\frac{1}{2}}C. \tag{11}$$

In the same way, equating the rate of transport of normal momentum $\int(m\zeta)\zeta\times x d\omega$ and energy $\int(\frac{1}{2}mv^2)\zeta\times nd\omega$ at the surface to their values in the vapor yields the conditions

$$\pi^{\frac{1}{2}}A+4(2-\alpha)Ba^2b^3\phi_2=(1+2s^2)2\pi^{\frac{1}{2}}C, \tag{12}$$

$$2A+2\alpha Ba^2b^2[a^2\phi_1+b^2\phi_3]=(5s+2s^3)\pi^{\frac{1}{2}}C. \tag{13}$$

Finally, we require the uniformity of stress components in the vapor. The normal stresses are already uniform by virtue of Eq. (12). Because of the cylindrical symmetry, the two diagonal tangential stresses will each be equal to half their sum, $\int m\xi^2\times nd\omega$. Equating these at the surface and in the vapor, one obtains

$$\pi^{\frac{1}{2}}A+2(2-\alpha)Ba^4b\phi_0=2\pi^{\frac{1}{2}}C. \tag{14}$$

Since the stress tensor is isotropic within the vapor, conditions (12) and (14) remove any possible anisotropy at the surface that might be introduced by the model. They incidentally have the effect of making the temperature a constant of the model also. To show this, we remark that the mean internal energy E per molecule in the vapor, resulting from the random translational motions, is defined by

$$E\int nd\omega\equiv\int\tfrac{1}{2}m(\mathbf{v}-\mathbf{u})^2nd\omega=\int\tfrac{1}{2}m(v^2+u^2-2\mathbf{u}\cdot\mathbf{v})nd\omega$$
$$=\int\tfrac{1}{2}mv^2nd\omega-\tfrac{1}{2}mu^2\int nd\omega,$$

so that we have $(E+\frac{1}{2}mu^2)\int nd\omega=\int\frac{1}{2}mv^2nd\omega$, inasmuch as Eq. (11) makes $\int\mathbf{v}nd\omega=\mathbf{u}\int nd\omega$. The uniformity of $\rho=\int mnd\omega$ and $\int v^2nd\omega=\int\xi^2nd\omega+\int\zeta^2nd\omega$ is already provided by Eqs. (12) and (14), and hence E must be the same at the surface as in the vapor. Using the definition of n_{vap}, one finds by straightforward integration that $E=(3m/4)(u/s)^2=(3/2)kT$ in terms of the parameter T.

A comparison of Eqs. (10) and (14) shows immediately that

$$a^2=1. \tag{15}$$

Thus the continuity relations simplify to the following set of simultaneous equations.

$$\pi^{\frac{1}{2}}A+2(2-\alpha)Bb\phi_0=2\pi^{\frac{1}{2}}C \tag{16a}$$

$$A+2\alpha Bb^2\phi_1=2s\pi^{\frac{1}{2}}C \tag{16b}$$

$$\pi^{\frac{1}{2}}A+4(2-\alpha)Bb^3\phi_2=2(1+2s^2)\pi^{\frac{1}{2}}C \tag{16c}$$

$$2A+2\alpha Bb^2(\phi_1+b^2\phi_3)=(5s+2s^3)\pi^{\frac{1}{2}}C. \tag{16d}$$

Properties of the ϕ_k

The functions ϕ_k in Eqs. (10)–(16) are defined by the formula

$$\left.\begin{aligned}\phi_k(\sigma)&=\int_0^\infty (-x)^k \exp[-(x+\sigma)^2]dx\\ &=\int_\sigma^\infty (\sigma-x)^k \exp(-x^2)dx,\end{aligned}\right\} \quad (17)$$

in which

$$\sigma\equiv ws/ub.$$

The velocity parameter w of the stressed distribution is thus given by

$$w=\sigma b(u/s)=\sigma b(2RT/M)^{\frac{1}{2}}$$

from (6). In the derivations above, the stress constant b was considered non-negative. However, w and hence σ may take on any (real) value.

By differentiating the two forms for ϕ_k in (17), one finds

$$d\phi_k/d\sigma=k\phi_{k-1}, \quad \phi_{k+1}=\sigma\phi_k+\tfrac{1}{2}k\phi_{k-1} \quad (k>0). \quad (18)$$

These recursion formulas, together with Eq. (17), lead to the table of functions

$$\left.\begin{aligned}\phi_0&=\tfrac{1}{2}\pi^{\frac{1}{2}}\operatorname{erfc}(\sigma)\\ \phi_1&=\sigma\phi_0-\tfrac{1}{2}\exp(-\sigma^2)\\ \phi_2&=(\sigma^2+\tfrac{1}{2})\phi_0-\tfrac{1}{2}\sigma\exp(-\sigma^2)\\ \phi_3&=(\sigma^3+\tfrac{3}{2}\sigma)\phi_0-\tfrac{1}{2}(\sigma^2+1)\exp(-\sigma^2).\end{aligned}\right\} \quad (19)$$

For real σ, ϕ_0 and ϕ_2 are positive; ϕ_1 and ϕ_3 are negative.

The ϕ_k are readily computed from Eq. (19) and the series expansion for ϕ_0

$$\phi_0(\sigma)=\tfrac{1}{2}\pi^{\frac{1}{2}}-\sigma\sum_{r=0}^{\infty}\frac{(-)^r\sigma^{2r}}{r!(2r+1)} \quad (20)$$

when $|\sigma|<\frac{1}{2}$. To avoid a loss of significant figures with larger values of σ, the following representation is convenient. Write

$$\phi_k(\sigma)=(-)^k k!(2\sigma)^{-k-1}\exp(-\sigma^2)f_k(\sigma).$$

Then for $\sigma>0$ (and k an integer)

$$\left.\begin{aligned}f_{2k}(\sigma)&=\frac{2}{\Gamma(k+\frac{1}{2})}\int_0^\infty x^{2k}\\ &\qquad\times\exp[-x^2]\left(\frac{\sigma^2}{x^2+\sigma^2}\right)^{k+1}dx\\ f_{2k+1}(\sigma)&=\frac{2}{\Gamma(k+\frac{3}{2})}\int_0^\infty x^{2k+2}\\ &\qquad\times\exp[-x^2]\left(\frac{\sigma^2}{x^2+\sigma^2}\right)^{k+1}dx.\end{aligned}\right\} \quad (21)$$

These forms are suitable for numerical integration when $\frac{1}{2}<\sigma<10$. For large σ the asymptotic expansion of (21) is useful.

$$f_k(\sigma)\sim\sum_{r=0}\frac{(-)^r}{r!}\frac{(k+2r)!}{k!(2\sigma)^{2r}} \quad (\sigma\to\infty). \quad (22)$$

The extension of (21) and (22) to negative values of σ follows from the polynomial relations

$$\begin{aligned}\phi_k(\sigma)+(-)^k\phi_k(-\sigma)&=\int_{-\infty}^{\infty}(\sigma-x)^k\exp(-x^2)dx\\ &=\pi^{\frac{1}{2}}\sum_{r=0}^{[k-2]}\frac{k!\sigma^k}{r!(k-2r)!(2\sigma)^{2r}},\end{aligned} \quad (23)$$

where $[k/2]$ denotes $k/2$ or $(k-1)/2$, whichever is an integer (or zero).

IV. METHOD OF SOLUTION

By subtracting Eq. (16a) from (16c), $\pi^{\frac{1}{2}}$ times (16b) from (16a), and twice (16b) from (16d), one obtains three homogeneous equations in B and C that do not involve A. These may be solved for $(2-\alpha)Bb\phi_0/\pi^{\frac{1}{2}}C$, to yield the relations

$$\begin{aligned}\frac{(2-\alpha)Bb\phi_0}{\pi^{\frac{1}{2}}C}&=\frac{2s^2\phi_0}{2b^2\phi_2-\phi_0}=\frac{(2-\alpha)(1-\pi^{\frac{1}{2}}s)\phi_0}{(2-\alpha)\phi_0-\alpha\pi^{\frac{1}{2}}b\phi_1}\\ &=\frac{(2-\alpha)(s+2s^3)\phi_0}{2\alpha b(b^2\phi_3-\phi_1)}.\end{aligned} \quad (24)$$

Next, put

$$\left.\begin{aligned}f&\equiv 1-b^2\left(\frac{\phi_2}{\phi_1}\right),\\ g&\equiv b^2\left(\frac{2\phi_2}{\phi_0}\right)-1,\\ z&=b\left(\frac{\alpha}{2-\alpha}\right)\left(-\pi^{\frac{1}{2}}\frac{\phi_1}{\phi_0}\right)\end{aligned}\right\} \quad (25)$$

and substitute into (24), giving

$$\frac{2s^2}{g}=\frac{1-\pi^{\frac{1}{2}}s}{1+z}=\frac{\pi^{\frac{1}{2}}s(1+2s^2)}{2fz}. \quad (26)$$

Thus

$$f=\frac{\pi^{\frac{1}{2}}s(1+2s^2)(1+z)}{2(1-\pi^{\frac{1}{2}}s)z}, \quad g=\frac{2s^2(1+z)}{1-\pi^{\frac{1}{2}}s}. \quad (27)$$

Finally, it is convenient to rearrange Eqs. (25) in the form

$$\left.\begin{aligned}h(\sigma)&\equiv 1-\frac{\phi_0(\sigma)\phi_2(\sigma)}{\phi_1(\sigma)\phi_2(\sigma)}=2\left(\frac{f+g}{1+g}\right)\\ z&=\left(\frac{\alpha}{2-\alpha}\right)\lambda(\sigma)(1+g)^{\frac{1}{2}}, \text{ where } \lambda(\sigma)\equiv\frac{-\pi^{\frac{1}{2}}\phi_1}{(2\phi_0\phi_2)^{\frac{1}{2}}}\\ b&=\mu(\sigma)(1+g)^{\frac{1}{2}}, \quad \text{in which} \quad \mu(\sigma)=(\phi_0/2\phi_2)^{\frac{1}{2}}.\end{aligned}\right\} \quad (28)$$

Suppose that s and z are specified in (27). Then f and g are known, and σ may be found by interpolating in the relation for h in (28).[4] The value of λ may next be calculated, and α computed from the expression in (28) for z. Finding b, B/C and A/C is then straightforward.

Actually, the parameters to be specified in the system of equations are the dimensionless vapor velocity s and the accommodation coefficient α, not s and z. An iteration step is therefore necessary: From the value of s chosen and an estimate for z, one finds f, g, σ and λ as above. Using the desired factor $\alpha/(2-\alpha)$ in (28), a corrected estimate for z may then be obtained. The procedure converges rapidly for all s and α (except for $\alpha=1$, $s\to-\infty$), since λ is slowly varying ($\lambda\approx1$) and in general $g\ll1$.

The quantity of physical interest to be obtained from the model is the ratio of actual vapor pressure (or density) to its values at equilibrium ($s=0$). Since by assumption (iii), $A=A(\alpha)$ does not depend on s, we may express these ratios as

$$\frac{p_{\text{vap}}}{p_{\text{eq}}}=\frac{\rho_{\text{vap}}}{\rho_{\text{eq}}}=\frac{C(\alpha,s)}{C(\alpha,0)}=\frac{C/A}{\lim\limits_{s\to0}\{C/A\}}. \tag{29}$$

According to Eqs. (24) and (16a),

$$C/A=\tfrac{1}{2}(z+1)/(z+\pi^{\frac{1}{2}}s). \tag{30}$$

Now, as $s\to0$ for fixed $\alpha(\neq0)$, $z\sim\alpha/(2-\alpha)$. [See Eqs. (36).] Hence the denominator in (29) becomes $\lim\limits_{s\to0}\{C/A\}=1/\alpha$, and the equation yields

$$\frac{p_{\text{vap}}}{p_{\text{eq}}}=\frac{\rho_{\text{vap}}}{\rho_{\text{eq}}}=\frac{\alpha}{2}\left(\frac{z+1}{z+\pi^{\frac{1}{2}}s}\right). \tag{31}$$

V. SPECIAL VALUES

Restrictions on the model are imposed by the requirements that z, b, $p_{\text{vap}}/p_{\text{eq}}$ exist and be non-negative, and that α lie between 0 and 1. Solutions are further limited by the circumstance that for real σ, the function $h(\sigma)$ in (28) never becomes less than -1 ($\sigma\to\infty$) and cannot exceed $+1$ ($\sigma\to-\infty$). Finding the bounds on the model is a matter of establishing precedence among these conditions.

Approximations for Small $|s|$

Consider for simplicity the region $|s|\ll1$. Here $g\sim0$, $f\sim h/2$, and so Eqs. (27), (28) reduce to

$$h\sim\left(\frac{\pi^{\frac{1}{2}}s}{1-\pi^{\frac{1}{2}}s}\right)\left(\frac{z+1}{z}\right),\quad z\sim\lambda\left(\frac{\alpha}{2-\alpha}\right),$$
$$b\sim\mu\quad(|s|\ll1). \tag{32}$$

[4] The following formulas for σ, λ, μ give the correct behavior at $h=0,\pm1$, and are in error by less that 1% at points in between:

$$\sigma\approx-h\left\{\frac{2(2-h)}{1-h^2}+\frac{1}{4}\right\}^{\frac{1}{2}},\quad \lambda\approx\left(\frac{\pi}{3-h}\right)^{\frac{1}{2}}\left\{1+\left[\left(\frac{\pi}{3}\right)^{\frac{1}{2}}-1\right](1-h^2)\right\}^{-1},$$
$$\mu\approx\left(\frac{1-h}{1+h}\right)^{\frac{1}{2}}\left\{1-(6^{\frac{1}{2}}-2)\frac{h(1-h)}{3-h}\right\}.$$

Since λ is a slowly varying function of h with the approximate value unity, a rough estimate for the system, when α is small, is given by $z\approx\frac{1}{2}\alpha$, $h\approx2\pi^{\frac{1}{2}}s/\alpha$, and $p_{\text{eq}}/p_{\text{vap}}\approx1+(2\pi^{\frac{1}{2}}s/\alpha)$ from Eq. (31). [The latter expression for $p_{\text{eq}}/p_{\text{vap}}$ happens to coincide with Mathews' result. See Eqs. (1), (2), (6).] These formulas imply that z and $p_{\text{eq}}/p_{\text{vap}}$ will be finite and positive so long as $-1<h<1$, or $\pi^{\frac{1}{2}}|s|<\frac{1}{2}\alpha$.

Actually, the limits on s indicated by (32) are (for z or $\alpha\ll1$)

$$-z<\pi^{\frac{1}{2}}s<z/(1+2z), \tag{33}$$

in which $z\sim(\pi/4)^{\frac{1}{2}}\alpha(2-\alpha)$ at the lower limit ($h=-1$), and $z\sim(\pi/2)^{\frac{1}{2}}\alpha/(2-\alpha)$ at the upper limit ($h=1$).

Condensation Limit

When α is not small, the limiting conditions $h=-1$ and $\pi^{\frac{1}{2}}s=-z$, from (33), are no longer the same. Since the latter gives the maximum flow rate in condensation for finite vapor pressure, according to Eq. (31), one may expect it to bound the model in general for $s<0$. Putting $z=\pi^{\frac{1}{2}}(-s)$ in (27) and (28), one finds $g=2s^2$, $2f=-(1+2s^2)$, and hence $h=-(1-2s^2)/(1+2s^2)$, which is more stringent than $h=-1$. In terms of the limiting flow parameter s, the system of equations may thus be written

$$\left.\begin{aligned}
&z=\pi^{\frac{1}{2}}|s|,\\
&h=-\left(\frac{1-2s^2}{1+2s^2}\right),\\
&\sigma=\sigma(h),\\
&b=\mu(h)(1+2s^2)^{\frac{1}{2}},\\
&\alpha=\frac{2\pi^{\frac{1}{2}}|s|}{\pi^{\frac{1}{2}}|s|+\lambda(h)(1+2s^2)^{\frac{1}{2}}}.
\end{aligned}\right\}\text{(Condensation Limit)} \tag{34}$$

For any finite flow in condensation, Eq. (34) makes z and b finite and $\alpha<1$. For a large flow to occur ($s\to-\infty$), (34) indicates that $h\sim1$, so that $\lambda\sim(\pi/2)^{\frac{1}{2}}$ and therefore $\alpha\sim1$. Putting the matter in reverse, the choking effect at the surface occurs only for $\alpha<1$ in the present model. For $\alpha\to1$, unlimited flows are possible.

Evaporation Limit

There appears to be no obvious physical effect which would define the minimum (steady-state) vapor pressure when a net evaporation occurs ($s>0$). Clearly a nonvanishing minimum exists, since it is impossible to pump a vacuum over an evaporating liquid (unless $\alpha=0$). However, this limit does not correspond to a vanishing flow of molecules toward the surface, for

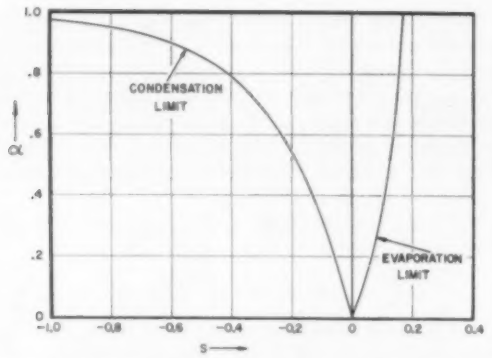

FIG. 2. Limiting values of the dimensionless vapor velocity $s=u(M/2RT)^{\frac{1}{2}}$ predicted by the model for condensation or evaporation, as a function of the surface accommodation coefficient α. The curve for the condensation limit becomes tangent to the line $\alpha=1$ as $s\to-\infty$.

instance, inasmuch as collisions between molecules evaporating from neighboring sites on the surface will create such a flow.

The evaporation limit of the model corresponds, as indicated above, to $h=1$, or $\sigma=-\infty$. In this limit $\mu\sim\frac{1}{2}|\sigma|$, so that the parameter b tends to zero as $1/|\sigma|$, which indicates a severe distortion of the velocity distribution function n_{appr} for vapor molecules reaching the surface. Since $b\sigma$ remains finite, the velocity parameter $w=\sigma b(2RT/M)^{\frac{1}{2}}$ takes on finite, negative values. Thus Eq. (5) indicates that in the evaporation limit of the model, all molecules reaching the surface from the vapor will arrive with the same normal velocity component w.

For $h=1$, Eqs. (28) give $g=1-2f$, which yields a quadratic equation for z for each limiting value of s. Using $|\sigma|\mu\sim 2^{-\frac{1}{2}}$, $\lambda\sim(\pi/2)^{\frac{1}{2}}$ in (28), and denoting the limit of $b|\sigma|$ at $h=1$ by β, we obtain

$$\left.\begin{aligned}&\beta=\left[\frac{1}{2}+\frac{s^2(1+z)}{1-\pi^{\frac{1}{2}}s}\right]^{\frac{1}{2}},\\&\alpha=\frac{2z}{z+\pi^{\frac{1}{2}}\beta},\\&w=-\beta\left(\frac{2RT}{M}\right)^{\frac{1}{2}};\end{aligned}\right\}\text{(Evaporation Limit)}$$

where z is the smaller root of

$$(2s^2)z-(1-2\pi^{\frac{1}{2}}s-2s^2-2\pi^{\frac{1}{2}}s^2)z+\pi^{\frac{1}{2}}s(1+2s^2)=0. \tag{35}$$

Here the choice of roots arises from the condition that (35) give the upper limit in (33) when $|s|\ll 1$.

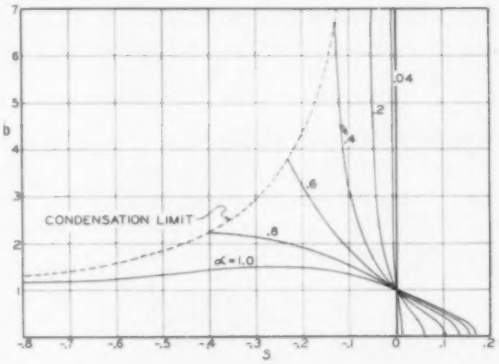

FIG. 4. Curves showing the values of the model parameter b as a function of the dimensionless vapor velocity s, for various α. In the evaporation limit of the model b tends to zero, which implies a vanishing dispersion in the normal velocity component for molecules reaching the surface from the vapor.

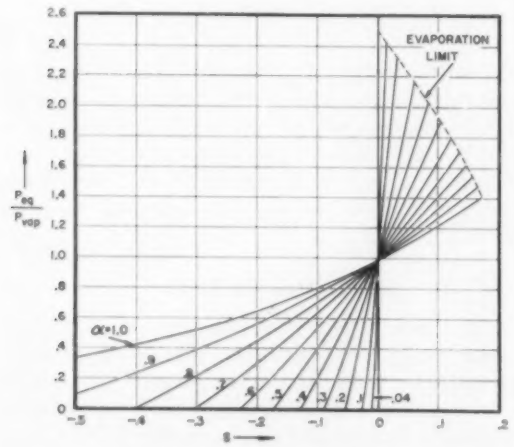

FIG. 3. The family of curves p_{eq}/p_{vap} vs s, for various values of α.

Equilibrium

By expanding the ϕ_k to order σ, one finds for $h\sim 0$ but α fixed $(0<\alpha<1)$,

$$\left.\begin{aligned}&b\sim 1-\left(\frac{2\pi^{\frac{1}{2}}}{4-\pi}\right)\frac{s}{\alpha},\quad \sigma\sim-\left(\frac{2\pi}{4-\pi}\right)\frac{s}{\alpha},\\&z\sim\left(\frac{\alpha}{2-\alpha}\right)+\left(\frac{\pi-3}{4-\pi}\right)\left(\frac{2\pi^{\frac{1}{2}}s}{2-\alpha}\right),\\&\frac{p_{eq}}{p_{vap}}\sim 1+\left(\frac{1}{4-\pi}\right)\left(\frac{2-\alpha}{\alpha}\right)\pi^{\frac{1}{2}}s.\end{aligned}\right\}\begin{array}{l}\text{as } s\to 0\\ \text{for fixed } \alpha\\ \text{(Equilibrium)}\end{array} \tag{36}$$

VI. CONCLUSION

Results of the calculations indicated above are presented in Figs. 2–5. Figure 2 gives the bounding

curves $s=s(\alpha)$ corresponding to the condensation and evaporation limits of the model. As $\alpha \to 1$ the values of s on the condensation curve tend to $-\infty$. Figure 3 depicts the general family of solutions p_{eq}/p_{vap} vs s, with each curve having a fixed value of α. Here the reciprocal values rather than the direct values (i.e., p_{vap}/p_{eq}) have been plotted, in order to present more information, and also to show clearly the deviation from the linear relation (2) obtained by Mathews for small s. Figures 4 and 5 give the families of curves for b vs s, and $b\sigma$ vs s.

A comparison with Mathews' result may be made in the neighborhood of equilibrium. In terms of the velocity u, Eq. (36) gives

$$\frac{p_{eq}}{p_{vap}} \sim 1+\left(\frac{2-\alpha}{4-\pi}\right)\left(\frac{\pi M}{2RT}\right)^{\frac{1}{2}}\frac{u}{\alpha} \quad \text{as} \quad u \to 0 \qquad (37)$$

for a given value of α. Thus we may identify a characteristic velocity

$$\tilde{u}_0=\frac{2(4-\pi)}{(2-\alpha)}\alpha\left(\frac{RT}{2\pi M}\right)^{\frac{1}{2}}, \qquad (38)$$

which differs by a factor $1.72/(2-\alpha)$ from Plesset's expression for $\tilde{u}$ in Eq. (1).

It should be noted that the coefficients $\tilde{u}$ or $\tilde{u}_0$ relate to the slope of p_{eq}/p_{vap} at vanishing velocity, and do not give the condensation or evaporation limits, even when α is small. From Eq. (33) one finds

$$-u_{cond} \sim 1.032\,\tilde{u}_0, \quad u_{evap} \sim 1.461\,\tilde{u}_0 \quad \text{for} \quad \alpha \to 0. \qquad (39)$$

Because $u_{cond} \neq -\tilde{u}_0$, we conclude that even the curves in Fig. 3 for small α involve a finite departure from linearity.

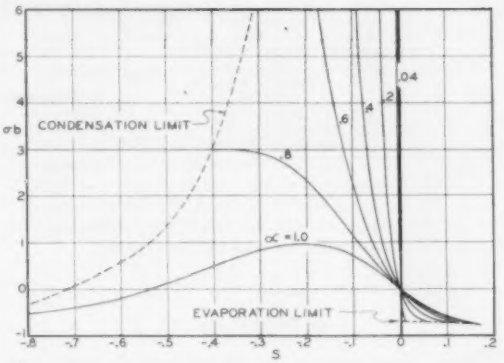

FIG. 5. Values of the dimensionless velocity parameter $\sigma b=w(M/2RT)^{\frac{1}{2}}$ as a function of s, for various α. In the evaporation limit, $\sigma b \approx -1/2^{\frac{1}{2}}$ for all α, so that the normal velocity of molecules reaching the surface in this limit would be approximately $|w|=(RT/M)^{\frac{1}{2}}$.

ACKNOWLEDGMENTS

The author wishes to thank D. Gonzales and Miss J. C. Kleinecke for their invaluable help with the calculations.

Aperture Fields in the Diffraction by a Slit*

HWEI-PIAO HSU
Case Institute of Technology, Cleveland, Ohio
(Received April 22, 1960)

Aperture fields in the diffraction by a slit was studied numerically and experimentally. Numerical calculations are based on the exact solution in the form of an infinite series of Mathieu functions. Experimental measurements, by means of a parallel-plate device, of the field distribution over the aperture in slits of 3.5λ, 3λ, 2.21λ, 1.27λ width (λ = wavelength) are discussed, and show satisfactory agreement with the exact solution for slits of width 1.27λ and 2.21λ. The exact solution of diffraction by a slit due to a line source is also presented in the Appendix.

I. INTRODUCTION

THE development of experimental microwave techniques in recent years has stimulated the study of slit diffraction problems. Several approximate techniques of solution have been developed and recent measurements of the diffraction pattern in the plane of a slit less than three wavelengths wide have been reported.[1] By virtue of Huygen's principle the study of actual field distributions in the aperture of a slit will greatly stimulate the development of approximate techniques. The detailed study of the aperture field, numerically or experimentally, is, therefore, of value.

An exact solution to the diffraction by a slit for an incident plane wave (polarized such as E vector is parallel to the edges of a slit) is available in the form of an infinite series of Mathieu functions.[2] However in the past the limited tables of Mathieu functions restricted the numerical calculations to the range of very small ratios of slit width to wavelength. Now that extended tables[3] are available it becomes possible to study numerically the field distribution over the slit aperture (slit width up to about 2.5 wavelengths) with oblique plane wave incidence as well as normal plane wave incidence. Several numerical calculations have been performed and the evaluation of the several approximation techniques, in the light of actual field solutions, has been accomplished.[3,4]

In this paper the field distribution (intensity and phase) over the aperture in slits of 0.45λ, 1.27λ and 2.21λ (λ = wavelength) width due to a normally incident plane wave and oblique incident waves are presented. Experimental measurements, by means of a parallel-plate device, of the field distribution over the aperture in slits of 3.5λ, 3λ, 2.21λ, and 1.27λ width are discussed, and show satisfactory agreement with the exact solution for slits of width 1.27λ and 2.21λ.

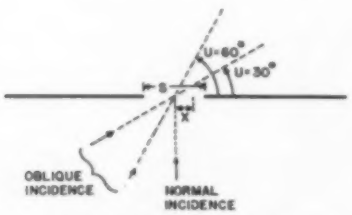

FIG. 1. u = angle of incident wave with positive x axis; x = distance between aperture field point and center; s = slit width.

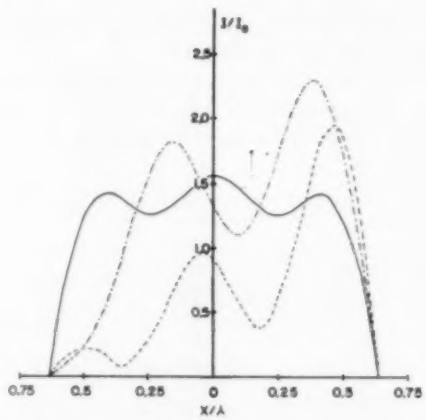

FIG. 2. Intensity distribution in the aperture of a slit as computed from the rigorous solution $s = 1.27\lambda$; ——— normal incidence; — · — · — oblique incidence ($u = 60°$); - - - - oblique incidence ($u = 30°$).

II. FIELD DISTRIBUTION OVER THE APERTURE IN A SLIT

A. Numerical Evaluation

Figure 1 shows the two infinite conducting planes with a slit s and indicates the coordinate system used in calculation. Using the rigorous solution (Mathieu functions series) the field distribution (intensity and phase) over the aperture in slits of 0.45λ, 1.27λ, and

* The research reported in this paper has been sponsored by the Electronics Research Directorate of the Air Force Cambridge Research Center, Air Research and Development Command under contract.

[1] R. K. Hadlock, J. Appl. Phys. **29**, 918 (1958).
[2] P. M. Morse and P. J. Rubenstein, Phys. Rev. **54**, 895 (1938).
[3] H. P. Hsu, Case Institute of Technology Sci. Rept. No. 5 (1959).
[4] R. Plonsey and H. P. Hsu, J. Appl. Phys. **30**, 1468 (1959).

2.21λ (λ:wavelength) width due to a normal incident plane wave and oblique incident waves were obtained. These results can be found in reference 3 and only the results for the case of 1.27λ are shown in Figs. 2 and 3.

B. Discussion

The field distribution (intensity and phase) over the aperture in a slit of 0.45λ width can be described as following[3]: (1) the intensity at the center is maximum (almost three times the unperturbed incident value) for normal incidence; (2) the peak shifted to right in the case of oblique incidence; (3) phase variation is almost linear for each angle of incidence, but deviates somewhat from the unperturbed distribution.

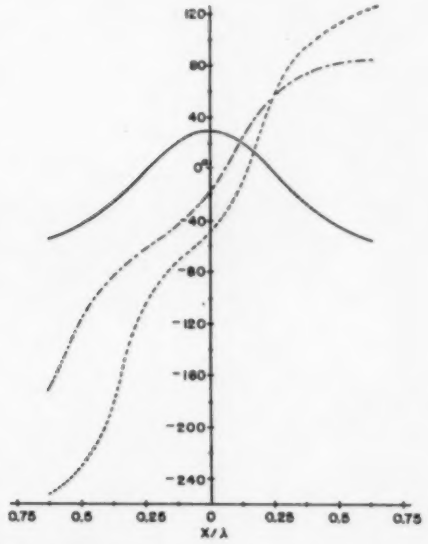

FIG. 3. Phase variation in the aperture of a slit (phase angle of incident wave at the center of slit is chosen as 0°) $s=1.27\lambda$; ————normal incidence; —·—·—oblique incidence ($u=60°$); - - - - -oblique incidence ($u=30°$).

The field distributions over the aperture for a slit of 1.27λ width is shown in Figs. 2 and 3. The results show that (1) the intensity at the center is still maximum (about 1.5 times the unperturbed value) for normal incidence; (2) the maximum intensity also shifted to the right for oblique incidence.

The field intensity variations over the aperture for the slit of 2.21λ width are found as following[3]: (1) for normal incidence the intensity at the center is no longer maximum and two peaks appear on both sides at the half way point from the center; (2) the field patterns for two angles of oblique incidence are quite different and almost mirror images of each other about the center line.

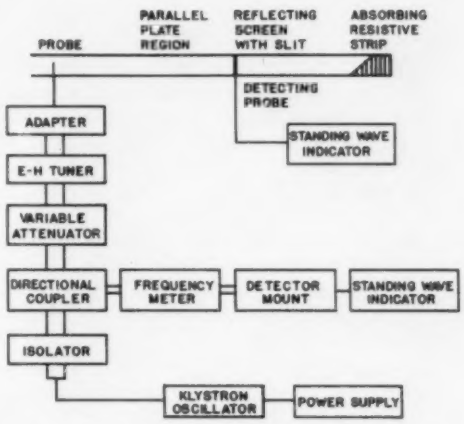

FIG. 4. Schematic diagram of an arrangement of components for measurement.

III. MEASUREMENTS

A. Description of Experimental Equipment

The infinite parallel-plate region is approximated experimentally as shown in Fig. 4 by two plane parallel 6- by 6-ft square magnesium alloy sheets spaced ½ in. apart. A turntable made of aluminum, 28 in. diam, is located at the center of the lower plate. Another small turntable also made of aluminum, 15 in. in diam is located eccentrically in the large turntable, both forming a portion of the lower electric surface. A pickup probe can be inserted into the small turntable. The distance between the centers of the two turntables is 11.375 in. and is just equal to the distance between the center of the small turntable and pickup probe. With this design the pickup probe can reach any point within a circle of 11.375-in. radius. Two verniers are attached to each turntable so that 0.25° of angular reading can be obtained. The exact position of pickup probe can be expressed by these two angular readings.

Six mounting holes for probe feeds are in the lower plate and are located at 2 ft 3.75 in. distance from the center of the large turntable (22 wavelengths at an operating wavelength of 3.2 cm); their polar angles differ by 15° intervals.

At X band, the spacing of the plates is about 0.40 wavelength. Space variation of 0.05 in. can be obtained by turning the screws attached on the lower plate.[5] The spacing of the plates, even allowing for this spacing variation, is less than half a free space wavelength so that the only propagating mode is a radial TEM wave.

In order to eliminate reflections from the edge of the parallel-plate region wedge-shaped resistor cards, 150 ohms per unit area, were inserted around the circumference of the parallel-plates. The resistor cards, 4 in.

[5] This adjustment facilitates making tight contact with reflectors placed within the parallel plates.

long, are tapered over 2 in. of their length, and have an even spacing of 1 in.

Several conducting screens with a slit width of 1.27λ, 2.21λ, 3λ, 3.5λ ($\lambda=3.2$ cm), subsequently inserted between the parallel-plates, were made by forming 0.001-in. aluminum foil over one side of a 1-in. thick polyfoam bar. This structure helps to insure good electrical contact between the screen and parallel plates. In order to obtain a smooth flat screen a second aluminum sheet was wrapped again over the first one.

An x-13 reflex klystron was used as a source at $\lambda=3.2$ cm, and broadband probe directly connected to a waveguide through an adapter was used for a line source. Probe penetration depth into the parallel plates was variable and was easily fixed in position by a locking ring.

For detection, an untuned probe was used. The measuring equipment is located underneath the parallel-plate region. A schematic diagram of the arrangement of components for the measurements is shown in Fig. 4.

B. Comparison of Rigorous and Experimental Results

The comparison of the measured relative amplitudes of the total electric field intensity along the aperture in the slit of 1.27λ and 2.21λ width ($\lambda=3.2$ cm) for normal incidence and an oblique incidence with the exact value is shown in Figs. 5 and 6. The scale for these measured results are normalized so that the measured field at the center point of the slit without conducting screen is equal to unity.

The intensity variation of the electric field over the aperture in the slit of 3λ and 3.5λ width due to normal incidence and several oblique incidences was also measured. Since the convergence of the rigorous solution becomes very slow as the width of the slit increases to more than 3λ, the comparison of these measured values and rigorous values is not made for these cases. However, the scale for these measured results are also normalized so that the measured field at the center point of the slit without conducting screens for each curve is equal to unity. These measured results are shown in Figs. 7 and 8.

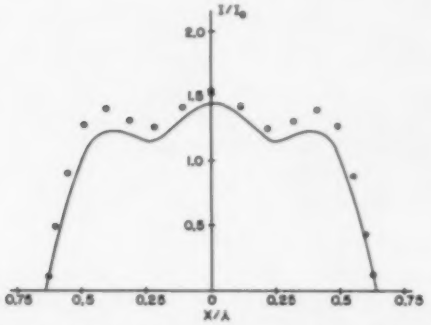

FIG. 5. Intensity distribution in the aperture of a slit ($s=1.27\lambda$), normal incidence; ○ Exact values; ————Measured values.

IV. CONCLUSION

From the rigorous and experimental results obtained certain remarks may be made. As a whole, the agreement between exact values and experimental results is good. If we shift the experimental curves so that the measured field at the center point of the slit for each curve is equal to the rigorous value, much better agreement is obtained. This suggests that the measured values involve an error due to normalization with the incident field. The possible sources of the deviations are:

(1) In the process of inserting the conducting screen in the parallel-plate region the incident wave is no longer exactly the same as it is without the conducting screen.

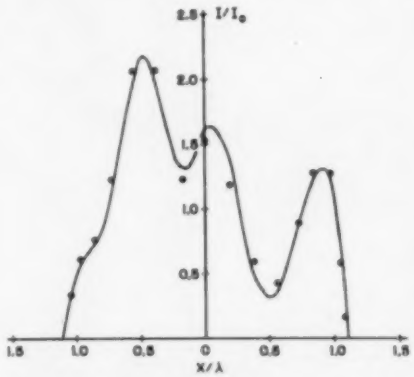

FIG. 6. Intensity distribution in the aperture of a slit ($s=2.21\lambda$), oblique incidence, $u=60°$; ○ Exact values; ————Measured values.

(2) The exact values are based on plane incident waves, and in the measurement the plane incident wave is approximated by a cylindrical wave from a line source, though the line source is located about 22 wavelengths distance from the center of the slit.

(3) The effect of conducting screen thickness. The exact theory for diffraction by a slit considers only the case where the conducting screen is of zero thickness. However, the screen used in the experiment has some thickness, and especially in order to obtain a flatter surface, the thickness of the screen was increased substantially.

(4) The effect of flatness of the conducting screen surface: It is needless to say that the exact theory for diffraction by a slit assumes zero thickness of screen and perfect flatness, but it is impossible to obtain

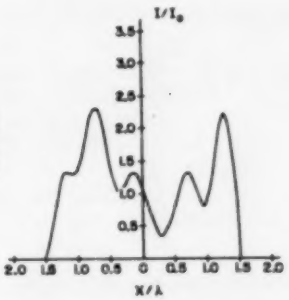

FIG. 7. Measured intensity distribution in the aperture of a slit ($s=3\lambda$), oblique incidence, $u=60°$.

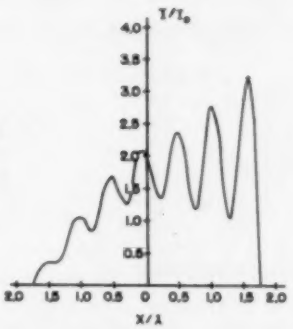

FIG. 8. Measured intensity distribution in the aperture of a slit ($s=3.5\lambda$), oblique incidence, $u=30°$.

perfect flatness of the screen used in any experiment. In order to obtain a flatter screen, brass shim stock was tried instead of aluminum foil, but the screen surface was bent over to form a curved surface when pressed between the parallel-plates.

(5) The effect of contacts of the screen and parallel-plates: Firm contacts of the screen and parallel plates are necessary.

(6) The effect of absorbers used: At present it is impossible to obtain perfect absorbers commercially. Though the characteristics of absorbers is not generally known an investigation showed that the resistor card absorbers were reasonably acceptable.

ACKNOWLEDGMENTS

The author gratefully acknowledges his indebtedness to Dr. Robert Plonsey and Dr. Robert E. Collin for their guidance and advice. He also wishes to thank A. E. Misek for his help in computation of tables.

APPENDIX

Diffraction by a Slit Due to a Line Source[6]

The source is located at (μ_0,θ_0) in elliptic coordinates and the field point is denoted by (μ,θ).

For $\mu<\mu_0$

$$H_0^{(1)}(kR)=4\Big[\sum_{m=0}^{\infty}\frac{Se_m(h,\cos\theta_0)}{M_m^{e}(h)}Se_m(h,\cos\theta)\times Je_m(h,\cosh\mu)He_m(h,\cosh\mu_0)+\sum_{m=1}^{\infty}\frac{So_m(h,\cos\theta_0)}{M_m^{o}(h)}So_m(h,\cos\theta)\times Jo_m(h,\cosh\mu)Ho_m(h,\cosh\mu)\Big].$$

If the line source is parallel to the z axis, the field can be expressed as (in the absence of the screen)

$$E_z=A'H_0^{(1)}(kR),$$

where R is the distance between the source and field point.

If the boundary condition requires that $E_z=0$ at $\theta=0$, $\theta=\pi$ a complete set of eigenfunctions is the set So_m. The incident plus reflected wave in region $\pi<\theta<2\pi$ is

$$\begin{aligned}A'H_0^{(1)}(kR)-A'H_0^{(1)}(kR')&=A\sum_{m=1}^{\infty}\frac{So_m(h,\cos\theta_0)}{M_m^{o}(h)}So_m(h,\cos\theta)Jo_m(h,\cosh\mu)\times Ho_m(h,\cosh\mu_0)\\&\quad-A\sum_{m=1}^{\infty}\frac{So_m(h,\cos(2\pi-\theta_0))}{M_m^{o}(h)}So_m(h,\cos\theta)\times Jo_m(h,\cosh\mu)Ho_m(h,\cosh\mu_0)\\&=2A\sum_{m=1}^{\infty}\frac{So_m(h,\cos\theta_0)}{M_m^{o}(h)}So_m(h,\cos\theta)Jo_m(h,\cosh\mu)\times Ho_m(h,\cosh\mu_0),\end{aligned}$$

where R' is the distance between the field point and the image of the source. To this we must add a diffracted wave to ensure continuity across the slit $\mu=0$. Then for region $\pi<\theta<2\pi$

$$E_z=\sum_{m=1}^{\infty}\frac{So_m(h,\cos\theta_0)}{M_m^{o}(h)}So_m(h,\cos\theta)[2AHo_m(h,\cosh\mu_0)\times Jo_m(h,\cosh\mu)+C_mHo_m(h,\cosh\mu)],$$

and for the region $0<\theta<\pi$

$$E_z'=\sum_{m=1}^{\infty}\frac{So_m(h,\cos\theta_0)}{M_m^{o}(h)}So_m(h,\cos\theta)D_mHo_m(h,\cosh\mu).$$

From the condition that

$$E_z|_{\mu=0}=E_z'|_{\mu=0}\qquad\left.\frac{\partial E_z}{\partial\mu}\right|_{\mu=0}=-\left.\frac{\partial E_z'}{\partial\mu}\right|_{\mu=0},$$

[6] For the notations used here see P. M. Morse and H. Feshbach, *Methods of Theoretical Physics* (McGraw-Hill Book Company, Inc., New York, 1953).

we can determine the coefficients C_m and D_m for each value of m

$$C_m = D_m = -[AJo_m'(h,1)/Ho_m'(h,1)]Ho_m(h, \cosh\mu_0).$$

Therefore, the diffracted field in region $0<\theta<\pi$ is

$$E_z' = -A\sum_{m=1}^{\infty}\frac{So_m(h,\cos\theta_0)}{M_m^0(h)}So_m(h,\cos\theta)\frac{Jo_m'(h,1)}{Ho_m'(h,1)} \times Ho_m(h,\cosh\mu_0)Ho_m(h,\cosh\mu).$$

In the aperture $\mu=0$

$$E_z' = -A\sum_{m=1}^{\infty}\frac{So_m(h,\cos\theta_0)}{M_m^0(h)}Ho_m(h,\cosh\mu_0)\frac{Jo_m'(h,1)}{Ho_m'(h,1)} \times Ho_m(h,1)So_m(h,\cos\theta).$$

For normal incidence $\theta_0=3\pi/2$

$$E_z' = -A\sum_{m=1}^{\infty}\frac{So_m(h,0)}{M_m^0(h)}Ho_m(h,\cosh\mu_0)\frac{-C_m^0\sin\delta_m^0}{jC_m^0\exp(j\delta_m^0)} \times[-jC_m^{0\prime\prime}\exp(j\delta_m^{0\prime\prime})]So_m(h,\cos\theta)$$

$$= A\sum_{m=1}^{\infty}\frac{So_m(h,0)}{M_m^0(h)}Ho_m(h,\cosh\mu_0)\frac{1}{C_m^0}\exp(-j\delta_m^0) \times So_m(h,\cos\theta).$$

Here the result was obtained by using the relations

$$\delta_m^{0\prime\prime}=0, \quad C_m^{0\prime\prime}=-(1/C_m^0\sin\delta_m^0) \quad \text{when} \quad \mu=0.$$

The field at the center of the slit $\theta=\pi/2$, $\mu=0$, is

$$E_z' = A\sum_{m=1}^{\infty}\frac{So_m(h,0)^2}{M_m^0(h)}\frac{\exp[-j\delta_m^0(h,1)]}{C_m^0(h,1)}Ho_m(h,\cosh\mu_0).$$

JOURNAL OF APPLIED PHYSICS VOLUME 31, NUMBER 10 OCTOBER, 1960

Grain-Boundary Photoresponse

W. W. LINDEMANN AND R. K. MUELLER
Mechanical Division of General Mills, Inc., Minneapolis, Minnesota

(Received April 15, 1960)

Measurements of the sensitivity of grain-boundary photodetectors indicate an expected minimum detectable power of better than 10^{-14} w. Major factors governing the sensitivity are the minority carrier lifetime and the distance of the boundary from the irradiated surface. Spectral measurements show an added absorption edge response at about 1.67 μ and 1.72 μ. This added response could be caused by deep-lying acceptor levels or by excitons with a long lifetime. However, the experimental evidence points to direct absorption at the grain boundary as the most likely reason for the absorption edge irregularities.

INTRODUCTION

GRAIN boundaries in n-type germanium present a high resistance to electron flow across the boundary. It is generally agreed that this high resistance is caused by electrons trapped at dangling bonds connected with the boundary. The resulting energy level diagram is as shown in Fig. 1. It has also been shown[1] that the equivalent electrical circuit for a grain boundary may be drawn as in Fig. 2. The resistances in this circuit are small at room temperature but increase to extremely high values at liquid-nitrogen temperature. The capacities connected with the boundary are frequency independent at low temperatures (<282°K) and have a magnitude which is dependent, among other things, upon the boundary charge.[2]

There are a number of ways in which the boundary charge and consequently the boundary capacity may be changed. The charge may be increased by applying a voltage pulse across the sample and decreased either by hole injection into the boundary region or by exciting the boundary electrons into the conduction band.[3] Hole injection may be accomplished by the optical production of hole-electron pairs in the bulk germanium and the subsequent diffusion of the holes into the boundary region, while the electron excitation may be accomplished by the direct absorption of optical radiation by the boundary electrons. In the first case one has the possibility as outlined in a previous publication[4] of producing a sensitive infrared-photocapacitive detector. In the latter case one has a sensitive means for obtaining

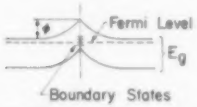

FIG. 1. Energy-level diagram for a grain boundary at equilibrium.

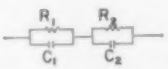

FIG. 2. Equivalent electrical circuit for a grain boundary.

[1] W. E. Taylor, N. H. Odell, and H. Y. Fan, Phys. Rev. **88**, 867 (1952).
[2] R. K. Mueller, J. Appl. Phys. **30**, 546 (1959).
[3] R. K. Mueller, J. Appl. Phys. **30**, 1004 (1959).
[4] W. W. Lindemann and R. K. Mueller, J. Appl. Phys. **29**, 1770 (1958).

basic information about the structure of the acceptor levels associated with the boundary.

This article consists of two major parts. In the first part measurements which indicate limitations to the sensitivity of grain-boundary photocapacitors and consequently lead to a prediction of the minimum detectable power obtainable with such a detector are discussed. The second part will deal with spectral measurements which show some irregularities in the absorption-edge response.

EXPERIMENTAL PROCEDURE

The method for monitoring the grain-boundary capacity changes with optical excitation was much the same as reported previously.[4] That is, the grain-boundary capacity was used as the frequency determining element of an rf oscillator and the frequency of that oscillator was monitored with a frequency counter. In contrast to the previous work where the grain boundary was operated about its equilibrium charge, however, the boundaries in these experiments were charged with a 1.5-v pulse and the impinging radiation was measured as a function of the rate of decay of the net boundary charge as shown by the monotonically changing grain-boundary capacity. This type of measurement is more sensitive than the equilibrium method and is possible at low temperatures (liquid-N_2 temperature was used in all of the experiments to be reported here) since at these temperatures a sample with a well-etched surface will lose its charge very slowly, having a time constant of several days if hole injection is avoided.

Also, in contrast to the previous work, the samples were mounted such that the incoming radiation impinged on the end of the sample perpendicular to the boundary as shown in Fig. 3 rather than on the edge of the boundary. With this method the active boundary area is well defined. In addition, the change in spectral response with boundary depth can be determined and checked against the theory given in Appendix II.

The samples used in these experiments contained carefully grown tilt boundaries with misfit angles of 1°, 2°, 4°, 6°, and 25°. The axis of relative rotation of the two components in the bicrystals was in all cases a common ⟨100⟩ direction. The boundary plane was a mean {110} plane containing the common ⟨100⟩ axis or a mean {100} plane containing the common ⟨100⟩ axis.

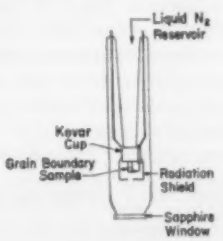

FIG. 3. Grain-boundary detector cell.

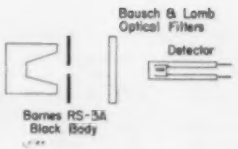

FIG. 4. Schematic of apparatus for making minimum detectable power measurements.

The samples were cut in the form of rectangular parallelepipeds with the boundary plane perpendicular to the main axis as indicated by Fig. 3.

Spectral measurements were made on a Beckmann DK-2 spectrophotometer. The sample was charged to a voltage of 1.5 v and the dark decay of the boundary charge was noted. The spectrophotometer slits were then opened to the point where the decay was at least 10 times the dark decay and the slit width was noted. The relative number of photons falling on the sample was then calculated using the expression

$$N_{ph}=(E_s\lambda s^\eta)/hc=BE_s\lambda s^\eta,$$

where E_s is the relative energy output of the source as measured with a thermocouple bolometer, λ is the center wavelength of the impinging radiation (measurements were made at 10-mμ intervals; the dispersion of the instrument was less than 100 mμ/mm slit width and the slit width never exceeded 0.1 mm in the region of interest), and s is the slit width in mm. (The exponent η for the instrument used was determined to be $\eta=1.5$. This value was checked with several different detectors.) At each wavelength the slit width was adjusted to give the same decay rate and the relative response of the detector could then be expressed as $1/N_{ph}$. Typical spectral-response curves obtained in this way are shown in Fig. 6.

Absolute response measurements were made using the system of Fig. 4. The source was a Barnes model RS-3A blackbody with an aperture variable in seven steps from 0.010-in. diam to 0.200-in. diam. The filters were Bausch and Lomb optical interference filters with bandpass characteristics centered at 1.38 μ, 1.575 μ, and 1.725 μ. The transmission characteristics of these filters were recorded on the Beckman DK-2 spectrophotometer.

Again the incident radiation was measured as the rate of change of the oscillator frequency. This was done at all seven blackbody apertures and the resultant plot of Δf vs incident power yielded a straight line which could be extrapolated to the inherent dark drift of the oscillator. The incident power at which Δf became equal to the dark drift gave the upper limit of the minimum detectable power of the device. The amount of incident power was of course calculated from the Stefan-Boltzmann law taking into account the attenuation of the optical filters.

TABLE I.

Sample	θ(°)	N_d(cm^{-3})	A(mm^2)	C($\mu\mu f$)	l_g(mm)	λ_{peak}(mμ)	K_{peak}(cm^{-1})	α_{peak}(%)	l_d(mm)	τ(μsec)	Minimum detectable power (w)
25-4-W	25	10^{15}	6.7	333	1.5	1570	6.67	0.348	0.0142	0.0234	5.0×10^{-12}
25-5-W	25	10^{15}	9.0	422	4.0	1615	2.50	0.312	0.0339	0.135	2.3×10^{-12}
6-2-A	6	10^{16}	2.9	400	0.5	1490	20.00	6.370	0.0865	0.880	3.6×10^{-12}
4-5-A	4	10^{15}	3.0	210	6.0	1625	1.67	0.710	0.115	1.570	1.4×10^{-12}
2-1-A	2	10^{15}	6.25	328	5.0	1620	2.00	0.838	0.114	1.520	5.0×10^{-12}
1-2-B	1	10^{14}	5.0	52	5.0	1620	2.00	0.780	0.106	1.320	5.5×10^{-12}
1-5-B	1	10^{14}	3.0	58	0.5	1490	20.00	1.440	0.0195	0.0447	1.2×10^{-12}

RESULTS

Sensitivity Measurements

Both sensitivity and spectral measurements were made on a large number of samples of which those listed in Table I are typical. Table I is a compilation of the pertinent data needed to compare various types of samples and to make a prediction as to the steps to be taken to improve device performance. The first column of the table gives the boundary tilt angle, the second gives the donor concentration in the bulk, and the third gives the cross-sectional area of the sample in a plane perpendicular to the main axis. Column 4 lists the sample capacities measured between opposite ends of the samples, 5 gives the distance of the boundary from the front of the sample, and 6 gives the wavelength at which the detector reaches its peak response. The next two columns give the absorption constant for germanium at the peak wavelength as determined by Macfarlane *et al.*,[5] and the hole production-collection efficiency α as calculated from Eq. (8) of Appendix I. Column 9 lists the diffusion lengths as calculated from the foregoing data and Eq. 12 of Appendix II. The τ of the following column is the hole lifetime as calculated from the well-known expression $l_d^2=D\tau$. The last column lists the values of incident energy at which the signal level becomes equal to the dark drift of the boundary charge. This value is arrived at by an extrapolation of the measured data (Fig. 5) to the point at which $\Delta f=0.08$-cycle change in frequency between 1-sec counts. The 0.08-cycle value was chosen because it represents the change measured for one of the more stable samples. It does not, however, represent the lowest noise obtainable since it is a predictable drift rather than a measure of the random fluctuations. Therefore, the values in the last column are maximum values and one could look for improvement if the predictable drift were cancelled by some means.

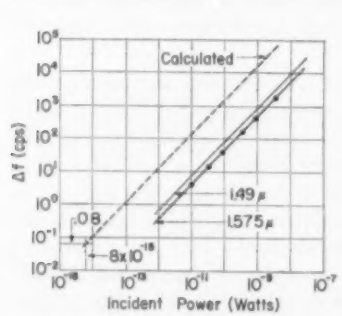

FIG. 5. Sensitivity measurement for sample 1-5-B.

Analyzing the data presented in Table I more carefully, one can sort out a number of facts which point the way to the improvement of grain-boundary photodetectors. First of all, one notes no correlation between the boundary angle or the donor concentration and the minimum detectable power of the device. Secondly, one notes that as the boundary is moved closer to the front surface of the sample the peak response moves to the shorter wavelengths and the sensitivity increases, other things remaining equal. Both of these results are expected from elementary considerations of optical absorption in germanium. The extent of the change can better be seen from Fig. 6 where the spectral response curves for three different samples are drawn. These samples, 25-2-W, 25-4-W, and 25-5-W, are as nearly identical as possible, having been cut from successive sections of the same ingot. The only difference among the samples is the distance from the front surface to the boundary, being 0.7, 2.5, and 4.5 mm for samples 25-2-W, 25-4-W, and 25-5-W, respectively. This behavior allows one to vary the peak response of grain-boundary detectors over a limited spectral range by varying the position of the boundary.

Some interesting information is contained in the tabulation of diffusion length and minority carrier lifetime. Three samples have lifetimes of about 1.5 μsec in good agreement with the recombination lifetime found by Fan, Navon, and Gebbie[6] and with pulse lifetime measurements made in this laboratory using the method of Pell.[7] The other samples show lifetimes ranging downward to 0.0234 μsec for sample 25-4-W. These short lifetimes are not understood and therefore more experiments to determine the exact mechanism governing these short lifetimes are being planned.

Finally, a look at the minimum detectable power column of Table I shows as expected that the greatest

[5] G. G. Macfarlane, T. P. McLean, J. E. Quarrington, and V. Roberts, Phys. Rev. **108**, 1377 (1957).

[6] H. Y. Fan, D. Navon, and H. A. Gebbie, Physica **20**, 855 (1954).

[7] E. M. Pell, Phys. Rev. **90**, 278 (1953).

sensitivity is shown by the samples with the longest minority carrier lifetime, 4-5-A, and with the shortest distance from the front face to the boundary, 1-5-B. Unfortunately, none of the samples tested combined both desirable features but one can estimate from the data of Table I the minimum detectable power to be expected if one had a sample with a minority carrier lifetime of about 1.5 μsec and a surface-to-boundary spacing of 0.5 mm. For instance, calculating and plotting the absolute response of sample 1-5-B (Fig. 5) and extrapolating to the 0.08-cps drift level discussed previously gives a minimum detectable power of about 8×10^{-15} w. A similar calculation for sample 4-5-A, assuming a surface-to-boundary spacing of 0.5 mm, yields a minimum detectable power of about 5×10^{-15} w. From these results it seems safe to say that under proper conditions the germanium grain-boundary photodetector can be made to have a minimum detectable power better than 10^{-14} w.

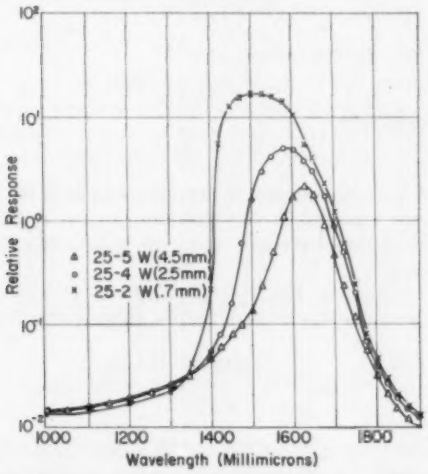

FIG. 6. Spectral-response curves for three 25° samples. Parameter is the distance of the boundary from the front of the sample.

Spectral Response Measurements

Some of the measurements of the spectral-response characteristics (Fig. 6) have already been discussed. However, the most interesting portion of the spectral-response curve, the absorption edge, has not been mentioned and will therefore be discussed in this section.

The reason for the interest in the absorption-edge spectrum is obvious. The boundary states occupy energy levels in the forbidden band as shown in Fig. 1 and direct absorption of optical energy by the trapped electrons should produce irregularities in the absorption-edge response. Such irregularities do occur as shown by the curves of Fig. 7 and of Fig. 8. Figure 7 gives the data for sample 4-5-A and represents the most extreme

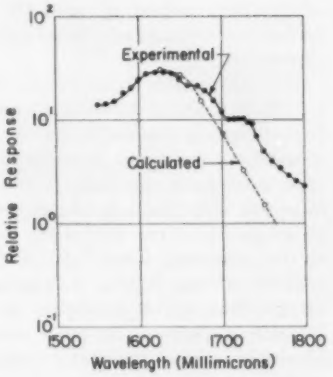

FIG. 7. Absorption-edge response for sample 4-5-A.

case of absorption-edge irregularities that has been encountered. Figure 8 on the other hand gives the data for sample 25-4-W and is somewhat more typical.

The dashed curves on the two diagrams just mentioned are calculated response curves which assume only hole-electron pair creation in the bulk material. The curves were calculated from Eq. 12 of Appendix II. The diffusion length was taken as the one calculated at the peak response, and the value of the absorption constant K was taken from the data of Macfarlane *et al.*[5]

The curves of Figs. 7 and 8, then, show an optical response which cannot be attributed entirely to the holes created by direct excitation of electrons from the valence to the conduction band in the bulk germanium. Two possibilities other than direct grain-boundary absorption present themselves as explanations for the added response. It is possible that indirect hole production due to ionization of deep-lying acceptor levels could explain the additional response. Such an explanation is discredited, however, by the diode curve of Fig. 8. This curve represents the absorption-edge photoconductive response for a p-n junction diode. This diode was made from a block of germanium from the same slice of a bicrystal as the one which provided the grain-boundary sample 25-4-W. This diode curve shows very little

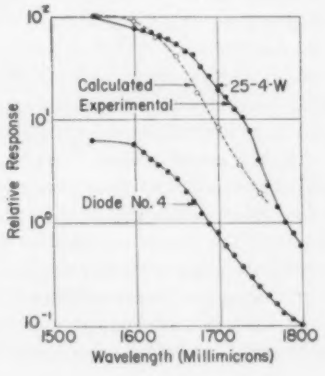

FIG. 8. Absorption-edge response for sample 25-4-W.

irregularity, indicating that the added response is probably not due to additional hole creation in the bulk germanium.

It is also possible that excitons such as the ones found by Macfarlane and co-workers[5] could explain the result. If excitons are responsible for the added response, one would have to assume, however, a diffusion length for these excitons of the order of millimeters and furthermore one would have to assume a higher probability of disintegration in the field of the boundary barrier than in the somewhat lower field of the *p-n* junction. In addition, a closer look at the curves of Fig. 7 and Fig. 8 reveals that the irregularities in the curves fall at different energies than those shown in the data of Macfarlane *et al.*[5] While the irregularities in the data presented here are rather broad and poorly defined, one can estimate their positions at roughly 1.67 μ and 1.72 μ or about 0.745 ev and 0.72 ev. Macfarlane's irregularities on the other hand, fall at about 0.762 ev and somewhere below 0.71 ev at liquid-N_2 temperature.

It is therefore felt that the irregularities observed are most likely connected with direct optical absorption at the grain boundary. The data are still rather crude and no effort has been made to relate these data to possible models for the grain-boundary levels. It is felt however that the method described here, in which changes of the boundary charge are observed directly, is the most sensitive method for studying the optical and electrical properties of grain boundaries and of the individual dislocations in low angle boundaries. Further refinements in the measuring technique, particularly in the resolution of the optical equipment, are being made, and it is believed that the results of further measurements will serve to give a more definite picture of the absorption-edge irregularities.

CONCLUSIONS

The data presented in the foregoing discussion have shown that the two most important parameters affecting the performance of grain-boundary photodetectors are the minority carrier lifetime and the distance of the boundary from the irradiated surface. Some samples show a short lifetime compared to the expected recombination lifetime. This short lifetime is unexplained at present. Present results indicate that with proper design, grain-boundary photodetectors can be made to have a minimum detectable power better than 10^{-14} w.

Spectral measurements indicate that grain-boundary photodetectors have absorptions at about 1.67 μ and 1.72 μ which do not appear to be a property of the bulk material. The results are taken to show a direct absorption by the grain-boundary electrons and it is suggested that more refined measurements of this absorption may yield valuable information concerning the electrical properties of grain boundaries and of dislocations.

APPENDIX I

A derivation of the expression for the production-collection parameter α used in the previous discussion begins with the definition for α.

$$\alpha=\frac{I_t/q}{S_0}, \tag{1}$$

where I_t/q is the number of holes collected at the boundary/unit area/sec and S_0 is the number of photons incident upon the surface of the sample/unit area/sec. Obviously

$$I_t/q=\Delta Q/q, \tag{2}$$

where ΔQ is the change in boundary charge/unit area/sec and q is the charge of a hole. Then, since[1] the boundary charge/unit area is

$$Q=qN_d(l_1+l_2) \tag{3}$$

and the capacitance/unit area is

$$C=\mathcal{K}/(l_1+l_2), \tag{4}$$

it follows that

$$\Delta Q/Q=-(\Delta C/C), \tag{5}$$

where N_d is the number of donors in the bulk, $\mathcal{K}$ is the dielectric constant of the bulk, and l_1 and l_2 are the widths of the depletion layers on either side of the boundary.

On combining Eqs. (3)–(5) and converting to an arbitrary area A, one finds for the total charge change

$$\Delta Q_1=A\Delta Q=-\frac{AQ\Delta C_1}{C_1}=-\frac{KqN_dA^2}{C_1^2}\Delta C_1, \tag{6}$$

where C_1 and ΔC_1 are for samples with an arbitrary cross section A. The number of photons incident upon the surface/unit area between counts is

$$S_0=W/E_\lambda, \tag{7}$$

where W is the incident flux in w/unit area and E_λ is the energy of an incident photon in w sec. Dividing I_t/q by S_0, the expression for α for a sample with an arbitrary cross section A becomes

$$\alpha=-[(\mathcal{K}N_dAE_\lambda)/(WC_1^2)]\Delta C_1. \tag{8}$$

All of the quantities in this expression are easily determined including ΔC_1 which is obtained from the relation

$$\Delta C_1/2C_1=\Delta w/w. \tag{9}$$

APPENDIX II

The relationship between the photon influx to the sample and the hole current into the boundary will be derived below. The considerations can be restricted to the steady-state case since the time between measure-

ments is large compared to the lifetime of the holes and since the boundary remains negatively charged above its equilibrium value throughout the time of measurement. This last condition guarantees a time independent boundary condition at the grain boundary, namely that the hole density remains practically zero at the edges of the depletion region surrounding the boundary.

If total reflection at the soldered end of the sample is assumed (Fig. 9), the photon flux S in the sample is given by

$$S=[S_0(1-r)/(1-r\gamma)](e^{-Kx}-\gamma e^{Kx}), \tag{1}$$

where S_0 is the flux (number of photons/sec/cm^2) impinging on the illuminated surface, r is the reflection coefficient at the front surface, K is the absorption coefficient of the photons, and x is the coordinate along the sample axis with the origin at the illuminated surface. The constant γ is given by

$$\gamma=e^{-2Kl_s}, \tag{2}$$

where l_s is the total sample length. Transferring the origin of x to the grain boundary which is parallel to the front surface and l_g cm away from it, one can write for the photon flux

$$S=[S_0(1-r)/(1-r\gamma)]e^{-Kl_g}(e^{-Kx}-\gamma' e^{Kx}), \tag{3}$$

with γ' given by

$$\gamma'=e^{-2K(l_s-l_g)}. \tag{4}$$

The hole generation/cm^3 due to the photon flux [Eq. (3)] is

$$-q\,\mathrm{div}S=qS_0\frac{(1-r)K}{1-r\gamma}e^{-Kl_g}(e^{-Kx}+\gamma' e^{Kx}). \tag{5}$$

In the temperature range of interest here the hole density without light influx is practically zero. The steady-state hole distribution due to the light influx averaged over the sample cross section is then given by

$$p''=-\frac{qS_0K(1-r)}{D(1-r\gamma)}e^{-Kl_g}(e^{-Kx}+\gamma' e^{Kx})+p/l_d^2, \tag{6}$$

where l_d is the diffusion length of holes incorporating the recombination at the surfaces parallel to the sample axis.

The general solution of this equation is given by

$$p=Ae^{x/l_d}+Be^{-x/l_d}+C(e^{-Kx}+\gamma' e^{Kx}). \tag{7}$$

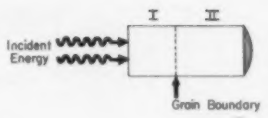

FIG. 9. Grain-boundary sample under consideration in Appendix II.

The constant C is

$$C=S_0\frac{q(1-r)Kl_d^2}{D[1-(Kl_d)^2](1-r\gamma)}e^{-Kl_g}. \tag{8}$$

The grain boundary which is at $x=0$ divides the sample into two regions. Region I is between the illuminated surface and the edge of the depletion region of the grain boundary. Region II is between the opposite edge of the depletion region and the soldered end of the sample (see Fig. 9). By neglecting the width of the depletion region one gets as a boundary condition at the grain boundary

$$p=0 \text{ at } x=0. \tag{9}$$

It can be shown that if the penetration depth of the photons $1/K$ is of the order of the grain-boundary distance l_g or larger, and provided that the diffusion length of the holes is very small compared to the boundary distances l_g and (l_s-l_g), the effect of the end surfaces on the hole distribution around the boundary becomes negligible and one can write for the hole densities in the neighborhood of the boundary for Regions I and II:

Region I

$$p=Ae^{-x/l_d}+C(e^{-Kx}+\gamma' e^{Kx}), \tag{10}$$

Region II

$$p=Be^{x/l_d}+C(e^{-Kx}+\gamma' e^{Kx}). \tag{11}$$

On considering the boundary condition of Eq. (9) this gives for the total hole-diffusion current density I_t into the boundary from both regions

$$I_t=2qS_0\frac{(1-r)(1+\gamma')}{1-r\gamma}Kl_de^{-Kl_g}, \tag{12}$$

if $Kl_g\lesssim 1$ and $l_d/l_g\ll 1$.

The current density given by Eq. (12) has a maximum with respect to K at

$$K_{\max}=l_g(1-2e^{-2l_s/l_g}\{[(l_s/l_g)-1]e^2+rl_s/l_g\}), \tag{13}$$

neglecting terms in e^{-2l_s/l_g} of higher order than the first.

Since this maximum is in the K range for which the approximations leading to Eq. (12) are valid, Eq. (12) describes the response of the boundary from the maximum response to longer wavelengths if no direct boundary absorption takes place.

Surface Space-Charge Calculations for Semiconductors

D. R. FRANKL
General Telephone and Electronics Laboratories, Inc., Bayside, New York
(Received June 8, 1960)

Approximation formulas for the surface excesses of carriers at large values of the reduced surface and bulk potentials are derived, and computed results are presented.

INTRODUCTION

CALCULATIONS pertaining to the space-charge region near a planar surface of a semiconductor sample involve solutions of a one-dimensional Poisson-Boltzmann equation. The following cases have been treated in the literature:

a. *Thermal equilibrium, complete ionization, nondegenerate statistics, thick slab.* Kingston and Neustadter[1] have solved this case in terms of two functions F and G defined by the relations

$$F(u,u_B)=du/dz, \tag{1}$$

$$G(u_S,u_B)=\int_{u_S}^{u_B}\frac{e^{-u}-e^{-u_B}}{F(u,u_B)}du, \tag{2}$$

where $u=(E_F-E_I)/kT$, and subscripts S and B denote values at the surface ($z=0$) and deep in the bulk ($z\to\infty$), respectively. Here E and E_I are the Fermi level and local intrinsic Fermi level, respectively. Numerical values of F and G are presented for

$$-10\leq u_S\leq 10,\ -10\leq u_B\leq 10 \text{ for } F, \text{ and } -10\leq u_B\leq 3$$

for G. Mowery[2] has used the same analysis to present extensive graphs of surface charge density and surface conductance for germanium and silicon at 300°K, and Dousmanis and Duncan[3] have plotted the relationship between u and z for a number of typical cases.

b. *Complete ionization, nondegenerate statistics, thick slab.* Garrett and Brattain[4] have treated this more general case analytically in detail, but numerical computations are lacking.

c. *Thermal equilibrium, incomplete ionization, degenerate statistics, thick slab.* For this almost completely general case, Seiwatz and Green[5] have obtained expressions for du/dz, and have tabulated the various functions involved.

d. *Thermal equilibrium, complete ionization, nondegenerate statistics, thin slab.* This case, which differs from case a. only in that the sample thickness is less than the space-charge layer thickness, has been treated analytically by Greene, Frankl, and Zemel.[6] Numerical computations are reported by Albers and Thomas.[7]

The present paper deals exclusively with case a., and comprises an extension of the computations of Kingston and Neustadter[1] to larger values of u_S and u_B, such as are encountered, for example, in germanium or silicon considerably below room temperature.

ANALYSIS

The function F, defined in Eq. (1), is found by Kingston and Neustadter[1] to be (− sign for $u_S>u_B$, + sign for $u_S<u_B$)

$$F(u,u_B)=\pm\sqrt{2}[(u_B-u)\sinh u_B+\cosh u-\cosh u_B]^{\frac{1}{2}}. \tag{3}$$

We now proceed to obtain approximations appropriate to various regions of large $|u_B|$, and to insert these into Eq. (2). For this purpose, it is convenient to rewrite Eq. (3) as

$$F(y,u_B)=\pm(2\cosh u_B)^{\frac{1}{2}}\times[\cosh y-1+(y-\sinh y)\tanh u_B]^{\frac{1}{2}}, \tag{4}$$

where $y=u_B-u$ (+ sign for $y>0$, − sign for $y<0$).

For $u_B>0$,

$$F_n(y,u_B)=\pm(2\cosh u_B)^{\frac{1}{2}}\times[e^{-y}+y-1+\theta_n(\sinh y-y)]^{\frac{1}{2}}, \tag{4a}$$

where

$$\theta_n=1-\tanh u_B=e^{-u_B}\operatorname{sech}u_B, \tag{4b}$$

and for $u_B<0$,

$$F_p(y,u_B)=\pm(2\cosh u_B)^{\frac{1}{2}}\times[e^{y}-y-1+\theta_p(y-\sinh y)]^{\frac{1}{2}}, \tag{4c}$$

where

$$\theta_p=1+\tanh u_B=e^{u_B}\operatorname{sech}u_B. \tag{4d}$$

For large $|u_B|$, θ_n and θ_p are small positive numbers.

Case 1. $u_B\gg 0$, $u_S>u_B$ (accumulation layer on n-type bulk). Since $|y-1|\gg|\theta_n(\sinh y-y)|$ for small $|y|$ and $e^{-y}\gg|\theta_n\sinh y|$ for large $|y|$, and since $2\cosh u_B=e^{u_B}$, Eq. (4a) becomes

$$F_n(y,u_B)=-e^{u_B/2}(e^{-y}+y-1)^{\frac{1}{2}}. \tag{5}$$

[1] R. H. Kingston and S. F. Neustadter, J. Appl. Phys. **26**, 718 (1955).
[2] V. O. Mowery, J. Appl. Phys. **29**, 1753 (1958).
[3] G. C. Dousmanis and R. C. Duncan, J. Appl. Phys. **29**, 1627 (1958).
[4] C. G. B. Garrett and W. H. Brattain, Phys. Rev. **99**, 376 (1955).
[5] R. Seiwatz and M. Green, J. Appl. Phys. **29**, 1034 (1958).
[6] R. F. Greene, D. R. Frankl, and J. N. Zemel, Phys. Rev. **118**, 967 (1960).
[7] W. A. Albers, Jr. and J. E. Thomas, Jr., J. Phys. Chem. Solids **14**, 181 (1960).

Then

$$G(u_S,u_B)=e^{-u_B}\int_0^{u_B-u_S}\frac{e^y-1}{F(y,u_B)}dy \tag{6}$$

$$=-e^{-3u_B/2}g_1(u_S-u_B),$$

where

$$g_1(Y)=\int_0^Y\frac{1-e^{-v}}{(e^v-v-1)^{\frac{1}{2}}}dv. \tag{6a}$$

Case 2. $u_B\gg 0$, $0<u_s<u_B$ (depletion layer on n-type bulk). For small y, the first three terms in Eq. (4a) dominate. As y increases, they remain dominant as long as $y\gg\theta_n \sinh y=\exp(y-2u_B)$. This will certainly hold for $y\leq u_B$ (and for considerably larger y when u_B is very large), hence Eq. (5) with reversed sign holds for the present case, and

$$G(u_S,u_B)=e^{-u_S-u_B/2}g_2(u_B-u_S), \tag{7}$$

where

$$g_2(Y)=e^{-Y}\int_0^Y\frac{e^y-1}{(e^{-y}+y-1)^{\frac{1}{2}}}dy. \tag{7a}$$

Case 3. $u_B\gg 0$, $-(u_B+12)\leq u_S\leq 0$ (inversion layer on n-type bulk). Here the dominant terms are $y-1$ and $\theta_n \sinh y$, and these may be comparable. Hence

$$F_n(y,u_B)=e^{u_B/2}[y-1+\exp(y-2u_B)]^{\frac{1}{2}}, \tag{8}$$

$$G(u_s,u_B)=G(0,u_B)$$

$$+e^{-u_B/2}\int_{u_B}^{u_B-u_S}\frac{e^y-1}{[y-1+\exp(y-2u_B)]^{\frac{1}{2}}}dy \tag{9}$$

$$=e^{-u_S-u_B/2}g_3(u_S,u_B),$$

where

$$g_3(u_S,u_B)\approx e^{u_S}g_2(u_B)$$

$$+e^{u_S-u_B}\int_{u_B}^{u_B-u_S}\frac{e^y dy}{[y-1+\exp(y-2u_B)]^{\frac{1}{2}}}. \tag{9a}$$

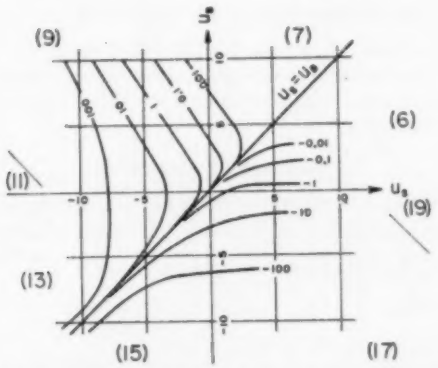

FIG. 1. Contour map of $G(u_S,u_B)$, from data of Kingston and Neustadter, footnote reference 1. Equation numbers of the approximation formulas of present paper shown in appropriate regions of the (u_S,u_B) plane.

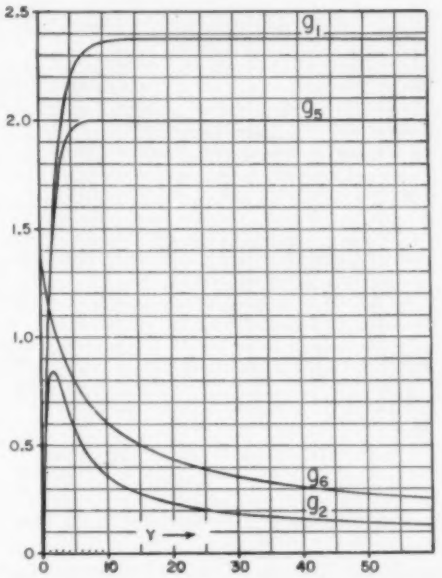

FIG. 2. The functions $g_1(Y)$, $g_2(Y)$, $g_5(Y)$, $g_6(Y)$, defined in Eqs. (6a), (7a), (13b), and (15b), respectively.

Case 4. $u_B\gg 0$, $u_S<-(u_B+12)$ (strong inversion layer on n-type bulk). For $y>2u_B+12$, the first two terms in Eq. (8) are less than 0.1% of the last term (for $u_B\leq 75$) and, to this approximation,

$$F_n(y,u_B)=e^{(y-u_B)/2}=e^{-u/2}, \tag{10}$$

$$G(u_S,u_B)=G(-u_B-12,u_B)+2[e^{-u_S/2}-e^{6+u_B/2}]. \tag{11}$$

For $u_B\ll 0$, the arguments proceed similarly, except that now $2\cosh u_B=e^{-u_B}$. We obtain

Case 5. $u_B\ll 0$, $u_S<u_B$ (accumulation layer on p-type bulk).

$$F_p(y,u_B)=e^{-u_B/2}(e^y-y-1)^{\frac{1}{2}}, \tag{12}$$

$$G(u_S,u_B)=e^{-u_S/2}g_5(u_B-u_S), \tag{13}$$

where

$$g_5(Y)=e^{-Y/2}\int_0^Y\frac{e^y-1}{(e^y-y-1)^{\frac{1}{2}}}dy \tag{13a}$$

$$=2e^{-Y/2}(e^Y-Y-1)^{\frac{1}{2}}. \tag{13b}$$

Case 6. $u_B\ll 0$, $u_B<u_S<0$ (depletion layer on p-type bulk).

$$F_p(y,u_B)=-e^{-u_B/2}(e^y-y-1)^{\frac{1}{2}}, \tag{14}$$

$$G(u_S,u_B)=-(u_S-u_B)e^{-u_B/2}g_6(u_S-u_B), \tag{15}$$

where

$$g_6(Y)=\frac{1}{Y}\int_0^Y\frac{1-e^{-v}}{(e^{-v}+v-1)^{\frac{1}{2}}}dv \tag{15a}$$

$$=2(Y+e^{-Y}-1)^{\frac{1}{2}}/Y. \tag{15b}$$

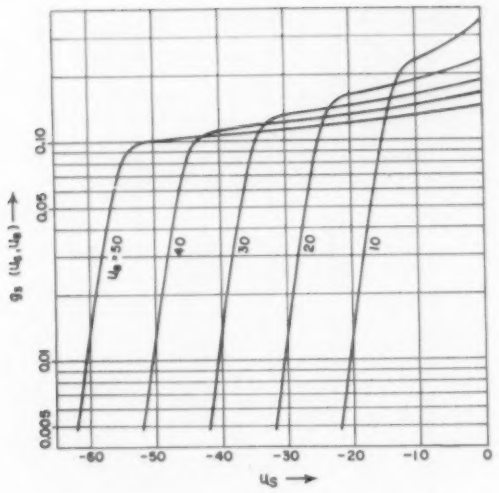

FIG. 3. The function $g_9(u_S,u_B)$, defined in Eq. (9a).

Case 7. $u_B \ll 0$, $0 \leq u_S \leq -u_B+12$ (inversion layer on p-type bulk).

$$F_p(y,u_B) = -e^{-u_B/2}[-y-1+\exp(2u_B-y)]^{\frac{1}{2}}, \tag{16}$$

$$G(u_S,u_B) = G(0,u_B) - e^{-u_B/2}\int_{-u_B}^{u_S-u_B} \frac{1-e^{-v}}{[v-1+\exp(v+2u_B)]^{\frac{1}{2}}}\,dv = e^{-u_B/2}g_7(u_S,u_B), \tag{17}$$

where

$$g_7(u_S,u_B) \approx -2(-u_B-1)^{\frac{1}{2}} - \int_{-u_B}^{u_S-u_B} [v-1+\exp(v+2u_B)]^{-\frac{1}{2}}\,dv. \tag{17a}$$

Case 8. $u_B \ll 0$, $u_S > -u_B+12$ (strong inversion layer on p-type bulk).

$$F_p(y,u_B) = -e^{(u_B-y)/2} = -e^{u/2}, \tag{18}$$

$$G(u_S,u_B) = G(-u_B+12,u_B). \tag{19}$$

RESULTS AND DISCUSSION

A concise summary of the results of the preceding section is presented in Fig. 1 in the form of a contour map of the function $G(u_S,u_B)$ with the equation numbers of the approximate formulas located in the appropriate regions. The auxiliary functions entering into these formulas are tabulated graphically in the subsequent figures; Fig. 2 presents the single-variable functions g_1, g_2, g_5, and g_6, and Figs. 3 and 4, the functions $g_9(u_S,u_B)$ and $g_7(u_S,u_B)$, respectively. These functions have been defined such that they vary slowly enough for concise graphical presentation yet require a minimum amount of arithmetical computation to obtain values of G.

The surface excesses (number of excess carriers per unit surface area) are given[1] by

$$\Delta P = n_i L_D G(u_S,u_B); \quad \Delta N = n_i L_D G(-u_S,-u_B), \tag{20}$$

where ΔN and ΔP are the surface excesses of electrons and holes respectively, n_i is the intrinsic carrier concentration, and L_D the intrinsic screening length (Debye length).

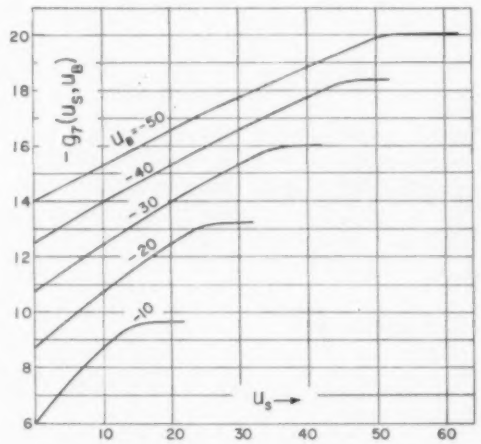

FIG. 4. The function $g_7(u_S,u_B)$, defined in Eq. (17a).

Formulas equivalent to Eqs. (13b) and (15b) have been obtained[3] by use of the identity

$$G(u_S,u_B) - G(-u_S,-u_B) \equiv 2F(u_S,u_B) \tag{12}$$

since, if one of the terms on the left is small, the other may be obtained from the approximation formulas for F, given in the preceding section. This situation will pertain in regions 1, 2, 5, and 6.

ACKNOWLEDGMENTS

Thanks are due to A. L. Brown for the numerical computations and to A. Many for helpful discussions.

[3] A. Many, private communication.

Oblique-Incidence Anisotropy in Evaporated Permalloy Films

D. O. Smith, M. S. Cohen, and G. P. Weiss
Lincoln Laboratory, MIT, Lexington, Massachusetts*
(Received May 20, 1960)

Magnetic anisotropy has been observed in evaporated Permalloy films deposited at oblique incidence of the vapor. Electron micrographs of such films reveal chains of crystallites whose long axes are oriented perpendicular to the vapor beam. A "self-shadowing" model is proposed to explain chain growth, i.e., the area behind a crystallite is left vacant because it is in the crystallite's shadow. Oriented crystallite chains are thus caused by a purely geometric process; their existence has also been demonstrated for Au, Pt, W, and Mg. Oriented chains give rise to a number of macroscopic effects: magnetic anisotropy, anisotropic resistance, dichroism, and anisotropic resonance linewidth. Experiments involving the stripping of oblique-incidence Permalloy films from their substrates indicate the presence of an anisotropic strain which, in conjunction with magnetostriction, gives another contribution to the magnetic anisotropy; this contribution explains the observed compositional dependence of the magnetic anisotropy. Surface tension, which tends to contract the crystallite chains, is postulated as the generating force of anisotropic strain; surface tension could similarly generate the isotropic strain which is found in normal-incidence films.

I. INTRODUCTION

MAGNETIC anisotropy can be induced in evaporated Permalloy films by applying a magnetic field during deposition.[1] However, Knorr and Hoffman,[2] and Smith[3] have discovered that even with no applied field, magnetic anisotropy can be induced in iron and Permalloy films by causing the metal vapor to strike the substrate at an oblique angle instead of normally. Knorr and Hoffman[2] have explained this oblique-incidence effect in terms of inclined crystallographic texture and strain in the film. Several workers, however, have presented experimental and theoretical results which are in contradiction with the Knorr and Hoffman model.[2-7]

The presence of microscopic geometric anisotropy in oblique-incidence films has been inferred from macroscopic measurements by Smith *et al.*[8] In the present study electron microscopy has exhibited the anticipated microscopic structure and furnished insight into its origin; further correlation of the microstructure with macroscopic behavior has also been made.

II. GEOMETRIC ANISOTROPY IN OBLIQUE-INCIDENCE FILMS

Electron microscopy provides direct evidence that geometric anisotropy on a microscopic scale exists in oblique-incidence films, and leads to an interpretation of the origin of this anisotropy. Specimens for electron microscopy were prepared by vacuum evaporation of Permalloy at oblique incidence on thin carbon substrates which were heated during the deposition. Figures 1(a)–(d) are electron micrographs of 80% Ni, 20% Fe (80-20)[9] films of various thicknesses, deposited at a substrate temperature of 200°C, with an angle of 65° between the vapor beam and the film normal. The "diffraction contrast" method of electron microscopy was used to obtain these micrographs,[10] i.e., an aperture was inserted into the objective lens. In these micrographs the beam direction[11] can be deduced from the shadows cast by dirt particles present on the substrate; the agglomeration of the crystallites into chains whose long axes are, on the average, perpendicular to the beam direction is clearly seen. No such geometric anisotropy, on the other hand, is seen in normally-deposited films [Fig. 1(e)]. It is noted that the observation of chain structure becomes difficult for thicker films [Fig. 1(d)]. Optical and magnetic measurements which are described later, however, show that chains are still present in these thick films.

An explanation of the origin of oriented crystallite chains can be given in terms of a "self-shadowing" mechanism. It is postulated that in the initial stages of the film formation a random distribution of small crystallites is created on the substrate and that each crystallite acts as a nucleus for further growth. The region of the substrate behind a growing crystallite is prevented from receiving metal vapor because this region is in the "shadow" of the crystallite; therefore, as the

* Operated with support from the U. S. Army, Navy, and Air Force.

[1] M. S. Blois, Jr., J. Appl. Phys. **26**, 975 (1955).
[2] T. G. Knorr and R. W. Hoffman, Phys. Rev. **113**, 1039 (1959).
[3] D. O. Smith, J. Appl. Phys. **30**, 264S (1959).
[4] R. D. Heidenreich and F. W. Reynolds, in *Structure and Properties of Thin Films*, edited by C. A. Neugebauer, J. B. Newkirk, and D. A. Vermilyea (John Wiley & Sons, Inc., New York, 1959), p. 402.
[5] E. W. Pugh, J. Matisoo, D. Speliotis, and E. L. Boyd, J. Appl. Phys. **31**, 293S (1960).
[6] E. W. Pugh, E. L. Boyd, and J. F. Freedman, I.B.M. J. Research Develop. **4**, 163 (1960).
[7] M. S. Cohen, E. E. Huber, Jr., G. P. Weiss, and D. O. Smith, J. Appl. Phys. **31**, 291S (1960).
[8] D. O. Smith, E. E. Huber, Jr., M. S. Cohen, and G. P. Weiss, J. Appl. Phys. **31**, 295S (1960).
[9] The compositions given are always compositions in weight percent of the evaporation melt; the film composition is slightly different. See footnote reference 3.
[10] G. A. Bassett, J. W. Menter, and D. W. Pashley, in *Structure and Properties of Thin Films*, edited by C. A. Neugebauer, J. B. Newkirk, and D. A. Vermilyea (John Wiley & Sons, Inc., New York, 1959), p. 11.
[11] The beam direction is defined as the projection on the film of the vapor beam.

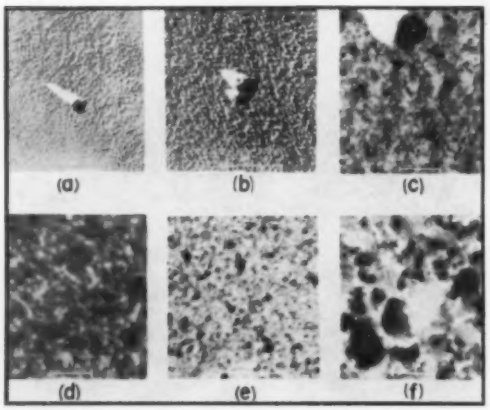

FIG. 1. Electron micrographs of 80% Ni, 20% Fe films deposited on thin carbon substrates. (a) 65° incidence angle, 200°C substrate temperature, 65 A thick; (b) 65° incidence angle, 200°C substrate temperature, 130 A thick; (c) 65° incidence angle, 200°C substrate temperature, 300 A thick; (d) 65° incidence angle, 200°C substrate temperature, 1100 A thick; (e) 0° incidence angle (normal incidence), 200°C substrate temperature, 130 A thick; (f) 70° incidence angle, 400°C substrate temperature, 270 A thick.

crystallites grow in the film they will leave vacant areas behind them. When the crystallites get large enough they will grow together and thus agglomerate into a two-dimensional array of chains whose long axis tends to be perpendicular to the beam direction. It is necessary to assume low mobility of the metal atoms on the substrate surface because otherwise metal atoms would diffuse into the shadowed regions. The presence, in the electron micrographs (Fig. 1), of sharp shadows cast by dirt particles and the observation that nickel films have an extremely high specific area[12] make this assumption plausible. This self-shadowing mechanism was first proposed by König and Helwig,[13] who observed similar geometric anisotropy in oblique-incidence films of Al, Pt, and tungsten oxide by electron microscopy.

A schematic illustration of self-shadowing can be constructed. It is reasonable to assume, because of surface tension, that in the early stages of film growth each crystallite maintains an approximately spherical shape as it grows. For a 60° incidence angle the growth of a crystallite which is behind another one will be strongly inhibited if the separation between the centers of the two is less than about two crystallite diameters. Self-shadowing under these assumptions is illustrated in Fig. 2. The coordinates of the points appearing in Fig. 2(a) were taken from a table of random numbers; these points represent the randomly distributed nuclei which appear in the initial stage of film growth. Growth inhibition in shadowed regions has been schematically illustrated in Figs. 2(b) and 2(c). The following rule was used: A nucleus of Fig. 2(a) was circled with a circle of diameter d only if the distance from the given nucleus to the next circled nucleus in the direction toward the evaporation source was greater than $2d$. The resemblance to the micrographs of oblique-incidence films in Fig. 1 is clear.

The spacing between crystallite chains has been observed to increase as the film thickness increases (Fig. 1). This result is consistent with the self-shadowing model since a higher crystallite chain should cast a longer shadow.

Oblique-incidence anisotropy decreases for high substrate temperatures; films made at a 500°C substrate temperature show little magnetic and optical anisotropy (see Sec. IV). Examination of electron micrographs of high-temperature films shows that the initial nucleation density is much smaller and the crystallite size is much larger [Fig. 1(f)] than in lower-temperature films. These effects are presumably caused by a decrease in the sticking probability at high temperatures and some sintering together of the crystallites. Sintering and decreased nucleation density should decrease the effect of self-shadowing thus causing a decrease in the density of aligned, elongated chains.

III. ANISOTROPIC RESISTIVITY

Another phenomenon interpretable in terms of crystallite chains is the anisotropic electrical resistivity found in oblique-incidence films. This effect was first reported by Maurain[14] in 1906 for sputtered films of Bi, Au, and Ni. It has been observed in this laboratory for Permalloy.[8] For films deposited at an incidence angle of 45°, the ratio of the resistivities which were measured parallel and perpendicular to the long axis of

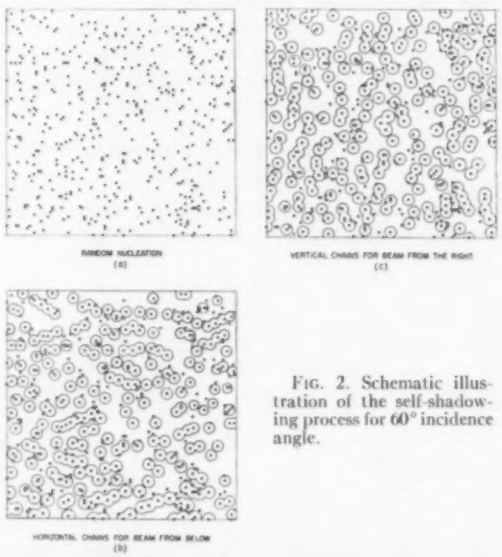

FIG. 2. Schematic illustration of the self-shadowing process for 60° incidence angle.

[12] O. Beeck, A. E. Smith, and A. Wheeler, Proc. Roy. Soc. (London) **A177**, 62 (1941).
[13] H. König and G. Helwig, Optik **6**, 111 (1950).
[14] C. Maurain, Compt. rend. **142**, 870 (1906).

the chains was approximately 0.5 for films about 30 A thick; for 200 A films the ratio was about 0.9. For films thicker than about 300 A, no difference in resistivity was detected; however, more accurate measurements recently made by Pugh *et al*[6] show a resistivity difference of several percent in films up to 1500 A thick. Such anisotropic resistivity would be expected in view of the better continuity along the long axis of the crystallite chains. As the film becomes thicker, however, the space between crystallite chains becomes filled and the resistivity becomes less dependent on the direction of measurement.

IV. OPTICAL ANISOTROPY

When polarized light is passed at normal incidence through an oblique-incidence film, the absorption and wave velocity are found to depend on the orientation of the electric vector of the incident light.[8] These effects are known as dichroism and birefringence, respectively. In the present work the dichroic properties of oblique-incidence films were studied without compensating for the phase shift caused by birefringence; the error thus caused was small. Birefringence and dichroism were first discovered in oblique-incidence sputtered films of Pt, Pd, Au, Ag, Fe, and Cu more than fifty years ago.[15–17] In this laboratory, oblique-incidence films of Permalloy, W, Al, Mg, and Ag were shown to exhibit dichroism.

It was found that polarized light of 5460 A wavelength suffers the greatest absorption on passage through an oblique-incidence film when the electric vector is parallel to the long axis of the crystallite chains. A useful characterization of the dichroism of a film is given by the ratio $E_\perp/E_\parallel$, where $E_\perp$ and $E_\parallel$ are the transmitted electric fields perpendicular and parallel to the long axis of the chains, respectively.

The ratio $E_\perp/E_\parallel$ was found by measuring the angular rotation ϕ of the electric vector caused by the passage of polarized light through the film [Fig. 3(a)]. To measure ϕ, the film was placed between two Glan-Thompson prisms of a polarimeter; by using a Nakamura half-shade to aid in recognizing extinction ϕ could be measured to within $\pm 0.05°$. When the film was rotated in its plane it was found that ϕ was a periodic function of θ with a period of 180° [Fig. 3(b)], where θ is the angle between the electric vector of the incident light and the long axis of the crystallite chains. The maximum value of ϕ, which will be denoted by δ, occurs when the angle between the electric vector and the long axis of the chains is 45°. Then by trigonometry

$$E_\perp/E_\parallel = (1+\tan\delta)/(1-\tan\delta). \tag{1}$$

If the customary exponential absorption law is assumed

$$E_\perp/E_\parallel = \exp[(\gamma_\parallel-\gamma_\perp)t] = e^{\Delta\gamma t} \tag{2}$$

where $\gamma_\perp$ and $\gamma_\parallel$ are the absorption coefficients for the two directions in question, and t is thickness of the film.

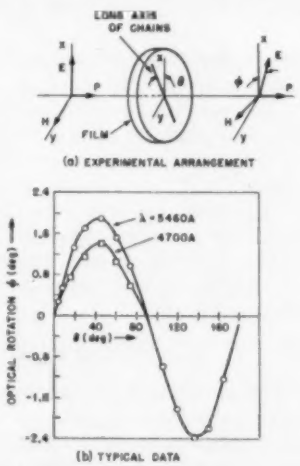

FIG. 3. (a) Schematic diagram of experimental arrangement for measuring dichroism. The Poynting vector of the light is denoted by P, θ is the angle of rotation of the film in its plane, and ϕ is the rotation of the electric vector suffered by the polarized light on passage through the film. (b) Typical data for light of wavelength 5460 A and 4700 A. Film characteristics: 85% Ni, 15% Fe, 45° incidence angle, 200°C substrate temperature, approximately 400 A thick.

A. Theory

The dependence of $\Delta\gamma$ on film thickness, incidence angle, and wavelength can be discussed qualitatively on the basis of crystallite chains represented by an aligned array of prolate ellipsoids. For light of intensity I_0 incident on an ellipsoid having a complex polarizability α, the intensity absorbed by the ellipsoid is $-(8\pi^2/\lambda)I_0\, Im\alpha$, where Im means the imaginary part of and λ is the wavelength of the light used.[18] If the light passes through a film of thickness t which contains ρ such ellipsoids/unit volume the intensity absorbed is $-\rho t[(8\pi^2/\lambda)I_0 Im\alpha]$. The transmitted intensity I is assumed to be related to the incident intensity by $I=I_0e^{-2\gamma t}$, where γ is the absorption coefficient for the electric field $\mathbf{E}$. Then by expanding the exponential one obtains

$$\gamma \approx (-4\pi^2\rho Im\alpha)/\lambda. \tag{3}$$

Now α depends on the complex index of refraction n of the metal and on the electric field in the ellipsoids; this internal field is in turn determined by the depolarization factor N parallel to the electric field. The dependence of α on n and N is given by[19]

$$\alpha = \frac{V(n^2-1)}{4\pi[N(n^2-1)+1]}, \tag{4}$$

where V is the volume of the ellipsoid. On using Eqs. 2–4,

$$\Delta\gamma = \gamma_\parallel-\gamma_\perp = \pi\rho V\, Im \times\left\{\frac{(n^2-1)}{\lambda[N_\perp(n^2-1)+1]}-\frac{(n^2-1)}{\lambda[N_\parallel(n^2-1)+1]}\right\}, \tag{5}$$

[15] A. Kundt, Ann. Physik **27**, 59 (1886).
[16] C. Bergholm, Ann. Physik **43**, 1 (1914).
[17] M. Cau, Ann. phys. **11**, 354 (1929).

[18] H. C. van de Hulst, *Light Scattering by Small Particles* (John Wiley & Sons, Inc., New York, 1957), p. 66.
[19] See footnote reference 18, p. 70.

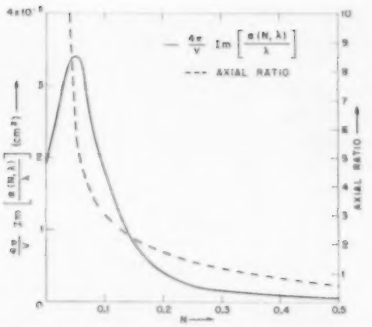

FIG. 4. The parameter $(4\pi Im\alpha)/(\lambda V)$ vs depolarization factor N for a wavelength of 5460 A. Axial ratio of an ellipsoid of revolution vs depolarization factor N.

where the subscripts $_{11}$ and $_{\perp}$ mean parallel and perpendicular to the long axis of the ellipsoids, respectively.

The parameter $Im((n^2-1)/\{\lambda[N(n^2-1)+1]\}) = 4\pi Im\alpha/\lambda V$ appearing in Eq. 5 is a surprisingly sensitive function of N and λ. In Figs. 4 and 5, $4\pi Im\alpha/\lambda V$ is plotted as a function of N and λ, respectively; the values of n for various wavelengths were obtained from Van de Hulst.[20] Two characteristics of $4\pi Im\alpha/\lambda V$ should be noted: The maximum value does not occur for $N=0$ (Fig. 4), and either an increase or decrease with wavelength is possible (Fig. 5). Both of these effects are caused by phase shifts introduced into the polarizability by lagging depolarizing fields.

From Fig. 1(a) or 1(b) it is seen that the axial ratio of oblique-incidence chains lies in the range from 3 to 10. For ellipsoids of revolution, the relation of the axial ratio to N_{11} (parallel to the axis of revolution) is shown in Fig. 4. The range in which N_{11} for chains lies is one for which $4\pi Im\alpha(N_{11},\lambda)/\lambda V$ changes rapidly with N_{11}. Similar considerations show that the absorption perpendicular to the chains will be small and insensitive to axial ratio. It is thus clear that one difficulty in making accurate theoretical predictions of $\Delta\gamma$ will be to specify N_{11} with sufficient accuracy.

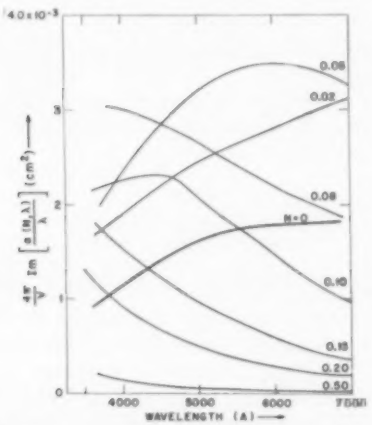

FIG. 5. The parameter $(4\pi Im\alpha)/(\lambda V)$ vs wavelength for various values of depolarizing factor N.

[20] See footnote reference 18, p. 273.

B. Experimental Results

Permalloy films were deposited on glass substrates in the same evaporation at the same incidence angle; different thicknesses were obtained by successively opening shutters covering the substrates. In Fig. 6, $\ln E_{\perp}/E_{11}$ is plotted against film thickness as measured by multiple-beam interferometry; the slope of this curve is the differential absorption coefficient $\Delta\gamma$. The data show that $\Delta\gamma$ increases with film thickness up to about 200 A; above 200 A $\Delta\gamma$ is independent of thickness. It is noted that the data are different for the two series presented in Fig. 6; the reason for this is not

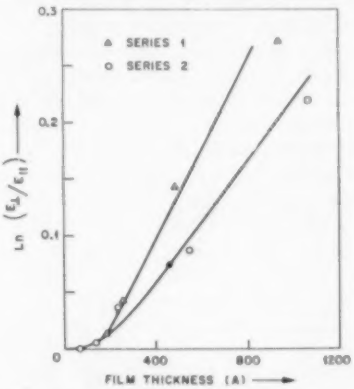

FIG. 6. $Ln\ E_{\perp}/E_{11}$ vs film thickness for Permalloy films deposited at 45° incidence angle and 200°C substrate temperature; all films in each series were deposited in the same evaporation. Series 1: 83% Ni, 17% Fe; Series 2: 80% Ni, 20% Fe.

known, but is not thought to be the difference in composition between the series.

The quantity $\Delta\gamma$ was also measured as a function of incidence angle for films of various thicknesses. In the reduction of the data it was assumed that $\Delta\gamma$ was independent of t, i.e., only films more than 400 A thick were studied. The data (Fig. 7) show a strong increase in $\Delta\gamma$ as the incidence angle increases.

The dispersion of $\Delta\gamma$ was studied by using color filters (Fig. 8); an increase of $\Delta\gamma$ with wavelength was always observed.

C. Discussion of Experimental Results

For a real film $\Delta\gamma$ will be a function of the following factors: the degree of alignment of the crystallite chains, interactions between the surface charges on different chains, and the shapes of the chains. In evaluating the last factor not only the axial ratios but also the possibility of wide deviations from ellipsoidal shape, e.g.,

protusions on the sides of the chains [see Fig. 1(b)] must be considered. Quantitative measure of the effects on $\Delta\gamma$ of the above factors could not be made.

The thickness dependence of $\Delta\gamma$ (Fig. 6) can partially be interpreted by the use of Eq. 5. For small t, before the nuclei have grown enough to touch, $\Delta\gamma$ will be zero; as t increases $\Delta\gamma$ will increase as adjacent nuclei grow together and cause the axial ratio to increase. It is not clear, however, how this process is modified so that $\Delta\gamma$ becomes independent of t for $t>300$ A.

The most important factor causing $\Delta\gamma$ to increase with incidence angle is thought to be improved chain alignment. As the incidence angle is increased, longer shadows will be cast by the crystallites and the lateral chain spacing will increase. Thus the lateral connection between growing chains will be reduced, which is equivalent to better chain alignment. By assuming no interaction between surface charges an upper bound

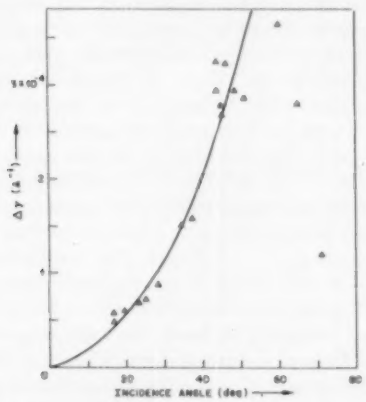

FIG. 7. Differential absorption constant $\Delta\gamma$ vs incidence angle for 83% Ni, 17% Fe films deposited at 200°C substrate temperature. All films were more than 400 A thick.

for $\Delta\gamma$, i.e., $\Delta\gamma$ for a 90° incidence angle, can be estimated. The film is assumed to be a single-layered array of contiguous, parallel ellipsoids of revolution. Each ellipsoid has a minor axis t equal to the film thickness and a major axis a such that the axial ratio a/t gives a value of N_{II} which leads to the maximum value of $4\pi\alpha_{\text{II}}/\lambda V$ (Fig. 4); for $\lambda=5460$ A this value of a/t is 8.5 and $4\pi\alpha_{\text{II}}/\lambda V=3.4\times10^{-3}$. Since $N_{\text{II}}+2N_{\perp}=1$, $N_{\perp}\approx0.5$, which leads to a negligible value of $4\pi\alpha_{\perp}/\lambda V$. From the assumed geometry the projected area of an ellipsoid on the substrate plane is $\pi at/4$, so the surface density of ellipsoids ρt is approximately $4/\pi at$. The volume of an ellipsoid is $\pi at^2/6$, so $\rho V=\frac{2}{3}$. By substituting these values in Eq. 5, one determines an upper bound for $\Delta\gamma$ of $7.4\times10^{-5}/A$.

The value of $\Delta\gamma$ for a 90° incidence angle, found by extrapolation of the curve in Fig. 7, is approximately 9×10^{-4}/A, an order of magnitude less than the estimated upper bound. Interactions between surface

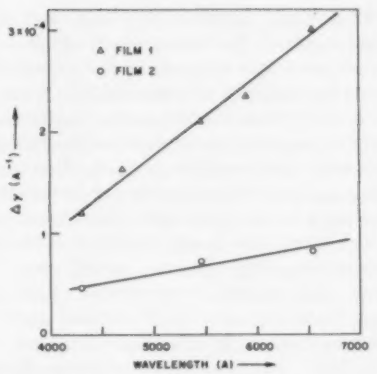

FIG. 8. Differential absorption constant $\Delta\gamma$ vs wavelength of light. Film 1: 83% Ni, 17% Fe, 45° incidence angle, 200°C substrate temperature, 520 A thick. Film 2: 83% Ni, 17% Fe, 25° incidence angle, 200°C substrate temperature, 510 A thick.

charges will decrease $\Delta\gamma$ by an amount which is related to the spacing between chains: For example a film in which there were no space between chains, i.e., a film having bulk density, would have a zero $\Delta\gamma$. Since in the films studied the crystallite chains are closely spaced (Fig. 1) the decrease in $\Delta\gamma$ from the value for noninteracting ellipsoids can be expected to be quite large; although no theoretical estimate has been attempted it is probable that the major part of the experimental deviation from the estimated upper bound of $\Delta\gamma$ is caused by surface-charge interaction. Deviations from perfect alignment and deviations from ellipsoidal shape will also tend to decrease $\Delta\gamma$.[20a]

The dispersion of $\Delta\gamma$ is caused by the explicit $1/\lambda$ dependence (Eq. 5) and the dispersion of n. It is evident from Fig. 5 that small changes in axial ratio causing small changes in $N_{\perp}$ and N_{II} lead to widely different types of dispersion. Since it is difficult to estimate $N_{\perp}$ and N_{II} precisely, calculations from Eq. 5 cannot be compared with experiment (Fig. 8). It should be noted that theoretically, for certain values of N, $\Delta\gamma$ could decrease with wavelength and become negative, i.e., $\gamma_{\perp}>\gamma_{\text{II}}$. Extrapolation of the curves in Fig. 8 shows that such an inversion of $\Delta\gamma$ should occur at wavelengths between 2000 and 3000 A.

V. MAGNETIC ANISOTROPY

Magnetic anisotropy can be induced in evaporated Permalloy films by the application of a magnetic field during deposition at normal incidence, or by evaporation at oblique incidence in no field. In either case the resultant anisotropy can be described by an energy $E_k=K\sin^2\theta$, where θ is the angle between the magnet-

[20a] *Note added in proof.*—The experimental points for $\Delta\gamma$ at incidence angles greater than 60° (Fig. 7) which appear to be anomalously low and through which no curve was drawn, have been shown to be real and represent the onset of an additional mechanism in film growth. A detailed account will be published later.

ization **M** and the magnetic easy axis, and K is the anisotropy constant. The anisotropy field[21] $H_k = 2K/\mathbf{M}$, which is a convenient measure of the anisotropy, was determined by means of a hysteresis-loop tracer.[22]

When a film is deposited at normal incidence in the absence of a magnetic field a magnetic anisotropy is still developed. However, the easy-axis direction is not predictable although H_k values are obtained which are about the same as those for normal-incidence films deposited in a field. This result implies that the applied field merely defines the direction of **M**, which in turn determines the magnetic anisotropy. Field-induced anisotropy is thus actually an **M**-induced anisotropy.[22] Now the direction of **M** in oblique-incidence films is defined by the crystallite chains so that an **M**-induced anisotropy should exist even in the absence of an applied field. It thus becomes necessary, in studying oblique-incidence films, to distinguish between the **M**-induced and the oblique-incidence components of the total magnetic anisotropy.

One method of experimentally eliminating **M**-induced anisotropy is to apply a rotating field during deposition such that **M** rotates in the plane of the film.[3] However, in the present work incidence angles greater than 15° were used; under these conditions the oblique-incidence H_k is so much larger than the **M**-induced H_k that the latter may be disregarded, if it is assumed that no enhancement of **M**-induced anisotropy occurs at high incidence angles.

Various manifestations of oblique-incidence magnetic anisotropy and their connection with the observed crystallite chains will be considered below.

A. H_k for Nonmagnetostrictive Permalloy

For nonmagnetostrictive (83-17) Permalloy films the easy axis for oblique-incidence films is perpendicular to the beam direction, i.e., parallel to the crystallite chains of Fig. 1. The anisotropy field H_k as a function of incidence angle is shown in Fig. 9. Instrumental limitations of the hysteresis-loop tracer did not permit measurement of H_k for incidence angles greater than 65°; these limitations also prevented measurement of H_k as a function of thickness. These data can be interpreted by assuming that the magnetic anisotropy is caused by the shape anisotropy of the oriented chains. The increase of H_k with incidence angle is assumed to be caused by improved chain alignment, in analogy with the assumption regarding $\Delta\gamma$ (Sec. IV).

An estimate of an upper bound for H_k (i.e., H_k for a 90° incidence angle) may be obtained which is analogous to that made for the maximum $\Delta\gamma$ (Sec. IV). For perfectly aligned, noninteracting ellipsoids of revolution, $H_k \approx \Delta N 4\pi \mathbf{M}$, where $\Delta N = N_\perp - N_\parallel$; for infinitely long cylinders, ΔN is 0.5 so H_k will be about 5000 oe. From Fig. 9 extrapolation of H_k to 90° incidence gives a value of approximately 600 oe; thus the maximum experimental H_k is an order of magnitude less than the calculated upper bound. A similar situation with respect to $\Delta\gamma$ has been encountered; since $\Delta\gamma$ and H_k both originate in anisotropic internal fields due to surface charges, this correspondence is understandable. Interactions between chains can be expected to be a major factor in reducing H_k from the estimated maximum, as was the case for $\Delta\gamma$. Misalignment and wide deviation from ellipsoidal shape will also reduce H_k.

B. Magnetic Replication

A clear demonstration of the presence of microscopic geometric anisotropy in nonmagnetic metals is given by a series of "magnetic replication" experiments.[7] In these experiments 83-17 Permalloy was deposited at normal incidence on films of aluminum, gold, silver, or platinum which had been previously deposited at oblique incidence. The Permalloy films showed magnetic anisotropy with the easy axis perpendicular to the nonmagnetic metal beam direction, i.e., the anisotropy of the underlayer was transmitted to the Permalloy.

This result may be interpreted by assuming that the oblique-incidence underlayer contains oriented chains similar to those seen in Fig. 1; the normal-incidence Permalloy overlayer fills in the region between chains thus replicating the structure of the underlayer and becoming anisotropic in much the same way as if deposited at oblique incidence itself. When a sufficiently thick intermediate layer of nonmagnetic metal (several hundred angstroms for aluminum) was evaporated at normal incidence on the oblique-incidence base film, and Permalloy was then evaporated at normal incidence on this composite film, the correlation of the magnetic

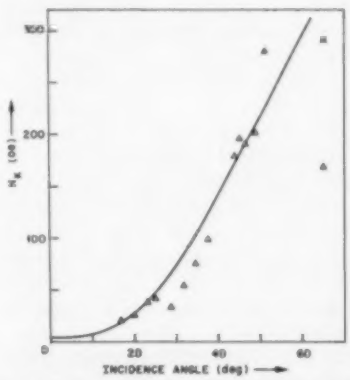

FIG. 9. Anisotropy field H_k vs incidence angle for 83% Ni, 17% Fe films deposited at 200°C substrate temperature. Film thicknesses were approximately 400 A.

[21] D. O. Smith, J. Appl. Phys. **29**, 264 (1958).

[22] E. C. Crittenden, Jr., A. A. Hudimac, and R. I. Strough, Rev. Sci. Instr. **22**, 872 (1951); D. O. Smith, *Proceedings of the Conference on Magnetism and Magnetic Materials, Boston, October, 1956* (American Institute of Electrical Engineers, New York, 1957), AIEE Spec. Publ. T-91, p. 625.

[23] W. Andrä, Z. Málek, W. Schüppel, and O. Stemme, J. Appl. Phys. **31**, 442 (1960).

easy-axis direction with the oblique-incidence nonmagnetic beam direction was lost.

C. Resonance Studies

Oblique-incidence Permalloy films have been studied by ferromagnetic resonance.[5,21] The linewidth for normal-incidence films is not a function of the film orientation; the resonance linewidth for oblique-incidence films is approximately 20% greater when the easy axis is perpendicular to the dc field than when it is parallel to the dc field.

This latter result can be interpreted by noting that because of demagnetizing effects more spatial dispersion in the direction of **M** should occur when **M** is perpendicular to the long axis of the crystallite chains than when it is parallel to them; thus different effective fields exist in different regions of the film. A broader line will therefore be expected in the former case since different spins go through resonance over a wider range of applied field. Any crystallite shape anisotropy that may be present in normal-incidence films is evidently too small to cause an observable linewidth anisotropy. The results of a more extended investigation will be published later.

D. Compositional Dependence of H_k

The dependence of H_k on composition for films deposited at a 45°-incidence angle is shown in Fig. 10. Positive values of H_k indicate an easy axis perpendicular to the beam; negative values indicate an easy axis parallel to the beam. The wide variation in H_k values shown is caused by instrumental limitations, and by the fact that films prepared under presumably identical conditions had widely different H_k values. The curve in Fig. 10 should therefore be considered only as an indication of the general trend of H_k as a function of composition. A striking feature of the data is the change in the easy-axis direction at a composition of approximately 90% Ni. More extensive compositional data have been presented by Pugh *et al.*[6]

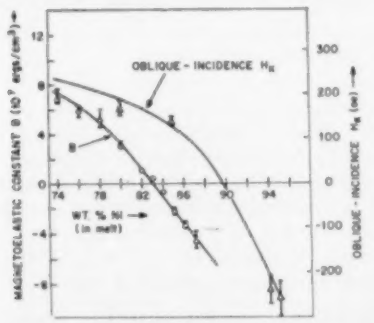

FIG. 10. Anisotropy field H_k vs composition. Film characteristics: 45°-incidence angle, 200°C substrate temperature, approximately 700 A film thickness. Magnetoelastic-coupling constant B vs composition, found for normal-incidence films.

The compositional dependence of H_k cannot be interpreted solely by consideration of the shape anisotropy of chains. Indication of an additional mechanism, as reported by Smith *et al.*,[5] is furnished by the change in sign at 83% Ni of the magnetoelastic coupling constant B, defined as dK/de where e is linear strain[24] (Fig. 10). In particular, assume the chains are in tension parallel to their long axis. Upon considering magnetoelasticity alone, anisotropy will thus be induced with the easy axis parallel to the long axis of the chains for positive B, and perpendicular to it for negative B. A zero value of H_k occurs for a composition of 90-10 (Fig. 10) because at this point the shape and magnetoelastic-anisotropy contributions are equal and opposite in sign.

If anisotropic strain of the type described above is present, relief of this strain should cause predictable changes in H_k, namely $\Delta H_k > 0$ for $B < 0$ and vice versa. Some degree of strain relief should be achieved by stripping the film from the substrate. Removal of a Permalloy film from glass is very difficult but it was found that films deposited on an intermediate layer of Victawet[25] dry-strip easily with pressure-sensitive tape.[26]

That the stripping process does not change the crystallite chain configuration, but only the state of strain in the film, was shown by measuring the dichroic properties of a film before and after stripping. The film was stripped from its Victawet-glass substrate by floating it on the surface of water[26]; it was then placed on a glass support. Although the value of H_k changed markedly on stripping the dichroism was unchanged, showing that stripping had not affected the crystallite chain configuration.

Using the stripping technique several films deposited at an incidence angle of 45° were studied; representative results are shown in Table I. The Victawet forms a weak link between the Permalloy and the glass as is shown by the ease with which films may be stripped from glass covered with Victawet. Any strain can thus be partially removed by slippage on one or both of the interfaces. Consequently, for some 95-5 films the strain is so low that positive values of H_k are observed, i.e., the crystallite chain anisotropy dominates the magnetoelastic anisotropy; for other films of the same composition the stress is higher and negative values of H_k are observed. For all compositions a ΔH_k after stripping is observed which corresponds to decreased tension along the crystallite chains. For some 95-5 films the easy-axis direction can even change from perpendicular to parallel to the long axes of the chains upon stripping.

The magnitude of the anisotropic tension can be estimated from the above results. Since $B = dK/de$, then $\Delta e = \Delta K/B = M\Delta H_k/2B$. Extrapolation of B to a composition of 95-5 (Fig. 10) gives a value of about

[24] C. Kittel, Revs. Modern Phys. 21, 541 (1949).
[25] Victor Chemical Works, Chicago, Illinois.
[26] C. Hall, *Introduction to Electron Microscopy* (McGraw-Hill Book Company, Inc., New York, 1953).

TABLE I. Changes in H_k caused by stripping Permalloy films from their substrates.

Composition % Ni-% Fe	Before stripping H_k(oe)	After stripping H_k(oe)	ΔH_k(oe)
95-5	−30	130	160
95-5	90	130	40
85-15	87	95	8
83-17	200	200	0
75-25	210	170	−40

$6\times10^{+7}$ ergs/cm³. Taking $M\approx10^3$ oe and $\Delta H_k\approx100$ oe (Table I) gives a value of $\Delta e\approx10^{-3}$.

Another method of measuring strain in thin films is to study the bending of thin glass substrates. The curvature is conveniently determined by observing optical interference fringes in a Newton's rings experiment.[27,28] Any departure from circularity of the rings indicates that the strain is anisotropic. Finegan and Hoffman[27] have found, using this technique, the presence of anisotropic strain in oblique-incidence iron films; the strain they reported is consistent in magnitude and direction with the present results. It should be noted, however, that in this laboratory difficulties were encountered in obtaining consistent results for anisotropic strain using the delicate Newton's rings technique[7]; the difficulties were probably caused by random anisotropies in the elastic properties of the glass substrates used. The stripping experiments discussed in the foregoing, however, have always yielded consistent results.

An explanation of the anisotropic strain in terms of surface tension is proposed: The surface energy of a chain could be reduced if the material in the chain flowed into a spherical shape. One of the factors which inhibits this flow is the bonding of the crystallites to the substrate. The final state of strain will be achieved when a balance is reached between the tendency of surface energy to make the chain into a sphere and the opposing tendency of the substrate bonds to keep the chain extended.

The magnitudes of the energies involved can be estimated. Consider two crystallite spheres in contact, each of radius r_1; if there were no inhibitory forces they would coalesce to form a sphere radius of r_2. Then $r_2=2^{\frac{1}{3}}r_1$ and the decrease in surface energy caused by the coalescence is $(2-2^{\frac{2}{3}})\approx\frac{1}{2}$ times the surface energy of one of the smaller spheres. If E_γ is the surface energy, for a metal sphere with a radius of 100 A,

$$E_\gamma=4\pi r_1^2\gamma\approx10^{-8}\text{ ergs},\qquad(3)$$

where γ (about 10^3 ergs/cm²) is the specific surface energy.[29] Thus an energy of 5×10^{-9} ergs is available for conversion to anisotropic strain energy.

The anisotropic strain energy E_σ actually present is

$$E_\sigma=2(\tfrac{1}{3}\pi r_1^3)\tfrac{1}{2}Ye^2\approx8\times10^{-12}\text{ ergs},\qquad(4)$$

where Y (about 2×10^{12} d/cm²) is Young's modulus, and the strain e is taken as 10^{-3} from the stripping experiment. Thus only about one part in 10^3 of the available surface energy would have to be converted into strain energy to account for the observed anisotropic strain. The specific mechanisms involved in this energy conversion have not yet been determined.

Although no explanation of the origin of anisotropic strain in thin films has been offered until now, several authors have given explanations of the origin of isotropic strain, whose existence in normal-incidence films is well established.[20–22] It is clear that surface tension acting between isotropically distributed crystallites will operate in the same manner as described above but will now result in a state of average isotropic tension. It is possible that this mechanism is the cause of isotropic tension in evaporated and electrodeposited films.

[27] E. E. Huber, Jr., and D. O. Smith, J. Appl. Phys. **30**, 267S (1959).
[28] J. D. Finegan and R. W. Hoffman, J. Appl. Phys. **30**, 597 (1959).
[29] C. Herring, *The Physics of Powder Metallurgy*, edited by W. E. Kingston (McGraw-Hill Book Company, Inc., New York, 1951), p. 143.
[20] H. P. Murbach and H. Wilman, Proc. Phys. Soc. (London) **B66**, 905 (1953).
[21] H. S. Story and R. W. Hoffman, Proc. Phys. Soc. (London) **B70**, 950 (1957).
[22] T. B. Rymer, Proc. Roy. Soc. (London) **A235**, 274 (1956).

Ordering in the Intermediate Phases TiFe, TiCo, and TiNi*

PAUL PIETROKOWSKY AND FRANK G. YOUNGKIN
University of California, Los Angeles 24, California

(Received May 31, 1960)

The intermediate phases TiFe, TiCo, and TiNi have been investigated by x-ray powder diffraction techniques. The atomic arrangements of these ensembles have been determined to be of the cesium chloride, B2 type. Monochromatic x radiation was utilized in the investigation.

THE determination of long-range order in a motif of matter which is periodic in real space requires that the distribution of electron density within the unit cell be established. When the techniques of x-ray diffraction are used for this purpose one may encounter difficulties in such an endeavor if the chemical species of atoms which reside within the unit cell possess atomic numbers which are not greatly different from one another. This is a consequence of the fact that the atomic scattering factors for x radiation, which depend on the atomic number, are well-behaved functions except when the incident radiation is of an energy which is of the order of magnitude of an absorption edge of a given class of electrons.

This may be the situation with which we are confronted in a crystal structure determination even for the case of relatively small unit cells in which symmetry considerations restrict the atoms to special space group positions. For example, this problem may arise when one attempts to ascertain if an alloy of equiatomic proportions is of the wolfram, A2 type, crystal structure or of the cesium chloride, B2 type, arrangement of atoms. In essence this is the problem of establishing if the atomic motif is to be represented by a random distribution of the entire population of atoms at corners and body centers of a cubic space lattice or if the individual species display a preference for equivalent crystallographic sites.

In an early investigation of the binary alloys of titanium and transition elements of the first long period by Laves and Wallbaum[1] the intermediate phases TiFe, TiCo, and TiNi were reported to be cesium chloride type crystal structures. This communication was very brief and did not contain x-ray diffraction data. In view of the relatively small difference in atomic number one may raise a question as to whether these alloys indeed represent A2 or B2 type ensembles of atoms. This point is important in several respects: first, it is essential to an understanding of the phase equilibria which exist in the respective binary constitution diagrams, and second it is of theoretical importance in formulation of the principles which underlie the theory of alloying. The reasons which have been enumerated were the motivations for several subsequent investigations,[2,3] neither of which was able to confirm or dispute the original observation that TiFe, TiCo, and TiNi are ordered phases. The present investigation has definitely established these intermediate phases to be of the cesium chloride type crystal structure by the application of x-ray powder diffraction experiments. The experimental apparatus which was used to solve this problem may be of interest to the reader since its utility is not limited to the simple case of ordering described in this paper. Therefore we shall describe the x-ray powder diffraction experiment in detail and discuss its utility with respect to the usual experimental methods.

DISCUSSION

If we assume that the monochromated x-ray beam consists of a bundle of parallel rays, a condition which we may approach in experiment by limiting the divergence of the primary beam with slits, then the expression for the intensity of a segment of a powder diffraction halo can be written

$$I(hkl) = \text{const}\, L(\theta) P(\theta,\theta_M) F(hkl) F(hkl)^* p \lambda^3 A(\mu r,\theta) D, \quad (1)$$

in which

$I(hkl)$ = Calculated intensity from (hkl) planes
$L(\theta)$ = Lorentz factor
$P(\theta,\theta_M)$ = A polarization factor
$F(hkl)$ = Structure factor
p = Multiplicity
$A(\mu r,\theta)$ = Absorption factor
D = Temperature factor
λ = Wavelength of radiation.

The absorption factor $A(\mu r,\theta)$ which we have employed is that given in the International Tables.[4] These data represent calculations for the case of cylindrical powder rods, of characteristic parameter μr, which are illuminated by a parallel beam of x rays. In practice the divergence of the primary beam was never more than one degree in the plane of the spectrometer. The reason for this can be seen in Fig. 1. We permit only enough

* This investigation is a part of a thesis by one of the authors (P. P.) which was submitted in partial fulfillment of the requirements for the degree of Doctor of Philosophy at the California Institute of Technology.

[1] F. Laves, Naturwissenschaften **27**, 674 (1939).

[2] P. Duwez and J. L. Taylor, Trans. AIME, **188**, 1173 (1950).

[3] T. V. Philip and P. A. Beck, Trans. AIME, **209**, 1269 (1957).

[4] International Tables for Crystal Structure Determination (Gebruder Borntraeger, Berlin, 1935), Vol. II.

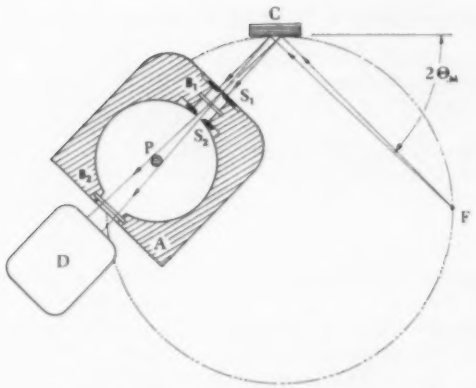

FIG. 1. Geometry of the diffraction experiment.

divergence so that the powder rod at P sees the entire beam.

Let us now consider how the wavelength of the incident radiation influences the intensity of a given diffraction halo. We shall first turn our attention to the structure factor which is comprised of a summation of terms, each of which consists of an atomic scattering factor and a geometrical form factor. It is the former which are influenced by the energy of the incident radiation, the magnitudes of these effects being especially pronounced when the frequency of the incident radiation is in the neighborhood of the absorption edge of a given class of electrons within the matter. The atomic scattering factor, corrected for dispersion due to K electrons, can be written in the notation used by Hönl[5]:

$$f=f_0+\Delta f_k'+i\Delta f''_k. \tag{2}$$

In this expression f_0 is the atomic scattering factor as obtained from a particular model of the atom, $\Delta f_k'$ and $\Delta f_k''$ being the real and imaginary corrections to f_0 which result from the anomalous dispersion by the K electrons. The quantative manner in which these effects influence the intensity expression depends on the geometrical form factors which describe the positions of the various atoms. Therefore, it is necessary to write the structure factor expression for the cesium chloride type crystal structure for a complex scattering factor. We turn our attention to binary alloys of elements in the first long period of the periodic table, consider those chemical species M for which the atomic number Z_M is greater than Z_{Ti}, and write the structure factor expression. One observes that a statistical distribution of atoms amongst all crystallographic sites will yield a nonvanishing structure factor only when the sum of the Miller indices is even, its magnitude is equal to the sum of the atomic scattering factors

$$F(hkl)_{(e)}=f_M+f_{\mathrm{Ti}}. \tag{3}$$

Should the individual species of atoms display a preference for equivalent sites within the unit cells we then observe that a similar structure factor will arise when $h+k+l=2n$, where $n=1, 2, \ldots$; however, if $h+k+l=2n+1$ we note that

$$F(hkl)_{(0)}=f_M-f_{\mathrm{Ti}}. \tag{4}$$

Thus the existence of complete order may be substantiated by observing relatively weak diffraction maxima whose intensities are proportional to $F(hkl)_{(0)}F(hkl)_{(0)}$.*

$$F(hkl)_{(0)}F(hkl)_{(0)}{}^*=[(f_0+\Delta f_k')_M-(f_0+\Delta f_k')_{\mathrm{Ti}}]^2 +[(\Delta f_k'')_M-(\Delta f_k'')_{\mathrm{Ti}}]^2. \tag{5}$$

The extent to which one may utilize anomalous dispersion to increase $F_{(0)}F_{(0)}{}^*$ depends on the atomic numbers, Z_M and Z_{Ti}, of the elements which act as scattering centers and the wavelength of incident radiation. For the atomic arrangement which we are considering this effect is pronounced if (Z_M-Z_{Ti}) is of the order of one to three electrons and the x-ray wavelength is properly selected so as to lie between the critical absorption edges of the elements M and Ti, for a specific class of electrons. Thus, if the frequency of the incident radiation is less than that of the absorption edge, the atomic scattering factor is a real quantity, whereas for the case in which the frequency of the radiation is greater than that of the edge, it is a complex quantity. It is these considerations which one utilizes in attempting to maximize Eq. (5) with respect to λ.

Let us now consider how large Z_M-Z_{Ti} must be before the ordinary powder diffraction techniques may be used to detect weak maxima or at least the reflection from the (100) plane. The arrangement which we consider is the usual Debye-Scherrer powder camera, in which air scattering occurs and the incident beam contains Bremsstrahlung in addition to characteristic radiation. If ΔZ is approximately eight, which means that $M=\mathrm{Zn}$, then it is possible to detect $F(hkl)_{(0)}$ maxima until the splitting of the $K\alpha_1$, $K\alpha_2$ doublet occurs. For example, weak diffraction maxima have been observed in x-ray patterns of $TiZn_2$[6] made with filtered radiation from a copper-anode tube.

Thus when the difference in atomic numbers is of the order of three to seven electrons we may experience difficulty, from the experimental point of view, in obtaining diffraction data which prove the existence of the cesium chloride type crystal structure. One might improve this situation to some extent by reducing the background intensity through the introduction of a crystal monochromator and in addition by evacuating the diffraction chamber. This was, in fact, accomplished in the present investigation. With such a diffraction geometry it is then possible to attempt to increase $L(\theta)P(\theta,\theta_M)$, which is a monatomic function of the Bragg angle, by decreasing the wavelength of the incident radiation. At first glance the λ^3 term in Eq. (1) appears

[5] H. Hönl, Ann. Physik **18**, 625 (1933).

[6] P. Pietrokowsky, Trans. AIME **200**, 219 (1954).

to offer an impediment, but this may be averted by increasing the exposure time for the diffraction experiment if the various sources of parasitic scattering are removed. Among the advantages to be gained by a substantial decrease in λ will be a favorable change in the absorption factor $A(\mu r,\theta)$, since μ is a function of wavelength, and a decrease in the film background intensity since there may be less fluorescence from excitation of the specimen by the incident radiation.

Thus the experimental apparatus was designed in such a manner so as to take advantage of the fact that one could gain a factor of approximately three in the Lorentz and polarization contributions to the intensity expression.

Diffraction Experiment

The experimental apparatus was comprised of a commercial spectrometer, based on the Bragg-Brentano focusing principle,[7,8] and a specially constructed 72.0-mm diffraction chamber which was deployed in the manner shown schematically in Fig. 1. The focus of the x-ray tube, which is viewed as a line source, is normal to the plane of the focusing circle and parallel to the powder rod specimen at the center of the diffraction chamber. The primary beam was limited to one degree of divergence in the plane of the focusing circle, vertical divergence of the primary beam being limited by a Soller slit which was part of the spectrometer. This may be seen adjacent to the x-ray tube in Fig. 2. In some experiments the vertical divergence of the monochromated primary beam was restricted by a set of horizontal slits on the outside of the diffraction chamber; these were placed in the plane of the vertical slits S_1 but are not displayed in the photographs for reasons of clarity. Flat plate monochromator crystals were placed on the periphery of the focusing circle at C, the position in the spectrometer which is normally occupied by a powder block specimen. Diffracting planes of the monochromator were oriented parallel to the ground surface. A lithium fluoride plate was used to obtain molybdenum $K\alpha$ radiation, diffraction occurring from the (200); and the $(10\bar{1}1)$ planes of quartz were used to select characteristic copper $K\alpha$.

The diffraction experiment is shown in Fig. 2. Air scattering of the incident beam was reduced by evacuating the diffraction chamber during the exposure; a vacuum of at least 25 μ was maintained. The monochromated incident radiation was granted passage to the detector, D, by two Mylar windows, B_1 and B_2, which were backed with black paper and sealed to the chamber with O-rings. Rotation of the powder rod specimen was achieved with an external electric motor, the drive shaft passing through a double O-ring seal in the body of the diffraction camera. Two pairs of adjustable slits, S_1 and S_2, were used to reduce the parasitic scattering of the monochromator crystal.

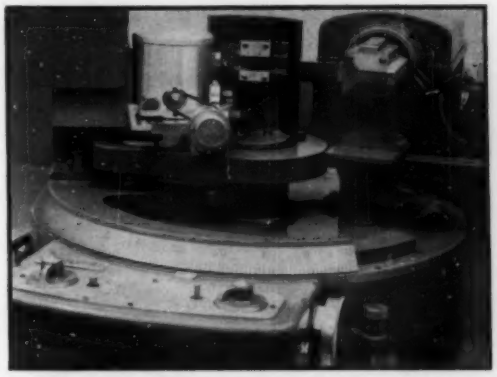

FIG. 2. The x-ray diffraction experiment. Relationship of diffraction chamber to the spectrometer.

Alignment of the Apparatus

In the alignment procedure both proportional counter and photographic techniques were used. With the diffraction chamber removed, both Soller slits in place, a monochromator crystal is selected and adjusted. The detector may be used to establish $2\theta_M$ as well as to determine when the power in the monochromated beam has been maximized. This step can be accomplished very readily even though one must choose from a large number of crystals which may require varying amounts of surface preparation prior to use. The Soller slit which is adjacent to the detector is then removed and the diffraction camera base plate, is located with respect to the spectrometer by the two pins which are an integral part of the commercial instrument. With the base plate screwed securely to the spectrometer, the diffraction chamber is placed into position on the three-point instrument mounting and may be leveled by movement of the cone-end adjusting screws so that its axis will be normal to the plane of the spectrometer. The axis of the camera is then made to coincide with the incident beam. A wolfram wire specimen is centered in the camera with a low-power telescope. The position of the specimen relative to the monochromated beam is then determined by photographic methods. Coincidence of the x-ray beam and specimen is possible since the diffraction chamber possesses a translational degree of freedom by virtue of the two opposed adjusting set screws. The alignment procedure may be performed rapidly if a darkroom is nearby; the camera may be removed from the spectrometer then loaded with a test film and returned, accurately positioned, for further adjustment or for a diffraction experiment with the specimen mounted in place of the test wire. Once the diffraction chamber has been aligned for a specific monochromator crystal it has been the authors experience that further adjustment is not required.

[7] W. H. Bragg, Proc. Roy. Soc. (London) **33**, 222 (1921).
[8] J. C. M. Brentano, Proc. Phys. Soc. (London) **B37**, 184 (1925).

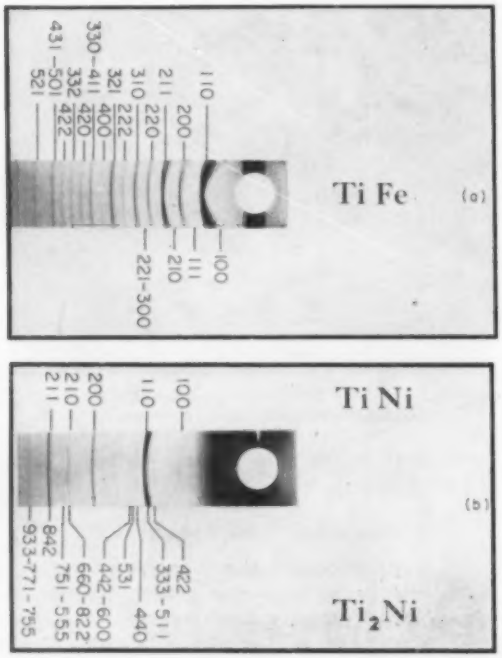

FIG. 3. (a) Powder diffraction photographs. Spectrum of TiFe made with Mo K, 120 hr, 20 ma. (b) Spectrum of TiNi made with Cu K, 72 hr, 15 ma.

Results

Evidence for the cesium chloride type crystal structure in TiFe is given in Fig. 3(a) which is a powder diffraction pattern made with molybdenum $K\alpha$ radiation. The exposure time was 120 hr and a space current of 20 ma was used. Four weak maxima were observed. Calculated intensities are presented in Table I, these were computed with the simplified expression

$$I(hkl) = \text{const}\, P(\theta,\theta_M) L(\theta) F(hkl) F(hkl)^* p A(\mu r,\theta). \quad (6)$$

The values of $A(\mu r,\theta)$ which were used correspond to $\mu r = 2.2$ for the powder rod specimen irradiated with Mo

TABLE I. X-ray powder diffraction data for TiFe made with a 72.00 mm camera. Exposure time 120 hours. Monochromated Mo $K\alpha$ radiation, 20 ma.

	$\sin^2\theta$		Relative Intensity[a]	
hkl	obs	calc	I_{obs}	I_{calc}
100α	0.0133	0.0142	W	365
110α	0.0273	0.0284	VS	22769
111α	0.0421	0.0426	VW	86
200α	0.0578	0.0568	MS	4262
210α	0.0706	0.0710	VW	138
211α	0.0852	0.0852	S	9458
220α	0.1144	0.1136	M	2999
300α	0.1280	0.1278	VW	18
221α				73
$310\alpha_1$	0.1424	0.1420	M	2730
$311\alpha_1$		0.1562	A	38

[a] Observed intensities are recorded in the following nomenclature: VS, very strong; S, strong; MS, medium strong; M, medium; WM, weak medium; W, weak; VW, very weak; and A indicated no reflection observed.

$K\alpha$. A similar diffraction photograph was obtained for TiCo, four weak reflections being recorded. To obtain evidence for TiNi the spectrometer was adjusted to receive monochromated Cu $K\alpha$ from a quartz plate. One of the resulting photographs, Fig. 3(b) represents an exposure time of 72 hr and space current of 15 ma. The resulting diffraction maxima indicated that two equilibrium phases were present, TiNi and Ti_2Ni. This observation is in agreement with the metallography since none of the homogenized ingots used for powder specimens were entirely one phase. Indexing of the Ti_2Ni spectrum is taken from footnote reference 2. We observe that the (100) of TiNi is very definitely present and that the (210) of TiNi, which could be present even if the (111) were not observed, is at a Bragg angle which permits superposition with the (660) and (822) reflections of Ti_2Ni. Although we have observed only one diffraction maxima which may be associated unequivocally with long range order in TiNi this evidence is strong since neither of the adjacent phases, Ti_2Ni and $TiNi_3$, in the constitution diagram produce constructive interference which is recorded at the same Bragg angle as the (100) of TiNi. Thus we have demonstrated, by x-ray powder diffraction experiments, that TiFe, TiCo, and TiNi are cesium chloride B2 type crystal structures.

On a Complex Recrystallization Texture in 3% Silicon Iron

C. G. DUNN
General Electric Research Laboratory, Schenectady, New York

AND

C. J. MCHARGUE
*Metallurgy Division, Oak Ridge National Laboratory, Oak Ridge, Tennessee**

(Received April 29, 1960)

Components in a complex primary recrystallization texture, which is a matrix texture for secondary recrystallization to the Goss texture in 3% silicon-iron strip, have been determined by the axis-chart method of Jetter, McHargue, and Williams. The results obtained are compared with former pole-figure results and found to include components not previously resolved or noted. It is found also that the components of the texture explain reasonably well the observed magnetic torque curve of the material.

INTRODUCTION

A MULTICOMPONENT recrystallization texture, which is a matrix texture for secondary recrystallization to the Goss texture in commercial iron-silicon alloys, has been investigated and discussed recently.[1] The pole-figure data obtained were interpreted as giving only a partial description of the texture, because the results failed to account for the observed magnetic anisotropy in the material. Koh and Dunn suggested that additional information possibly could be obtained on this complex recrystallization texture by the Jetter-McHargue-Williams method of texture analysis.[2] This method has now been used and the information found is given in the present paper.

Knowledge of the present primary recrystallization texture, or one with similar properties, is important because such a texture may influence the secondary recrystallization texture and thus the magnetic properties of the annealed silicon iron. An appropriate secondary recrystallization anneal should develop a strong Goss or (110)[001] texture with its associated directional magnetic properties. The primary recrystallization material also has directional magnetic properties, but much weaker. A satisfactory description of the texture should account for the observed magnetic anisotropy.[1,3] Also, a better description undoubtedly would help clarify the obscure nature of the observed growth selectivity,[1] i.e., the dependence of rate of growth of secondary recrystallization grains on orientation.

EXPERIMENTAL PROCEDURE

Pieces of 0.014-in. thick silicon-iron strip, which had been decarburized in a 3-min anneal at 800°C (see footnote references 1 and 3 for a more complete description of the initial material) were descaled chemically and then bonded together with an adhesive to make a laminated structure. A spherical diffraction specimen 0.200 in. in diameter was machined from the laminated structure. Highly strained surface layers of the spherical specimen were removed chemically.

Filtered Mo-K_α radiation was used with each of the following kinds of diffracting planes: 110, 200, 112, 130, 222, 123, and 240. The specimen was rotated rapidly about the normal direction ND, the rolling direction RD, or the transverse direction TD, while being scanned slowly through an angle ϕ that varied from 0–90°. The chart recordings obtained were corrected for background radiation and then analyzed as described elsewhere[2] to give axis-distribution charts, i.e., axis-density figures.

RESULTS AND DISCUSSION

The axis-density figures deduced from the chart recordings are given in Fig. 1. At $\phi=0$ the values of density and averaged $\{hkl\}$ pole density are equal.[4] Thus there are a number of points in the figures (black dots) where the axis densities have been measured directly. Other values in the figures are assigned to provide agreement with pole-distribution data. Quantitatively, if the calculated average $\{hkl\}$ pole density for all directions ϕ degrees from the axis of spin (i.e., ND, RD, or TD) is $R(\phi)$ and the associated axis densities are $T(\phi,\beta)$, where β is the angle between the axis of spin and some arbitrary zero along the path through the unit triangle traced out by the locus of points ϕ degrees from the pole of the diffracting plane and $\beta_{\max}$ is the total length of the path, then the values assigned to $T(\phi,\beta)$ require that

$$\left[\int_0^{\beta_{\max}} T(\phi,\beta)d\beta\right] \Big/ \beta_{\max} = R(\phi). \qquad (1)$$

In writing Eq. (1) use has been made of the following

* Operated for U. S. Atomic Energy Commission by Union Carbide Corporation.

[1] P. K. Koh and C. G. Dunn, AIME Trans. **218**, 65 (1960).

[2] L. K. Jetter, C. J. McHargue, and R. O. Williams, J. Appl. Phys. **27**, 368 (1956).

[3] P. K. Koh, AIME Trans. **215**, 1043 (1959).

[4] For example, as $\phi \to 0$, $T(\phi,\beta)$ in Eq. (1) becomes more and more independent of β, resulting in $T(\phi)=R(\phi)$ at $\phi=0$.

TABLE I. Resolved {*hkl*} pole concentrations.

ND	RD	TD
{556}	{056}	near {112}
{117}	near {116}	{116}
···	{001}	···

relationship[5]:

$$R(\phi) = I(\phi)/I_{\text{random}},$$

where $I(\phi)$ is the *corrected* intensity of {*hkl*} diffraction at an angle setting of ϕ and I_{random} is a *calculated* intensity for random orientations given by

$$I_{\text{random}} = \int_0^{\pi/2} I(\phi) \sin\phi d\phi.^{5}$$

The assigned values of the axis densities are summarized in the figures by contour lines of constant density. The density corresponding to a random texture has the value of unity. Clearly resolved {*hkl*} pole concentrations parallel to the three axes of the specimen are listed in Table I.

The components of the texture deduced from the figures are listed in Table II. Four (556)⟨065⟩-type components and four (117)⟨near 116⟩-type components are given to account for the two-fold symmetry of the texture, which is evident for example in a (110) pole figure of the material. In addition to these there may be two fiber-type components—⟨001⟩‖RD and ⟨111⟩‖ND—and two (112)⟨110⟩-type components. The ⟨001⟩ component should provide some (110)[001]; but possibly not enough (100)[001] to be resolved from the neighboring (117)⟨near 116⟩ components. Furthermore, it is important to note that the (111) pole density in the rolling direction [Fig. 1(b)] is zero. This permits us to conclude that there are no (*hkl*)⟨111⟩ components in the texture. Consequently there is no significant part of the texture which is random, because a random part would include all orientations.

Before comparing the results in Table II with previous ones we should like to consider the question of torque data. Prior data have shown that the torque curve is nearly that of (110)[001] single crystal, but with one-fifth the amplitude.[1] To a first approximation

TABLE II. Components of the recrystallization texture.

Rolling plane	Rolling direction	Transverse direction
(556)	[065]	[61,25,30] or near [211]
(556)	[065]	[61,25,30] or near [211]
(556)	[605]	[25,61,30] or near [121]
(556)	[605]	[25,61,30] or near [121]
(117)	[8,43,5] or near [181]	[611]
(117)	[8,43,5] or near [161]	[611]
(117)	[43,8,5] or near [611]	[161]
(117)	[43,8,5] or near [611]	[161]
(112)	[110]	[111]*
	[001] Fiber texture, Approx.	
(111) Fiber texture	···	···

* Could be part of the spread of (556)⟨065⟩ components.

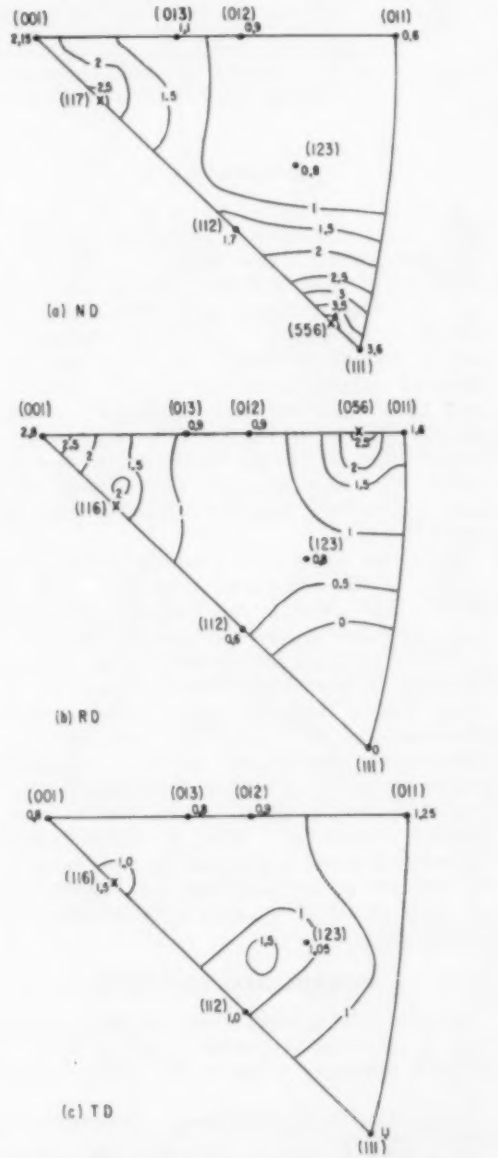

FIG. 1. Axis density figures for (a) the normal direction, (b) the rolling direction, and (c) the transverse direction of silicon-iron strip after primary recrystallization.

[5] I_{random} is of course constant and equal to the average value of $I(\phi)$ of the specimen over a solid angle of 2π; such an average reduces to the previously mentioned expression.

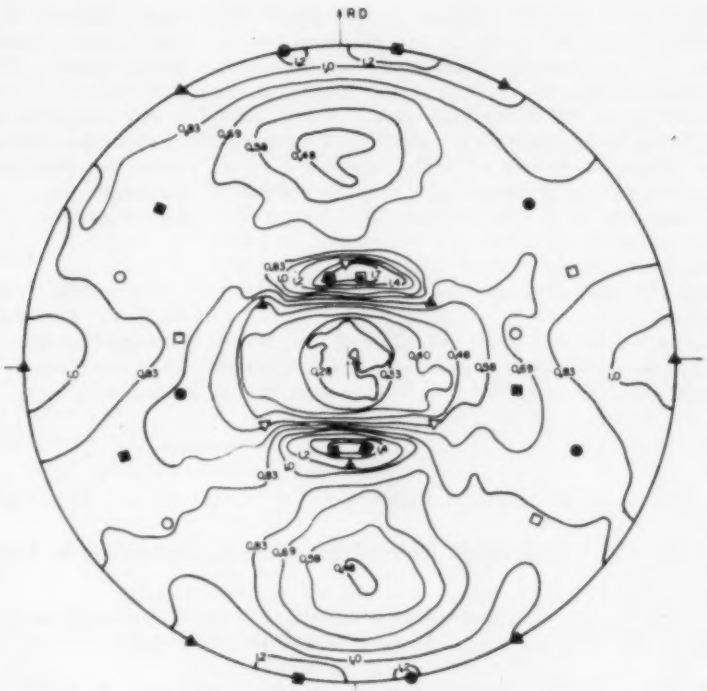

FIG. 2. A {110} pole density figure after primary recrystallization at 800°C. Solid and open circles and solid and open squares give the (112)⟨681⟩ orientations. (See footnote reference 1.)

it may be represented as follows[6]:

$$2L/K_1 = -0.10 \sin 2\theta - 0.15 \sin 4\theta, \qquad (2)$$

where L is the torque, K_1 is the first anisotropy constant, and θ is the angle between the rolling direction and the direction of the applied field. In the same connection Dunn and Walter[7] have already considered the texture of a different material having a torque curve represented by $2L/K_1 = -0.12 \sin 2\theta - 0.18 \sin 4\theta$, which is not far different from the present curve. The material also had a multicomponent texture. If one compares this texture with the present texture, one finds that both are similar in having a concentration of (001) poles in the neighborhood of the rolling direction, but more importantly the (017)⟨271⟩ components are close to the present (117)⟨near 116⟩ components. Such a component has a large influence on the coefficient of the $\sin 4\theta$ term. This information and other pertinent information is given in Table III.

TABLE III. Coefficients A_1 and A_2 of $\sin 2\theta$ and $\sin 4\theta$, respectively, for either single crystals or two-fold symmetrized orientations.

Orientation	A_1	A_2
(110)[001]	−0.5	−0.75
(100)[001]	0	−1
(111)⟨*uvw*⟩	0	0
⟨556⟩⟨065⟩	0.03	−0.10
(112)⟨110⟩	−0.17	0.58
(112)⟨681⟩	−0.16	0.47
(123)⟨210⟩	−0.25	0.067
(117)⟨near 116⟩	−0.01	−0.82
(017)⟨271⟩	0.025	−0.493

The former texture results are needed for a continuation of the discussion and a comparison with present results. Figure 2 shows a reproduction of a (110) pole figure.[8] The interpretation given for the texture was four (112)⟨681⟩ components and two (111)⟨112⟩ components, which alone could not explain the torque data. The present (556)⟨065⟩ components are the nearest components to (112)⟨681⟩ but they also tend to have little effect on the torque curve, because the torque vanishes for (111)⟨*uvw*⟩. However, the (112)⟨110⟩ edge of the spread out (556)⟨065⟩ orientations of the present texture could provide something toward the A_1 coefficient, while the (117)⟨near 116⟩ components contribute heavily to the A_2 coefficient. If we should assign about 6–7% of the texture to a spread out (110)[001] component, then 37% (112)⟨110⟩ and 39% (117)⟨near 116⟩ for the remainder would explain the

[6] L. P. Tarasov and F. Bitter, Phys. Rev. **52**, 352 (1937).
[7] C. G. Dunn and J. L. Walter, J. Appl. Phys. **30**, 1067 (1959).

[8] (110) pole figure, determined from the present spherical specimen, qualitatively agreed with Fig. 2, thus indicating no significant differences due to sampling or specimen shape. The (110) pole densities‖ ND, RD, and TD were, however, quantitatively in better agreement with results shown in Fig. 1 than are the similar values from Fig. 2.

torque curve. However, 26% of (123)⟨210⟩ and 14% (117)⟨near 116⟩ will make up the difference just as well, and the numerical values seem more reasonable. A simple calculation shows that the fraction of the sample within 10° of the (123) pole ∥ ND position, which is not a large spread, is about 30%. We conclude that the present texture can explain the torque curve. The principal new information making this possible is the identification of the (117)⟨near 116⟩ components. It is therefore concluded that the method of Jetter *et al.* more directly resolves components in a multi-component texture than does the usual pole-figure method.

Little can be said about the effect of the present texture on growth rates of secondary recrystallization grains; but little is known even for the more simple matrix textures. As before[1] it can be said that the orientation with maximum rate of growth of secondary grains—namely, (110)[001]—is in deviating orientation to the main components of the texture. The relationship is very roughly a 40° rotation about a ⟨100⟩ axis but whether this relationship is better for rapid growth than others involving a high angle of rotation remains an important question for further work. In any such work the texture needs to be known.

ACKNOWLEDGMENTS

The authors wish to thank Dr. P. K. Koh and the Allegheny Research and Development Laboratories for supplying the silicon iron used in the investigation. They also thank J. C. Ogle of O.R.N.L. for aid in the experimental work.

JOURNAL OF APPLIED PHYSICS VOLUME 31, NUMBER 10 OCTOBER, 1960

Hall Field Relaxation in Semiconductors at High Frequency*

KEITH S. CHAMPLIN
Electrical Engineering Dept., University of Minnesota, Minneapolis, Minnesota
(Received March 18, 1960; and in final form May 11, 1960)

Using a simple extension of standard magneto-ionic theory, the frequency dependence of the complex Hall field is calculated for samples with rectangular, cylindrical, and spherical geometry. The result has application to "open-circuit" Hall effect measurements on semiconductors at microwave frequencies.

SEVERAL persons have reported observing the Hall effect in semiconductors while employing either a microwave electric field and steady magnetic field, or both microwave electric and magnetic fields.[1–5] The experiments with only one microwave field utilized a direct connection between the sample and the walls of the cavity[1] or waveguide[2,3] and were thus of the "closed-circuit" type; the Hall effect causing microwave wall currents to flow at right angles to the currents associated with the driven mode. The experiments employing both microwave electric and magnetic fields were essentially "open circuit"; however, in this case, the resultant Hall voltage had a dc component.[4,5]

In an "open-circuit" Hall effect experiment employing one microwave field and one steady field, the magnitude of the observed microwave Hall field should decrease when the frequency becomes of the order of the inverse dielectric relaxation time $(\sigma/\kappa\epsilon_0)$ of the material. The effect is caused by the fact that $(\kappa\epsilon_0/\sigma)$ is approximately the time required to establish the microwave Hall field. It is the purpose of this article to present a simple calculation demonstrating this relaxation phenomenon.

Consider a rectangular p-type sample as shown in Fig. 1. The applied electric and magnetic fields are in the x and z directions, respectively. Assuming a single lattice collision time τ_c and charge to mass ratio (e/m^*) for the carriers, the average y component of hole velocity v_y approximately satisfies (in mks units)

$$(d/dt)v_y = -(v_y/\tau_c) + (e/m^*)\{E_y - v_x B_z\}. \quad (1)$$

The y component of electric field results from displacement of free charge. If the dimensions in the x and z direction are much larger than the dimension in the

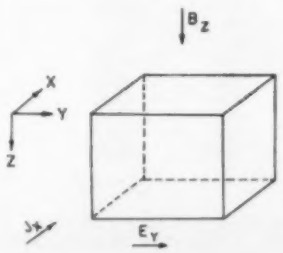

FIG. 1. Rectangular sample of p-type semiconductor showing direction of fields and current flow.

* Work supported by the U. S. Air Force through the Air Force Office of Scientific Research (ARDC).
[1] Y. Nishina and W. J. Spry, J. Appl. Phys. **29**, 230 (1958).
[2] G. E. Hambleton and W. W. Gartner, Bull. Am. Phys. Soc. II, **3**, 259 (1958).
[3] G. E. Hambleton and W. W. Gartner, Phys. and Chem. Solids **8**, 329 (1959).
[4] H. M. Barlow, and L. M. Stephenson, Proc. Inst. Elec. Engrs. (London), **Pt. B**, **103**, 110 (1956).
[5] H. M. Barlow, Proc. I.R.E. **46**, 1411 (1958).

y direction, we may write

$$\kappa\epsilon_0 E_y = -pe\int v_y dt, \tag{2}$$

where p is the hole density. Differentiating (2) twice and substituting into (1) while noting that $\mu = e\tau_c/m^*$ is the dc mobility and $\sigma = pe\mu$ is the dc conductivity, one obtains

$$\tau_c\left(\frac{\kappa\epsilon_0}{\sigma}\right)\frac{d^2}{dt^2}E_y + \left(\frac{\kappa\epsilon_0}{\sigma}\right)\frac{d}{dt}E_y + E_y = v_x B_z. \tag{3}$$

Assuming sinusoidal variation of E_y and $(v_x B_z)$, the steady state solution of Eq. (3) is

$$E_y = (\mu B_z E_x) \Big/ \left\{1 - (\omega\tau_c)\left(\frac{\omega\kappa\epsilon_0}{\sigma}\right) + j\left(\frac{\omega\kappa\epsilon_0}{\sigma}\right)\right\}, \tag{4}$$

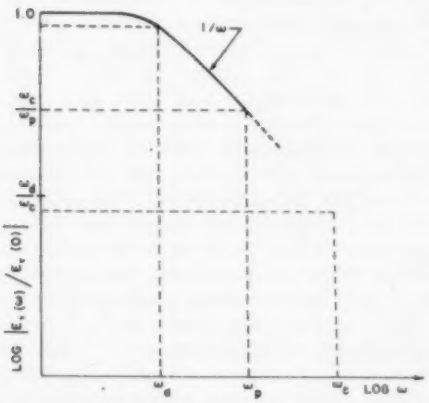

FIG. 2. Magnitude of Hall field as a function of frequency.

where μE_x has been written for v_x by assuming conditions sufficiently far removed from those required for cyclotron resonance, i.e., that both ω and the cyclotron frequency eB_z/m^* are much smaller than the inverse collision time $(1/\tau_c)$. Equation (4) can be written more conveniently by defining the following angular frequencies which are characteristic of the material:

$$\begin{aligned} \omega_c &= 1/\tau_c, \\ \omega_d &= \sigma/\kappa\epsilon_0, \\ \omega_p &= (\omega_c\omega_d)^{\frac{1}{2}}. \end{aligned} \tag{5}$$

These frequencies are the angular collision frequency, the angular dielectric relaxation frequency, and the angular plasma frequency, respectively. In terms of ω_d

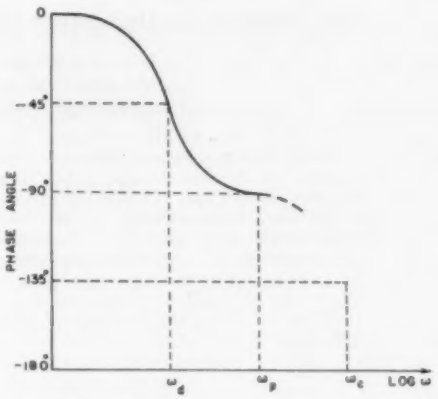

FIG. 3. Phase of Hall field as a function of frequency.

and ω_p, (4) becomes

$$E_y = (\mu B_z E_x)/\{[1 - (\omega^2/\omega_p^2) + j(\omega/\omega_d)\}. \tag{6}$$

The dielectric relaxation frequency ω_d depends somewhat upon geometry. By utilizing depolarizing factors in Eq. (2), one can show that for circular cylindrical and spherical geometry, the previous result is again correct if κ is replaced by $(\kappa+1)$ and $(\kappa+2)$, respectively. For germanium $(\kappa = 16)$, this is a minor change.

Ususally the condition $\omega_p^2 \gg \omega_d^2$ prevails. Thus, in an experiment employing a constant magnetic field B_z and an alternating electric field E_x, the Hall field E_y is equal in magnitude to the dc Hall field and is in phase with E_x at frequencies sufficiently less than ω_d (Figs. 2 and 3). For $\omega = \omega_d$, however, E_y has decreased in magnitude by $1/\sqrt{2}$ and lags E_x by 45 deg. As frequency is further increased, the magnitude decreases approximately as $1/\omega$ while the phase difference between E_y and E_x increases to 90 deg at $\omega = \omega_p$. At frequencies such that $\omega \ll \omega_c$ is no longer satisfied, Eq. (6) becomes invalid.

For a flat germanium sample of resistivity 11 ohm-cm, the dielectric relaxation frequency is about 10 kMc. (The plasma frequency at room temperature is typically above 40 kMc.) Thus, for an open-circuit Hall effect experiment on such material at x band, the resultant electric field in the material would be elliptically polarized due to the 45° phase difference between E_x and E_y and the apparent Hall angle $\theta_H = |E_y|/|E_x|$ would be approximately 0.707 times its dc value.

ACKNOWLEDGMENTS

The author gratefully acknowledges discussions with Professor A. J. Dekker and Professor H. J. Oskam.

Fast Neutron Bombardment of Germanium and Silicon Esaki Diodes*

J. W. EASLEY† AND R. R. BLAIR
Bell Telephone Laboratories, Inc., Whippany, New Jersey
(Received May 3, 1960; and in final form, June 13, 1960)

The fast neutron irradiation behavior of germanium and silicon Esaki diodes has been experimentally examined. The dominant change produced is an increase in the "excess" current which is proportional to integrated neutron flux. The observed increase in the vicinity of the current minimum is approximately 2.6×10^{-15} amp/fast neutron and 1.1×10^{-14} amp/fast neutron for germanium and silicon diodes respectively. Substantial changes result in the voltage-current characteristics of the diodes employed in the decade of exposure between $10^{16}-10^{17}$ fast neutrons/cm^2 for germanium diodes and between $10^{15}-10^{16}$ fast neutrons/cm^2 for silicon diodes. One kilomegacycle cavity oscillators employing germanium diodes exhibit a marked reduction in power output in the decade of exposure between $10^{16}-10^{17}$ fast neutrons/cm^2. The magnitude of the decrease is in approximate agreement with the observed bombardment reduction of diode negative conductance.

AT low forward voltage the Esaki diode[1] characteristic exhibits a peak in its current, this current being the result of electrons tunneling from the conduction to the valence band. As this phenomenom is independent of carrier lifetime, the effect of neutron bombardment upon it should be brought about only through reduction of the density of ionized donors and acceptors. The high initial net-donor and acceptor concentrations of these devices in conjunction with previously reported[2–4] carrier removal rates lead to an estimate of the order of 10^{18} fast neutrons/cm^2 required to produce substantial changes in the voltage-current characteristics by this mechanism. Thus, it could be expected that Esaki junctions would be very insensitive to radiation damage.

The experimental data reported herein show that the peak current is relatively insensitive to radiation damage but that fast neutron irradiation produces a large increase in the "excess"[5] current. The magnitude of this increase is such that substantial increases in the valley current occur in the decade of exposure between 10^{16} and 10^{17} fast neutrons/cm^2 for germanium units and in the decade between 10^{15} and 10^{16} fast neutrons/cm^2 for silicon units. Qualitatively similar results are found by Chynoweth and Logan[6] for 0.8 Mev electron bombardment of silicon junctions and by Longo[7] for 7 Mev electron bombardment of germanium junctions.

The germanium diodes employed in these measurements were fabricated from wafers of 7×10^{-4} ohm-cm n-type arsenic doped germanium on which a junction was formed by alloying a 0.0016-in. diam aluminum wire. The silicon diodes were formed by alloying a 0.003-in. diam aluminum wire containing 1% boron on approximately 0.001 ohm-cm n-type arsenic doped silicon. All measurements of germanium diodes were made concurrent with irradiation with samples in close proximity to the core of the Pennsylvania State University reactor. The exposure of silicon diodes was similar but measurements were made after removal of samples from the reactor at successive levels of bombardment. No appreciable annealing in the time scale of bombardment and measurement was observed in either case. The flux of fast neutrons of energy greater than 0.1 Mev at the location of the diodes was approximately 1.0×10^{12} cm^{-2} sec^{-1} as determined from normalization of the calculated neutron energy spectrum via activation analysis of the product nucleus of the S^{32} $(n,p)^{32}$ reaction. The temperature of the diodes during exposure was approximately 70°C and thermal equilibrium in the reactor environment was established in less than 1% of the total irradiation time. In order to prevent diode oscillation or blocking in the negative resistance region of the voltage-current characteristic, diodes were shunted with a resistance R_{sh} such that $R_{sh}<|R_-|$ and $L<R_{sh}(R_-C)$. The quantity R_{sh} includes

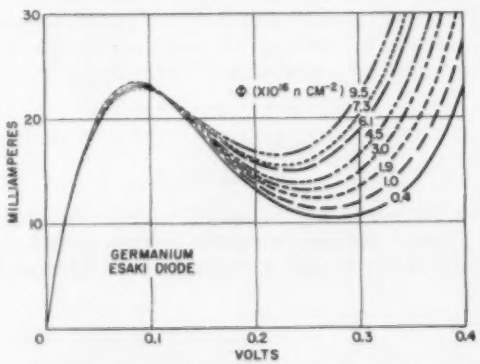

FIG. 1. Voltage-current characteristics of a germanium Esaki diode at several levels of fast neutron exposure.

* This work was supported by the Air Research and Development Command, United States Air Force.
† Present address: Sandia Corporation, Albuquerque, New Mexico
[1] L. Esaki, Phys. Rev. **109**, 603 (1958).
[2] J. W. Cleland, J. H. Crawford, and J. C. Pigg, Phys. Rev. **98**, 1742 (1955); **99**, 1170 (1955).
[3] K. Lark-Horovitz in *Semiconducting Materials*, edited by H. K. Henish (Academic Press, Inc., New York, 1951) p. 47.
[4] G. K. Wertheim, Phys. Rev. **111**, 1500 (1958).
[5] T. Yajima and L. Esaki, J. Phys. Soc. Japan **13**, 1281 (1958).
[6] A. G. Chynoweth and R. A. Logan, Private Communication (to be published).
[7] T. A. Longo, Bull. Am. Phys. Soc. Ser. II, **5**, 160 (1960).

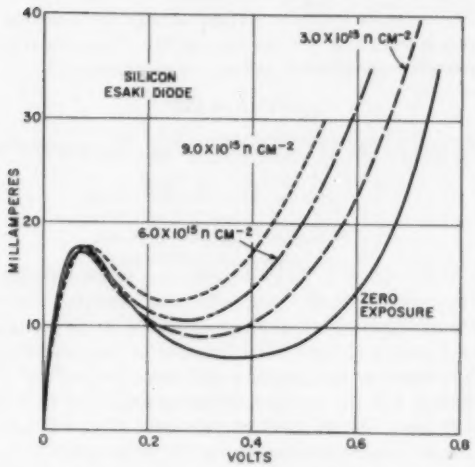

FIG. 2. Voltage-current characteristics of a silicon Esaki diode at several levels of fast neutron exposure. Note that the exposure values are approximately one-tenth of those shown in Fig. 1 for a Ge diode.

the parallel external resistance plus any diode internal series resistance; R_- is the diode negative resistance; L, the inductance of the diode, mount, connections and shunt resistor; and C is the diode junction capacity. A bridge circuit provided compensation for this shunt resistance and permitted the direct measurement of diode voltage-current characteristics on an X-Y recorder. The resistance of the type of shunt resistor employed was experimentally determined to be stable in the reactor environment to within $\pm 0.15\%$ throughout the bombardment.

The voltage-current characteristics obtained from the X-Y recorder and corresponding to several levels of fast neutron bombardment are shown for a germanium diode in Fig. 1 and for a silicon diode in Fig. 2. The qualitative nature of the bombardment alteration of the V-I characteristic is the same for both germanium and silicon diodes and is dominated by an increase in the valley, or "excess" current. A given change in the characteristics of silicon diodes is produced by an integrated fast neutron flux approximately one-tenth of that required to produce an equivalent change in germanium diodes. The increase in excess current at a given voltage is proportional to integrated fast neutron flux for both germanium and silicon junctions, as shown in Fig. 3. In the vicinity of the current minimum this increase, taking account of approximate junction area, is 2.6×10^{-15} amp/fast neutron and 1.1×10^{-14} amp/fast neutron for germanium and silicon diodes, respectively.

The fast neutron behavior of the diodes, as shown in Figs. 1–3, is in qualitative agreement with a mechanism for the excess current as suggested by Yajima and Esaki[5] by which tunneling occurs via impurity energy levels located within the band gap. It is well known that fast neutron bombardment produces defects with energy levels in the band-gap in both germanium[2,8] and silicon.[4] Certain of these levels have appeared not to be discrete but to consist of a close-spaced distribution, or band, of levels. On this basis, the increase in excess current at a given voltage should be proportional to the increase in defect density and therefore to integrated neutron flux as is observed.

The observed absence of any large decrease in the peak current is consistent for germanium diodes with measured changes in the carrier concentration with irradiation. Hall effect and conductivity measurements were obtained before and after the bombardment, employing bridges cut from the same n-type crystal from which the germanium diodes were fabricated. The observed decrease in carrier concentration was approximately 8% which yields a carrier removal rate of approximately 30 cm^{-3} per incident fast neutron cm^{-2}. This value is one order of magnitude higher than that reported by Cleland *et al.*[2] for nondegenerate material. Similar measurements in silicon were not made.

The percentage decrease in capacity of Ge junctions during bombardment was in approximate agreement, i.e., within a factor of two, with the measured change in majority carrier concentration of the n-type material on which the junction was formed. The capacity of a step junction in Ge is given by[9]

$$C = 3.4 \times 10^{-4} \left(\frac{pn}{p+n} \right)^{\frac{1}{3}} (V_i + V)^{\frac{1}{3}} \mu\mu f/cm^2, \qquad (1)$$

where p and n are the majority carrier concentrations,

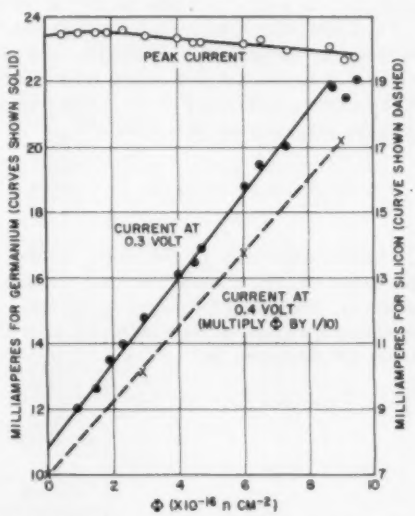

FIG. 3. Bombardment curves of peak current and current at 0.3 v for a Ge Esaki diode (solid lines); and of current at 0.4 v for a Si Esaki diode (dashed line).

[8] J. H. Crawford and J. W. Cleland, J. Appl. Phys. **30**, 1204 (1959).

[9] W. Shockley, Bell System Tech. J., **28**, 435 (1949).

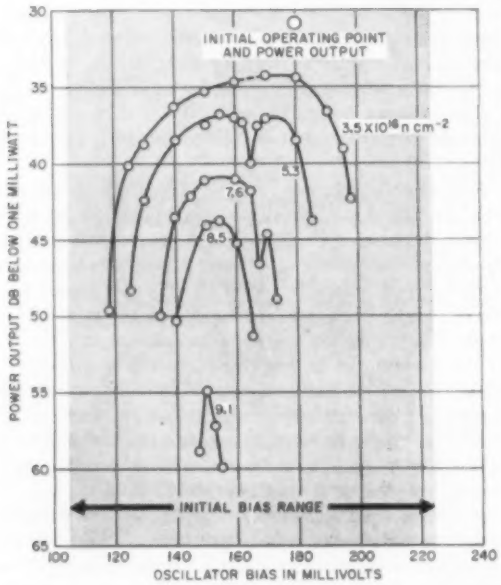

FIG. 4. Curves of power output vs diode voltage bias for a one kMc germanium Esaki diode cavity oscillator at several levels of fast-neutron exposure. Shaded portion indicates the prebombardment range of bias over which oscillation occurred. Dips at approx. 170 mv are attributed to cable reflections.

V_i the built-in voltage, and V, the applied voltage. To calculate the change, an *a priori* assumption was made that the carrier removal rate in degenerate p-type Ge is equal to that in n-type Ge. The measured change in capacity was determined from the change during bombardment of the frequency of oscillation of a coaxial cavity oscillator in which a germanium Esaki diode was part of the center conductor. For the cavity and diodes employed the frequency of oscillation is

$$f \simeq \frac{1}{2\pi}(1/LC)^{\frac{1}{2}}, \tag{2}$$

where L is the inductance of the diode, its mounting and the coaxial cavity, which is constant throughout a bombardment. The initial frequency of oscillation was approximately 1015 Mc/sec and increased at a rate of 1.4 Mc per 10^{16} neutrons/cm^2.

The decrease in power output of such an oscillator is shown in Fig. 4. If the voltage-current characteristic in the negative resistance region in approximated by

$$i = (V/R) + bV^3, \tag{3}$$

the power output of the oscillator P can be expressed[10] as

$$\frac{P}{a} = \frac{(R_s/R) - (R_s/Z_0)^2}{3bR^2(R_s/Z_0)^2[1+(Z_0/R_s)^2]}, \tag{4}$$

where $Z_0 = (L/C)^{\frac{1}{2}}$, R_s is the effective series resistance in the oscillator tank circuit, R is the absolute value of the diode negative resistance, b is a curve fitting parameter defined by (3) and a is a constant of proportionality which depends on coupling and loss external to the oscillator. For the cavity and diodes employed both Z_0 and R are of the order of 10 ohms and R_s equals a few tenths of an ohm. Consequently (4) reduces to

$$P/a \simeq R_s/3bR^3. \tag{5}$$

Employing values of b and R derived from Fig. 1 in (5), the calculated decrease in power at an exposure of 6.1×10^{16} fast neutrons/cm^2 is approximately 63%. The observed decrease in power output of the oscillator was 79% at a bias of approximately 155 mv, and therefore at the approximate peak of power output vs bias as shown in the curves of Fig. 4. The decrease in oscillator power output is therefore in approximate agreement with the observed change in the voltage-current characteristics of diodes similar to that employed in the oscillator. The observed power decrease for an operating point away from the relatively broad peaks of the family of curves in Fig. 4 is substantially larger. This is apparently due to the greater proximity of this operating point to the valley minimum and, therefore, region of greater change as reflected in both Figs. 1 and 4.

ACKNOWLEDGMENTS

The authors are indebted to E. Dickten and W. L. Feldmann for the diodes employed, W. M. Augustyniak for measurement of carrier concentration and conductivity, N. D. Newby for suggesting the bridge method of measurement, and to A. G. Chynoweth, R. A. Logan, and W. W. Anderson for helpful discussion.

[10] W. W. Anderson, private communication.

Interaction between High-Power Microwave Losses and Magnetic Flux Reversal

E. M. Gyorgy and F. B. Hagedorn
Bell Telephone Laboratories, Inc., Murray Hill, New Jersey
(Received June 27, 1960)

The off-resonance microwave absorption (subsidiary absorption) which frequently occurs at high-microwave power and which may exist even in the absence of an external dc magnetic field has been used to observe the interaction between the magnetic flux reversal and the microwave loss processes in polycrystalline ferrite. These experiments have shown that the spin waves associated with high-power, off-resonance microwave absorption have a negligible effect on the flux reversal process. However, the flux reversal process has a marked effect on the high-power microwave loss. During the flux reversal process, this high-power, off-resonance microwave absorption was found in some cases to be negligible.

INTRODUCTION

THE off-resonance (or subsidiary) absorption observed in high-power microwave loss measurements has been explained by Suhl[1] on the basis of the unstable growth of certain spin waves. The frequencies of these spin waves are approximately half the frequency of the microwave power. This subsidiary absorption can exist even in the absence of an external dc magnetic field if the microwave fields are sufficiently large. Suhl has considered the case of a spherical sample and shows that removing the external dc magnetic field increases the required microwave fields by a factor of 3 to 6, depending on the microwave frequency and on the saturation magnetization of the magnetic material.

Using a toroidal rather than a spherical sample could lead to substantial change in the quantitative predictions made by Suhl. Nonetheless, one would expect to be able to excite the subsidiary absorption spin waves in a square loop ferrite toroid with sufficiently large microwave fields even in the absence of an external dc magnetic field. The absence of a dc magnetic field would then make it possible to reverse the magnetization of the toroid from one of its stable remanent states to the other by applying a circumferential magnetic field pulse of a few oersteds.

Our experiments show that the high-power, subsidiary microwave absorption does occur in the absence of an external dc magnetic field with a ferrite toroid mounted in a cavity. By initiating the magnetic flux reversal when the ferrite toroid is in the high-loss condition, we have observed both the influence of the flux reversal process on the microwave subsidiary absorption and the influence of the spin waves connected with the subsidiary absorption on the flux reversal process.

EXPERIMENT

The ferrite torrid was mounted in an X-band TE_{102} cavity for these measurements as shown in Fig. 1. The toroid was glued to a rectangular loop of copper wire. Current pulses through this loop supplied the circumferential switching field. A pickup loop also encircled the toroid. These wires were positioned so as to minimize their interaction with the microwaves. The rf power was supplied by a pulsed X-band magnetron. The magnetron pulse length was approximately 1.0 μsec. A power divider was used to vary the microwave power level, and the absolute power level was measured approximately with a power meter. However, the changes in the insertion loss of the cavity were measured by using precision attenuators as is indicated in Fig. 2.

The magnetic field pulses used to switch the toroid were generated by discharging lengths of charged co-

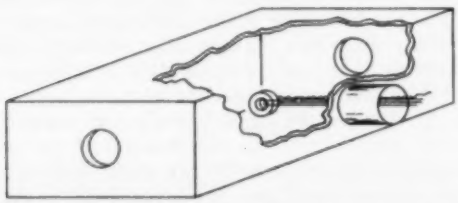

FIG. 1. The microwave cavity showing the position of the ferrite toroid.

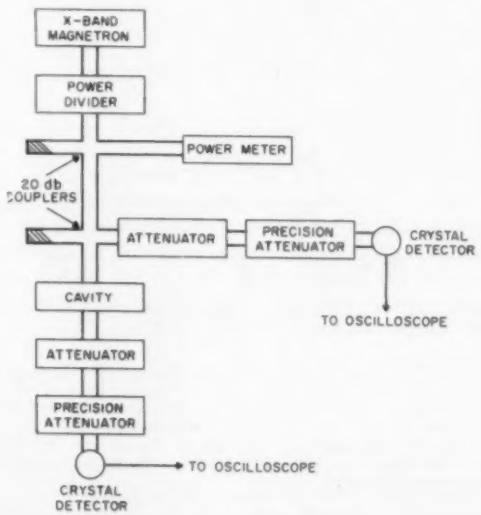

FIG. 2. The microwave circuit.

[1] H. Suhl, Phys. and Chem. Solids 1, 209 (1957).

axial cable through coaxial mercury relays as we have described previously.[2] The toroid was first placed in a reproducible remanent state by a large negative pulse of 0.5-μsec duration. Then the toroid was switched by a positive pulse which was 0.5 μsec long and which was of variable amplitude. The magnetron was triggered from the second pulse. In order to compensate for the 0.9 μsec required to shape and amplify the trigger pulse for the magnetron and in order for the magnetron to fire 0.5 μsec before the switching pulse arrived at the toroid, a coaxial cable long enough to delay the positive pulse for 1.4 μsec was inserted between the trigger pick-off and the toroid. Cable with solid copper inner and outer conductors and with 93% air dielectric was used to minimize dispersion and attenuation effects on the pulse. A variable delay of 0 to 1 μsec in the magnetron trigger circuit made possible a continuous change from the arrival of the rf pulse at the toroid 0.5 μsec before the switching pulse to its arrival 0.5 μsec after the switching pulse. The rates at which the above pulse sequence could be generated were 60, 30, and 15 cps. Heating effects due to rf power absorption in the ferrite were shown to be negligible by comparing results obtained at these different rates. The nominal ferrite composition was $Mg_{0.71}\,Zn_{0.2}\,Fe_{1.98}\,Mn_{0.11}\,O_4$.

RESULTS

The general features of the experimental results are shown in Fig. 3. A magnetic field pulse of 10.5 oe was applied circumferentially to the toroid 0.4 μsec after the start of the rf pulse. In Fig. 3(a), we show the rf power transmitted through the cavity. In this case, the input rf power was 0.009 kw, subsidiary absorption was negligible, and the transmission through the cavity was not affected by the flux reversal process. In Fig. 3(b), we show the voltage induced on the pickup winding as the flux in the toroid reversed. In Fig. 3(c), the rf power has been increased to 0.51 kw, and we see that during the flux reversal process, the transmitted microwave power increases. From Fig. 3(d), we see that the increased rf power has not affected the reversal process. Figure 4 shows the effect of decreasing the switching field applied to the toroid. The rf power level is the same as in Fig. 3(c), but the applied field has been decreased to 5.8 oe in Fig. 4(a) and (b) and to 2.8 oe in Fig. 4(c) and (d). The change in the signal from the pickup winding as the switching field is decreased is typical for ferrites.[3]

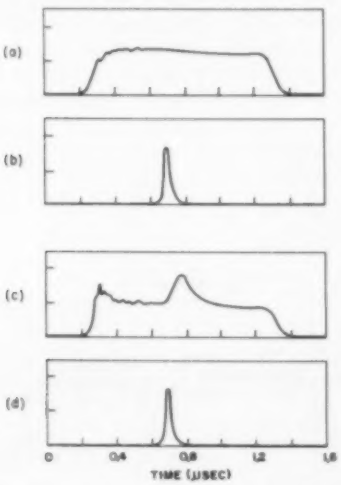

FIG. 3. Tracings of the oscilloscope photographs showing the transmitted microwave power and the voltage induced on the pickup loop as the flux in the toroid is reversed by an applied field pulse. In (a) and (b) the input rf power was 0.009 kw and the applied switching field was 10.5 oe. In (c) and (d) the rf power has been increased to 0.51 kw while the applied switching field was unchanged.

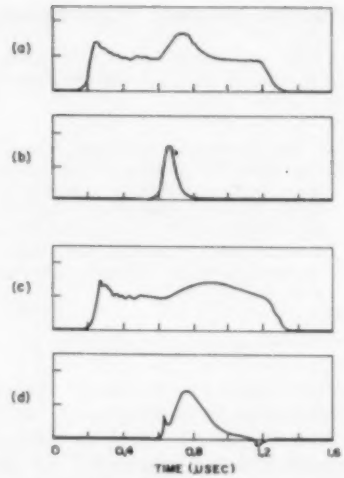

FIG. 4. Tracings of the oscilloscope photographs showing the transmitted microwave pulse and the voltage induced on the pickup loop as the flux in the toroid was reversed. The input rf power was 0.51 kw. The applied switching fields were 5.8 oe in (a) and (b) and 2.8 oe in (c) and (d). The vertical scale is arbitrary but it is the same for (a) and (c).

The amount of rf power absorbed by the ferrite in the absence of the flux reversal process under conditions similar to those pertaining to Fig. 3(c) depends markedly on the orientation of the toroid in the cavity. For the results given here, the orientation was for maximum absorption. In this case, the axis of the toroid was parallel to the propagation direction of the rf power (see Fig. 1). Moving the toroid laterally and vertically in a plane perpendicular to the direction of the power transmission slightly affected the absorption, but this effect was small until part of the toroid was inside the pipe on the side of the cavity.

The maximum power transmitted during the flux

[2] E. M. Gyorgy and F. B. Hagedorn, J. Appl. Phys. **30**, 1368 (1959).

[3] E. M. Gyorgy, J. Appl. Phys. **31**, 110S (1960).

reversal process and the power transmitted in the absence of flux reversal are plotted in Fig. 5 as a function of the input power. The scales are normalized near the lowest point where the input power was 0.009 kw and the transmitted power was 0.0014 kw. The switching field H_a applied to the toroid is given as a parameter. The values of H_a are 10.5, 5.8, and 2.8 oe, leading to reversal times of 0.044, 0.090, and 0.260 μsec, respectively. From Fig. 5, we see that the steady state transmission loss of the cavity increases when the rf power is increased beyond the threshold for the high-power effects. However, during the flux reversal process, this added high-power loss disappears if the reversal is sufficiently fast. Effects very similar to the ones discussed here are observed if the toroid is only partially reversed before the switching pulse is terminated or if the toroid is initially in some partially reversed state before the microwave pulse is applied. In addition, the added high-power loss does not appear to be present at the beginning of the rf pulse. As is seen in Fig. 3 and in Fig. 4, the transmitted power decreases after an initial peak. This phenomenon has been previously reported[4] and is related to the unstable growth of spin waves as discussed by Suhl.[1] However, the exact nature of the early portion of the rf pulse is also substantially influenced by the magnetron itself, by the power divider, by the power level, and by the cavity. As a result, we have not attempted to interpret further the detailed features of the initial part of the microwave pulse.

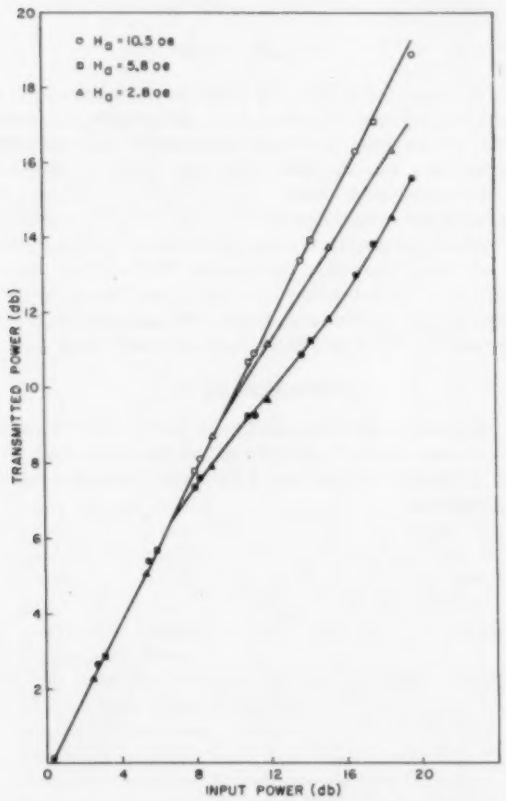

FIG. 5. Microwave power transmitted through the cavity as a function of the input rf power with the applied switching field amplitude as a parameter. The solid points correspond to the power transmitted in the absence of the flux reversal process, and the open points indicate the maximum power transmitted during flux reversal. At lower power levels, the solid and open points have merged. At the lowest point on the curve, the input and transmitted powers were 0.009 and 0.0014 kw, respectively.

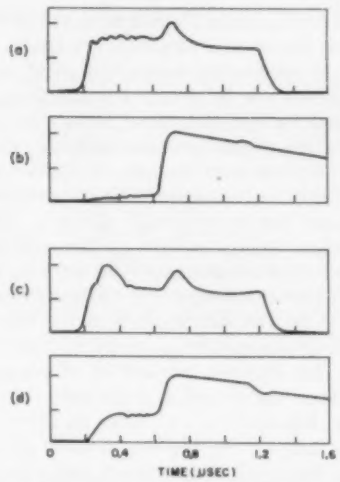

FIG. 6. Tracings of the oscilloscope photographs showing the transmitted microwave power and the integrated flux change observed on the pickup loop. The applied switching field was 10.5 oe. In (a) and (b), the input power was 2.2 kw. In (c) and (d), the input power was 16.5 kw. The vertical scale is arbitrary but is the same for (b) and (d).

If the microwave power is increased beyond the levels considered so far, the onset of the microwave power tends to decrease the net circumferential flux in the toroid. In Fig. 6, we show the rf pulse and the integrated flux change observed on the pickup loop. The power level of the pulse shown in Fig. 6(a) was 2.2 kw, and it is seen in Fig. 6(b) that a small flux change resulted from the rf pulse. For Fig. 6(c), the input power was 16.1 kw, and in Fig. 6(d) it is seen that the rf power has reduced the circumferential flux to approximately zero before the pulsed switching field completes the reversal. Here again, the power transmission in the early portion of the microwave pulse is greater than at later times. In both Fig. 6(a) and Fig. 6(c), this increased transmission appears to be associated with the demagnetization process induced by the microwave fields.

DISCUSSION

It is impractical to make a detailed analysis of the interaction of the microwave fields with the magnetiza-

[4] R. L. Martin, J. Appl. Phys. **30**, 159S (1959).

tion of the ferrite toroid. Furthermore, the flux configuration during the reversal process is not known in detail.[3] However, a qualitative interpretation of the experimental results can be given. For simplicity, we will assume that for low microwave power the interaction is between the rf field and the uniform precession of the magnetization even though the applied dc field is zero. In this case, the magnetization presumably precesses around the internal field, which is composed of the crystalline anisotropy field (of the order of 100 oe) and the effective rf demagnetizing field (of the order of $2\pi M_s$ or 1000 oe). Resonance at X-band would require about 3300 oe. Detailed analysis of the behavior of a a toroidal sample in a TE_{102} cavity is impractical, but it is clear that a certain amount of off-resonance coupling between the rf field and the uniform precession does exist. Because the low-power microwave absorption is not affected by the flux reversal process as is shown by Fig. 3(a), we conclude that changing the internal fields by the flux reversal process has little effect on the low-power absorption. Our experiments also indicate that the application of 10 oe of magnetic field has negligible effect on the coupling between the rf and the magnetization and that the coupling is not dependent on the rate of change of magnetization.

If we assume that increasing the rf power does not modify the coupling of the rf field to the uniform precession, we can interpret our results in terms of spin wave growth and decay. Suhl[1] has shown that the added losses at high microwave power are due to coupling between the uniform precession and spin waves which have frequencies approximately half that of the microwave power. The experimental observations summarized in Fig. 5 indicate that a rapid change in the magnetization interrupts this coupling. The original spin waves will then presumably decay, and a new spin wave configuration will arise which is coupled to the uniform precession in its new orientation. These new spin waves will require a finite time to grow. For the conditions pertaining to Fig. 4(a), we see that this time is of the order of 0.1 usec. During the time the spin waves are growing, the microwave loss will, of course, be decreased from its steady state value. For sufficiently rapid motion of the average magnetization, the experimental data indicate that it is possible to decouple completely the uniform precession from the spin waves.

The effect of these decoupled spin waves on the flux reversal process appears to be negligible. It is possible that these spin waves are of the wrong frequency and direction or that their amplitudes are still too small compared to the amplitudes involved in the reversal process. However, because we do not have specific information about the dynamic flux configurations pertaining to flux reversal,[3] little more than noting the absence of an effect can be done at this time. Similarly, the complexity of the process involved in the rf demagnetization of the toroid, discussed in conjunction with Fig. 6, precludes a detailed discussion. This demagnetization phenomenon, however, is not too surprising in the context of unstable spin wave growth.

CONCLUSION

We have found that the coupling which leads to subsidiary absorption in ferrites at high microwave power may be decreased by rapid reorientation of the average magnetization. In some cases, the effects of the subsidiary absorption were made negligible in this way. A qualitative interpretation of this decreased coupling in terms of the growth and decay of relatively large amplitude spin waves has been given. Although no direct effect of the subsidiary absorption spin waves on the flux reversal process was found, demagnetization of the ferrite by very large microwave fields did occur.

ACKNOWLEDGMENTS

We would like to thank Dr. H. E. Scovil for his collaboration in the early phases of this work and Dr. R. L. Martin for the use of the high-power microwave equipment.

JOURNAL OF APPLIED PHYSICS VOLUME 31, NUMBER 10 OCTOBER, 1960

On the Strength of Glass in Water Vapor

F. R. L. SCHOENING
*Department of Physics, University of the Witwatersrand, Johannesburg, Union of South Africa**
(Received May 24, 1960)

The bending strength of glass slides, which had the dimensions 38×6×0.16 mm, was measured at different relative pressures of water vapor. The adsorption isotherms of water vapor on powdered glass, which had the same composition as the slides, were measured in a separate experiment. The reduction of the surface free energy as function of the vapor pressure was calculated from the isotherms. The observed variation of the strength was compared with the strength variation calculated from the reduction of the surface free energy. The Griffith equation for brittle fracture was used to relate strength and surface free energy. Two cases were considered: (1) the specimens were weakened by the reduction of the surface free energy and (2) the specimens were weakened by the reduction of the surface free energy and by a deepening of the surface cracks. Both interpretations agreed with the experimental results because, by using the Griffith equation, only the lower limits for the strength of the specimens could be calculated.

It was found that the observed strength did not decrease steadily with increasing vapor pressure, but had a secondary maximum at a relative pressure of about 0.2. The maximum reduction of the strength corresponding to complete wetting with water was already reached at a relative pressure of about 0.5. The ratio of the strength in saturated water vapor to the strength in vacuum was found to be independent of the surface damage of the specimens.

INTRODUCTION

THE influence of water on the strength of glass has been the subject of many investigations. Recently Charles[1] explained his observations on the delayed fracture of glass by stress corrosion at the tips of surface cracks in the specimens. In this investigation, which was completed approximately at the time Charles's results were published, the observed weakening was compared to the observed reduction of the surface free energy of the specimens. Because the failure of glass affords a good example of brittle fracture, the Griffith[2] and Orowan[3] formulations of the brittle strength can be applied.

Griffith[2] derived for the brittle strength B of a specimen containing a surface flaw of depth c the equation

$$B=(2Y\gamma/\pi c)^{\frac{1}{2}}, \tag{1}$$

where Y is Young's modulus and γ is the surface free energy of the solid. The Griffith equation expresses the critical condition that an increase in the length of the crack decreases the strain energy in the specimen sufficiently to provide the surface free energy of the newly created surfaces of the crack. If the depth of the crack is greater than or equal to c then the specimen breaks instantaneously. Fracture occurs whether the specimen is under a constant load or under constant constraint [Orowan[3]].

As pointed out by Orowan,[3] the Griffith equation, which expresses the energy balance in the case of brittle fracture, is a necessary condition for brittle fracture, but might not be a sufficient condition. Orowan derived the sufficient condition for brittle fracture by evaluating the externally applied stress which is sufficient to break the bonds between the atoms in the tip of the crack. The cohesive force between the atoms or molecules in the solid was estimated from the surface free energy and Young's modulus of the solid. Orowan[3] obtained the expression

$$B=(Y\gamma/2c)^{\frac{1}{2}}, \tag{2}$$

which is within the factor $(\pi/4)^{\frac{1}{2}}$ formally identical to the Griffith equation. Orowan[3] then concluded that the equation derived by Griffith is not only a necessary but also a sufficient condition for brittle fracture. Nevertheless the Griffith and the Orowan equations represent different physical aspects and, hence, could predict different effects when the interaction with an external medium is considered.

Both equations indicate that the reduction of the surface free energy γ by adsorption of foreign molecules weakens the solid. A distinction has to be made between the reduction of γ for an open surface, on which an unlimited amount of vapor can be adsorbed, and the reduction of γ at the tip of a crack, where the amount of adsorbed molecules is limited by the space available. For the Orowan equation this restriction is important because the cohesive force between the atoms at the tip of the crack depends on the reduction of γ before the crack begins to spread. Hence, the greatest amount of weakening which could be observed would depend on the number of foreign molecules which fit into the crack. A quantitative estimation of the strength in terms of the Orowan equation is not only complicated by the lack of knowledge about the dimensions of the cracks, but also by the possibility that the adsorbed molecules in the narrow parts of the cracks form a rigid structure which contributes to the strength [Schoening[4]].

The restriction imposed by the size of the crack is less important in the case of the Griffith equation

* Present Address: Franklin Institute Laboratories for Research and Development, Philadelphia, Pennsylvania.

[1] R. J. Charles, J. Appl. Phys. **29**, 1549, 1554 (1958).

[2] A. A. Griffith, Proc. Intern. Congr. Appl. Mech., Delft, 55 (1924).

[3] E. Orowan, Welding J. Research Suppl. **34**, 157s (1955).

[4] F. R. L. Schoening, 1959 thesis, University of the Witwatersrand, Johannesburg (1959).

because now γ refers to the surfaces created after the crack begins to spread and not, as in the Orowan case, to the surface which is present before the crack propagates. When the crack spreads it will also become wider, thereby allowing more molecules to enter the crack. In the interpretation of the observations reported here the reduction of γ measured for an open surface has been used in conjunction with the Griffith equation.

The Young's modulus which appears in the two equations, refers to different locations in the specimen. The expression for the strain energy around the crack introduces the modulus into the Griffith equation. Because the strain energy is located in the bulk of the specimen, the modulus refers to a bulk property of the specimen. It is unlikely that the adsorption of foreign molecules on the surfaces of the specimen can influence the modulus in the Griffith equation. The modulus in the Orowan equation refers to the bond between the atoms which have to be separated when fracture takes place. It is related to the force constant, which expresses the resistance against stretching the bond between surface atoms. Adsorption, especially chemisorption, may influence the force constant.

The crack length c refers in both equations to the same physical property in the specimen. An external medium, which reacts chemically with the solid, can by the process of stress corrosion deepen the crack and thereby weaken the solid. Charles[4] and Moorthy and Tooley[5] attribute all the observed weakening of their glass specimens to such a geometrical change of the cracks in the surface of the specimens. A crack of original length c_0 enlarges to a length c in the presence of water vapor.

EXPERIMENTS

Two sets of experiments were performed; the strength of glass was measured as function of the relative water vapor pressure, and the adsorption isotherms of water on glass were recorded. The reduction of the surface free energy $\pi=\gamma_0-\gamma$, where γ_0 and γ are the surface free energy in vacuum and in vapor respectively, was calculated from the observed adsorption isotherms.

Fracture Experiment

The specimens used were microscope cover slides for which the manufacturer, Chance Brothers Ltd., gave the composition as follows: SiO_2 71.6, CaO 8.2, Na_2O 12.4, MgO 3.6, Fe_2O_3 0.02, Al_2O_3 1.7, TiO_2 1.8, Sb_2O_3 0.6. The slides were cut and glued together in packets. The four sides of a packet, where the edges of the slides emerged, were ground smooth with a paste consisting of grade 4F carborundum powder and water. The slides, whose final dimensions were about $38\times6\times0.16$ mm, were cleaned in carbon tetrachloride, concentrated sulphuric acid (10 to 15 min), methyl alcohol and acetone. They were stored in a desiccator containing calcium chloride for two weeks before the tests were begun.

The specimens were fractured in a three point bending apparatus, which allowed the tests to be performed in vacuum or in water vapor. The apparatus with the specimen in position could be baked at elevated temperatures. The temperature in the apparatus was measured with a thermocouple which was attached to one of the knife edges. The load on the specimen was increased on the average every 18 sec by about 2.8% of the average breaking load of 50 g. From a plot of load versus deflection Young's modulus and the bending strength were calculated, using the measured dimensions of the specimens.

In a typical experiment the apparatus with the specimen in position was evacuated and then baked at 350°C for one hour. After cooling to room temperature the pressure of the residual gas in the apparatus was between 0.01 and 0.001 μHg. Now, either the specimen was tested in vacuum or water vapor was let into the test chamber. Two hours after letting the vapor into the chamber the pressure and the temperature were measured and the test was begun.

Adsorption Experiment

The adsorbent was prepared by crushing the fragments of the slides used in the fracture tests. The resulting powder was cleaned in a manner identical to that applied to the fracture specimens. The crushing of the slides ensured that the adsorption measurements were done on a surface which was similar to that in a crack.

The adsorption and desorption isotherms of water, nitrogen and argon were measured by using the volumetric method and an apparatus similar to that described by Harkins and Jura.[6] Before every new series of adsorption runs the adsorbent was degassed at 350°C for one hour. This degassing treatment was sufficient to remove all the water which had been adsorbed in the previous experiment. After some months it became noticeable that the adsorbent had changed its adsorptive capacity. A fresh glass powder was prepared and used for further experiments.

Fracture Results

The three aspects of the results which will be described here are, the effect produced by grinding the edges of the specimens, the influence of the water vapor on the strength of the specimens and the influence of the vapor on Young's modulus.

If the grinding of the edges of the specimens created the cracks, which later determined the strength of the specimens, then the strength results would be dependent on the grinding treatment. It was found that the

[5] V. K. Moorthy and F. V. Tooley, J. Am. Ceram. Soc. **39**, 215 (1956).

[6] W. D. Harkins and G. Jura, J. Am. Chem. Soc. **66**, 1356 (1944).

strength of the specimens ground together in one packet differed from that for another packet. Since all specimens in one packet got the same grinding treatment, but different packets were ground separately, it was concluded that during grinding of the edges the strength-determining cracks were produced. However, the ratio of the strength in water to that in vacuum was, within the scatter of the experiments, the same for all packets. The relevant data are shown in Table I.

This result indicated that the relative strength was independent of the length of the cracks. It also made it possible to pool the data for all packets for the purpose of obtaining the relative strength as a function of the relative vapor pressure.

The results for tests in water vapor are shown in Fig. 1. Single measurements are shown except for $p/p_0=0$ where 16 measurements were taken and for $p/p_0=1$ where 19 measurements were recorded. In order to obtain a better representation of the results, the measurements in the intervals indicated by broken lines were combined by taking mean values. The mean values and their standard deviations are shown in Fig. 1 by vertical lines terminating at ± 1 standard deviation.

TABLE I. Strength-data.

B_0, strength in vacuum (10^6g/mm^2)	1.95 ±0.05	1.48 ±0.03	1.67 ±0.04
B/B_0, relative strength in water	0.564±0.035	0.574±0.022	0.557±0.053

TABLE II.

p/p_0	0.043	0.098	0.042	0.092	0.032	0.044	0.172
B/B_0	0.713	0.816	0.607	0.785	0.628	0.650	0.828

It was of interest to test whether the difference between the first mean, $B/B_0=0.684\pm0.024$, and the following two means, $B/B_0=0.774\pm0.026$ and $B/B_0=0.784\pm0.032$, was statistically significant. For this purpose the t test was applied to the first mean and the mean of the data in the combined second and third interval. For 19 deg of freedom t became 3.09 which showed that the chance for the difference being due to statistical fluctuations was less than one percent. This result was substantiated by considering the results in chronological order. Table II shows results of consecutive experiments.

Results quoted so far were obtained with specimens tested within one month of preparation. A few tests were carried out with samples which had been in the desiccator for 4½ months. The results, given in Fig. 2, showed the same early drop of the strength but did not reproduce the secondary maximum in the strength versus pressure curve. From this it appeared that the sharp falling off of the strength at low vapor pressures was a more general property of the specimens and that the intermediate maximum was specific to specimens containing "fresh" surface cracks.

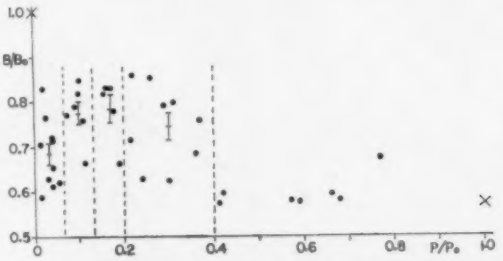

FIG. 1. Relative strength B/B_0 plotted against the relative water vapor pressure p/p_0. The full circles represent single measurements. The two crosses at $p/p_0=0$ and $p/p=1$ are mean values of 16 and 19 measurements respectively. Mean values for measurements within the broken lines are indicated by vertical lines which terminate at ± 1 standard deviation of the mean.

In view of results obtained by Sato[7] who found that the strength and Young's modulus were equally affected by wetting glass with water, it was of interest to compare the mean values of the moduli of the specimens tested at $p/p_0=0$ and $p/p_0=1$. 18 specimens tested in vacuum gave a modulus of $7.33\pm0.07\times10^6$ g/mm^2, as compared to $7.49\pm0.09\times10^6$ g/mm^2 obtained for 28 specimens tested in water. The observed increased of 2% may be compared to a decrease of 33% reported by Sato[7] for the result of three experiments.

Adsorption Results

A short description of the adsorption results is given below and illustrated in Fig. 3.

(a) The adsorption of water was measured at 26.95°C. At $p/p_0=0.694$ adsorption was discontinued and desorption begun. The desorption isotherm did not follow the adsorption isotherm but stayed continually above it.

(b) The following two water isotherms were recorded at 26.95°C and 27.00°C. In each case the desorption was not measured immediately after the adsorption run but instead the adsorbent was degased at 50°C for 45 min. If there had been a strict division between chemisorbed and physisorbed water, a second adsorption

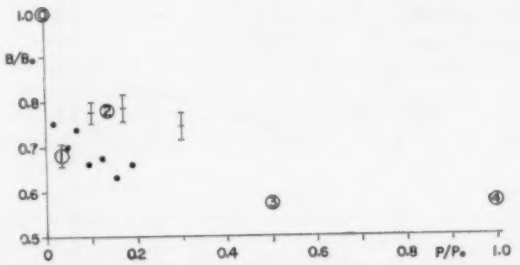

FIG. 2. Relative strength plotted against the relative water vapor pressure. Full circles are measurements taken with aged specimens. Numbers indicate points referred to in the text.

[7] M. Sato, Proc. Japan Acad. 30, 445 (1954).

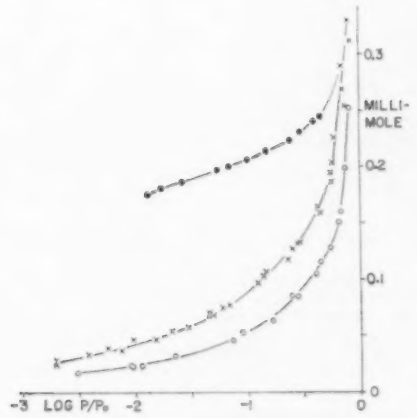

FIG. 3. Adsorption isotherms plotted as amount adsorbed against the logarithm of the relative water vapor pressure. Crosses represent three different adsorption experiments at 27°C. Full circles are desorption points obtained at 27°C. Open circles are two adsorption runs at 27°C after degasing at 50°C for 45 min.

would have been reversible. This second adsorption was recorded, but the following desorption showed that it was not fully reversible at the temperature of the adsorption experiment. After about five months it became evident that the adsorption properties of the glass powder had changed considerably.

(c) On a new adsorbent the adsorption of water was measured and compared to that on the first adsorbent. The agreement between isotherms was good when the new adsorption values were divided by five. It was concluded that the surface area of the second adsorbent was five times that of the first adsorbent.

(d) Two nitrogen isotherms were recorded at −197°C. One nitrogen and one argon isotherm were measured at −185°C. The new adsorbent was used in these experiments.

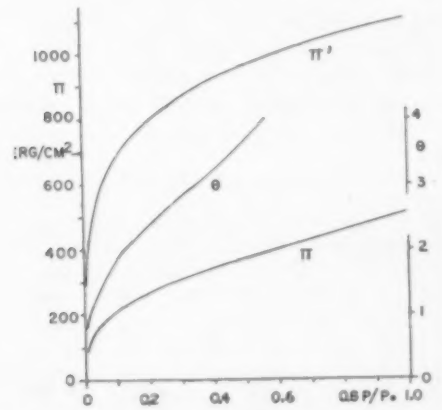

FIG. 4. Reduction of the surface free energy π, π' and coverage θ of the surface with layers of molecules plotted against the relative water vapor pressure. π and π' are calculated from the adsorption and desorption isotherms respectively. θ refers to the adsorption of water vapor.

The three adsorption isotherms of water on a freshly degassed sample, mentioned in Secs. (a) and (b), were replotted as large scale plots of amount adsorbed versus log p/p_0. After extrapolation to zero amount adsorbed the curves were integrated graphically. In this way, as was first shown by Bangham,[8] it was possible to obtain the reduction of the surface free energy from the adsorption isotherm. This method is, however, only valid when the adsorption is reversible. In order to obtain an estimate of the error introduced by the irreversibility of the water adsorption, the desorption isotherm mentioned in Sec. (a) was treated in a similar manner. The results of the integration are shown in Fig. 4. The correct value for the reduction of the surface free energy was taken to lie between those obtained from the adsorption and the desorption isotherms.

The results of the surface area determinations are shown in Table III. The data from the nitrogen and argon adsorption have already been converted from the experimental values, obtained with the second adsorbent, to those appropriate to the first adsorbent.

TABLE III. Results of surface area determinations.

Method of area determination	Temp. °C	Molecular area A²	Surface area m²
N_2 adsorption, BET analysis	−197	16.2	3.34
N_2 adsorption, BET analysis	−197	16.2	2.99
N_2 adsorption, BET analysis	−185	16.2	3.20
A adsorption, BET analysis	−185	16.0	2.89
Irreversible H_2O adsorption	27	10.5	3.52
Irreversible H_2O adsorption	27	10.5	3.32
		Mean	3.21

From the difference between the first and second adsorption mentioned in Sec. (b) it was possible to determine the amount of water which was not desorbed by degassing at 50°C. The surface area was calculated on the assumption that this water formed a monolayer. The results are included in Table III. With a mean value of 3.21 m² for the surface area the specific surface area becomes 0.423 m²/g.

DISCUSSION

The strength results may best be discussed by referring to the points which are indicated in Fig. 2 as follows, (0) the strength at $p/p_0=0$, (1) the strength minimum at $p/p_0=0.03$, (2) the strength maximum at $p/p_0=0.13$, (3) the strength at $p/p_0=0.5$ and (4) the strength at $p/p_0=1$.

As mentioned above, the probability that the difference between (1) and (2) is due to statistical fluctuations is less than one percent. Analyzing the data, no correlation was found between this strength difference and experimental fluctuations of temperature, rate of

[8] D. H. Bangham, Trans. Faraday Soc. 33, 805 (1937).

loading, Young's modulus or specimen dimensions. However, aging of the specimens appeared to have the effect of suppressing the secondary maximum at (2).

If the maximum at (2) is real, it could be due to a strengthening of the cracks by the adsorbate. Beginning in vacuum and proceeding to higher vapor pressures, the cracks are filled with increasing amounts of water molecules which could strengthen the cracks. A strengthening resulting from the adsorbed molecules in the cracks would oppose the general weakening of the specimens. Since only a solid adsorbate could contribute appreciably to the strength, the strengthening action would cease to increase when the adsorbing molecules become fluid. From then on further adsorption could have only the effect of decreasing the strength of the solid part of the filling. A quantitative treatment of such a strengthening effect would have to make use of the Orowan equation (2).

The explanation given for the occurrence of the maximum at (2) cannot be more than a suggestion, because the strength of glass is time dependent, and because it is possible that the time dependence is different for different vapor pressures. In that case the interpretation may simply be that the specimens fatigue slower at (2) than at (1), (3), and (4).

The observation that the lowest strength is already reached at (3) instead at (4) can be explained by capillary condensation of water in the cracks. According to observations by Amberg and McIntosh[9] capillary condensation in porous glass begins at $p/p_0=0.6$. McFarlane and Tabor[10] measured capillary forces at $p/p_0=0.8$. Observations on glass have shown that the strength in a humid atmosphere is the same as that in water. If the cracks were already filled with liquid water at (3), no further strength reduction could be expected by further adsorption.

In order to combine the adsorption data, which were obtained on an open surface, with the strength data, which were influenced by processes in capillaries, the advanced adsorption in the cracks had to be taken into account. This was done by compressing the p/p_0 scale of the adsorption data uniformly to such an extent that the point $p/p_0=1$ on the adsorption scale coincided with $p/p_0=0.5$ [point (3)] of the fracture scale.

By using the Griffith equation (1), the observed strength, B/B_0 as a function of p/p_0, was compared to a calculated strength which was obtained from the measured reduction of the surface free energy, π as a function of p/p_0. The restriction to the necessary condition for brittle fracture requires that the calculated strength is not greater than the observed strength. The relative strength can be written

$$B/B_0=(c_0/c)^{\frac{1}{2}}(1-\pi/\gamma_0)^{\frac{1}{2}}, \qquad (3)$$

[9] C. H. Amberg and R. McIntosh, Canad. J. Chem. **30**, 1012 (1952).

[10] J. S. McFarlane and D. Tabor, Proc. Roy. Soc. (London) **A202**, 224 (1950).

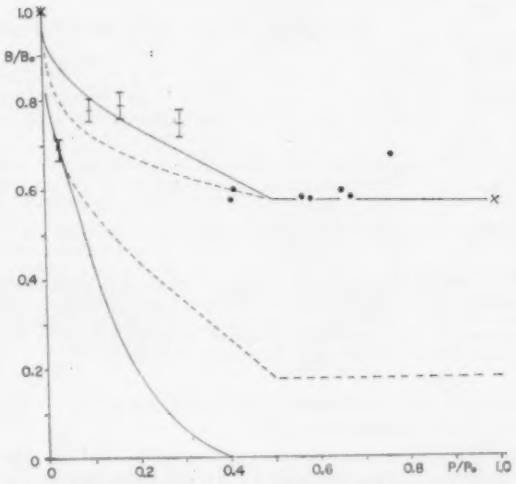

FIG. 5. Relative strength plotted against the relative water vapor pressure. Upper set of full and broken lines are calculated from Eq. (3) by taking $c_0/c=1$ and $\gamma_0=761$ erg/cm², $\gamma_0'=1660$ erg/cm², respectively, lower set taking $c_0/c=1$ and $\gamma_0=338$ erg/cm², $\gamma_0'=1146$ erg/cm². The full lines are calculated using the adsorption isotherms, the broken lines using the desorption isotherms.

where γ_0 is the surface free energy in vacuum, π is the reduction of the surface free energy due to the adsorption of water, and c_0/c is the ratio of the length of the crack in vacuum to that in vapor. Equation (3) allows the calculation of B/B_0 in terms of π, or p/p_0 if c_0/c and γ_0 are known.

At first the calculated strength was obtained from Eq. (3) by assuming that all weakening was due to the reduction of the surface free energy; c_0/c was assumed to be one. Because γ_0 was unknown, the strength calculated from the Eq. (3) had to be fitted to one observed strength point. The results of the calculations when taking points (1) or (3) as the observed strength point are shown in Fig. 5. The full lines in the figure were calculated from the adsorption data, π, the broken lines from the desorption data, π'.

Matching the observed strength and the calculated strength at (3) was rejected because it left the minimum (1) unexplained. Matching the observed strength and the calculated strength at (1) gave for the surface free energy $\gamma_0=340$ erg/cm² and $\gamma_0'=1150$ erg/cm². For saturated water vapor the calculated strength was considerably less than the observed strength, as may be seen in Fig. 5.

It might be considered that this difference between the observed and calculated strength is due to a slow crack propagation caused by the slowness with which the adsorption equilibrium is established. Observations do not support such interpretation, because if this interpretation were correct, then the relative strength would depend on the length of the cracks [Schoening[4]]. As mentioned earlier, it was observed that the relative

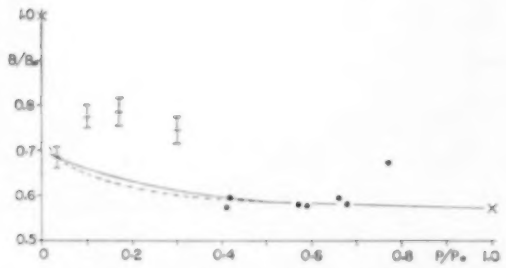

FIG. 6. Relative strength plotted against relative water vapor pressure. Full and broken lines are obtained from Eq. (3) by taking $c_0/c=0.543$, $\gamma_0=1306$ erg/cm² and $c_0/c'=0.634$, $\gamma_0'=2320$ erg/cm² respectively. The full line is calculated using the adsorption isotherm, the broken line using the desorption isotherm.

strength was independent of variations of the crack length of the order of 1:1.7.

The finding that the strength calculated from the Griffith equation, by taking only the reduction of the surface free energy into account, is smaller than the observed strength is acceptable because the Griffith equation expresses the necessary condition for brittle fracture. The Orowan equation would have to be used to account for the strength at vapor pressures greater than p/p_0 about 0.03.

However, the Griffith equation (3) could account for the strength at (1) and (3) if the crack was assumed to be deeper in vapor than in vacuum. In general, the difference in length could be a function of the vapor pressure; but because the explicit dependence of c_0/c on p/p_0 was unknown, it was assumed that c_0/c was the same for the points, (1), (3), and (4). The result of fitting the calculated strength to the points (1) and (3) is shown in Fig. 6. The values obtained for γ_0 and c_0/c are $\gamma_0=1310$ erg/cm², $\gamma'_0=2320$ erg/cm², and $c_0/c=0.54$ $c_0/c'=0.63$.

The latter interpretation for the observations indicates that in saturated water vapor the strength of glass is reduced by a factor between 0.78 and 0.72 because of the reduction of its surface free energy, and by a factor between 0.74 and 0.80 because of a deepening of the cracks. The finding that both effects contribute approximately equally to the observed weakening may, however, be due to the rate of loading employed in the experiments. As shown by Charles,[1] the crack length may increase with increasing times of loading.

The two interpretations discussed above give different values for the surface free energy of glass in vacuum. Assuming that all weakening is due to the reduction of the surface free energy results in a value for γ_0 which can lie between 340 and 1150 erg/cm². Assuming that in addition, crack deepening takes place gives for γ_0 a value between 1310 and 2320 erg/cm². Published values for γ_0 cover the whole range. Berdennikow's[11] value of 1210 erg/cm² which is often quoted does not decide between the possible interpretations.

Since the observations presented here give no indication for the correct interpretation, the results may be summarized as follows. Under the assumption that all weakening is caused by the reduction of the surface free energy, the Griffith equation predicts a strength which is lower than the observed strength. The Griffith equation can predict the observed strength if it is assumed that, in addition to the weakening caused by the reduction of the surface free energy, the surface cracks are longer in the presence of water vapor than they are in vacuum. In contact with saturated water vapor the surface free energy of the glass used in the experiments is reduced by an amount which lies between 510 and 1110 erg/cm². Taking 810 erg/cm² as a likely value, and using Berdennikow's[11] value of 1210 erg/cm² for γ_0, it follows that the strength of the glass could be reduced by factor of 0.57 on account of the lowering of the surface free energy alone.

ACKNOWLEDGMENTS

The author wishes to thank Professor F. R. N. Nabarro for helpful discussions during the course of the investigation and Professor G. D. L. Schreiner and Dr. H. H. Schlössin for their interest in the work. The research was sponsored by Boart & Hard Metals Ltd., to whom the author expresses his gratitude.

[11] W. P. Berdennikow, Phys. Z. Sowjetunion 4, 397 (1933).

JOURNAL OF APPLIED PHYSICS VOLUME 31, NUMBER 10 OCTOBER, 1960

Study of Irradiation Effects and the H^2+H^2 Buildup in Tantalum

A. F. Gabrysh, H. Eyring, M. E. Wadsworth, G. S. Baker, and T. Ree
Rate Processes Institute, University of Utah, Salt Lake City, Utah

(Received January 5, 1960; and in final form June 16, 1960)

The irradiation effects and the increase of neutron yield from the deuterium-deuterium reaction in tantalum has been studied at a bombarding energy of 350 kev and a target current 100 μa. Saturation (the neutron yield becomes a steady maximum) is reached in a new target, maintained at temperatures below 45°C, after about 2 hours of steady bombardment or on the order of 1 coulomb of deuterons per square centimeter. The irradiated targets were annealed at temperatures from 45°C to 770°C. A thermal analysis shows that a prominent exothermic maximum in the annealing spectrum occurs at approximately 612°C. This maximum is associated with an increase in pressure, indicating an abrupt increase in diffusion of deuterium from the target at this temperature. From a study of diffusion of deuterium from the specimen at three temperatures, an activation energy of 0.24 ev is calculated for diffusion of deuterium in tantalum.

X-ray traces were taken of the specimen before and after bombardment and after annealing. These showed an expansion of the lattice together with changes in line intensities indicating a distortion in the lattice structure.

I. INTRODUCTION

THE use of metals along the path of an ion beam, or as stopping baffles and target backings, in accelerators producing intense deuteron beams, requires that the metal intercept the beam for some period of time during the running cycle. Some of the incident beam particles are retained in these metals. In the case of deuteron bombardment this results in the production of high-energy (2.5-mev) neutrons by means of the D-D reaction.

Neutron or charged particle irradiation is known to produce changes in metals which may be retained as permanent damage as long as the metals are held at sufficiently low temperatures. The nature of these lattice distortions has been the subject of considerable theoretical study.[1-3]

To determine the mechanism and effect of deuterium buildup and the magnitude of neutron background arising from deuterium retained in a tantalum target, an investigation has been made of the neutron yields from 350 kev incident deuterons. This is studied by (1) measuring the production of neutrons from the D-D reaction, (2) thermal analysis of the annealing spectrum, and (3) x ray studies of the tantalum targets. The x ray studies show that, presumably as a result of bombardment, the (220) and (310) crystalline planes of the body-centered cubic tantalum structure are eliminated while reflection intensities from others are enhanced or decreased, and still others are shifted such that calculations indicate an approximate 0.10% volume increase in the metal. Thus the conclusion can be drawn that this observation is the evidence that the deuterium forms interstitial solid solution with the tantalum. Tantalum was chosen for bombardment because it has been the subject of previous study[4] and appeared most suited to the easy purging needed in target backings. Fiebiger[5,6] has included tantalum in his study of hydrogen diffusion in many metals.

II. EXPERIMENTAL DETAILS

1. Accelerator

The accelerator employed was a Cockcroft-Walton consisting of a four-stage 400-kv voltage supply and an accelerator fitted with an rf ion source and a 15° analyzing magnet for separating the beam components.

2. X Ray Measurements

Traces were made with a North American Philips Company x ray diffraction unit and a wide range goniometer around whose periphery a Geiger counter moved. The unit was located in a temperature controlled (21.5°C) room. The weighted average wavelength of $K\alpha_1$ and $K\alpha_2$ copper radiation were employed; the tube voltage and current being 35 kv and 20 ma, respectively.

The specimen was mounted on the central axis of the goniometer. Primary radiation passed through a collimator and slit system to the specimen which was marked with an arbitrary orientation; this orientation was maintained throughout the study. After leaving the specimen, the diffracted beam passed through another collimator and slit system to the Geiger counter. The specimen was maintained in the proper relationship with respect to the Geiger counter to satisfy Bragg's law at every position of the scanning arc. The scanning rate was $\frac{1}{2}$° per minute.

3. Targets

The targets used in this study were taken from the tantalum sheet obtained from Fansteel Metallurgical Corporation. The purity was specified as 99.9% pure. It was in the so-called "factory annealed" state and had a uniform small grain size.

[1] F. Seitz and J. S. Koehler, in *Solid State Physics*, edited by F. Seitz and D. Turnbull (Academic Press, Inc., New York, 1956), Vol. 2, p. 305.
[2] F. Seitz, Phys. Today 5, No. 6, (1952).
[3] S. Siegel, Phys. Rev. 75, 1823 (1949).
[4] W. Good and C. D. Moak (unpublished).
[5] K. Fiebiger, Z. Naturforsch. 11A, 607 (1956).
[6] K. Fiebiger, Z. angew. Phys. 9, 213 (1957).

The samples were cleaned ultrasonically and by hand methods. There were no detectable differences in the neutron buildup rates for the two types of cleaning. Before and after irradiation, microscopic examination of the targets showed no detectable difference in surface cleanliness, indicating that diffusion-pump oil did not contaminate target surfaces during bombardment.

4. Target-Thermocouple Calibration

Figure 1(a) shows the arrangement of target, heating element, and cooling piston. The tantalum disk, 2.2 cm in diam, was used as the junction of the thermoelements which were spot welded 180° apart to the under side of the target and just inside of the resting ridge of the target seat. Thus the Brown recorder plotted a curve of the average target temperature.

Calibration curves for the target-thermocouple were obtained by resting the positioned target on a temperature-controlled metal block. The temperature of the block was read at intervals (while a recorder was plotting the thermocouple curve) on a thermometer which was placed in a hole drilled horizontally to a point directly under the target and very near the surface of the block.

5. Target Cooling and Heating

During bombardment the target [Fig. 1(a)] was kept cool by screwing the water-cooled piston tightly against the target which had a bearing on an annular shoulder of 1.6-cm diam opening. Atmospheric-pressure gas contact between target and piston was made by letting in gas through the vacuum valve. The O-ring on the piston prevented the gas from leaking into the accelerator tube. Target temperature could be maintained at approximately 45°C for 100 μa beam current.

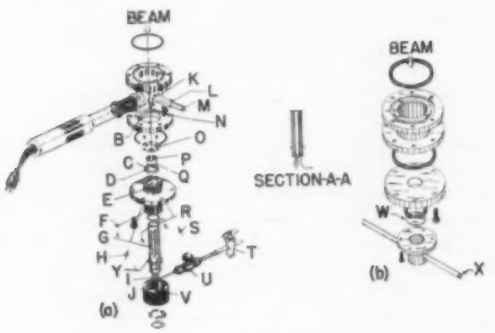

FIG. 1(a). Heating and target arrangement. (b). Water-cooled target arrangement. *A-A*, Cross section of cooling piston; *B*, vinyl seal; *C*, stainless steel target seat; *D*, platinum thermocouple wire; *E*, O-ring; *F*, piston guide key; *G*, water-cooled target cooling copper piston; *H*, kovar insulated terminal (for Pt. thermoelement); *I*, water inlet; *J*, water outlet; *K*, Pyrex; *L*, kovar seal; *M*, heating electrode; *N*, tungsten filament (.040 inch); *O*, stainless steel target shoulder; *P*, tantalum target; *Q*, platinum 90%, rhodium 10% thermocouple wire; *R*, O-ring; *S*, kovar insulated terminal (for Pt-Rh thermoelement); *T*, volume calibrated stopcock; *U*, vacuum valve; *V*, raise and lower piston; *W*, target; *X*, water pipe; *Y*, keyway.

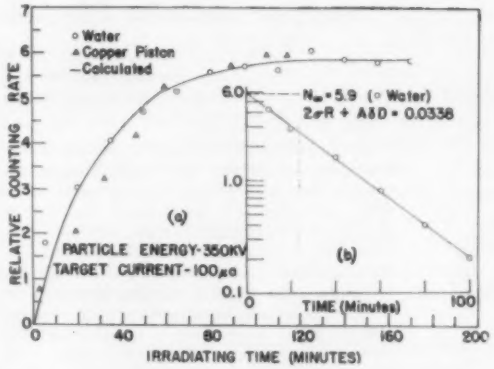

FIG. 2. (a) H^2+H^2 buildup in contact-cooled and water-cooled target. (b) Plot of $(N_\infty - N)$ vs time.

After bombardment, the targets were radiantly heated by a tungsten filament-loop which was suspended above the target. The current to the loop was supplied through a variac-controlled filament transformer. It was possible to reach target temperatures up to 770°C by controlling the distance (0–0.020 in.) between filament and target. It was noted that if the filament loop was very close and not exactly level with the surface of the target, "hot spots" developed quickly in that part of the filament which was nearest the target or touching it, and there resulted a sharp drop of the average temperature of the target. The filament's position was carefully adjusted in order to avoid the occurrence of hot spots.

6. Temperature and Pressure Recording

Two recorders fitted with edge timing markers of 2-sec frequency were used to record pressure and temperature changes. The markers were energized by a common source. Pressure changes were plotted by a recorder monitoring the voltage across a resistance which, through a switch, replaced the meter in an ionization gauge. The recorder plotting temperature changes was connected directly to the Pt, Pt-Rh thermoelements at the kovar insulated terminals.

III. RESULTS

1. H^2+H^2 Buildup in Targets

The H^2+H^2 buildup was observed, for comparative purposes, in two tantalum targets which were cooled differently during irradiation. Relative count rates of neutrons, due to the D-D reaction, were obtained with a Long[7] counter positioned at an angle of 39° with beam direction. A target maintained at approximately 45°C by contact with a water-cooled piston [Fig. 1(a)] and

[7] A. O. Hanson and J. L. McKibben, Phys. Rev. **72**, 673 (1947).

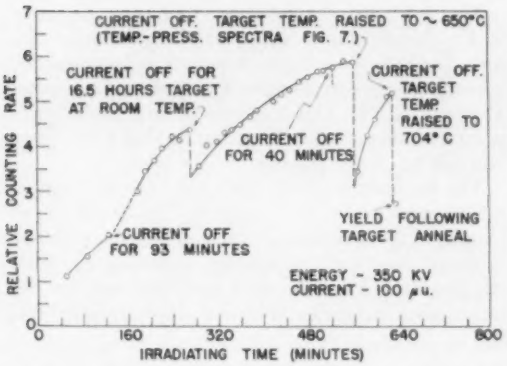

FIG. 3. Neutron count rate vs time showing effects of (1) interruption of irradiation and (2) annealing.

a water-cooled target [Fig. 1(b)] maintained at approximately 25°C showed essentially the same rate of H^2 buildup for both temperatures and similar neutron yields [Fig. 2(a)] which increase with time and essentially reached saturation in both targets after a bombardment for approximately 105 min or of the order of 1 coulomb per square centimeter of deuterons. Campbell[8] has reported a similar observation. The target arrangement of Fig. 1(a) allowed target heating and the use of temperature recording instruments; therefore, it was used for subsequent study.

Targets once irradiated and heated under similar conditions did not reach saturation in equal time on subsequent irradiations. Figure 3 shows the slower buildup in a target after it had been irradiated many times and heated after each irradiation. Complete saturation appears only after a total but interrupted bombarding time of 9.3 hours. Target irradiation here was discontinuous, the beam being stopped, in order to check for diffusion of deuterium out of the target. Extrapolations of the parts of the curve following the rest periods show a decrease of neutron yield for the 93-min and 16.5-hour rests, the target temperature being the same as room temperature of about 21°C. On continued bombardment the yield increased somewhat rapidly at the beginning, then appeared to bend into the extension of the previous bombardment curve. No detectable difference of neutron yield is observed for the saturated target after the 40-min rest period.

After saturation was reached, the bombardment was stopped and, over a period of 209 sec, the temperature of the target was increased to 612°C (Fig. 7). Appreciable purging of deuterium from the target resulted. A following short irradiation gave a relative neutron yield which was about 54% of that given by the saturated target.

A rebombardment (69 min) was made, and the yield again increased rapidly, at first, then appeared to bend (Fig. 3) into the shape of the initial bombardment curve. Irradiation was interrupted and the target temperature raised to 704°C. Following the cooling of the target, a short irradiation indicated a complete purging of the deuterium, due to the second bombardment, together with further purging of deuterium, which remained in the target after the original bombardment, by an additional 8%; thus the yield was reduced to about 46% of saturation. The increased temperature and heating time effected the additional 8% purge.

The bending behavior of the curves following rest periods shows different rates of approach to target saturation of deuterium.

2. Temperature and Pressure Curves

The principal difficulty in measuring the stored energy and the quantity of gas which was released during the anneal of an irradiated sample was one of sensitivity. Sudden pressure changes produced off-scale reading for small volumes (a pancake valve was used to isolate the target from the main vacuum system) when an irradiated sample was heated. Isolating the target in larger volumes resulted in decreased sensitivity and a flatter spectrum. The greatest number of resolved pressure changes, as a function of time and temperature, were recorded by keeping the maximum of the pressure curve on the recorder tape. This was achieved by placing a valve for the smallest volume [the valve was placed atop electrode section of Fig. 1(a)] and "cracking" it slightly to allow constant gas drainage into the pumping system. Relative quantities of gas for successive irradiation of varied duration were then obtained by cracking the valve the same amount for each anneal. The variations of pressure with temperature, in a standard and an irradiated target, are shown in Figs. 4–7.

Figure 4 represents the annealing and pressure spectra for a nonirradiated sample. The initial two peaks were typical for the outgassing of the fast-heating filament and the slow-warming of surrounding material, respectively. The dependence of the pressure changes due to the filament outgassing on the variance of pressure in

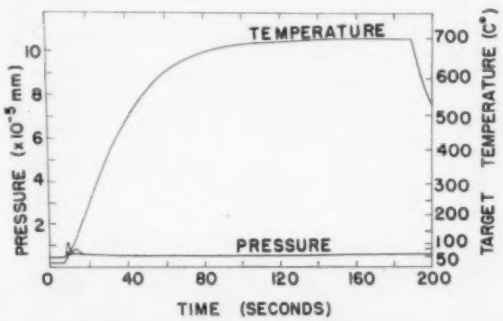

FIG. 4. Pressure-temperature curves for a nonirradiated "standard" tantalum disk.

[8] R. C. Campbell, J. D. Korsmeyer, and D. C. Ralph, Phys. Rev. 94, 791 (1954).

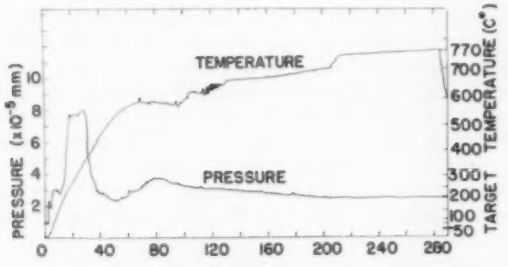

FIG. 5. Pressure-temperature curves for a target irradiated for 31 min.

the system is shown by the solid and broken curves. The intensity of the filament peak is seen to increase (broken curve) for the first anneal following its exposure to higher pressures, while the peak for subsequent anneals (solid curve) obtains a much lower maximum.

The pressure and temperature curves in Fig. 5 were obtained on a fresh target which was exposed to the ion beam for 31 min. The target was heated within 2 min after bombardment. Corresponding pressure changes, with increase of temperature, indicate the initial pressure rise peak due to filament heating and subsequent peaks due to purging the target of deuterium.

Target purging appears to begin at a temperature of about 150°C when the pressure rises to about 3×10^{-5} mm of mercury. While the target temperature is further increasing, the deuterium continues to evolve essentially at the same rate with which it is being pumped out of the system through the slightly open valve. A subsequent slight drop in the purging rate is followed, at a target temperature of about 225°C, by the apparent diffusion of the main bulk of deuterium from the target. After passing the peak at 8×10^{-5} mm and 390°C, the evolution of deuterium from the target decreases rapidly and continues to decrease for increasing target temperature until at about 545°C where a further increase of temperature effects a moderate increase in pressure.

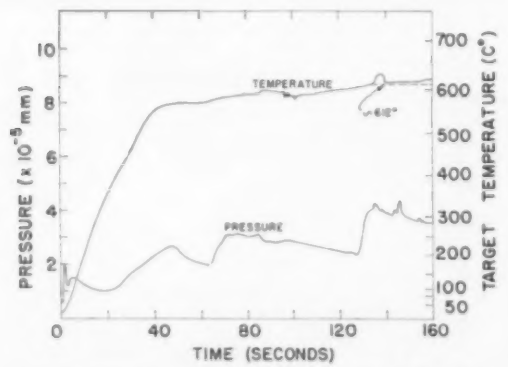

FIG. 6. Pressure-temperature curves for a target irradiated for 111 min.

Figure 6 shows the behavior of the same specimen as in Fig. 5 following a subsequent bombardment of 111 min. The rate of evolution of deuterium from the target is low for the low temperatures and becomes a maximum at around 612°C. This is associated with a sudden temperature increase to 650°C indicating that an exothermic reaction has taken place in the specimen.

The specimen was then subjected to several bombardment-anneal cycles. The curves in Fig. 7 show (1) slow purging at low temperatures and (2) the sharp increases in the pressure and temperature, indicating an exothermic process. This exothermic peak was seen for every target when the temperature was slowly raised through 600°C.

3. X Ray Examination of Deuterium-Irradiated Tantalum

X ray traces were taken of irradiated specimens. The apparent changes which appeared in the x ray diffraction patterns, for three targets irradiated for the noted lengths of time, are shown in Figs. 8–10.

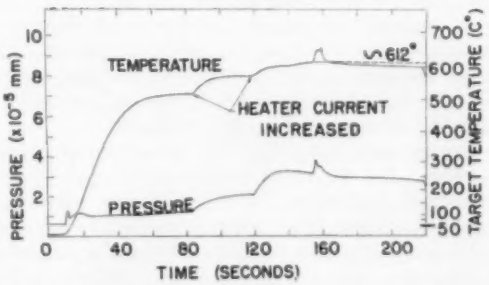

FIG. 7. Pressure-temperature curves for a target which was irradiated and annealed many times.

Figure 8 shows the x ray diffraction pattern for a nonirradiated sample, used as a comparison standard. In both instances [(a) nonannealed and (b) annealed] the traces were identical for both sides of the 20-mil thick target.

Traces shown in Fig. 9 were recorded for a target which had been subjected to deuteron bombardment for 105 min. The temperature of the target during bombardment was approximately 45°C; the time elapsing between irradiation and x ray examination was 8 days. A decrease is noted in the reflection from the (110) plane and there is an apparent absence of any reflection from the (220) plane for the irradiated side, whereas the nonirradiated side appears unaffected.

The diffraction pattern of a target "first-time" bombarded, for 170 min, produced the traces shown in Fig. 10. Eleven days elapsed between the irradiation of the target and the x ray analysis. Diffractometer traces were made in the region of bombardment and in an adjacent area. The patterns obtained from the bom-

barded region show similar crystalline alterations on both the irradiated and nonirradiated sides of the target, and a decrease is noted in the reflection from the (110) plane with the apparent disappearance of reflections from both the (220) and (310) planes. The decreased intensity of the (110) trace is comparable to that for the irradiated side in Fig. 9. The pattern obtained from an off-center, nonbombarded region showed traces similar to that of Fig. 8.

Trace (b) of Fig. 8 is identical to the traces resulting from a target which was annealed after bombardment. The target had been subjected to several irradiations and anneals. On the final anneal the target reached a temperature of 650°C. The x ray patterns show the enhancement of the (110) plane when compared with the standard [Fig. 8(b)] and the presence of the (220) and (310) planes, which are absent for irradiated non-annealed targets (Figs. 9 and 10).

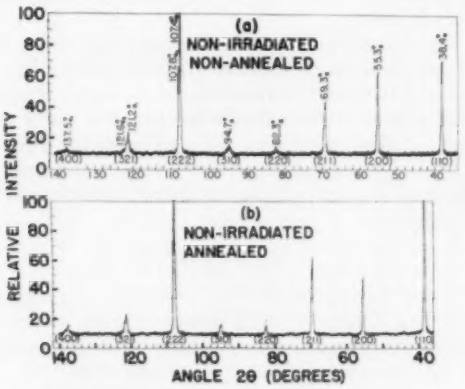

FIG. 8. Diffractometer pattern of a standard nonirradiated tantalum disk.

Annealed specimens which were not subjected to bombardment showed none of the changes seen for irradiated targets. For example, four samples were heated between tantalum electrodes in an electrical welding unit. Two of the disks were heated above the melting point for tantalum, one was heated somewhat below the melting point, and the fourth sample was heated to a point considerably below the melting point. All four samples gave patterns identical with that shown in Fig. 8(b).

IV. DISCUSSION

1. Buildup Rate

The penetration of 350-kev deuterons into the specimen is at most a few microns.[9,10] At the end of their

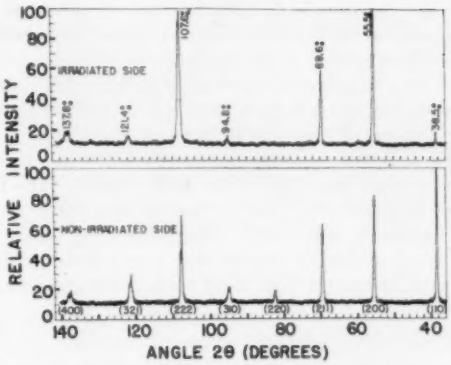

FIG. 9. Diffractometer pattern of a tantalum disk target which was irradiated for 105 min.

penetration the deuterons stop in the matter to form a layer source at this depth, from which they then diffuse in the metal. The diffusion rate in the bombarded region is several orders of magnitude greater than in the remainder of the metal. Thus, during bombardment the diffusion is primarily diffusion of the deuterium to the surface followed by escape from the metal. Fiebiger[6] has given an extensive discussion and theoretical analysis of the above model. In the light of Fiebiger's model and the analysis of the diffusion process in this geometry, the data of the work presented here can be satisfactorily explained by the following equations.

The buildup rate of deuterons in the penetrated layer dn/dt (atoms sec^{-1}) is expressed to a good approximation by the following formula:

$$dn/dt = AR - ADn\gamma - 2Rn\sigma. \quad (1)$$

Here A is the area of the layer, R is the bombarding rate (atoms cm^{-2} sec^{-2}). The first term represents the rate of deuterons entering the penetrated layer due to the impinging deuteron beam. The second term is the rate of diffusion of the deuterons to the surface and out

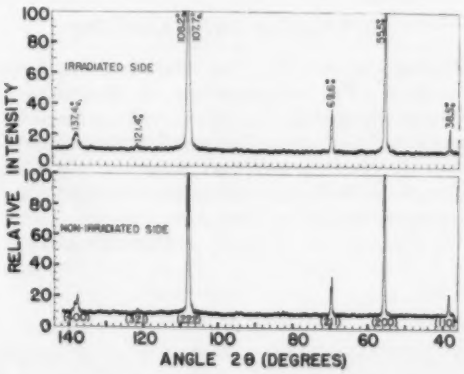

FIG. 10. Diffractometer pattern of a tantalum disk target which was irradiated for 170 min.

[9] S. K. Allison and S. D. Warshaw, Revs. Modern Phys. 25, 779 (1953).

[10] H. A. Bethe and J. Ashkin, in *Experimental Nuclear Physics*, edited by E. Segrè (John Wiley & Sons, Inc., New York, 1953), Vol. 1, pt. 2.

of the specimen. γ is a factor that depends on the geometry of the specimen and distribution of deuterium in the bombarded region. Although it really depends on time of bombardment one can, to a reasonable approximation, assume it to be a constant. A detailed theoretical analysis of this term is given by Fiebiger.[6]

There is one more mechanism by which the concentration decreases. This is the D-D reaction ($D+D \rightarrow He^3+n_0$), and the rate of the decrease due to this mechanism is expressed by the third term, where σ is the cross section of the reaction and is assumed independent of energy. This third term is not important in our case.

Integrating (1) yields

$$n=n_\infty[1-e^{-(AD\gamma+2R\sigma)t}], \tag{2}$$

where

$$n_\infty=\frac{AR}{AD\gamma+2R\sigma}.$$

Now consider the rate of neutron production which is directly proportional to the neutron counting rate, N (atoms sec^{-1}). Since neutrons are produced by the collision between the impinging deuterons and those staying in the penetrated layer, there exists the relation for the rate of production of neutrons

$$N=nR\sigma=N_\infty[1-e^{-(2R\sigma+AD\gamma)t}], \tag{3}$$

where

$$N_\infty=R\sigma n_\infty.$$

From (3), one obtains

$$\ln(N_\infty-N)=\ln N_\infty-(2R\sigma+AD\gamma)t. \tag{4}$$

Thus, the plot of $\ln(N_\infty-N)$ against t (time) yields a straight line as shown in Fig. 2(b), where the necessary data of $(N_\infty-N)$ were obtained from Fig. 2(a). The slope of the straight line gives the coefficient of t in Eq. (4). In Fig. 2(a), the solid curve was calculated from (4) using the experimentally determined values of N_∞ and $(2R\sigma+AD\gamma)$. The agreement between theory and experiment is satisfactory.

2. Diffusion during Annealing

During the annealing, the irradiation was stopped, i.e., $R=0$. The concentration of deuterium then decreases due to diffusion. This is well expressed by the Eqs. (1) to (4). It should be noted, however, that since enhanced diffusivity no longer exists in the bombarded region, the boundary conditions have changed and thus the proportionality constant γ has changed.

Let the quantity, $(N_\infty-N)$, at time zero and t be N_0 and N_t, respectively. By introducing $R=0$ into Eq. (4), one has

$$\ln(N_t/N_0)=-A\gamma D(T)t. \tag{5}$$

The activation energy for diffusion, E_D, of deuterium in tantalum, associated with the neutron counting-rate drops (Fig. 3) at 275 min and 560 min, can be estimated from this equation. Thus, for annealing at two temperatures T_1 (294°K) and T_2 (885°K), one can write

$$\frac{\ln(N_t/N_0)_1}{\ln(N_t/N_0)_2}=\frac{D(T_1)t_1}{D(T_2)t_2}=\frac{t_1[\exp(-E_D/kT_1)]}{t_2[\exp(-E_D/kT_2)]}. \tag{6}$$

Using the experimental values from Fig. 3 $[(N_t/N_0)_1=3.25/4.35$; $(N_t/N_0)_2=3.05/5.85]$ and Fig. 7 ($t_1=5.76\times10^4$ sec; $t_2=168$ sec[11]) a calculation indicates that the activation energy for diffusion of deuterium through a tantalum lattice is about 0.24 ev per atom. A similar calculation based on the data for the 704°C anneal in Fig. 3 $[(N_t/N_0)_1=3.25/4.35$; $(N_t/N_0)_2=2.40/5.17]$ and $t_1=5.76\times10^4$ sec; $t_2=148$ sec yields an activation energy of 0.245 ev per atom. It should be pointed out, however, that since only one point was taken following the anneal at 704°C for 148 sec, a buildup curve similar to the previous one was assumed in order to extrapolate to bombarding-time zero for the relative "background" count of 2.40.

The activation energy of 0.24 ev is in agreement with a value obtained (6 kilocalories) from internal friction studies.[12] It should be remembered, however, that this result is based on the assumption that all of the original atoms of deuterium (i.e., N_0) can leave the effective target area. Although this is not the case, the resulting difference would affect the calculated activation energy only slightly.

3. X Rays

During irradiation of the target, the impregnated deuterium bombarded with deuterons gives rise to two possible reactions, easily detectable with deuterons of 100 kev, with approximately equal probability.[12]

$$(1)\ {}_1H^2+{}_1H^2 \rightarrow ({}_2He^4) \rightarrow {}_1H^1+{}_1H^3+Q$$

$$(2)\ {}_1H^2+{}_1H^2 \rightarrow ({}_2He^4) \rightarrow {}_2He^3+{}_0N^1+Q$$

Thus the lattice distortion, evidenced by Figs. 9 and 10, is caused by (1) the occluded deuterium, (2) helium impurities resulting from the D-D reaction, and (3) radiation damage[14–16] due to (a) impinging deuterons, (b) helium atoms and protons resulting from the two reactions, and (c) neutrons.

The measurements observed with a counter, cali-

[11] The 168 sec results by subtraction from the total time (ordinate of Fig. 7) of about 217 sec, 9 sec during which the temperature did not increase, and approximately 40 sec during which the target was "heating up". Using the time of 168 sec in Eq. (6), an activation energy of .244 ev was obtained. If the total heating time of 208 sec (217 sec−9 sec) is used, an activation energy of .238 ev is obtained.

[12] J. W. Marx, G. S. Baker, and J. M. Sivertsen, Acta Met. **1**, 193 (1953).

[13] M. L. E. Oliphant, P. Harteck, and Lord Rutherford, Proc. Roy. Soc. (London) **144**, 693 (1934).

[14] J. A. Brinkman, J. Appl. Phys. **25**, 961 (1954).

[15] F. Seitz and J. S. Koehler, in *Impurities and Imperfections*, (Am. Soc. Metals. Seminar, 1955), p. 231.

[16] D. K. Holmes and D. O. Thompson in *The Investigations of Radiation Damage Using Mechanical Vibrations* (ASM, 1960).

brated with a "standard" neutron source for efficiency with respect to geometry, showed that a yield of approximately 10^{10} neutrons occurred in the target during the time of bombardment.

In the present experiment, radiation damage is localized, in depth, to the point of neutron production (few microns). However, Fig. 10 shows similar lattice distortions on both the irradiated and nonirradiated side of the target. The radiation damage due to neutrons and all the other product particles will be spread throughout the specimen, but the amount would probably be too small to detect.[17–19] Therefore, the observed lattice expansion and other changes evidenced by Figs. 9 and 10 are thought to be, most importantly, brought about at distant points in the lattice through diffusion of the remaining deuterium atoms not involved in the D-D reaction and which have not diffused out of the target. It is possible that the changes in peak intensities are brought about when the diffusing deuterium takes up interstitial position, causing displacement by local strains of atoms out of reflecting planes.

[17] D. S. Billington and J. H. Crawford, *Radiation Damage in Solids* (to be published by Princeton University Press).
[18] A. Sosin and L. L. Bienvenue, Bull. Am. Phys. Soc., **4**, 169 (1959).
[19] D. O. Thompson and D. K. Holmes, J. Appl. Phys. **27**, 713 (1956).

ACKNOWLEDGMENTS

We thank the National Science Foundation and the University of Utah Research Fund for supporting this work, Mrs. M. Howell for typing the manuscript, and Miss D. McKee for assistance in calculations, preparation of drawings and the manuscript.

JOURNAL OF APPLIED PHYSICS VOLUME 31, NUMBER 10 OCTOBER, 1960

Anomalous Surface Channels on Silicon *p-n* Junctions

RAYMOND SOLOMON
Hughes Semiconductor Laboratory, Newport Beach, California
(Received April 18, 1960; and in final form June 14, 1960)

A chopped-light spot has been used to explore the photoresponse of silicon *p-n* junction surfaces. Anomalous channel responses extending in some cases to distances of 100 mils or more, have been observed on accumulation layer and intrinsic barrier surfaces. The phase shift of the induced ac photocurrent is measured as a function of the distance of the light spot from the junction, and phase shifts of more than 380° have been observed for the anomalous channels. Experimental evidence is offered to show that the excessive phase shift is due to multiple trapping of the injected carriers at surface interface states. Additional evidence indicates that the anomalous channels are a result of an interaction of the fringing field with the slow surface states.

I. INTRODUCTION

MUCH of the anomalous behavior of germanium-device characteristics has been attributed to the formation of inversion layer channels at the surface of the device.[1] Direct confirmation of the existence of these channels was provided by Christensen.[2] Using a traveling-light-spot experiment he observed that the high photoresponse at the junction extended for some distance over the *p* side. Subsequent work by others[3–6] has shown excellent correlation between the growth of inversion layer channels and the incidence of high-leakage currents.

While inversion layer channels have been shown to exist on silicon devices,[5] there is not sufficient evidence that this is the predominant mechanism for the degradation of the reverse characteristic. In a study of silicon-device surfaces conducted at this laboratory, it was found that the occurrence of inversion layer channels could account for only a small fraction of those devices whose characteristics had degraded during normal processing. Furthermore, considerable difficulty was experienced in trying to fit the experimental data to the presently accepted surface model.

In the present work an ac traveling-light probe technique has been used to explore surfaces near a silicon junction. In addition to the usual inversion layer channels, extended photoresponses have been observed on accumulation layers and Schottky (intrinsic) barriers. One of the most interesting properties of these anomalous channels is the excessively large phase shift of the ac photocurrent.

II. APPARATUS

A diagram of the apparatus used in this work is shown in Fig. 1. Light from a high-pressure mercury lamp is filtered to produce monochromatic radiation in the range 3400–4500 A. The light is chopped by a mechanical chopper at 230 cps and focused by a micro-

[1] W. L. Brown, Phys. Rev. **91**, 518 (1953).
[2] H. Christensen, Proc. IRE **42**, 1371 (1954).
[3] R. H. Kingston, Phys. Rev. **93**, 346 (1954).
[4] M. Cutler and H. Bath, Proc. IRE **45**, 39 (1957).
[5] W. T. Eriksen, H. Statz, and G. A. de Mars, J. Appl. Phys. **28**, 133 (1957).
[6] A. R. F. Plummer, Proc. Phys. Soc. (London) **V69**, 539 (1956).

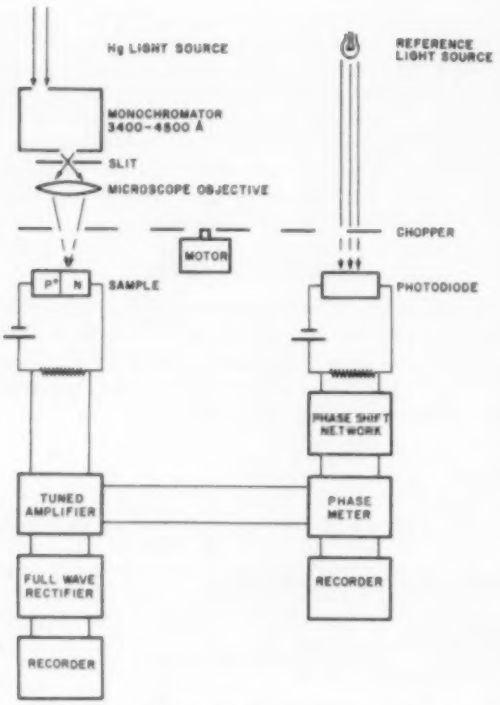

FIG. 1. Block diagram of traveling-light probe apparatus.

scope objective on to the surface of a motor-driven junction bar. The final dimensions of the light spot are 0.2×20 mils. A tuned amplifier with a two-cycle bandwidth allows measurements to be made on noisy and unstable surfaces.

During some early measurements, peculiarities were observed which seemed to be associated with the transport of the injected carriers along the surface, and in order to study this phenomenon a phase-shift measurement was added to the apparatus. The phase angle between the measured photocurrent and a constant reference signal, produced from a flashlight bulb and a photodiode, is measured by an Acton Labs phase meter and recorded as a function of distance of the light slit from the junction. Since we are interested only in the change in phase as the light spot traverses the surface, the fixed phase shifts introduced by the amplifiers are canceled with a phase shifting network.

Most of the samples used in these experiments are p^+-n grown junction silicon bars, with 0.01 ohm-cm p-type and 10 ohm-cm n-type resistivities. Since the junction space-charge region extends almost wholly into the n-side, only the surfaces over this region will have a significant effect on the electrical characteristics. A few experiments have been performed with n^+-p junction bars and alloy-junction devices, and the results are in qualitative agreement.

The bars are etched in an HF-HNO_3 etch and placed in a sample chamber with a thin glass window. Both the ambient flow and temperature inside the chamber could be readily controlled. The surfaces of the junction bar are usually preconditioned by cycling a number of times between ozone and wet oxygen (or wet N_2). While the conditioning treatment is not essential it seems to sensitize the surface so that either accumulation layers or inversion layers could be grown much more readily. Following the conditioning treatment the appropriate ambient was passed over the sample for a time sufficient to establish a steady state condition.

III. EXPERIMENTAL RESULTS

A. Inversion Layer Channels

P-type inversion layers have been grown over the n region by passing ozone over the sample for a time varying from several minutes to several hours. A typical photoresponse obtained for this case is shown in Fig. 2(a). The phase shift [Fig. 2(b)] is negligibly small for this case.

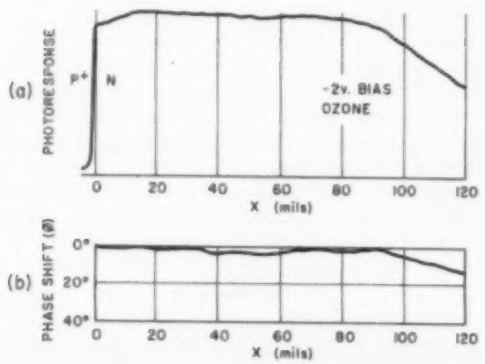

FIG. 2. (a) p-type inversion layer channel grown in ozone. (b) Phase shift of the ac photocurrent as a function of distance of the light spot from the junction.

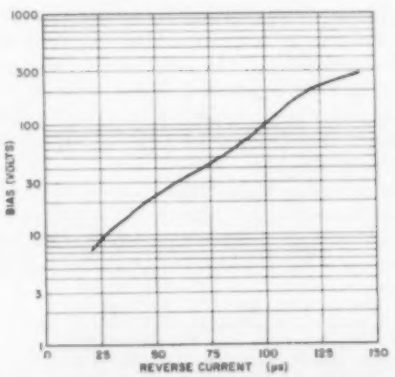

FIG. 3. Reverse characteristic with a p-type inversion layer over the n side of a silicon p^+-n junction.

The reverse characteristic for an inversion channel (Fig. 3) is approximately proportional to the log of the applied voltage, in agreement with the work of Eriksen, Statz, and de Mars.[8] The bias dependence of the channel length is difficult to measure due to the extreme length of the channels, in many cases extending to the end of the bar. It can be stated, however, that the channel appears to be approximately independent of the applied bias.

B. Anomalous Channels

Anomalous channel responses have been observed for both accumulation layers and moderately p-type (Schottky barrier) surfaces. Figure 4(a) shows a typical response for an accumulation layer grown over the n region by passing wet nitrogen over the surface (maintained at 80% rel. humidity by bubbling N_2 through a solution of LiCl). This type of response differs from an inversion-layer channel in that the slope of the plateau region is steeper and may be either linear or approximately exponential. Also the phase shift of the ac photocurrent [Figure 4(b)] is linear with distance and has shifted by more than 250° at the end of the channel. The phase of the photocurrent always lags the reference signal, and the amount of lag increases with increasing distance from the junction. The reverse characteristic for this case, shown in Fig. 5, is often approximately ohmic, although more generally I varies as V^n where $o<n\leq 3$. Anomalous channels similar to these are also observed over the p region of an n^+-p junction when ozone is passed over the surface.

The photoresponse for a moderately p-type surface [Fig. 6(a)] is obtained by passing dry oxygen over the surface. This type of channel response does not have a distinct plateau region, but decays approximately exponentially. The width of these responses (defined as the distance at which it falls to one-third of its peak value) may vary from 10 to 50 mils. The corresponding phase shift, shown in Fig. 6(b), is comparable to those obtained for accumulation-layer channels. If ozone is introduced at this point, the response gradually broadens until an inversion layer channel is formed, and at the same time the phase shift gradually decreases until it becomes negligibly small.

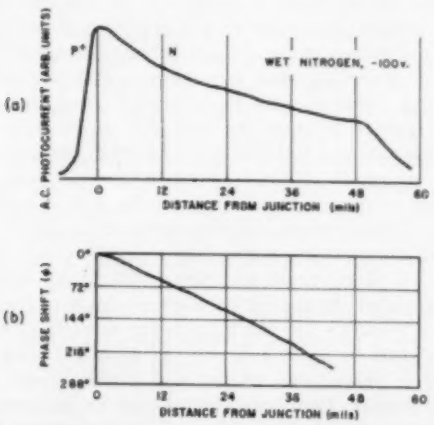

FIG. 4. (a) Anomalous accumulation layer response grown in wet N_2. (b) Phase shift of photocurrent with distance from the junction.

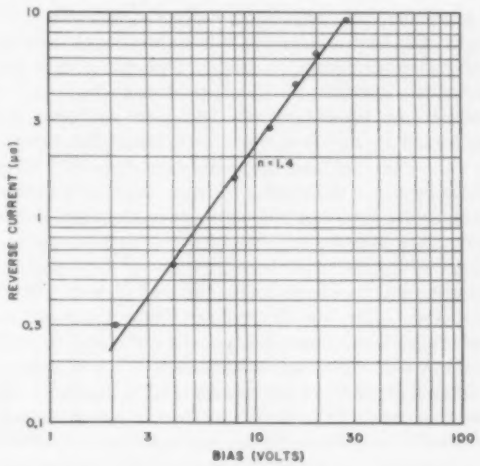

FIG. 5. Reverse characteristic with an accumulation layer grown over the n-region of a silicon p^+-n junction.

The bias dependence of the anomalous channels is often rather complicated. In the low-voltage range (-1 to -50 v) the channel is quite sensitive to voltage, there generally being a marked increase in channel length with increasing reverse bias. Above this range the channel often saturates, i.e., further increases in bias do not have a pronounced effect on the channel. On the other hand, some channels continue to grow with increasing bias up to quite high voltages. At present this behavior is not completely understood.

We have referred to the photoresponses shown in Figs. 4 and 6 as anomalous because they were formed

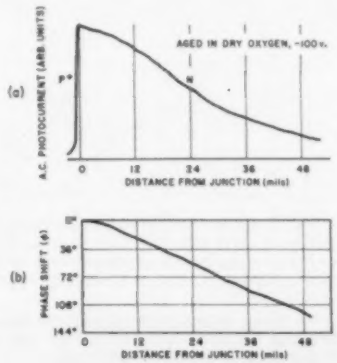

FIG. 6. (a) Anomalous photoresponse for a surface aged in dry O_2. (b) Phase shift as a function of distance.

in ambients, e.g., wet N_2 and dry O_2, which we have found to form accumulation layers and intrinsic barriers, respectively, in silicon filament surface conductance experiments. It is necessary, however, to consider the possibility that an inversion layer may be formed in the immediate vicinity of the junction by the action of the applied bias. This may occur either by ionic movement of impurities on the oxide layer, or by field-induced changes in the slow surface states.[1] While either or both of these mechanisms may be operable, the experimental evidence does not lend support to the view that bias-induced inversion layers are formed. For one thing, large phase shifts are not observed in true inversion layer channels, and secondly the slope of the plateau region (when it is well defined) is much steeper than for inversion layer channels. The strongest evidence against the formation of voltage-produced inversion layers can be obtained by observing the dynamics of channel growth during a modified Brattain-Bardeen gas cycle. Figure 7(a) shows an accumulation-layer response grown over the *n* region by exposing the surface to wet N_2. With the bias maintained constant, the ambient was changed to dry O_2. Figures 7(b)–(e) show the responses after 2, 5, 8, and 15 min, respectively, in dry O_2. It is seen that the response decreases to a minimum and then increases again. If ozone is introduced at (e), the channel continues to broaden until a true inversion layer channel is formed.[7] On the other hand, if wet N_2 is introduced at (e), the response reverses itself, going from (e) back to (a). The reverse current goes through a similar cycle, shown in Fig. 7(f). The cyclic behavior of the reverse current and channel response is quite reproducible on the same junction and between junctions, with differences only in details, i.e., the value of the current minimum, the sensitivity of the junction to ambient cycle, etc.

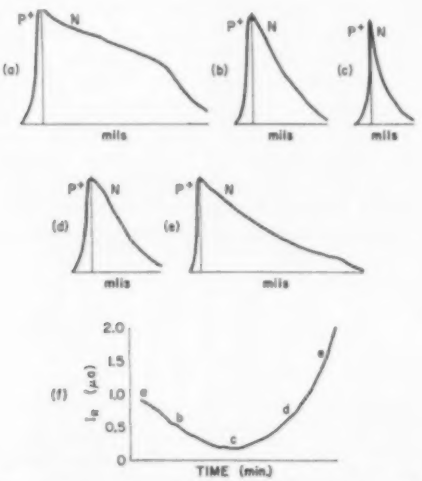

FIG. 7. Change in anomalous photoresponse during a Brattain gas cycle. (a) Wet N_2 channel; (b) response 2 min after introducing dry O_2; (c) response 5 min in dry O_2; (d) 8 min in dry O_2; (e) 10 min in dry O_2; (f) change in reverse current during the gas cycle.

[7] If ozone were introduced initially instead of dry θ_2 the same behavior would be observed, except that the minimum response would occur in a much shorter time.

Several conclusions can be drawn from the ambient cycle experiment illustrated in Fig. 7. If the response shown in Fig. 7(a) were a bias-induced inversion layer, then the introduction of dry O_2 (or ozone) should cause the surface to become even more inverted with a consequent increase in the channel length. Since it decreases to a minimum before increasing again, it is evident that this hypothesis fails to explain the observed behavior.

Secondly, the results are at variance with an ionic movement hypothesis, since according to this hypothesis the introduction of dry O_2, with the bias maintained constant, should "freeze" the ions in place so that the channel response remains unchanged. This is clearly contrary to the behavior shown in Fig. 7. Ambient-cycle experiments performed at $-20°C$ have provided additional evidence against the ionic hypothesis. The channel response continues to cycle at low temperatures, except that it proceeds very rapidly when going from dry O_2 to wet N_2, and very slowly in the reverse direction. This leads us to believe that it is the density of slow surface states which plays an important role in the formation of these channels, since the number of water molecules adhering to the surface should increase at low temperatures, so that the buildup of an accumulation layer channel at these temperatures would be more rapid.

C. Phase Shift Measurement

The phase shift of the injected photocurrent as the light spot moves away from the junction is clearly a surface phenomenon, since the use of nonpenetrating light insures that most of the carriers are generated within a micron of the surface. When penetrating light is used no phase shift is measured, and the photoresponse shows the usual exponential decay. In order to determine whether the excessive phase shift was peculiar to silicon surfaces, several germanium junctions were examined. Despite rather extensive cycling in various ambients, excess phase shifts and anomalous channel responses could not be detected.

The injection of carriers near a junction with an ac light source will result in a phase shift of the external photocurrent depending on whether the rate limiting step is minority- or majority-carrier flow. If it is the latter then no phase shift will be measured since the signal is propagated to the end contacts with the speed of light. This should be the case for an inversion layer, since injected holes flow in a thin *p*-type surface layer which is more or less in equilibrium with the *p*-side of the junction. On the other hand, if the rate

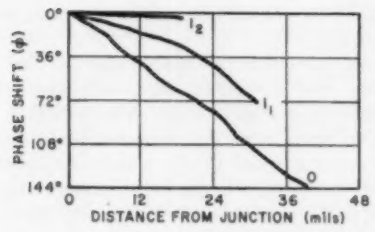

FIG. 8. Change in phase shift when surface is illuminated with nonpenetrating dc light. I_2 represents a higher light intensity than I_1.

limiting step is minority-carrier flow at the surface, a phase shift will arise as a result of the finite time for the minority carriers to reach the junction.[8] The magnitude of the shift depends on the mode of conduction, i.e., whether by diffusion or by drift under the influence of an applied field. An order-of-magnitude estimate for both cases can readily be made. Considering first, drift in an applied field, and assuming a constant drift field, the phase shift is easily shown to be $\phi=(360°/2\pi)(x\omega/\mu E)$, where x is the distance of the light spot from the junction; ω, the angular frequency of the chopped radiation; μ, the drift mobility; and E, the drift field. We shall show later that a drift field of about 1 v/cm is a reasonable estimate. Hence the phase shift for a light spot 10 mils from the junction is calculated to be less than one degree.

Although the shape and extent of the photoresponses shown in Figs. 4 and 6 preclude diffusion in the presence of recombination as the dominant mechanism, we can nevertheless estimate the phase shift for this case. With the light spot located a diffusion length from the junction the phase shift is given by $\phi=360°(\tau_s/T)$, where τ_s is the surface minority-carrier lifetime, and T is the period of the ac excitation. Assuming a surface lifetime of 1 μ sec, the phase shift for this case is 0.06 deg/mil.

Since the measured phase shifts may be orders of magnitude in excess of the above estimates, it is apparent that another mechanism will need to be considered. The explanation which best fits the experimental facts is that the phase shift arises from multiple trapping of the injected minority carriers at surface interface states. We will neglect for the moment any explanation of how this may occur, and consider possible experimental tests for the hypothesis. Unfortunately, the techniques developed by Haynes and Hornbeck[9] in their study of multiple trapping in the bulk are not readily adaptable to surfaces, especially surfaces adjacent to a junction. It is possible, however, to predict qualitative changes in the phase shift from ambient dc light, and temperature measurements. In the first named experiment the surface is uniformly illuminated with low intensity nonpenetrating dc light, and the surface is probed with the ac light spot. If the ac carriers are being trapped, then the added dc carriers should tend to saturate the traps, thereby reducing the magnitude of the phase shift. This effect can be seen in Fig. 8, where I_1, I_2, represent increasing dc light intensities. At the higher light intensity (I_2) the phase shift is almost completely wiped out. In performing this experiment one must consider the possibility that the dc light may produce a secondary effect in that it tends to flatten the surface barrier, and may thereby alter the conditions which result in the phase shift. This would be especially true at the higher light intensities. However, we have been able to observe a decrease in the phase shift for very low intensities, where the calculated number of injected carriers is too small to appreciably affect the surface barrier. That this is true is substantiated by the fact that the ac photoresponse is not perceptibly altered at these low intensities.

Since the time constant for trapping may be expected to be temperature dependent, the slope of the phase shift should increase with decreasing temperature. In practice, however, interpretation of the experiment is complicated by the fact that the channel response is not a constant with changing temperature, so that both the surface potential and trapping time constant may be changing simultaneously. It is possible to minimize this effect by performing an ambient cycle at several temperatures and comparing the phase shifts for channel responses of approximately the same shape and extent. Figure 9 shows the slope of the phase shift as a function of temperature. The significant fact, here, is that the slope of the phase shift increases with decreasing temperature, and no significance can be attached to the fact that the points fall on a straight line.

It must be admitted that the evidence in favor of trapping is largely qualitative, and is a reflection of the fact that significant quantitative measurements are extremely difficult to make on device surfaces. The main virtue of the trapping hypothesis is that it fits

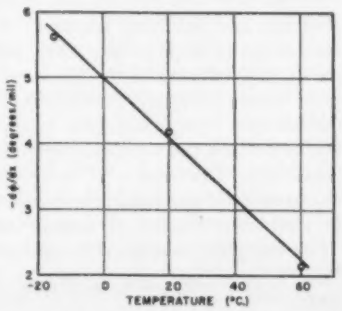

FIG. 9. Slope of the phase shift vs temperature for an anomalous channel.

[8] A discussion of these points can be found in *Electrons and Holes in Semiconductors* by William Shockley (D. Van Nostrand Company, Inc., Princeton, New Jersey, 1950).

[9] J. R. Haynes and S. A. Hornbeck, Phys. Rev. **90**, 1952 (1953); Phys. Rev. **100**, 606 (1955).

the body of experimental evidence to a much greater extent than any other proposed hypotheses. Perhaps it would not be out of order to discuss briefly some of the other mechanisms that have been considered. The most interesting of these, and historically the first to be considered, is that the surface behaves like a distributed RC transmission line, so that as the light spot traverses the surface more and more elements of surface capacitance and surface resistance are added to the circuit. By using an RC transmission line model one can calculate the differential surface capacitance and surface resistance as a function of distance from the junction, using the measured values for the phase shift and amplitude of the photoresponse. The resultant values of capacitance, however, are much larger by many orders of magnitude (a typical value is 10 μfarad/cm^2) than the space charge capacitance calculated from Poisson's equation. Furthermore, the values for capacitance obtained from this model sometimes go negative, indicating that the surface cannot be described by a simple RC transmission line. A second possible mechanism is that the extended photoresponse is associated with a surface breakdown phenomena. If this were true, however, one would expect to observe noise pulses in both the reverse current and the ac photocurrent. The fact is that both measurements are usually remarkably steady and free of pulses, even when observed on fast responding equipment. When the surface is noisy it is still usually possible to distinguish between this and the kind of pulses one observes when the junction is biased into the surface breakdown region. And finally, it need hardly be pointed out that this hypothesis does not offer a ready explanation for the large shifts that are observed. Several other hypotheses, e.g., conduction in an oxide layer, or conduction in a surface impurity band, appear to offer little of value. Beside the theoretical difficulties inherent in these models, it is apparent that the experimental behavior with respect to dc light, temperature, and ambient flow, are not easily reconciled.

IV. DISCUSSION

A. Calculation of Fringing Field

It is clear that the presently accepted model for surfaces does not predict the presence of anomalous channels and multiple trapping. Therefore, it seems reasonable to assume that they are a result of some perturbing influence of the junction. One such influence may be caused by an interaction of the fringing field outside the junction, which exists by virtue of the fact that the p and n regions are maintained at different potentials. The effect of fringing fields on device characteristics was considered by Garrett and Brattain[10] in their examination of surface breakdown voltage. Their analysis, however, did not disclose the magnitude of this field or the distance from the junction over which it acts.

One can calculate the magnitude of the normal component of the fringing field with the simplified model shown in Fig. 10(b).[11] The junction bar is assumed to be replaced by two metal plates separated by a distance d equal to the width of the junction. The plate on the right is grounded, and a potential V_a is applied to the plate on the left. By using the Schwarz-Christoffel transformation

$$Z=d\cosh W=d\cosh(u+iv), \tag{1}$$

the upper half of the Z plane is mapped into a strip in the W plane with the positive and negative x axis forming the lower and upper bounds of the strip. By using a scale factor so that $v=\pi$ at the upper bound, the harmonic potential function inside the strip is

$$V=(V_a/\pi)v. \tag{2}$$

On differentiating (2) and making use of (1), the fringing field normal to the surface is

$$E_f=-\frac{\partial V}{\partial y}=-\frac{V_a}{\pi}\frac{\sinh u\cos v}{\sinh^2 u\cos^2 v+\cosh^2 u\sin^2 v}. \tag{3}$$

Transforming back to x-y coordinates and evaluating for $y=0$, the field outside the surface of the right-handed plate is given by

$$\begin{aligned} E_f|_{y=0}&=-(V_a/\pi)d(\cosh^2 u-1)^{-\frac{1}{2}}\\ &=-V_a[\pi(x^2-d^2)^{\frac{1}{2}}]^{-1}. \end{aligned} \tag{4}$$

Figure 11 shows a plot of E_f vs x for several applied biases. It can be seen that the fringing field may be quite appreciable at large distances from the junction.

At first thought the use of a metal plate in the above model might seem to be a poor approximation to a semiconductor surface, since the metal plate imposes the boundary condition that the surface be an

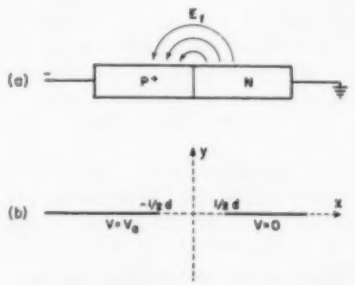

FIG. 10. (a) Representation of the fringing field across the junction. (b) Simplified model of a junction in which two metal plates, separated by a distance d equal to the width of the junction, have a potential difference applied to them.

[10] C. G. B. Garrett and W. H. Brattain, J. Appl. Phys. **27**, 299 (1956).

[11] The author wishes to thank Dr. R. A. Gudmundsen for suggesting this approach.

equipotential. However, in the case of the semiconductor there will certainly be some equipotential surface located within a Debye length of the surface. Hence as long as the Debye length is much less than the width of the junction the approximation will be a good one.

An experimental check of the above considerations can be obtained by placing a field plate over the n region, since the external field produced by applying a voltage between the field plate and the semiconductor approximates the fringing field across the junction. We have, in fact, been able to grow large anomalous channels and phase shifts on a freshly etched junction simply by applying a negative voltage to the field plate. Figure 12(a) shows the photoresponse of a freshly etched junction, and 12(b) shows the same junction after a negative voltage has been applied to the field plate. The field required to grow this channel, approximately 5×10^5 v/cm, is about an order of magnitude higher than that calculated in Fig. 11. This is to be expected, however, since the fringing field at zero field voltage was not large enough in this case to grow an anomalous channel. In order to measure

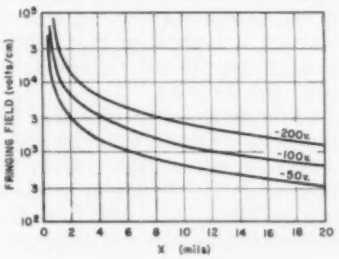

FIG. 11. Calculation of the fringing field as a function of distance from the edge of the junction for several reverse biases.

the average value of the fringing field, an anomalous channel was grown in dry O_2. With a constant reverse bias of -100 v applied to the junction, a series of positive voltage steps were applied to the field plate. The minimum field which caused a reduction in the anomalous channel, and thus cancelling the fringing field, was approximately 4×10^4 v/cm. This agrees reasonably well with the calculated values in Fig. 11.

An objection can be raised to the field-effect experiment in that the field plate over the n region could cause changes at the surface which compromises this experiment as a test for the fringing field hypothesis. To meet these objections an experiment was performed in which the field plate was placed over the p^+ region rather than the n region. It was thought that by applying a negative bias to the field plate over the p^+ region a synthetic fringing field could be produced which might affect the photoresponse over the n region, and since the plate was not in direct contact with the n region there could be no secondary effects. The plate was carefully aligned so that the edge was approximately 0.0005 in. from the junction over the p^+ side.

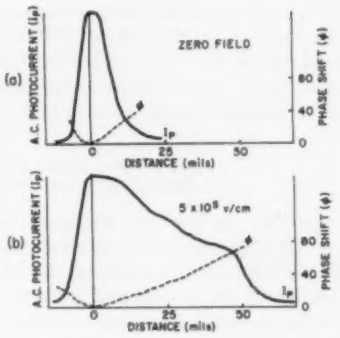

FIG. 12. Direct current field - effect measurement on a silicon junction. (a) Response of freshly etched junction; (b) response after a negative voltage is applied to the field plate.

When a negative voltage was applied to the field plate the channel response over the n region was observed to increase by about 25%. The increase was greatest nearest the junction, but changes were observed as far as 25 mils from the junction. In view of the relative crudeness of the experiment this is felt to be excellent confirmation of both the existence of a fringing field and its role in the growth of anomalous channels.

Since anomalous channels are grown only after cycling a number of times in various ambients, it is apparent that there must be some interaction between the fringing field and the slow surface states. From dc field effect measurements on single-crystal filaments, we know that the perturbed surface potential eventually relaxes back to its equilibrium condition, due to trapping of the excess charge in the slow surface states. On the other hand, when a sudden increase in reverse bias is applied to the junction (or alternately, a negative voltage to the field plate) the channel response increases within a few seconds to a new steady-state value, with no sign of a subsequent relaxation. Hence it is apparent that the surface near a junction is somehow prevented from relaxing to its original condition. This is probably due to the fact that current is flowing parallel to the surface, so that excess charge is removed before it can decay into the slow states.

Without additional information it is difficult to speculate on the nature of the interaction of the fringing field with the slow surface states. Nevertheless, certain general conclusions can be drawn about its effect on the surface space charge region. The very existance of anomalous channels, indicating that carriers injected at a distance can be collected at the junction before they recombine, suggest that one effect of the fringing field is to severely lower the surface recombination rate. When we consider this together with the fact that anomalous channels are always accompanied by trapping of the injected carriers, we are led to the conclusion that the injected holes are trapped at the interface states which normally act as the recombination centers at equilibrium. Since the surface recombination rate is reduced, due possibly to a depletion of surface electrons, the trapped holes are

eventually re-emitted to the valence band where they are free to conduct in a drift field. We shall offer evidence in the next section to show that the parallel component of drift field arises from a nonuniformity of the normal component of the fringing field.

V. DRIFT OF CARRIERS IN THE PRESENCE OF TRAPS

In this section we consider some details of the surface trapping process. We will use the Shockley-Read-Fan[12,13] model to calculate the drift of ac injected carriers in the presence of traps. A single energy level at the surface is assumed at which both trapping and recombination may occur. The transition rates/unit surface area/sec are given by the usual expressions

$$R_{tv}=r_v n_t p_s$$
$$R_{ct}=r_c n_s(N-n_t)$$
$$R_{vt}=r_v p_{s1}(N-n_t)$$
$$R_{tc}=r_c n_{s1} n_t$$

where the last two equations make use of the principle of detailed balancing; and p_s and n_s are the surface concentrations of holes and electrons; p_{s1} and n_{s1}, the concentration of holes and electrons when the fermi level lies at the trap energy; N, the concentration of traps; n_t, the concentration of electrons in the traps; and r_c, r_v are rate constants. The rate of change of the electron population in the traps is

$$\partial n_t/\partial t=(R_{tc}-R_{ct})+(R_{tv}-R_{vt}). \tag{5}$$

This can be expressed in terms of two time constants,[13]

$$\partial n_t/\partial t=(1/\tau_\theta)\Delta n_t+(1/\tau_t)(n_t\Delta p_s)/(n_{t0}), \tag{6}$$

where τ_θ is the average time to release a trapped hole, and τ_t the average time to trap a free hole.

If we assume a constant drift field and neglect diffusion, then the continuity equation for excess holes is given by

$$\partial\Delta p_s/\partial t=-E_x\mu_p(\partial\Delta p_s/\partial x)-(\Delta p_s/\tau_s)+(\partial n_t/\partial t), \tag{7}$$

where τ_s is the effective recombination time at the surface. On differentiating Eq. (7) and substituting Eq. (6) we get

$$\frac{\partial^2\Delta p_s}{\partial t^2}+\left(\frac{1}{\tau_s}+\frac{1}{\tau_\theta}+\frac{1}{\tau_t}\right)\frac{\partial\Delta p_s}{\partial t}+E_x\mu_p\frac{\partial^2\Delta p_s}{\partial x\partial t}+\frac{E_x\mu_p}{\tau_\theta}\frac{\partial\Delta p_s}{\partial x}+\frac{1}{\tau_\theta\tau_s}\Delta p_s=0. \tag{8}$$

By assuming a solution of the form

$$\Delta p_s=P(x)\epsilon^{-j\omega t},$$

and substituting into Eq. (8), we find that

$$\Delta p_s=P_0\epsilon^{-ux}\epsilon^{-j(\omega t+\theta)},$$

where u is the decay constant and θ the phase shift of the ac photoresponse, approximately given by

$$u\simeq\frac{1}{E_x\mu_p}\left[\frac{1/\tau_s+(\omega\tau_\theta)^2/\tau_t}{1+\omega^2\tau_\theta^2}\right], \tag{9}$$

$$\theta\simeq\frac{\omega x}{E_x\mu_p}\left[1+\frac{\tau_\theta/\tau_t}{1+\omega^2\tau_\theta^2}\right]. \tag{10}$$

On combining Eqs. (9) and (10),

$$K=\frac{u}{d\theta/dx}=\frac{1}{\omega}\left[\frac{1/\tau_s+(\omega\tau_\theta)^2/\tau_t}{1+\omega^2\tau_\theta^2+\tau_\theta/\tau_t}\right],$$

where K is an experimentally determined constant. Since τ_t, the average time to trap a free hole, should be of the order of the equilibrium surface lifetime it is reasonable to assume a value of 10^{-6} sec. Then for $\omega^2\tau_\theta^2\lesssim 1$, $\tau_\theta\simeq K/\omega$. For a typical dry O_2 response $K\approx 0.6$, so that the average time to free a trapped hole is $\tau_\theta\approx 400$ μsec. Since this is approximately equal to the time it takes an injected carrier to reach the junction, it is apparent that injected holes are on the average trapped only a few times before they are collected.

Substituting the above value for τ_θ into Eq. (10) and using a typical value for the slope of the phase shift we find that $E_x\approx 1$ v/cm. This is a relatively large value for the parallel component of drift field, and can be shown to arise from the non-uniformity of the normal component of fringing field.

At the surface we have the boundary condition

$$D_{\text{out}}-D_{\text{in}}=\omega_s, \tag{11}$$

where ω is the surface charge density. Hence we can match the fringing field (Eq. 4) to a solution of Poisson's equation in the space-charge region. If we assume that in the space-charge region $E_y\gg E_x$, then a one-dimensional solution[14] can be used. Furthermore we shall assume, for simplicity, that ω remains constant and is equal to the equilibrium surface field. Then we have

$$-\frac{V_a}{\pi(x^2-d^2)^{\frac{1}{2}}}-2\epsilon\left(\frac{n_i kT}{\epsilon\epsilon_0}\right)^{\frac{1}{2}}\left(\cosh u_s-\cosh u_B-\frac{N_d}{2n_i}(u_s-u_B)\right)^{\frac{1}{2}}=\frac{\omega}{\epsilon_0}$$
$$=-2\epsilon\left(\frac{n_i kT}{\epsilon\epsilon_0}\right)^{\frac{1}{2}}\left(\cosh u_\infty-\cosh u_B-\frac{N_d}{2n_i}(u_\infty-u_B)\right)^{\frac{1}{2}} \tag{12}$$

[12] W. Shockley and W. T. Read, Jr., Phys. Rev. **87**, 835 (1952).
[13] H. Y. Fan, Phys. Rev. **92**, 1424 (1953).
[14] See, for example, R. H. Kingston and S. F. Neustadter, J. Appl. Phys. **26**, 718 (1955).

where u_s is the surface barrier in units of q/kT; $u_{s\infty}$, the surface barrier far from the junction; and u_B, the potential of the bulk Fermi level relative to the center of the band.

On substituting for d the usual expression for a step junction, and solving for x,

$$x^2=\frac{2\epsilon\epsilon_o}{qN_d}V_a+\left(\frac{V_a}{2\pi}\right)^2\frac{\epsilon_o}{\epsilon n_i kT}\times\left\{\left[\cosh u_s-\cosh u_B-\frac{N_d}{2n_i}(u_s-u_B)\right]^{\frac{1}{2}}-\left[\cosh u_{s\infty}-\cosh u_B-\frac{N_d}{2n_i}(u_s-u_B)\right]^{\frac{1}{2}}\right\}^2. \quad (13)$$

Assuming $V_a=-100$ v, $u_B=8$, $u_{s\infty}=4$, Eq. (13) can be solved numerically for u_s as a function of x. Differentiating u_s with respect to x, the parallel component of drift field is obtained. Table I shows several values of the drift field calculated from Eq. (13). The calculation neglects the effect of the diffusion component of the current, so that the true drift field may be larger or smaller depending on the net direction of the diffusion current.

TABLE I. Calculated values for drift field at several distances from the junction.

x (mils)	E_x (v/cm)
2.0	10
5.4	1
9.0	0.1

VI. CONCLUSIONS

We have shown that silicon junctions, unlike germanium, exhibit anomalous channel responses which differ from the usual inversion layer channel in several respects. The most important of these is the rather large phase shift of the ac photocurrent, which we attribute to temporary trapping of the injected holes at the surface interface states. We have suggested that the surprisingly extensive fringing field which exists outside the junction may be a factor in the formation of anomalous channels, with a consequent modification of the recombination process to include trapping of minority carriers. Experimental evidence supporting the fringing field hypothesis rests primarily on the results obtained with a dc field plate over the junction region. Other evidence of a qualitative nature also tends to support this view. For example, we have observed that if the resistivity on the p-side of the junction is increased to about 10 Ω-cm, anomalous channels can only be formed at very high reverse biases. This is presumably due to the fact that the much wider junction width reduces the magnitude of the fringing field in the region adjacent to the junction.

It should be pointed out that there are several questions which we have not been able to resolve. The fringing field by itself is evidently not sufficient to form an anomalous channel, since a high density of surface states is apparently prerequisite. Furthermore, the sign of the slow states evidently makes little difference, for anomalous channels are formed equally well on moderately p-type surfaces grown in dry O_2, as for accumulation layer surfaces grown in wet N_2. There is, of course, some question as to whether we are actually changing surface type by changing ambients; however, the fact that the channel response goes through a minimum (Fig. 7) when the ambient is changed leaves little doubt that the surface is indeed converting type.

One other point not yet resolved is the fact that the fringing field calculated in the previous section, although quite significant, does not appear to be large enough to effect an appreciable reduction in the surface recombination velocity. It is possible that another effect might contribute to a reduction in s. For example, the drift field parallel to the surface could cause sweep-out of minority carriers at the surface. This would have the effect of causing the Fermi level for holes on the p side to extend deeper into the surface on the n side, thereby causing a large voltage to appear between the surface and the n-type bulk. As an additonal complication we must consider the fact that recent information indicates that s in silicon is not a constant but varies linearly with the minority carrier concentration at the surface.[15] In view of our rather incomplete knowledge of the surface recombination process, it is unlikely that we can resolve these questions until a more thorough investigation is made.

ACKNOWLEDGMENT

The writer is greatly indebted to Phillip Johnson for his valuable aid in the performance of the experiments. He would also like to thank Dr. Evan Kane and Dr. William Portnoy for useful discussions.

[15] H. M. Bath and M. Cutler, Phys. and Chem. Solids 5, 171 (1958).

Effect of Thermal History on the Dislocation Substructure near the Surfaces of a Lithium Fluoride Crystal

J. M. SCHULTZ* AND J. WASHBURN†
Department of Metallurgy, University of California
(Received April 18, 1960; and in final form June 13, 1960)

A series of x ray and etch pit experiments has been performed to determine some of the effects of temperature on the perfection of surface layers in LiF. It was found that the perfection of a cleaved surface is substantially increased at temperatures near the melting point, that rearrangement and annihilation of dislocations takes place at much lower temperatures, and that rapid cooling promotes the formation of shallow dislocation loops.

PLASTIC properties of crystals having the NaCl structure are greatly affected by the perfection of the surface layers. Large cleavage steps or other surface damage may greatly reduce the amount of plastic deformation that precedes fracture by promoting nonuniform distribution of slip, or by blocking the emergence of dislocations from the surface. Even if care is taken to avoid surface damage there is considerable variation in the uniformity with which slip is distributed. It has been shown that slip bands in LiF originate primarily at the surfaces.[1] The distribution of slip is probably determined by the density of free dislocations in the surface layers of the crystal. One way in which annealing may affect the plastic properties of an ionic crystal is to change the density of surface slip sources. The purpose of the experiments reported here was to determine the effect of typical annealing treatments on the density of dislocations in the vicinity of the free surface.

The dislocation within about 20 μ of the surface in a relatively perfect crystal can be conveniently observed by x ray microscopy.[2] Figure 1(a) shows individual dislocations and small angle boundaries as revealed by this technique; 1(b) shows a region of the crystal which had been plastically deformed.[3] Slip took place on three systems of the type $\langle 110 \rangle \{110\}$. The diagonal bands are on planes at 90° to the plane of the surface and the horizontal bands represent slip on planes at 45° to the specimen surface. Individual dislocations can be seen extending into the crystal on these 45° planes. From the length of dislocation lines that were observed in these bands it was determined that the effective depth of penetration for the x ray microscopy technique was about 20 μ.

When a specimen is cleaved from a large as-grown crystal new surfaces are created. The dislocation segments ending at these new surfaces have been cut free from their previous anchor points. It might therefore be expected that heating to a temperature at which dislocations would have climb as well as glide mobility would result in considerable rearrangement of disloca-

(a)

(b)

FIG. 1. Dislocations in the surface layers at an LiF crystal as revealed by x ray microscopy. (a) Isolated dislocations and small angle boundaries, (b) dislocations in slip bands. (Magnification 66.6×.)

FIG. 2. Decrease in dislocation density near surfaces caused by heating to 800°C for 16 hrs. Bottom edge of micrograph is the original surface. (Magnification 66.6×.)

* Now at Westinghouse Research Laboratories, Pittsburgh, Pennsylvania.
† Associate Professor of Metallurgy, University of California, Berkeley, California.
[1] J. J. Gilman, J. Appl. Phys. **30**, 1584 (1959).
[2] J. B. Newkirk, Trans. AIME **215**, No. 3, 483 (1959).
[3] All figures in this paper were obtained using (220) reflection of CrK_α radiation from the (010) cleavage face of LiF single crystals.

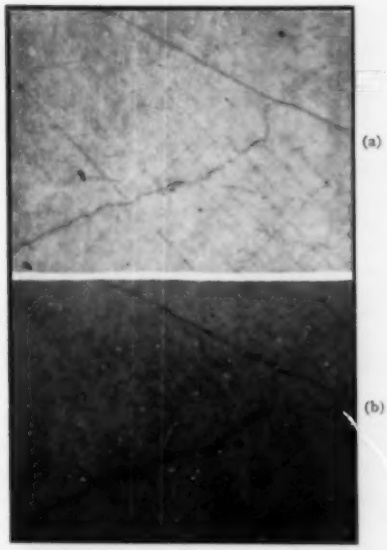

FIG. 3. Annihilation and climb of dislocations in slip bands after heating for 1 hr at 426°C. (a) Before heating, (b) after heating. (Magnification 66.6×.)

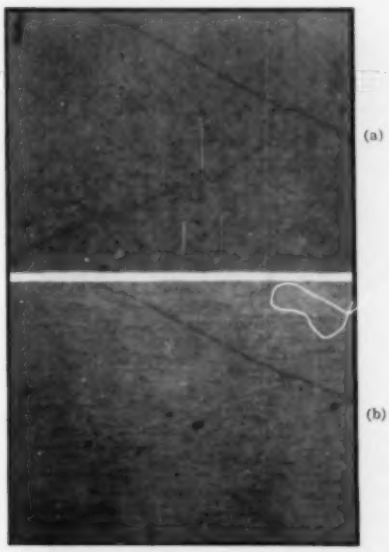

FIG. 4. Surface damage caused by rapid cooling from elevated temperature. (a) Cooled from 400°C at 125°C per minute, (b) cooled from 600°C at 125°C per minute. (Magnification 66.6×.)

tions near the new surfaces. It was found that long annealing relatively close to the melting temperature was required to produce marked changes in the grown-in dislocation population. Figure 2 shows a lower dislocation density near the surface than in the interior of a crystal which had been held at 800°C in air for 16 hr. The bottom edge of the micrograph is one of the original surfaces, the specimen having been cleaved again after heating to reveal the interior. The density of dislocations emergent at the surfaces was decreased from $10^5/cm^2$ to $2\times10^4/cm^2$ whereas the interior dislocation population was essentially unchanged.

In crystals which had been plastically deformed slightly, prior to annealing, dislocation rearrangement near surfaces within the slip bands started at much lower temperatures. Figure 3 shows slip bands at 90° to the surface for which the slip vector is parallel to the plane of the surface. After heating for one hour at 426°C it can be seen that considerable annihilation of dislocations has taken place within the bands, and climb of some dislocations out of their original planes of slip appears to have occurred.

Although annealing treatments generally tended to eliminate dislocations preferentially from the surface layers, relatively rapid cooling from the elevated temperature could reintroduce large numbers of dislocation loops. Figures 4(a)(b) show the effect of cooling at approximately 125°C per minute. Biaxial tension stresses were set up in the surface layers; these stresses were high enough to cause formation of dislocation loops in the four $(110)\{1\bar{1}0\}$ systems at 45° to the plane of the surface. Such dislocation loops must be elongated and quite shallow since most of them seem to lie within the 20-μ depth of penetration of the x rays. In the diffraction arrangement chosen for the pictures only one set of loops is revealed; the components of the Burgers vectors normal to the diffracting plane were either zero or small in the other three sets.[2] Rotating the crystal 90° about an axis normal to the surface revealed the presence of a similar set of loops at 90° to the ones shown.

SUMMARY

Annealing after cleavage to final shape tended to eliminate dislocations preferentially from the surface layers of a specimen of LiF. Although short range rearrangements began below 400°C, prolonged annealing at 800°C was required to cause marked changes in the grown-in substructure. A high density of shallow dislocation loops could be introduced into the surface layers of a specimen by cooling at a rate of 125°C/min or greater.

ACKNOWLEDGMENTS

The work was made possible by a grant from the National Science Foundation. The authors would also like to thank Dr. Alfonso Merlini for his help during the early stages of the project.

Anisotropy of the Magnetic Susceptibility of Gallium*

TITUS PANKEY, JR.
Howard University and U. S. Geological Survey, Washington, D. C.
(Received May 16, 1960; and in final form July 5, 1960)

The bulk magnetic susceptibilities of single gallium crystals and polycrystalline gallium spheres were measured at 25°C. The following anisotropic diamagnetic susceptibilities were found: a axis $(-0.119\pm0.001)\times10^{-6}$ emu/g, b axis $(-0.416\pm0.002)\times10^{-6}$ emu/g, and c axis (-0.229 ± 0.001) emu/g. The susceptibility of the polycrystalline spheres, assumed to be the average value for the bulk susceptibility of gallium, was $(-0.257\pm0.003)\times10^{-6}$ emu/g at 25°C, and $(-0.299\pm0.003)\times10^{-6}$ emu/g at −196°C. The susceptibility of liquid gallium was $(0.0031\pm0.001)\times10^{-6}$ emu/g at 30°C and 100°C. Rotational diagrams of the susceptibilities in the three orthogonal planes of the unit cell were not sinusoidal. The anisotropy in the single crystals was presumably caused by the partial overlap of Brillouin zone boundaries by the Fermi-energy surface. The large change in susceptibility associated with the change in state was attributed to the absence of effective mass influence in the liquid state.

INTRODUCTION

GALLIUM is orthorhombic,[1] with a, b, and c unit cell dimensions of 4.5167, 4.5107, and 7.6448 angstrom units, respectively. Its melting point is given as 29.78°C, but it may be easily supercooled to temperatures near 0°C. The first Brillouin zone is a sphere-like polyhedron containing three electron states/atom.[2] Therefore, the Fermi-energy surface in trivalent gallium should overlap the zone boundaries in various directions and cause large anisotropy in effective mass and related properties such as magnetic susceptibility.

The magnetic susceptibility of gallium was measured by Owen[3] in 1912 and by Marchand[4] in 1955. Marchand, who worked with single crystals, gave values for each of the three-orthogonal axes. The values reported are compatible with calculated values. However, the literature on the susceptibility of gallium is rather scant, and it was believed that the work of Owen, Marchand, and others should be checked and extended. Furthermore, the following discrepancies in their work should be clarified.

(1) Although Owen and Marchand both found gallium in the solid state to be diamagnetic, Owen found it to be diamagnetic and Marchand found it to be paramagnetic in the liquid state.

(2) Marchand's average value calculated from the three anisotropic susceptibilities was not compatible with the value determined on a powdered sample.

It is the purpose of this paper to redetermine the anisotropy of the magnetic susceptibility of gallium to check the above work and clarify these two points.

EXPERIMENTAL PROCEDURE

A single crystal of electronic grade gallium containing no spectroscopic trace of iron (Table I) was measured on a quartz helix balance of the Curie-Cheneveau type.[5] A quartz helix of 1-mg/cm sensitivity was used for the accurate quantitative measurements. A series of permanent magnets ranging from 1800–9000 gauss supplied the magnetic fields.

Larger crystals of gallium from the same lot were also used to measure the relative anisotropy of the magnetic susceptibility. To check these larger macroscopic crystals for relative anisotropy, a special Pyrex spring was constructed which possessed a marked curvature in its deflection vs force curve. A least-square relationship of the type $y=ax-bx^2$, where $y=$ extension and $x=$ mass, was fitted to the curvature. This equation was differentiated to give the spring force constant dy/dx as a function of x (i.e., $dy/dx=a-2bx$). The equation was solved for x as a function of y, thus giving mass as a function of extension.

To correct for traces of ferromagnetic impurities, whose field dependent susceptibilities may contribute appreciably to the bulk susceptibility at the field strengths used, it was necessary to plot bulk susceptibility vs $1/H$, and extrapolate to infinite field, where the field dependent ferromagnetic susceptibilities are zero.

TABLE I. Semiquantitative spectrographic analysis of gallium.

Ga	10–100%
Fe	none detected
Ag	0.001 –0.01
Cu	0.0001–0.001
Pb	0.01 –0.1
Mg	0.001 –0.0001
Ca	0.001 –0.0001
Cr	none detected
Ni	none detected
Co	none detected
Mn	none detected

* This work was performed for the U. S. Geological Survey in the laboratory at Howard University and used as partial fulfillment of the requirements for a Master's degree, Department of Physics, Howard University. Publication authorized by the Director, U. S. Geological Survey.

[1] A. J. Bradley, Z. Krist. **91**, 302–316 (1955).
[2] G. V. Raynor, Phil. Mag. **31**, 140 (1941).
[3] M. Owen, Ann. Physik, **342**, 694 (1912).
[4] A. Marchand, Compt. rend. **241**, 470 (1955).
[5] F. E. Senftle, M. D. Lee, A. A. Monkewicz, J. W. Mayo, and Titus Pankey, Rev. Sci. Instr. **29**, 429 (1958).

TABLE II. Magnetic susceptibility of gallium (10^{-6} emu/g).

Investigator or calculation model	Solid	Liquid	Measurements along axes		
			a	*b*	*c*
Owen	−0.25 (16°−30°C)	−0.04 (16°−30°C)	...	...	...
Marchand	−0.31[a] (17°C)	0.038 (40°C)	−0.15	−0.51 (17°C)	−0.28
This work	−0.257[b] (25°C)	0.0031 (30°C)	−0.12	−0.42 (room temp)	−0.23
Calculated after Pines[c,d,e]	−0.23	...	...	...	...

[a] Rejected the −0.27 value for a powder sample.
[b] Quenched sample. See text.
[c] Assumed that real mass was effective mass.
[d] Pines considers correlation and exchange interactions among the free electrons in making spin-susceptibility calculations. *Solid State Physics* 1 (Academic Press, Inc., New York, 1955), pp. 417–420.
[e] Used core correction of −0.33; J. C. Slater, Phys. Rev. **36**, 57–64 (1930).

The change in susceptibility as a function of change of state was observed by performing the measurement at a temperature below the melting point (29.78°C). By supercooling the specimen it could be measured in both the liquid and solid state at the same temperature.

RESULTS

A sample of solid gallium was measured at 26°C and found to be diamagnetic. However, the same sample liquefied and supercooled to the same temperature was slightly paramagnetic, thus demonstrating that the large change in susceptibility is directly related to the change of state. A similar experiment had been performed by Owen with the same results.

Accurate measurements on three samples in the liquid state were averaged to give a mean value of $(0.0031\pm0.001)\times10^{-6}$ emu/g at 30°C as the sucseptibility of liquid gallium (Table II). Each of the samples had a very small field-dependent susceptibility even though the spectrographic analysis revealed no trace of ferromagnetic impurities.

The rather large standard deviation of the mean, and hence a significant range of values for the susceptibility, is believed to be due to the effect of variations in the small impurity content from sample to sample. However, most of the impurities shown in the analysis of Table I are diamagnetic and will tend to depress the susceptibility of gallium. Gallium must therefore have a positive bulk susceptibility in the liquid state contrary to the results of Owen. No change in this susceptibility was noted from room temperature up to the steam point.

Similar measurements on a solid-crystalline sample at 26°C gave the following anisotropic susceptibilities along the axes determined by x-ray diffraction: *a* axis $(-0.119\pm0.001)\times10^{-6}$ emu/g, *b* axis $(-0.416\pm0.002)\times10^{-6}$ emu/g, and *c* axis $(-0.229\pm0.001)\times10^{-6}$ emu/g. (In one preferred orientation, a value of −0.0259 was found.)

To compare the values determined along axes found by x-ray diffraction with the values for axes determined by symmetry, measurements were made on a truncated bi-pyramid crystal similar to that which has been reported by Blom.[6] A narrow slice of the pyramid was sawed off in a plane parallel to the tops of the pyramids (see Fig. 1) and cleaned with cold hydrochloric acid and water. It was assumed that a normal to this plane was the *c* axis, and that the two shorter axes (*a* and *b*) were diagonals of the plane. With the *c* axis parallel to the magnetic field, both the highest and the lowest values were measured along the shorter axes. The largest, -0.35×10^{-6} emu/g, was five times the smallest, and twice the value obtained with the *c* axis as field axis. The magnitudes of these values are somewhat lower than the previously mentioned values, since 100-mg samples are too large to fully utilize maximum Hdh/ds in the fields of the magnets used. The relative magnitudes, however, confirmed the susceptibilities found along the axes determined from the x-ray data. The rotational diagrams (Fig. 2) clearly indicate orthogonality, but are not sinusoidal. Reversing the field direction did not affect the magni-

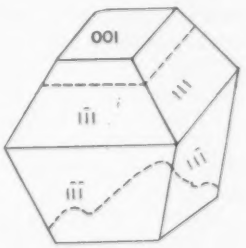

FIG. 1. Bi-pyramid segment of gallium crystal used for rotational diagrams.

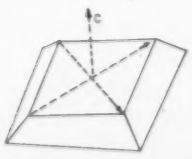

[6] J. W. Blom, *Magneto-resistance for Crystals of Gallium* (Martinus Nijhoff, The Hague, 1950), pp. 3, 4.

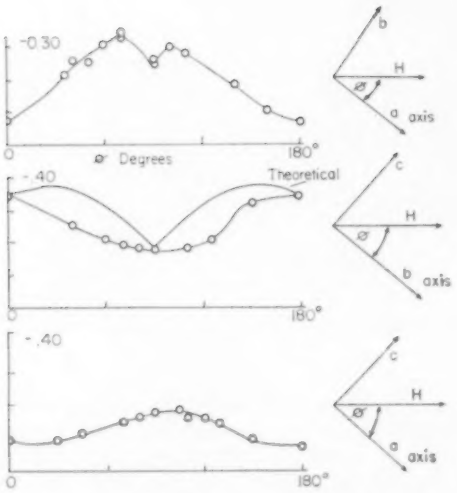

FIG. 2. Rotational diagrams in three orthogonal planes. Values of the magnetic susceptibility (in 10^{-6} emu/g) are less than the absolute values due to effect of crystal size (see text).

tude of the measured susceptibility appreciably; hence it was necessary to rotate through only 180 deg.

The anisotropic nature of gallium prohibited the finding of a mean value for the susceptibility by averaging the values found along orthogonal axes (see double peak in rotational diagrams). Marchand[7] had already attempted to find an average value by making measurements on a powder sample and rejected these on the basis of deformation that took place during the powdering process. Therefore it was decided to attempt to produce polycrystalline gallium by rapid quenching in liquid nitrogen. A fall of 25 cm through liquid nitrogen was found to be sufficient to produce spheres of an isotropic nature from droplets of molten gallium. Samples that were not perfect spheres exhibited some anisotropy even when treated in this manner.

Measurements on an 11-mg sphere in several orientations were averaged to give $(-0.257\pm0.003)\times10^{-6}$ emu/g as the average susceptibility of gallium. This value agrees with the value Marchand found for the powder sample.

The susceptibility of one of these quenched spheres was measured at liquid nitrogen temperature, and an increase of 17% in the diamagnetic susceptibility was noted.

[7] See footnote reference 4, p. 468.

No attempt to determine the temperature gradients as functions of axial directions was made because special problems in keeping the crystals orientated at low temperatures were prohibitive[8] with the equipment available.

DISCUSSION

Theoretical values of susceptibility for rotation in the ij plane calculated from $\chi(\theta)=\chi_i\sin\theta+\chi_j\cos\theta$ agree with the experimental diagrams only at intervals of $\frac{1}{2}\pi$ (see Fig. 2). Therefore it may be assumed that anisotropic effective mass appreciably affects the bulk susceptibility. Apparently Landau diamagnetism,[9] highly dependent upon effective mass, is the source of the diamagnetic part of the anisotropy, with anisotropic spin susceptibility of the free electrons constituting the remainder. Bulk susceptibility is therefore the sum of several effects, each with a different dependence upon effective mass. Thus, a one-to-one correspondence between effective mass anisotropy and anisotropy in bulk susceptibility is not feasible. It has been assumed *a priori* that effective mass anisotropy, caused by the overlap of Brillouin zone boundaries by the Fermi-energy surface[10,11] in gallium is the cause of the anisotropy of the magnetic susceptibility.

The change in susceptibility with the change in state may be satisfactorily explained by the lifting of effective mass restrictions with the disappearance of periodicity of potential and energy discontinuities[12] in the change to the liquid state.

The general results of this work agree with Marchand's results, and it must be concluded that gallium is slightly paramagnetic in the liquid state. However, as the value for the anisotropic quenched sample agrees with Marchand's value for a powder sample, these values rather than an average of the anisotropic susceptibilities should be accepted as the average susceptibility of gallium.

ACKNOWLEDGMENTS

The author is grateful to Dr. Frank Senftle for his technical advice, to Dr. H. T. Evans, who performed the x-ray determinations, and to Dr. E. Salkovitz, who suggested the problem. I also wish to express sincere thanks to Dr. H. Branson for his advice and instruction throughout this work.

[8] See footnote reference 4.
[9] C. Kittel, *Introduction to Solid State Physics* (John Wiley & Sons, Inc., New York, 1957), 2nd ed., p. 294.
[10] See footnote reference 9.
[11] G. V. Raynor, *op. cit.*, pp. 139–141.
[12] C. Kittel, *op. cit.*, pp. 284–288.

Measurements of the Dielectric Constant of $BaTiO_3$ Single Crystals in the Paraelectric Region at X Band

A. Lurio and E. Stern
IBM Watson Research Laboratories, New York, New York
(Received May 18, 1960)

The dielectric constant and loss tangent of single crystals of $BaTiO_3$ were measured as a function of temperature in the frequency range of 8.2 to 12.4 kMc. The technique consisted of looking for transmission resonances through the crystal whenever its thickness became $\lambda/2$ (where λ is the wavelength in the material). From the Curie-Weiss behavior of the dielectric constant in the paraelectric region, the A constant was determined to be 3.77×10^{-5}°C^{-1}.

INTRODUCTION

THE dielectric constant of single crystals of $BaTiO_3$ has been previously measured by the authors up to 2500 Mc.[1] No relaxation of ϵ' has been observed at these frequencies in the paraelectric region. The present experiment was devised to study single crystal behavior at X band. Since the start of this experiment, Benedict and Durand[2] have reported on measurements at 24 kMc performed by a different technique.

There are a number of ways in which the permittivity of materials can be measured at microwave frequencies. The dielectric constant ϵ' may be measured by looking at the reflections in a waveguide terminated by the sample. However, as the dielectric constant becomes very high, the VSWR and the position of the voltage minimum in the waveguide approaches that of a short circuit. Thus this technique could not easily be used with $BaTiO_3$. Similarly, the cavity perturbation method, which consists of measuring the Q and resonant frequency of a cavity before and after insertion of the sample, fails with high permittivity materials. Once again the effect of the sample upon the cavity resembles that of a piece of metal, and small changes in permittivity cannot be detected.

The measurement technique described below was found highly satisfactory for materials with moderate loss tangents and high dielectric constants in the frequency range from 8.2 to 12.4 kMc. It was not, however, adequate for precise measurements of the losses in the $BaTiO_3$ crystals.

EXPERIMENTAL TECHNIQUE

A single crystal of $BaTiO_3$ with dimensions 0.280 in. $\times$0.140 in.$\times l$, where l varied from 0.006 in. to 0.015 in. was placed in a specially designed waveguide test line such that its 0.280-in.$\times$0.140-in. face completely filled the cross section of the waveguide.

The test line was placed inside an oven so that its temperature could be varied from room temperature to 200°C. The transmission of power through the crystal was observed when an HP686A backward wave oscillator was connected to the line and swept through the 8–12 kMc frequency range.

Because of the high-dielectric constant of the sample, most of the energy incident on its surface is reflected. The experiment consists of looking for a transmission resonance[3] through the crystal which should occur whenever its thickness l is

$$l=\frac{n\lambda}{2(\epsilon')^{\frac{1}{2}}}-\frac{\lambda\cos\phi}{\pi\epsilon'}\tan\delta\ (n=1,\ 2,\ 3,\cdots), \qquad (1)$$

where λ is the guide wavelength, $\cos\phi$ is defined below, $\tan\delta=\epsilon''/\epsilon'$, and ϵ' and ϵ'' are the real and imaginary parts of the permitivity, respectively.

With a lossless sample, 100% transmission would take place at resonance. The amount of transmission T for a lossy sample is given by the expression derived in the Appendix:

$$T=\left\{1+\frac{\epsilon'}{4\cos^2\phi\cos\delta}\left[\sinh^2\left(\frac{2\pi lX}{\lambda}\right)+\sin^2\left(\frac{2\pi lU}{\lambda}\right)\right]+\frac{1}{2\cos\phi}\left(U\sinh\frac{4\pi lX}{\lambda}+X\sin\frac{4\pi lU}{\lambda}\right)\right\}^{-1}, \qquad (2)$$

where

$$U=\left(\frac{\epsilon'(1+\cos\delta)}{2\cos\delta}\right)^{\frac{1}{2}};\quad X=\left(\frac{\epsilon'(1-\cos\delta)}{2\cos\delta}\right)^{\frac{1}{2}};$$

$$\cos\phi=[k'-(\lambda/\lambda_c)^2]^{\frac{1}{2}};\quad \delta=\tan^{-1}(\epsilon''/\epsilon');$$

and k' = dielectric constant of medium surrounding the sample.

Thus, given a sample of known thickness, the dielectric constant ϵ' can be determined simply from the frequencies at which the resonance occurs. Similarly, from the height or the half width of the resonance, the losses can be deduced using Eq. (2). As the temperature in

[1] E. Stern and A. Lurio, Bull. Am. Phys. Soc. **4**, 242 (1959).
[2] T. S. Benedict and J. L. Durand, Phys. Rev. **109**, 1091 (1958).
[3] H. J. Schmitt, Z. angew. Phys. **9**, 107 (1957).

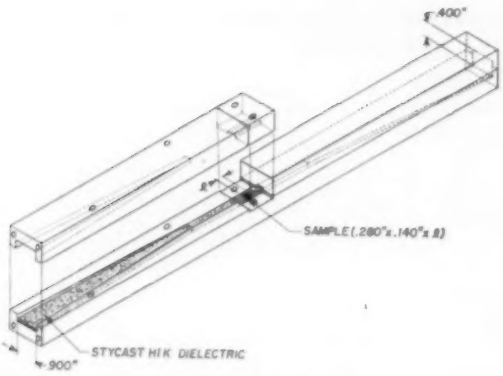

FIG. 1. Tapered test line.

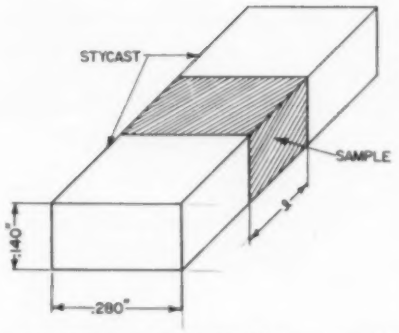

FIG. 2 $BaTiO_3$ crystal sandwiched between two blocks of stycast HiK material

the oven varies, the position of the resonance shifts and its shape changes. The power transmitted through the sample as a function of frequency is displayed on an oscilloscope.

APPARATUS

Due to the limitations on the size of $BaTiO_3$ crystals that can be grown, a test line had to be designed which could support the fundamental waveguide mode over the X-band region in a cross section 0.280 in.×0.140 in. In order to achieve this, the line was tapered from standard X-band size down to the above dimension while being gradually filled with a reverse-tapered dielectric material (see Fig. 1). Stycast HiK dielectric[4] was used to fill the small cross-section waveguide except for a gap where the sample and its holder would fit in. The stycast had a dielectric constant $k'=9$; thus a constant cutoff frequency was maintained throughout the test line.

A test specimen shown in Fig. 2 was formed by placing a barium titanate crystal in a sandwich of stycast material and cementing it together with a stycast cement of equal dielectric constant. The entire sandwich was then coated with silver paste and baked. This procedure actually molded the sample and its holder into a silver waveguide; it avoided complications due to air gaps between the $BaTiO_3$ and the waveguide walls.

The test line was 22 in. long and made out of solid brass. It rested in a long, Fiberglas insulated oven. Thin stainless steel waveguide sections were used to connect the line with the external microwave circuitry in order to minimize heat losses. Due to the high thermal inertia of the system, it took over 3 hr to heat the sample up beyond the Curie temperature; it took an entire day to make a run from 160° down to room temperature. This resulted in a very homogeneous temperature distribution around the sample.

A block diagram of the measuring equipment is shown in Fig. 3. The 1-kc modulated output of the swept BWO

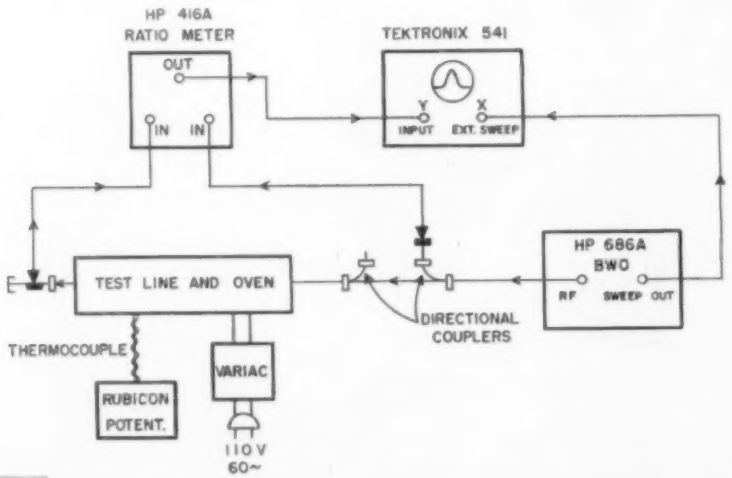

FIG. 3. Block diagram of apparatus.

[4] Supplied by Emerson and Cuming, Boston, Massachusetts.

is sampled by a directional coupler and fed to the reference input of an HP ratiometer. The power transmitted through the sample is detected and introduced into the second channel of the ratiometer. The output of the ratiometer, which is proportional to the percent power transmitted through the sample, goes to the vertical deflection plates of an oscilloscope which is triggered by the sweep output of the BWO. Thus a pattern of power transmitted through the sample vs frequency is displayed on the oscilloscope.

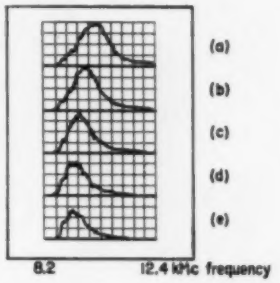

FIG. 5. Transmission through a single crystal of $BaTiO_3$ as a function of frequency and temperature. The temperatures for the various frames in this photograph are (a) 161°C, (b) 157.5°C, (c) 153°C and (d) 151°C, and (e) 148.5°C.

RESULTS

The technique was checked by first measuring the dielectric constant of TiO_2 (rutile) ceramic. For this test the rutile sample was placed inside a standard X-band guide. Figure 4 is a photograph of transmitted power T through a block of TiO_2 vs frequency. The top frame displays the sweep from 8.2 to 12.4 kMc which contains several resonances, and the bottom frames show an expanded view of a single resonance. If λ_1, λ_2 are wavelengths at any two adjacent resonance peaks, then

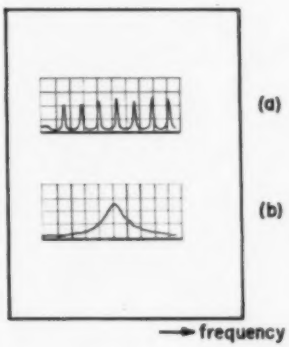

FIG. 4. Transmission T through a block of TiO_2 filling the cross section of X-band waveguide. (a) Frequency swept over 8.2 to 12.4 kMc range. (b) Frequency swept over 440 Mc range.

$$n\lambda_1=(n+1)\lambda_2 \tag{3}$$

where $\lambda_1>\lambda_2$, so that

$$n=\frac{\nu_1}{\nu_2-\nu_1} \tag{4}$$

where $\nu_1<\nu_2$ an $\Delta\nu=\nu_2-\nu_1$. Therefore,

$$(\epsilon')^{\frac{1}{2}}=\frac{nc}{2\nu_1 l}=\frac{c}{2l\Delta\nu} \tag{5}$$

where $c=3\times10^{10}$ cm/sec which results in a dielectric constant $\epsilon'=98$ for the TiO_2. This is in agreement with values other observers have reported for rutile.[5]

A large number of $BaTiO_3$ crystals were run through in similar fashion. For each sample, however, a run was made over the entire temperature range from 160°C down to room temperature. A crystal of given thickness l would only yield values over a narrow range of ϵ'. Thus a number of samples of different thicknesses were used to obtain a smooth curve of ϵ' vs temperature in the paraelectric region. Data were always taken on the cooling cycle. A reproduction of a photograph of typical data as seen on the oscilloscope is presented in Fig. 5. Each frame represents a different temperature; from top to bottom the temperature is changing from 161°C to 149°C. The position of the resonance along the frequency axis is seen to shift with changing temperature; in the photograph this shift represents a change in dielectric constant from 3050 to 3770 from top to bottom. The small wiggles superimposed on the resonance are due to mismatches in the test line.

The results of data taken with nine samples are plotted in Fig. 6. From Eq. (1) it is clear that in thick samples, a second resonance ($n=2$) should be visible; these second resonances were observed in some samples, but they were very broad due to the high losses in the region of their occurrence. Some very high values of $\epsilon'(\sim15\,000)$ were seen in this fashion. The Curie-Weiss behavior is plotted in Fig. 7; from the slope of the curve, we compute $A=3.77\times10^{-5}$ °C^{-1} which is in agreement with our low-frequency data. The peak dielectric constant measured in this experiment is some-

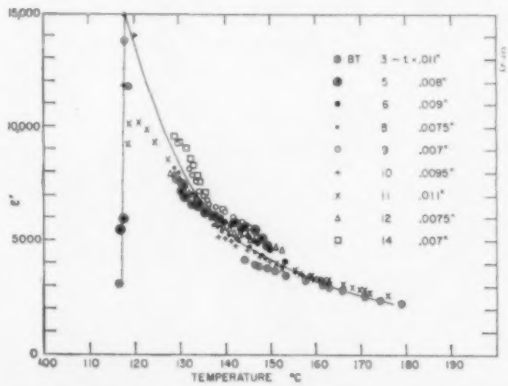

FIG. 6. Dielectric constant vs temperature as derived from a number of samples.

[5] A. Von Hippel, *Dielectric Materials and Applications* (The Technology Press of MIT and John Wiley & Sons, Inc., New York, 1954), p. 302.

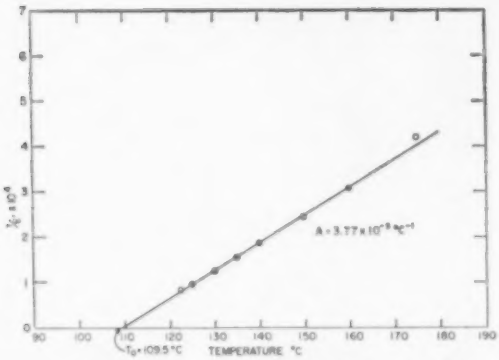

FIG. 7. Curie-Weiss behavior in the paraelectric region.

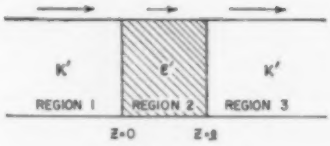

FIG. 8. Schematic of sample in waveguide.

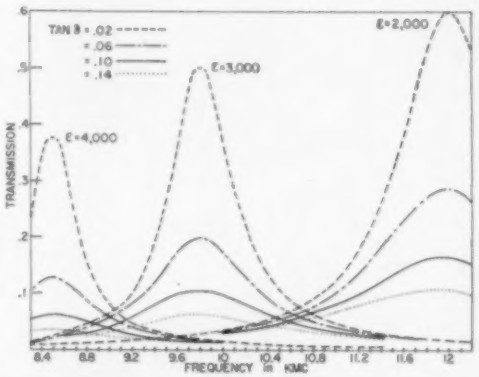

FIG. 9. Calculated transmission T through a slab of lossy dielectric filling the cross section of a waveguide as a function of frequency, dielectric constant, and tanδ, for a sample of thickness $t=0.011$ in.

what higher from that reported by the authors at lower frequencies; this probably results from the improved temperature stability. Measurements of the losses were not nearly as satisfactory. Values of tanδ that could be observed ranged from 0.01 at 175°C to 0.14 at 130°C. Close to the Curie point, however, the losses increased so rapidly that the resonance became too broad for accurate measurement.

The data clearly indicates that at 10 kMc, no dispersion has taken place in the permittivity of $BaTiO_3$ above the Curie temperature.

ACKNOWLEDGMENTS

We wish to thank B. L. Havens for suggesting this problem and for his support and encouragement during the course of the work. The crystals used for this research were supplied by S. Triebwasser of the IBM Poughkeepsie Laboratory. The advice and criticism of Professor N. Kroll and Dr. S. Triebwasser is gratefully acknowledged.

APPENDIX

This appendix contains a derivation of an expression for transmission T, through a lossy slap of dielectric in a waveguide. A technique for measuring high permittivity values at microwave frequencies was developed by Powles and Jackson,[6] in their investigation of the dielectric properties of ceramic ferroelectrics. Subsequently, the technique was also used by Schmitt[3] to make similar measurements. In the experiment described in this communication, the sample fills the cross section of a waveguide as seen in Fig. 8. If we use Schmitt's notation, the transmission coefficient through the slab of dielectric material filling region 2 is given by

$$t=\frac{4\cos\phi\,\exp(\gamma_2+\gamma_1)l}{\alpha^2 Z[\exp(2\gamma_2 l)-(\beta/\alpha)^2]}, \tag{1}$$

where $\alpha=1+(\cos\phi/Z)$; $\beta=1-(\cos\phi/Z)$; $Z=U-jX=[\epsilon'-j\epsilon''-(\lambda/\lambda_c)^2]^{\frac{1}{2}}=-j(\lambda/2\pi)\gamma_2$; $\gamma_1=\alpha_1+j\beta_1=j\beta_1$, since losses are negligible in region 1, $\gamma_2=\alpha_2+j\beta_2$. Then the amount of transmission through the sample is

$$T=t\bar{t}=\frac{16\cos^2\phi\,\exp(2\alpha_2 l)}{Z\bar{Z}\{\alpha^2\exp 2l(\alpha_2+j\beta_2)-\beta^2\}\{\bar{\alpha}^2\exp 2l(\alpha_2-j\beta_2)-\bar{\beta}^2\}}, \tag{2}$$

where the bar over the symbol means complex conjugate. If we neglect terms of the order ϵ'^{-2} which occur in the denominator of (2), and remember that $(e^x+e^{-x})/2=\cosh x$, and $(e^x-e^{-x})/2=\sinh x$, then after some lengthy algebraic manipulation, Eq. (2) leads to

$$T=\frac{1}{1+\dfrac{U^2+X^2}{4\cos^2\phi}(\sinh^2\alpha_2 l+\sin^2\beta_2 l)+\dfrac{1}{2\cos\phi}(U\sinh 2\alpha_2 l+X\sin 2\beta_2 l)}. \tag{3}$$

[6] J. G. Powles and W. Jackson, Proc. IRE **96**, 383 (1949).

Since $Z \simeq (\epsilon' - j\epsilon'')^{\frac{1}{2}}$ and $\gamma_2 \simeq j(2\pi/x)(\epsilon' - j\epsilon'')^{\frac{1}{2}}$ and $\tan\delta = (\epsilon''/\epsilon')$, we finally obtain

$$T = \left[1 + \frac{\epsilon'}{4\cos^2\phi\cos\delta}\left\{\sinh^2\left(\frac{2\pi lX}{\lambda}\right) + \sin^2\left(\frac{2\pi lU}{\lambda}\right)\right\} + \frac{1}{2\cos\phi}\left\{U\sinh\left(\frac{4\pi lX}{\lambda}\right) + X\sin\left(\frac{4\pi lU}{\lambda}\right)\right\}\right]^{-1}. \quad (4)$$

This equation was programed for an IBM 650 computer, so that T could be calculated as a function of frequency as we varied $\tan\delta$, ϵ', and l, respectively. This resulted in the series of curves shown in Fig. 9 for one particular sample thickness ($l = 0.011$ in.). It is evident that as the losses increase much beyond the highest seen in Fig. 9, the transmission through the sample becomes undetectable.

If the losses in the sample are negligible, $X = 0$, $U = (\epsilon')^{\frac{1}{2}}$ and we get the expression for a lossless sample

$$T = \left(1 + \frac{\epsilon'}{4\cos^2\phi}\sin^2\frac{2\pi l(\epsilon')^{\frac{1}{2}}}{\lambda}\right)^{-1}. \quad (5)$$

JOURNAL OF APPLIED PHYSICS VOLUME 31, NUMBER 10 OCTOBER, 1960

Experimental Determination of Stresses Generated by an Electric Detonator*†

JOHN S. RINEHART AND WILLIAM C. MCCLAIN
Mining Research Laboratory, Department of Mining Engineering, Colorado School of Mines, Golden, Colorado
(Received June 27, 1960)

The magnitude, duration and spatial distribution within a solid body (Plexiglas) of the transient stress disturbance generated by an electric detonator detonated in intimate contact with the body has been experimentally determined. The technique is to affix to one surface of the body a small pellet of the same material, which flies off when the disturbance reaches the surface, the velocity of the pellet being determined. The complete stress-time curves are built up by using pellets of several thicknesses. Three types of detonators have been used with these being placed flat ended against the surface of a Plexiglas block. A few were confined. The stress in the Plexiglas was found to be distributed more or less uniformly about the axis of the detonator. Along the axis both peak pressure and total momentum decreased with distance from the detonator: peak pressure exerted by an Olin Mathieson No. 6 Plasti-cap ranged from 9500 lb/in.^{2} at 1.25 in. from the detonator to 7000 lb/in.^{2} at 2.0 in.; and the momentum ranged from 16×10^{-3} lb-sec/in.^{2} at 1.25 in. to 9.0×10^{-3} lb-sec/in.^{2} at 2.0 in. The disturbance lasted about two μsec. Similar results were obtained with the other detonators.

INTRODUCTION

SMALL detonators or blasting caps are commonly used to initiate the explosion of a ponderable mass of explosive. There exists a wide variety of such detonators, each designed for one or more specialized uses, some being electrically activated and others mechanically. The electrically activated cap usually contains a match in a small cylindrical case made of plastic or metal which, when heated by the passage of an electric current, ignites, thereby setting off a few grains of highly sensitive explosive also contained in the case. The force of the small explosion is usually sufficient to initiate detonation of a much larger mass of less sensitive explosive placed in intimate contact with the cap. Constructural details of caps manufactured by different companies are not the same, there being variation in type of explosive, explosive content, match composition, and case design, with much of the detailed information being proprietary in nature. The external and case features of three common No. 6 electric caps are illustrated in Fig. 1, the one on the left being a plastic-cased, flat-ended cap manufactured by the Olin Mathieson Company; the one in the center, a copper cased, rounded-end cap manufactured by the Atlas Powder Company; and the one on the right, a copper cased cap manufactured by E. I. du Pont de Nemours Company, which differs from the Atlas cap by having the front of the cap indented, thereby creating a situation conducive to the formation of a shaped charge jet.[1] Although these caps are widely used and several engineering tests have been devised for testing their efficacy, there is essentially no quantitative data on the magnitude and duration of the stress generated within a body when the cap is exploded while in close contact with the body (which normally would be an explosive). In this study detailed quantitative data on these stresses have been obtained for the first time from experiments made using three types of No. 6 instantaneous electric blasting caps.

METHOD

The experimental arrangement used in many of the tests is shown schematically in Fig. 2, the cap being

* Work partially supported by National Science Foundation.
† Contribution No. 13.

[1] R. W. Wood, Proc. Roy. Soc. (London) **A157**, 249 (1936).

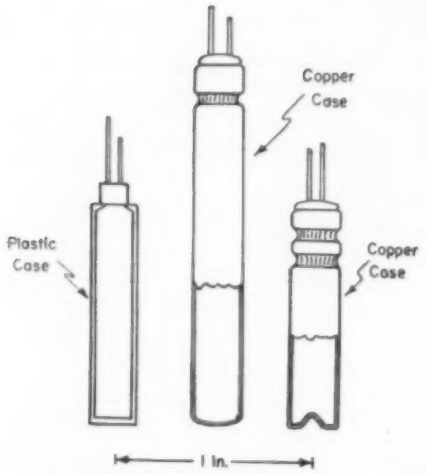

FIG. 1. External features of three caps studies. Left: plastic cased, flat ended cap manufactured by Olin Mathieson; middle: copper cased, rounded end cap manufactured by Atlas Powder; right: copper cased, re-entrant ended cap manufactured by du Pont.

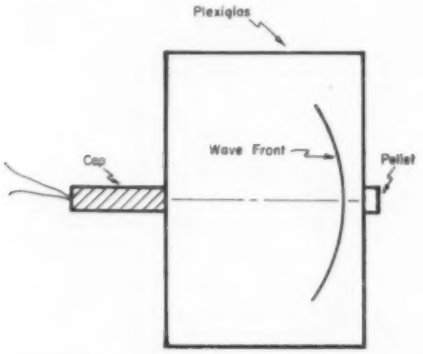

FIG. 2. Experimental arrangement for along-the-axis tests.

unconfined and butted end on against a small block of Plexiglas, usually an inch thick and of a few inches in other dimensions. A sharp-fronted transient compressional stress disturbance of the form illustrated in Fig. 3 is developed when the cap is exploded; on striking the far (right) surface, it causes a pellet of the same material, affixed lightly thereto with oil, to fly off with some of the momentum of the disturbance trapped in it. By using successively thicker pellets and repeating the experiment, complete and detailed stress-time profiles of the pulse can be drawn; this technique has been successfully employed by several investigators[2–4]. In the present tests Plexiglas cylindrical pellets $\frac{1}{4}$ in. in diameter were used, with pellet thicknesses ranging from $\frac{1}{32}$ in. to $\frac{1}{4}$ in., roughly in $\frac{1}{32}$ in. steps. The velocity of each pellet, which usually lay in the range from 30 ft/sec to 180 ft/sec, was measured by photographing its flight over a path several inches long, using either a high intensity, short duration stroboscopic light or a slotted rotating disk light source in conjunction with an open shutter Polaroid camera, containing ultrafast film, 3000 ASA.

A typical momentum trapped (reduced to momentum per unit area) versus thickness of pellet curve is drawn in Fig. 4, the distance from cap to pellet being 2 in. and the cap an Olin Mathieson No. 6 Plasti-cap. The curve has become substantially flat for a pellet thickness of $\frac{1}{8}$ in., implying that most of the impulse or momentum of the disturbance lies in a region just twice this thickness, or $\frac{1}{4}$ in. The longitudinal wave velocity of the Plexiglas used in these experiments was measured using a standard pulse technique and found to be 9070 ft/sec; the duration of the $\frac{1}{4}$ in. pulse would therefore be about 2.3 μsec.

Both stress-distance and stress-time curves for the disturbance can be derived from the momentum per unit area versus pellet thickness curve, provided certain assumptions are made. The first of these is that the particle velocity in the disturbance is linearly related

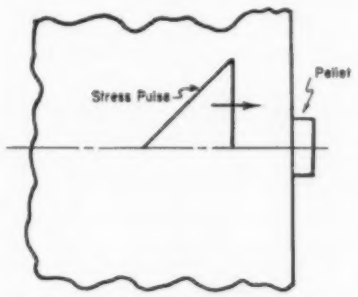

FIG. 3. Dynamics of momentum entrapment.

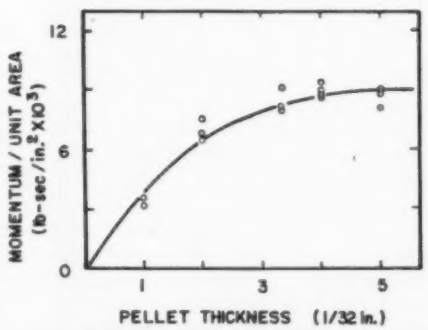

FIG. 4. Momentum per unit area versus thickness of pellet. Free surface perpendicular to axis of cap. Olin Plasti-cap. Cap to pellet distance, 2 in.

[2] B. Hopkinson, Trans. Roy. Soc. (London) **A213**, 437 (1914).
[3] J. S. Rinehart and J. Pearson, *Behavior of Metals under Impulsive Loads* (American Society of Metals, Cleveland, Ohio, 1954), p. 78.
[4] J. S. Buchanan and H. J. James, Brit. J. Appl. Phys. **10**, 290 (1959).

to stress through the equation

$$\sigma = \rho c v,$$

where σ is the instantaneous value of the stress; ρ is the density of the material (73.6 lb/ft³ for Plexiglas); c is the longitudinal wave velocity (taken in all calculations as 9070 ft/sec); and v is the instantaneous value of particle velocity in the disturbance. The second assumption, needed only in drawing the stress-distance curve, is that the pulse does not change shape over the distance under consideration as it progresses through the body. This is not a particularly good assumption, as will be seen later, since measurable attenuation, dispersion, and divergence do occur. Stress versus distance and stress versus time curves, deduced from the curve of Fig. 4, are plotted in Figs. 5 and 6, respectively. The stress, initially about 10 000 lb/in.², decays essentially to zero in 2 to 3 μsec with the length of the pulse being about $\frac{1}{4}$ in.

CHANGE OF PULSE SHAPE WITH DISTANCE

It is to be expected that a pulse of this type will change its shape due to divergence, attenuation, and dispersion as it moves through the Plexiglas. Tests were

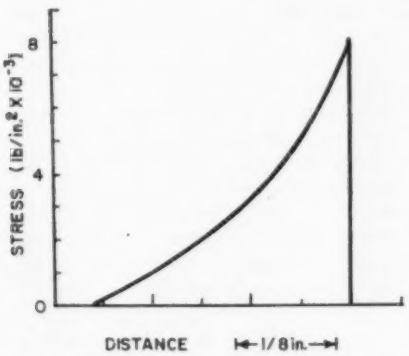

FIG. 5. Stress versus distance. Derived from Fig. 4.

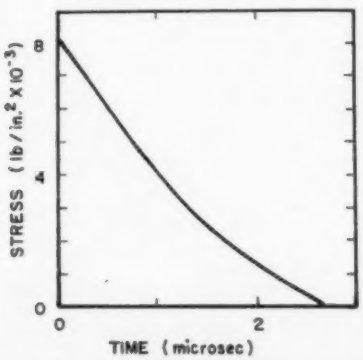

FIG. 6. Stress versus time. Derived from Fig. 4.

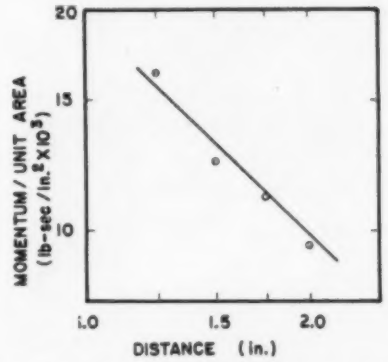

FIG. 7. Log of total momentum per unit area versus log of distance from cap. Experimental arrangement shown in Fig. 2. Olin Plasti-cap. Line has slope of minus one.

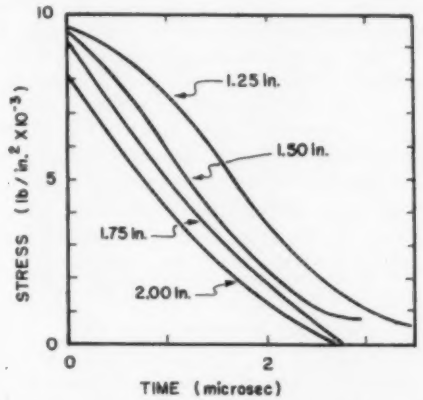

FIG. 8. Stress versus time for four cap to pellet distances. Data taken on axis. Olin Plasti-cap.

run for cap to pellet distances of 1.25 in., 1.50 in., 1.75 in., and 2.0 in., with the results plotted in Figs. 7 and 8, Fig. 7 being a log-log plot of total momentum per unit area in the pulse versus cap to pellet distance, and Fig. 8 being plots of the four respective stress versus time curves. The straight line in the log-log plot, (Fig. 7), drawn with a slope of minus one, is a good fit to the data, indicating that the total impulse delivered by the disturbance varies inversely with the first power of distance, a more or less reasonable result since in a spherically expanding wave stress decays inversely with the first power of the distance.[5] The principal change in pulse shape with distance, (Fig. 8), is a decay in stress at all points along the pulse; there is also a tendency for the wave to sharpen up, losing some of its bell shape and becoming more nearly exponential as the distance from the cap increases. This change may be due to a frequency dependent absorption, strongly felt

[5] H. J. Selberg, Arkiv Fysik 5, 97 (1952).

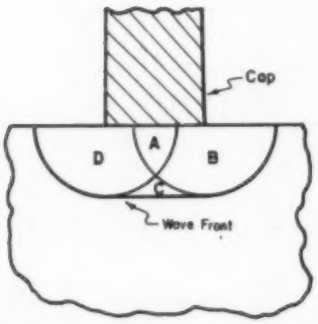

FIG. 9. Schematic of longitudinal wave pattern generated by unconfined cap.

in this frequency range[6]; but more probably it arises from the fact, as illustrated in Fig. 9, that the front of the disturbance is not precisely spherical, this lack of sphericity having its origin in the finite lateral dimensions of the detonator. This particular stress situation has been treated[7] for the elastic case, the salient relevant features being sketched in Fig. 9. Rarefaction waves moving inward create several distinct regions, labeled *A*, *B*, *C*, and *D*. Region *C*, originally quite thick, becomes thinner and thinner as the wave expands, with the wave approaching sphericity more and more closely. The stress near the center of the wave will be sustained a shorter and shorter time with increasing distance from cap, supporting the present observation.

EFFECT OF CAP CONFINEMENT

If the cap is confined by placing it in a hole in the block, as illustrated in Fig. 10, the stress situation ought to be quite different, both because there is no opportunity for rarefaction waves originating at a free surface

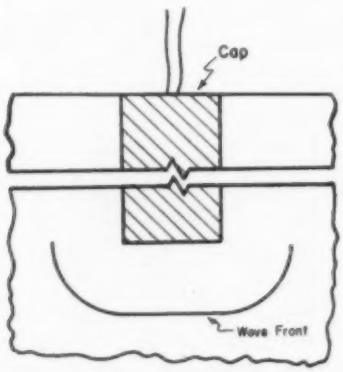

FIG. 10. Schematic of longitudinal wave pattern generated by confined cap.

[6] Unpublished results.
[7] J. H. Huth and J. D. Cole, J. Appl. Mech. **21**, 294 (1954).

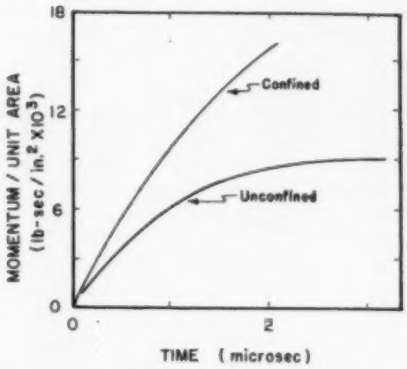

FIG. 11. Comparison of momentum per unit area as a function of time for confined and unconfined caps. Along axis. Cap to pellet distance, 2 in. Olin Plasti-cap.

to move into the solid hard on the heels of the front of the disturbance, and because the explosion products cannot disperse as readily, causing the pressure to be sustained longer. A few tests were run with confined caps, the cap being inserted into a one inch deep hole bored in the Plexiglas block. Only Plasti-caps were used. The results are compared with similar results for unconfined caps in Figs. 11 and 12, the figures containing plots of momentum per unit area as a function of time, and stress as a function of time, respectively. Cap to pellet distance was 2 in. in each case. Under these conditions the total impulse per unit area, about 16×10^{-3} lb-sec/in.^{2} in the disturbance created by the confined cap, is nearly twice that of 9.0×10^{-3} lb-sec/in.^{2} in the disturbance produced by the unconfined cap. The maximum stress, 10,000 lb/in.^{2} for the confined cap is only somewhat, 20%, higher than the 8000 lb/in.^{2} stress of the unconfined cap, but the stress is maintained at this high level for a longer time.

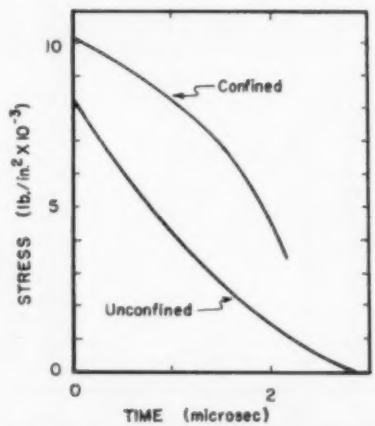

FIG. 12. Comparison of stress versus time curves for confined caps. Derived from Fig. 11.

DIFFERENT CAPS

Results for the three types of caps are compared in Fig. 13; momentum per unit area is plotted against time for each cap for a cap to pellet distance of 2 in. In general, the impulse delivered by each of the caps is about the same, differences in construction shown in Fig. 1 appearing to be not especially significant. This result is to be anticipated since in practice the three caps are similarly and competitively used.

ANGULAR DISTRIBUTION OF IMPULSE

In the tests discussed thus far the pellet was placed along an extension of the axis of the cylindrical cap. Of equal interest is the magnitude and duration of the off-axis stress and impulse. The experimental arrangement shown in Fig. 14 was used to make such determinations. Here the front of the disturbance, assumed spherical, is made to strike normally a surface so cut that the normal to it forms an angle θ with an extension of the axis of the cap. Results of these off-axis measurements are summarized in Fig. 15, a plot of momentum per unit area against the angle θ. Only the Plasti-cap was tested over a complete hemisphere, tests on the other caps being limited to off-axis angles of 60 deg. The curve for the Plasti-cap indicates remarkable uniformity of impulse over the whole wave front, with the 90 deg value, 7.2×10^{-3} lb-sec/in.^{2}, being only 18% lower than the zero deg value of 8.8×10^{-3} lb-sec/in.^{2}. The Atlas rounded-nose cap follows essentially the same pattern. Although the data are not definitive, the du Pont cap, with its indented shaped charge like front face, appears to concentrate the impulse somewhat more in the forward direction. At θ equal to 60 deg the impulse seems to be dropping rapidly.

The upper curve of Fig. 15, with its steep slope, indicates that confinement greatly enhances the magnitude of the impulse delivered off-axis.

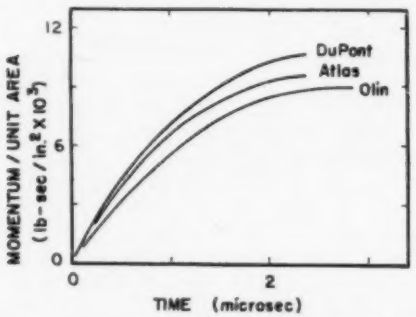

FIG. 13. Momentum per unit area versus time for three types of No. 6 caps. Along axis. Cap to pellet distance, 2 in.

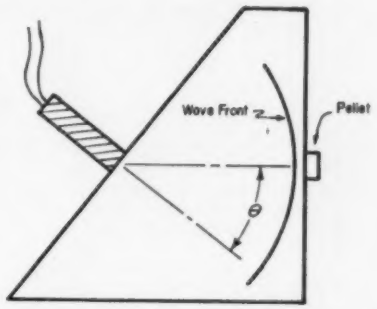

FIG. 14. Experimental arrangement for determining distribution of impulse off-axis.

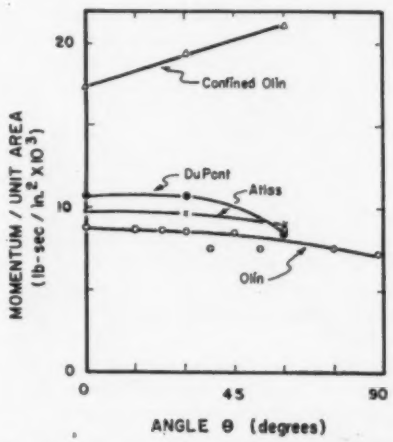

FIG. 15. Momentum per unit area as function of angle off-axis for confined and unconfined caps of three types. Experimental arrangement shown in Fig. 14. Distance from cap to pellet, 2 in.

ACKNOWLEDGMENTS

In conclusion the authors wish to thank Larry McCune, Richard Pitney, and José del Solar, who performed the experiments and made the calculations.

Electron Sheet Beam Focusing with Tape Ladder Lines

WILLIAM E. WATERS*
Diamond Ordnance Fuze Laboratory, Washington, D. C.
(Received May 25, 1960)

The dc properties of a periodic focusing system consisting of a parallel pair of ladder lines, together with focusing plates parallel to the lines, are calculated. First, Laplace's equation is solved in an approximate way; following this, the paraxial-ray equation for an electron sheet beam, injected into the system halfway between the ladder lines, is solved for perveance, plasma frequency, beam stiffness, and average beam potential. Finally, a numerical example is presented and discussed.

1. INTRODUCTION

WHEN electrostatic focusing is employed in microwave traveling-wave tubes, one structure serves both for focusing of the beam and as the rf circuit. One arrangement which has proven useful for backward-wave operation consists of a pair of "ladder lines," arranged so that the rungs of one line are opposite the rungs of the other; the arrangement is shown in perspective in Fig. 1(a). In addition to the ladder lines it is necessary to employ "ridge plates," parallel to the ladders. These are shown in the end view, Fig. 1(b). These plates have a twofold purpose. First, they provide for a bandpass rf dispersion curve; the absence of these plates would eliminate the coupling between one rung of the ladder and the next, and the resulting rf circuit would be a nonpropagating "easitron." Second, by maintaining the ridge plates at a lower (or higher) dc potential than that of the ladder lines, electron lenses are made to occur in the region between the ladders. It is these lenses that provide the focusing of a sheet electron beam through the system. The system is also depicted in cross section in Fig. 1(c).

The rf properties of single ladder-line circuits, loaded by ridge plates, have been discussed by Pierce[1] and by Butcher.[2] It has been found by rf bench measurements that the dispersion curves of the double arragnement are very similar to the corresponding curves for single ladder lines. By suitably proportioning the lengths of the ladder slots, the center-to-center spacing of adjacent slots (i.e., the period of the ladder), and finally the separation between the ridge plates and the ladders, it is possible to obtain dispersion curves which would permit backward-wave oscillations over a range of more than an octave (2:1). It is also possible to design the system so that the operating potential to be applied to the ladder lines will fall in the range 100–200 v at the low frequency end, rising to perhaps 1200–1600 v, or even higher, at the high-frequency end. The exact details of this system depend upon the particular set of dimensions chosen, and how close the low and high cutoff frequencies of the propagating circuit can be approached.

The rf properties of the ladder-line circuit are a subject in and of themselves; in this work only the dc focusing properties are discussed. In particular, approximate expressions suitable for the calculation of the perveance which the system can focus, as a function of the geometrical dimensions and the applied potentials, will be obtained. Also, the beam stiffness, the electron plasma frequency for a beam possessing the theoretical perveance, the electronic wavelength associated with beam perturbations, and finally, certain potentials within the beam which are important to the design of a backward-wave traveling-wave tube will be calculated. First an approximate solution for Laplace's equation will be obtained. Next, using this potential function, the paraxial-ray equation for sheet beams carrying finite current[3] will be solved in order to calculate the above-mentioned quantities.

2. SOLUTION OF LAPLACE'S EQUATION

For convenience in the analysis the ladder-line potential is taken to be unity; thus, any potential is to be considered as a fraction of the ladder-line potential. In addition, the ladders are considered to be infinitesimally thin. The system is divided into three regions, *I*, *II*, and *III*, as shown in Fig. 2. Region *I* is the region between the ladders, and extends to the planes of the ladders. Region *II* is the region between the upper ladder and the upper ridge plate, and region *III* is the corresponding lower region. If the two ladder lines are at potential unity, and the two-ridge plates are at the same potential $V_2<1$, the potential is completely symmetrical with respect to a plane halfway between the ladders, and only the upper half of region *I*, as well as of region *II*, need be considered.

A difficulty is experienced if the electron beam is as wide as the ridge plates. This trouble arises because of the fringing fields at the outer "edges" of the ridge plates. Two effects which are deleterious to the operation of a backward-wave oscillator are associated with these fringing fields. First, the fringing reduces the strength of the electron lenses, and thereby reduces both the local beam stiffness and the ability to focus current.

* Present Address: Microwave Electronics Corporation, 4061 Transport Street, Palo Alto, California.
[1] J. R. Pierce, IRE Trans. on Electron Devices, **ED-2**, 13 (1955).
[2] P. N. Butcher, Proc. Inst. Elec. Engs. (London) **104B**, 169 (1957). This paper is mainly concerned with dispersion curves.
[3] W. E. Waters, J. Appl. Phys. **29**, 100 (1958).

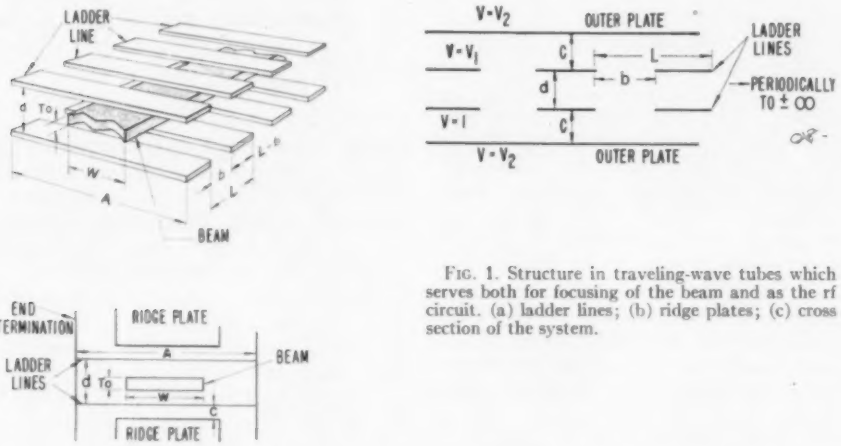

FIG. 1. Structure in traveling-wave tubes which serves both for focusing of the beam and as the rf circuit. (a) ladder lines; (b) ridge plates; (c) cross section of the system.

Second, if $V_2<1$, the most usual arrangement, the fringing causes the average potential in the beam to be higher for those portions of the beam close to the outer edges of the ridge plates than for those portions which are near the center of the plates. As a result, the forward velocity of the beam will not be uniform, and different portions of the beam will attempt to excite backward-wave oscillations at different frequencies; such an effect can only be harmful to a backward-wave oscillator. For both reasons the width of the beam must be less than the width of the ridge plates. A useful criterion is that the edges of the beam must be kept back from the edges of the plates by a distance which is at least 1.5 times the separation of the two plates; this rule of thumb will ensure that the fringing fields have little effect on the electron beam. Provided this criterion is met, the potential in the vicinity of the beam may be considered to be two dimensional, i.e., independent of position parallel to the rungs of the ladders. This is tantamount to saying that the arrangement depicted in Fig. 2 is a cross section of a system which is infinite in the direction normal to the plane of the figure.

If $V_2<1$, the potential in a gap will decrease monotonically from unity at the edge of a rung to a minimum value V_m in the center of a gap, and then will increase symmetrically back to unity at the edge of the next rung. This is depicted in Fig. 3. The potential in the gap whose center is $x=0$ may be written in the form

$$V_{gap}=V_m+(1-V_m)g(x), \qquad (1)$$

in which $g(x)$ represents the variation of potential in the gap, and must be normalized so that $g(0)=0$, $g(b/2)=1$. Except for these restrictions, $g(x)$ must be considered arbitrary for the moment.

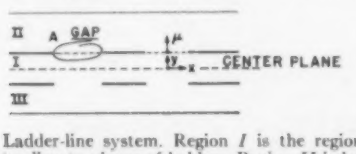

FIG. 2. Ladder-line system. Region *I* is the region between ladders, extending to planes of ladders. Region *II* is between the upper ladder and the upper ridge plate. Region *III* is between the lower ladder and lower ridge.

Because of the symmetry, the potential in region *I* is an even function of y, and is an even periodic function of x, with period L. Hence, this potential may be represented by a Fourier cosine series,

$$V_I(x,y)=\sum_{n=0}^{\infty} V_{nI}\cos 2n\pi x/L\cosh 2n\pi y/L. \qquad (2)$$

Of necessity this function must have the value unity on a rung of the ladder, and must be of the form given by (1) in a gap between rungs. Standard Fourier integrals may be employed to obtain the coefficients V_{nI}; these integrals will involve V_m and the specific form of $g(x)$. Let us proceed, however, without dwelling further on this matter.

In region *II* a distance μ is measured from the plane of the ladder. The potential is an even periodic function of x, with period L, but is neither even nor odd in μ. In addition, a term $a_0+b_0\mu$ must be included to account for the average electric field existing between the ridge plate and the ladder. The potential must reduce to the constant value V_2 on the ridge plate ($\mu=c$), must reduce to unity on a rung of the ladder, and must reduce to the form given by (1) in a gap. A suitable potential function is given by

$$V_{II}(x,\mu)=a_0+b_0\mu+\sum_{n=1}^{\infty}\cos 2n\pi x/L[a_n\cosh 2n\pi\mu/L + b_n\sinh 2n\pi\mu/L]. \qquad (3)$$

Again standard Fourier integrals may be employed to evaluate the a's and b's in terms of V_m and the specific form of $g(x)$.

Once the coefficients in the potential functions are obtained, these functions may be differentiated with respect to y and μ, respectively, to yield the "transverse" electric field components E_{yI} and $E_{\mu II}$. Unless $g(x)$ is

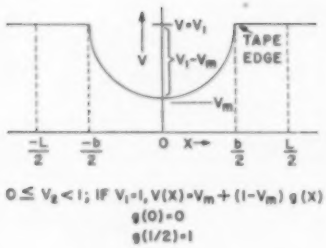

FIG. 3. Variation of potential in the gap between ladder rungs, edge to edge.

properly chosen these field components will not be equal in the gaps; hence, an important part of the problem is to select a suitable form for $g(x)$. However, the potential functions V_I and V_{II} have been forced to match, both on the rungs and across each of the gaps. Because of surface charges on the rungs the transverse electric field components will not be expected to match at the rungs. Hence, $g(x)$ need be chosen only to ensure that the transverse field components will match in the gaps. It is found that V_m is determined once a specified form for $g(x)$ is chosen.

Upon making a number of measurements on a conducting-paper analog, with the electrodes painted on with silver paint, it was found that a good approximation to $g(x)$ in a typical case is $g(x)=(2x/b)^4$. This is called the *quartic approximation*. This approximation gives an error which is positive in the central half of a gap, and negative in the remainder. In the worst case examined, the average error was about 3%. For this case b/L was 0.75; the error decreased steadily, to less than 1% for $b/L=0.25$. Hence, it is expected that any formula dederived from the quartic approximation will be sufficiently precise for any except the most stringent requirements, particularly for small values of b/L.

The quartic approximation, of course, is not expected to yield final forms for the potential functions $V_I(x,y)$ and $V_{II}(x,\mu)$ which may be differentiated repeatedly in the vicinity of the edges of the rungs. Strictly speaking, the assumption that the rungs are of infinitesimal thickness gives rise to an awkward singularity in the electric-field vector right at the rung edges. In practice the ladder line must be of finite thickness. Also, if the line is etched from a metallic sheet, it is found that the rung edges are well-rounded, the radius of the "rounding" being perhaps 0.5–2 times the thickness of the sheet. In such a *practical* system the assumption that $g(x)$ is quartic in x is at best a convenient approximation.

However, it is intended that the electron beam shall be kept away from the rung edges. In the region occupied by the beam it is unlikely that the amplitudes of the space harmonics of the potential $V_I(x,y)$ will be appreciably affected by the specific details of $g(x)$, provided, of course, that $g(x)$ is chosen so as to represent the true gap potential to within a few percent at each point, and provided the average error over the entire gap is small.

Application of the Quartic Approximation

In view of the previous discussion, $g(x)$ is taken to be of the form

$$g(x)=(2x/b)^4. \tag{4}$$

Because this form for $g(x)$ contains no unknown coefficients, it appears that available information does not permit matching of the transverse fields at *any* point in a gap. However, the minimum gap potential V_m has not yet been specified, and it is therefore, permissible to equate the transverse fields at ONE point in the gaps.

For two reasons the fields are equated at the center of a gap. First, at the center of the gap $x=0$ and all the cosine functions in the potentials V_I and V_{II} assume very simple forms, namely $\cos(2n\pi x/L)=1$, for all n. Second, because the continuity of the potential throughout the gap has been assured, a good, though perhaps not the best possible, match of the fields is expected by equating them at a gap point halfway between the edges of adjacent rungs.

Upon using the quartic approximation and equating the transverse fields at the center of the gap, the following relation for V_m is obtained,

$$1-V_2=[1-V_m][4b/5L+32c/L\Sigma_{II}(b/L)], \tag{5}$$

in which

$$\Sigma_{II}(b/L)=\sum_{n=1}^{\infty}\left\{\begin{matrix}3/(nb/L)^2[1-2/(nb/L)^2\sin nb/L]\\-1/(nb/L)[1-6/(nb/L)^2\cos nb/L]\end{matrix}\right\}$$

$$=\sum_{n=1}^{\infty}q_n(n,b/L). \tag{6}$$

In deriving (5) and (6) it has been assumed that $\tanh n\pi d/L+\coth 2n\pi c/L=2$, for every value of n. This will be a good approximation if d/L and c/L are not too small. For example, if $d/L=0.5$, and $c/L=0.25$, it is found that $\tanh\pi d/L=0.917$ and $\coth 2\pi c/L=1.091$, so that the sum is 2.008. For these same values of d/L and c/L, for $n=2$, the sum is 1.996. For all higher values of n, the sum is even closer to 2.

Even if d/L is considerably less than 0.5, say $d/L=0.3$, it is possible to find a value of c/L such that the sum

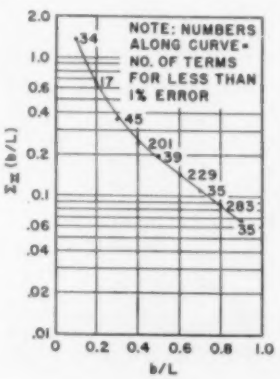

FIG. 4. Curve of $\Sigma_{II}(b/L)$ as a function of b/L. Series were summed on an IBM 704 digital computer.

of the two functions is equal to 2, to within a few percent, for all values of n. The analysis which follows is therefore confined to the approximation that $\tanh n\pi d/L + \coth 2n\pi c/L = 2$.

In Fig. 4 a curve of $\sum_{II}(b/L)$ as a function of b/L is presented; the numerical values were obtained by summing the series on an IBM 704 digital computer. The relative error is less than 1% at each point. The small figures lying along the curve represent the number of terms needed to achieve an error of less than 1%.

In the paraxial theory the average potential V_0 and the amplitude of the nth space harmonic of potential V_n are needed, but only on the line $y=0$. Upon using Eq. (5) to replace $1-V_n$ wherever it occurs, it is found that

$$V_0 = 1-[b/5L(1-V_2)]/[b/5L+8c/L\textstyle\sum_{II}(b/L)]. \quad (7)$$

Upon making use of the paraxial theory a need for the series $\sum_{n=1}^{\infty}(nV_n/V_0)^2$ arises. On using the quartic approximation, it is found that

$$(nV_n/V_0)^2 = 4/\pi^2[1-V_2]^2 \times \frac{\sum_I(d/L, b/L)}{[V_2 b/5L+8c/L\sum_{II}(b/L)]^2}, \quad (8)$$

in which:

$$\textstyle\sum_I(d/L, b/L) = \sum_{n=1}^{\infty}(q_n/\cosh n\pi d/L)^2, \quad (9)$$

and q_n is the nth term of the series given in Eq. (6).

The function given by (9) is presented in graphical form in Fig. 5. The series was summed on an IBM 704 digital computer, and was obtained with a relative error of less than 1% at each point. The small figures lying along the curves indicate the number of terms needed to obtain a relative error of less than 1%.

Solution of the Paraxial Equation

The important properties of an electron sheet beam which is injected halfway between the ladders of Fig. 1 may be calculated to a good approximation from the paraxial-ray equation for electrostatically-focused sheet beams. This equation has been derived and discussed in the literature,[3] and particular solutions have been obtained for certain types of periodic focusing.[4] The perturbation technique which is discussed in footnote reference 4 is repeated in the appendix of the present work. A particular solution of the paraxial-ray equation, in the form of a convergent infinite series, is obtained; only the first two terms are needed to obtain first approximations to the beam rippling and values of the perveance of beams which may be successfully focused. Here only the final results which arise from this solution are presented; these are, in the order in which they will be discussed, the "equilibrium perveance," i.e., the perveance with which a beam must be injected into the focusing system in order to minimize the rippling, the rippling of the beam, the electron plasma frequency, the *transverse resonant frequency*, the *transverse resonant wavelength*, and finally, the beam stiffness. Following this presentation a numerical example is discussed.

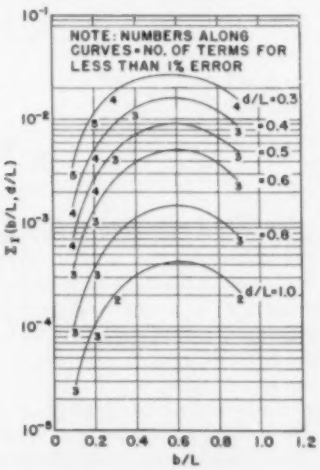

FIG. 5. Curve of $\sum_I(b/L, d/L)$ as a function of b/L. Series were summed on an IBM 704 digital computer.

Beam Perveance

From the paraxial-ray equation it is found that the equilibrium perveance[5] may be calculated from the equation

$$P = 42.1[WT_0/L^2][1-V_2]^2 \times \frac{\sum_I(d/L, b/L)}{[V_2 b/5L+8c/L\sum_{II}(b/L)]^2 \text{microperv}}. \quad (10)$$

In the event that $V_2=0$, a particularly convenient special case, (10) reduces to the special form

$$P = 0.659[WT_0/c^2]\frac{\sum_I(d/L, b/L)\text{microperv}}{[\sum_{II}(b/L)]^2}. \quad (11)$$

It is to be noted that the perveance is inversely proportional to the square of the ridge-to-ladder spacing c. Thus, a decrease in c will increase the equilibrium perveance; it will also be found that this decrease in c will lower the low-frequency cutoff of the rf circuit, and thereby will increase the range over which backward-wave oscillations may be obtained. However, as noted previously, if c/L becomes too small, less than about 0.25, the accuracy of (11) is open to some question. Fortunately, a value of 0.25 for c/L is very small from an rf point of view, and ordinarily larger values will exist.

For a given value of b/L, $\sum_I(d/L, b/L)$ is proportional to $\exp(-2\pi d/L)$, to within about 13% if $d/L>0.3$, and to within about 1.6% if $d/L>0.4$. Thus, the equilibrium perveance will decrease rapidly with an

[4] W. E. Waters, "Periodic focusing of thin electron sheet beams," Diamond Ordnance Fuze Laboratories Tech. Rev. 2, 1 (1959).

[5] Perveance is defined as the beam current I, divided by the $\frac{3}{2}$ power of the average beam potential V_0.

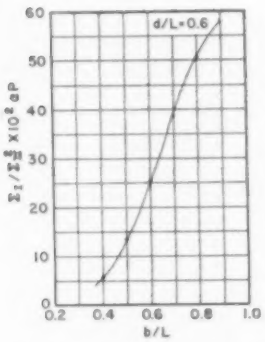

FIG. 6. Perveance variation according to b/L when $d/L=0.60$.

increase in d/L. For a given value of d/L it is necessary to evaluate the ratio of the two series, as they appear in equation (11). Figure 6 shows how the perveance varies with b/L, with $d/L=0.60$. It is seen that the perveance increases almost linearly, and rather rapidly, with increasing b/L, i/e, as the slot is made wider and wider relative to the period L. The main effect seems to be that, as the slots are made wider, the average potential V_0 is decreased, all other things remaining the same; this effect is readily calcuable from Eq. (7), the equation for V_0 on the line $y=0$. In a paper by Butcher,[6] Fig. 2, it is shown that the beam interaction impedance for the first backward wave on the ladder line is almost completely independent of b/L (Butcher uses the notation s for the b employed herein, and D for L), for $0.05<b/L<0.95$. Thus, the choice for b/L would be dictated in an actual design by dc focusing considerations, and by considerations of the thermal and mechanical properties of the ladder lines. From a dc point of view it is seen that b/L should be made as high as possible, if the aim is to obtain the highest possible equilibrium perveance (and, as will be seen, the highest possible beam stiffness). On the other hand, it must be kept in mind that a large value of b/L will reduce the average potential in the beam to something considerably less than the potential on the ladder lines themselves; this is a matter which could be of considerable importance in attempting to produce synchronism between the beam and rf backward waves near the high-frequency cutoff.

Beam Rippling

Because each lens of the periodic array is partially convergent and partially divergent, with a net effect of convergence, and because the space-charge forces are entirely divergent, it is impossible for the sheet beam to pass through the focusing system with a constant beam thickness. On the other hand the thickness may oscillate (spacewise, not time-wise) about some average value T_0, the amplitude of the oscillations increasing with an increase in lens strength. The appropriate solution of the paraxial equation reveals that the expression for the beam thickness is, using only two terms,

$$T=T_0[1-1/2\sum_n V_n/V_0\cos 2n\pi x/L], \qquad (12)$$

in which V_n is, as previously specified, the amplitude of the nth space harmonic of potential on the line $y=0$. If the potential on the line $y=0$ is written $V(x,0)=V_0[1+f(x)]$, in which $f(x)$ is the periodic variable part of the potential, the thickness is found to be of the form $T=T_0[1-1/2f(x)]$. Thus, the thickness is greatest where the potential is least, and vice versa. The beam will therefore oscillate away from the rungs of the ladder, where the potential is highest, and will oscillate outward, into the gaps between rungs, where the potential is lowest. This is a very fortunate state of affairs, for it permits the possibility of good rf interaction on the one hand, and provides a mechanism for small interception of current by the ladder lines on the other. However, this type of beam oscillation will occur if, and only if, the perveance of the injected beam is exactly equal to that calculated from Eq. (10); for other values of injected perveance the nature of the oscillations will be somewhat different, and will be discussed later.

Electron Plasma Frequency

The electron plasma frequency is given by the standard expression

$$\omega_p^2=\eta\rho/\epsilon_0, \qquad (13)$$

in which η is the specific charge of the electron, ρ is the volumetric charge density, and ϵ_0 is the permittivity of free space. Now ρ is related to the current density J and the forward velocity of the beam u by the relation $J=\rho u$. Furthermore, $J=I/WT$, and in view of the energy equation for the electrons, $u^2=2\eta V(x,0)$. If space-averages are denoted by the subscript $_0$ it is readily found that

$$\omega_{p0}^2=Iu_0/[2WT_0V_0\epsilon_0]. \qquad (14)$$

Upon substituting for I from the perveance formula (10), it is found that

$$\omega_{p0}=\frac{2}{L}u_0[1-V_2]\frac{[\sum_I(d/L,b/L)]^{\frac{1}{2}}}{V_2b/L+8c/L\sum_{II}(b/L)}. \qquad (15)$$

Because the beam is thin where the potential is high, and conversely, to a first approximation the plasma frequency is constant throughout the beam, i.e., independent of x. As far as a transverse variation of ω_p is concerned, we will only state without proof that, though the paraxial method does not demand that ρ be independent of transverse position y, within the beam, the method gives no information concerning any such possible variations of ρ. For this reason it may be assumed that ω_p is constant across the beam at any position x;

[6] P. N. Butcher, Proc. Inst. Elec. Engs., **104B**, 177 (1957).

this approximation is as good as the paraxial method itself.[7]

Transverse Resonant Frequency and Wavelength

Provided the beam current is adjusted to the critical value which will satisfy Eq. (10), *and* provided the beam is injected with zero slope (injection at the point $x=0$ is assumed), the beam will ripple with period L. If either the initial slope or the injected current is changed a different type of rippling will occur. For example, if the current is just right but the beam is diverging upon injection, the rippling will contain not only components having period L, but in addition a component having a much longer wavelength λ_e, as depicted in Fig. 7(a). It is convenient to neglect the components having period L, and consider only the long-wavelength ripple, as depicted in Fig. 7(b).

The time required for one complete cycle of the long-wavelength oscillation will be designated T_e; if u_0 is the average value of the forward velocity it is clear that $T_e=\lambda_e/u_0$. A *transverse resonant frequency* ω_e is defined by the relation $\omega_e=2\pi/T_e$. Then the long-wavelength ripple is representable by terms such as $\sin\omega_e x/u_0$, or $\sin\omega_e t$.

The solution of the paraxial equation which leads to the foregoing conclusion permits one to obtain an explicit formula for ω_e, provided the lenses are weak. It is found that the expression for ω_e is identical with Eq. (15), for the electron plasma frequency. In fact, it is possible to show that in electrostatically-focused sheet beams, the transverse resonant frequency is always equal to the electron plasma frequency for a beam possessing the equilibrium perveance.

The electronic wavelength λ_e may be expressed in units of L through the relation $\lambda_e/L=2\pi u_0/L\omega_e$. Upon replacing ω_e by the RHS of (15) one obtains

$$\lambda_e/L=\pi\frac{[V_2 b/L+8c/L\sum_{II}(b/L)]}{[1-V_2][\sum_I(d/L,\,b/L)]^{\frac{1}{2}}}. \tag{16}$$

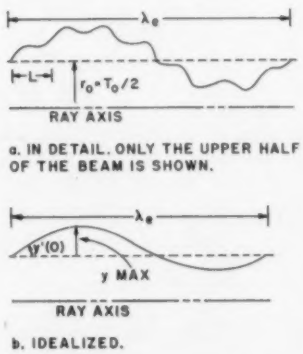

FIG. 7. Occurrence of different types of rippling (a) when the current is just right but the beam is diverging upon injection, and (b) when components having period L are neglected and the long-wavelength ripple is considered.

Beam Stiffness

If the current is such that Eq. (10) is satisfied, but the injection slope is incorrect, an approximate solution of the paraxial equation would be of the form $T=T_0+2y_{\max}\sin\omega_e x/u_0$ [see Fig. 7(b)], where the components possessing period L have been omitted. If $y'(0)$ is the injection slope it follows that $y_{\max}=y'(0)u_0/\omega_e$. Now clearly the maximum amplitude of the transverse oscillation is $y_{\max}$. The amplitude $y_{\max}$ should be as small as possible for a given value of $y'(0)$, in order that the focusing system shall be as tolerant as possible to improper injection conditions. Therefore, a quantity S, known as *beam stiffness*, is defined to be the ratio of $y'(0)$ to $y_{\max}$; $S=y'(0)/y_{\max}$. Thus,

$$S=\omega_e/u_0 \tag{17}$$

and the approximate solution of the paraxial-ray equation may be written in the form $T=T_0+[2y'(0)/S]\times\sin\omega_e x/u_0$. In this form it is easy to see that, the larger S is, the smaller will be the amplitude of the long-wavelength ripple arising from an improper injection slope.

Beam stiffness has the dimension of reciprocal length; upon substituting into (17) from (15) it follows that

$$S=2/L[1-V_2]\frac{[\sum_I(d/L,\,b/L)]^{\frac{1}{2}}}{V_2 b/L+8c/L\sum_{II}(b/L)}\ \text{rad/unit length}. \tag{18}$$

It is also possible to demonstrate that, if the beam is injected with the proper slope, but with a perveance which does not satisfy (10), again the long-wavelength ripple will occur, and the amplitude of this ripple will be $T_0[1-(P_{\text{injected}}/P_{\text{theoretical}})]$, where $P_{\text{theoretical}}$ is the perveance which satisfies (10). The above formula will be valid only if the injected perveance is greater than about one-half the theoretical perveance.

Numerical Example

In order to illustrate the use of the formulas which have been derived, some of the properties of a particular system will be calculated numerically. The following specific numbers are chosen: $b=0.035$ in., $L=0.050$ in., $d=0.030$ in., $c=0.030$ in., $T_0=0.010$ in., W$=0.500$ in. These numbers are compatible with the design of an X-band backward-wave oscillator.

From Figs. 4 and 5, respectively, $\sum_{II}=0.110$, and $\sum_I=4.62\times10^{-3}$; also, $WT_0/C^2=5.55$. On taking $V_2=0$, from (11) it follows that $P=1.4$ microperv, which is quite adequate for operation of an X-band oscillator. If c were to be reduced to 0.015 in. the theoretical perveance would increase to 5.6 microperv. A major problem arises concerning the formation of a beam having such a high perveance; in fact, it is far easier to design the focusing system for high perveance than to design an electron gun which can actually produce that perveance.

[7] P. T. Kirstein, J. Appl. Phys. **30**, 967 (1959); especially Sec. 3.

Next, from (7) it is found that $V_0=1-0.210=0.790$; the average potential in the beam is only 79% of the potential on the ladders. If c is reduced to 0.015 in. the beam potential is reduced still further.

Third, the stiffness is calculated to be $0.258/L$ rad/unit length. From this it follows that the amplitude of the long-wavelength ripple is 0.194 in./rad, or 3.5 mils/degree.

Finally, (5) is used to calculate that $V_m=0.626$.

In order to check the validity of this numerical example measurements on a scale model were made on conducting paper. Electrodes were represented by thin strips of silver paint. The important results of these measurements were: $V_0=0.797$, measured, compared with 0.790, calculated, and $V_m=0.640$, measured, compared with 0.626, calculated. The measured values are sufficiently close to the calculated values to justify the belief that all subsequent calculations based on the quartic approximation are of sufficient accuracy for most engineering purposes.

ACKNOWLEDGMENTS

The author wishes to express his appreciation to Dr. R. T. Young, Diamond Ordnance Fuze Laboratories, to Dr. Don A. Mittelman, National Bureau of Standards for many interesting discussions of this problem, and to Alfred Beam, Computation Laboratory, National Bureau of Standards, for evaluating the series $\sum_I$ and $\sum_{II}$.

APPENDIX I

Solutions of the Paraxial-Ray Equation

In making use of the paraxial equation the form of the potential is needed, in the absence of the beam, along a line which is considered to be the "ray axis," Here the ray axis is the line $y=0$, in Fig. 1. The potential on the ray axis is written in the form

$$V(x,0)=V_0+\delta\sum_n v_n\cos 2n\pi x/L. \qquad (1A)$$

The coefficients v_n give the form of the potential variation, whereas the *perturbation parameter* δ gives the magnitude of the potential variation, all on the ray axis. Let us now proceed to obtain a particular solution of the paraxial equation, under the assumption that $\delta\ll 1$.

The paraxial equation is

$$2Vr''+V'r'+V''r=\pm I/[2\epsilon_0 W(2\eta V)^{\frac{1}{2}}], \qquad (2A)$$

in which V is the ray axis potential, $V'=dV/dx$, r is the half-thickness of the beam at any point x, I is the total beam current, and W is the beam width, assumed constant. A series solution of (2A) is sought in the form

$$r=r_0+\delta r_1(x)+\delta^2 r_2(x)+\cdots, \qquad (3A)$$

in which r_0 represents the average half-thickness, r_1 represents first-order "rippling," r_2 represents second-order rippling, etc., and r_1, r_2, etc., are periodic functions of x, with period L. Upon inserting (1A) and (3A) into (2A), expanding, and collecting the complete coefficient of each power of δ,

$$\begin{aligned}&\delta[2V_0r_1''-r_0\textstyle\sum_n(2n\pi/L)^2v_n\cos 2n\pi x/L]\\&\quad+\delta^2[V_0r_2''+2r_1''\textstyle\sum_n v_n\cos 2n\pi x/L\\&\quad-r_1'\textstyle\sum_n(2n\pi/L)v_n\sin 2n\pi x/L\\&\quad-r_1\textstyle\sum(2n\pi/L)^2v_n\cos 2n\pi x/L]\\&\quad+\delta^3[\ ]+\cdots=I/[\epsilon_0W(2\eta V_0)^{\frac{1}{2}}]+\delta[\ ]+\cdots. \qquad (4A)\end{aligned}$$

The first-order term r_1 is obtained from (4A) by setting the coefficient of δ to zero, using only the expression on the LHS of (4A). In this fashion it is found that

$$r_1=-r_0/2V_0\textstyle\sum_n v_n\cos 2n\pi x/L. \qquad (5A)$$

Next this expression for r_1 is inserted into the bracketed coefficient of δ^2 in the LHS of (4A). It is found that the terms involving r_1 and its derivatives give rise to constants, which come from the expansion of each of the terms $\cos^2 2n\pi x/L$ or $\sin^2 2n\pi x/L$; the leading term in the RHS of (4A) is a constant. Therefore, all the constants arising from the δ^2 term in the LHS of (4A) are collected and equated the sum to the leading term in the RHS. This leads to

$$r_0/V_0\textstyle\sum_n(2n\pi\delta v_n/L)^2=I/[\epsilon_0W(2\eta V_0)^{\frac{1}{2}}]; \qquad (6A)$$

note that δv_n is the V_n of Eq. (8).

The remaining terms in the coefficient of δ^2 in the LHS are collected and set equal to zero. All these are sinusoidal in nature, with the exception of r_2''. Therefore, integration yields r_2, which will be found to consist of sinusoidal terms only. In this fashion the second-order ripping is obtained. The process may be iterated to obtain a refined perveance formula in place of (6A). However, a series of very careful measurements by B. J. Udelson, at the Diamond Ordnance Fuze Laboratories,[8] revealed that, in a particular periodic sheet beam focusing system, the electronic transverse wavelength, calculated from Eq. (16), agreed with the measured wavelength to within about 14%, even for values of δ as great as about 0.5; the agreement became progressively better as δ was decreased. The formula for the electronic wavelength is ultimately derived from our present equation (6A). This agreement is interpreted as valididating the use of (6A) for purposes of calculating perveance, plasma frequency, transverse resonant frequency and transverse electronic wavelength.

For purposes of calculating the stiffness, it is convenient to set $I=0$, and then to consider the motion of an electron which starts moving from, but at some angle with respect to, the ray axis. An approximate solution of the paraxial equation, of the form

$$r=a\sin\beta_e x(1+b\textstyle\sum v_n\cos 2n\pi x/L) \qquad (7A)$$

is assumed, and as stated, $I=0$. It is also assumed that $\delta\ll 1$. Then $b\simeq(-\delta/2)$ is found to be necessary, and $\beta_e(=2\pi/\lambda_e)$ eventually is given by (16).

[8] B. J. Udelson, private communication. A paper describing these measurements is to be published.

Metal Precipitates in Silicon p-n Junctions*

A. GOETZBERGER AND W. SHOCKLEY
Shockley Transistor Unit of Clevite Transistor, Mountain View, California
(Received May 24, 1960)

Metal precipitates in junctions were found to cause excess reverse current below avalanche breakdown, which is conjectured to be due to Zener tunneling at localized high-field points. This current varies as V^n where n is between 4 and 7. By a potential plotting method, it was shown that this excess current is not caused by a surface effect. Metal precipitates can be removed or prevented by "gettering" from surface layers. Metallic coatings and certain glassy oxide layers were investigated. Results indicate that layers of Ni and Zn have a limited gettering effect. Glassy layers, especially those of boron and phosphorus, have the greatest gettering effect.

A NUMBER of metals, such as Cu, Au, and Fe, have a strongly temperature-dependent solid solubility in silicon which causes supersaturation and formation of precipitates during the cooling cycle. Dash[1] observed precipitation of Cu preferentially on dislocations. The first part of this paper reports effects of precipitates on p-n junctions; the second part is concerned with methods of improving junctions by removing these precipitates by means of gettering.

EXPERIMENTS ON JUNCTIONS CONTAINING PRECIPITATES

Goetzberger and Shockley[2] found a localized current path through junctions that had been treated in a manner expected to produce metal precipitates. Phosphorus was diffused into p-type silicon slices of 0.04 ohm cm resistivity to a depth of approximately 6 μ. They were treated for 5 min in hydrofluoric acid, then nitrates of different metals were applied in aqueous solution to one of the pair of slices that were used for each experiment, the untreated slice serving as a control. After drying, both slices were heated for 60 min in H_2 at 1000°C, then cooled within 6 min to room temperature. Wax dots were placed on both slices and dice were etched by spraying with CP8 (5 parts concentrated HNO_3, 3 parts concentrated HF) to produce diode chips.

The avalanche breakdown voltage was about 12 v. A large percentage of the treated diodes had a rounded or "soft" reverse characteristic caused by excess current below avalanche breakdown voltage. The control diodes that were made from a slice subjected to the same heat treatment were predominantly hard. Figure 1 shows a statistical evaluation of softness and hardness after treatment with different metals, each run consisting of at least 50 diodes. Diodes with more than 10 μa reverse current at breakdown were defined as soft.

Evidence that the reverse current flowed at a localized spot was obtained by using a potential plotting method applied to one diode that had been softened by diffusion of iron (Fig. 2). A constant reverse current was fed into the diode through a small wire contact. A second probe at fixed location was used as a voltage reference, and the voltage between it and a third movable probe was measured for an array of points spaced typically at 0.05 mm on the surface. (The potential probes were formed by passing a current pulse to obtain low impedance contacts.) From the sheet conductance of 1.0 mhos and the potential profile, it follows that all the reverse current of 200 μa can be accounted for within experimental error at the localized point.

The reverse characteristic of this diode is given in Fig. 3. The $-70°$ line shows a current that varies as $V^{5.5}$ where V is the reverse voltage. Since this soft current obeys the $V^{5.5}$ law to voltages as low as 0.8 v, it cannot be due to avalanche, and is conjectured to be due to Zener tunneling at localized high-field points caused by precipitates.

In general, diodes softened by processes expected to produce metal precipitates have soft currents which vary as V^n with n lying between 3 and 7. These characteristics are readily distinguishable from junctions having points of low voltage avalanche breakdown, which show a sharp upward bend on a plot like Fig. 3.[2]

Soft currents, which followed a power law of voltage,

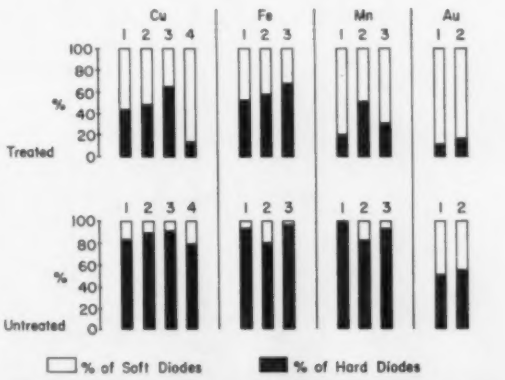

FIG. 1. Percentage of hard and soft diodes after treatment with different metals. (The number above each bar is the number of the test run.)

* Work sponsored by Air Force Cambridge Research Center.
[1] W. C. Dash, J. Appl. Phys. 27, 10, 1193 (1959).
[2] A. Goetzberger and W. Shockley, *Structure and Properties of Thin Films* (John Wiley & Sons, Inc., New York, 1959), pp. 298–301; Bull. Am. Phys. Soc. Ser. II, 4, 409 (1959).

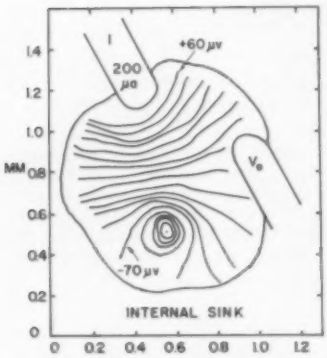

FIG. 2. Equipotential plot of iron diffused junction.

were also observed by Pell[3] in germanium and Plummer[4] in silicon. Both associated this current with a volume effect rather than a surface effect.

REMOVAL OF PRECIPITATES BY GETTERING

Because soft characteristics are undesirable in most devices, there is considerable interest in techniques which avoid formation of precipitates during the diffusion process.

One way of obtaining good junctions consists in excluding every trace of softening metals from the silicon. However, this is extremely difficult since in some cases a fraction of an atomic layer on a slice of silicon is sufficient to achieve saturation.

A more practical procedure is one which allows removal of metal precipitates during or after diffusion

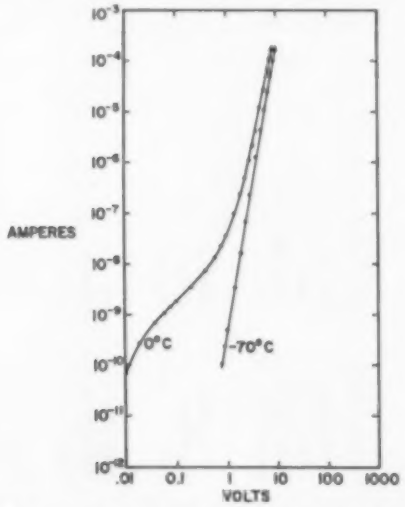

FIG. 3. Current-voltage characteristic of iron diffused junction.

[3] E. M. Pell, J. Appl. Phys. **28**, 4, 459 (1956).
[4] A. R. Plummer, J. Electronics and Control **V**, 5, 405 (1958).

by means of gettering.[5] Two possible methods of gettering were investigated. One consisted of gettering by a thin layer of Zn or Ni on the surface; the other was gettering by a glassy layer of oxides. Only the second method proved satisfactory.

A. Gettering with Zn and Ni

This procedure was tried because it was found by Bemski and co-workers[6] that coating silicon with Ni and heating it to temperatures of 1000°C or more was very effective in improving minority carrier lifetimes in the silicon. The reason for this effect is believed to be the gettering action of a liquid Ni-Si phase on the surface, due to a very low distribution coefficient of certain recombination centers. Since some of the metals which reduce lifetime in silicon also cause softness of characteristics, it was thought that this treatment might reduce softness. In addition to Ni, Zn was tried in our experiments because it had been found previously that Zn

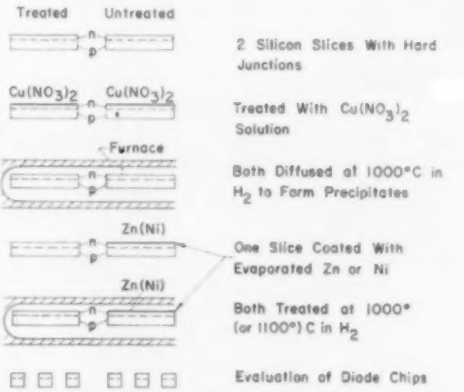

FIG. 4. Gettering experiment with Zn and Ni.

seemed to improve characteristics. The procedure is shown in Fig. 4.

Four identical silicon slices which contained originally hard junctions were used for each experiment. (Only two of them are represented in Fig. 4.) One of them was evaluated before treatment, the remaining three were coated with $Cu(NO_3)_2$ solution and subjected to heat treatment in order to form precipitates. One of these was coated with a layer of evaporated Ni and another with Zn, followed by 60 min heat treatment at 1000°C in hydrogen. Diode chips were then etched from each slice and the hardness evaluated. Again, characteristics with more than 10 μa reverse current at breakdown were defined as soft. The results of six experiments, shown in Fig. 5, indicate that both the Ni and the Zn treatments improve the junctions somewhat, but fail to restore the hardness present before treatment.

[5] A. Goetzberger, Bull. Am. Phys. Soc. Ser. II, **5**, 160 (1960).
[6] G. Bemski, Phys. Rev. **103**, 567 (1956).

Since there was some doubt whether the gettering temperature of 1000°C was high enough, the same test was repeated at 1100°C. Results were similar to those obtained at 1000°C.

B. Gettering with Oxide Layers

1. Predeposition Treatment

The second method of gettering studied was one which used oxide layers on the surface. It had been observed that junctions which were measured after predeposition with P_2O_5 or B_2O_3 vapors without further diffusion were predominantly hard. Therefore, it was concluded that the layer formed on the surface of the silicon and consisting of a glassy mixture of these oxides with SiO_2 might have gettering properties. A possible mechanism is shown in Fig. 6. Metal atoms diffuse from the precipitate within the space charge region to the surface where they react with the getter material by

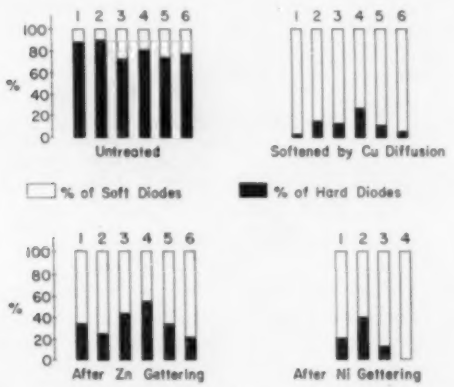

FIG. 5. Results of gettering with Zn and Ni (numbers again indicate number of test run).

formation of chemical compounds, such as phosphates or borates. Concentration of free metal on the surface will be extremely low, a condition favorable for gettering. Simultaneously with the diffusion of the metal atom, a vacancy has to diffuse from the precipitate to the surface in order to keep the volume constant. This process, which involves self-diffusion of silicon, may be of importance in limiting the rate and controlling the temperature dependence of the gettering effect.

In order to test the hypothesis that the glassy layers getter the softening impurities, silicon slices containing hard junctions like those in the preceding experiment were doped with Cu. Then they were subjected to another predeposition with P_2O_5 in dry nitrogen at 1050°C for 30 min. The results [Fig. 7(a)] show a strong gettering effect.

Soft diodes are not only obtained by metal doping, but also by a long diffusion at high temperatures, if the furnace chamber is not exceptionally clean. A 2-hr

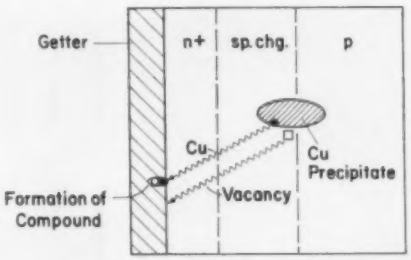

FIG. 6. Mechanism of oxide gettering.

diffusion at 1300°C usually yields 100% soft diodes. This type of softness, which is conjectured to result from ever-present metal impurities in the diffusion furnace, responds to the same gettering treatment, as can be seen in Fig. 7(b).

Figure 8 gives some information about time and temperature dependence of the gettering efficiency of P_2O_5 and B_2O_3 predeposits. In both cases, silicon slices which had been diffused for 2 hrs at 1300°C, and which contained 100% soft junctions, were used. The phosphorus oxide treatment was carried out in a two-temperature-zone furnace with a source temperature of 210°C. For the boron predeposit the silicon slices were enclosed in a platinum box together with a pure B_2O_3 source. (No gettering effect could be observed with a diluted source of 25% B_2O_3 and 75% SiO_2.) Figure 8 shows that the phosphorus pentoxide seems to be effective at a slightly lower temperature than the boron oxide. The transition between hard and soft in the case of the phosphorus predeposit is not so abrupt as it appears, due to the arbitrary value of 10 μa, which was chosen as the definition of softness. The results of Fig. 8 are representative of only one set of experiments. Slight variations can be observed under different diffusion conditions.

2. Paint-on Treatment

Phosphorus and boron oxides can be applied to the silicon surface not only from the vapor phase, but also by the so-called "paint-on" technique.[7] This procedure

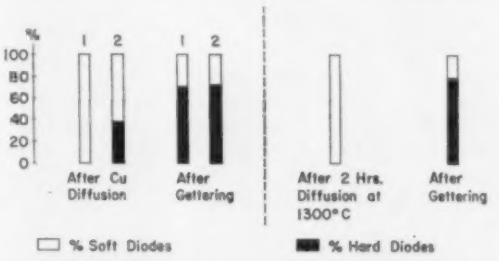

FIG. 7. (Left) P_2O_5 gettering on copper diffused junction. (Right) P_2O_5 gettering on junction softened by 1300°C diffusion.

[7] H. E. Hughes, J. H. Wiley, and P. Zuk, *IRE Wescon Convention Record, 1957*; Part 3, Electron Devices; p. 80.

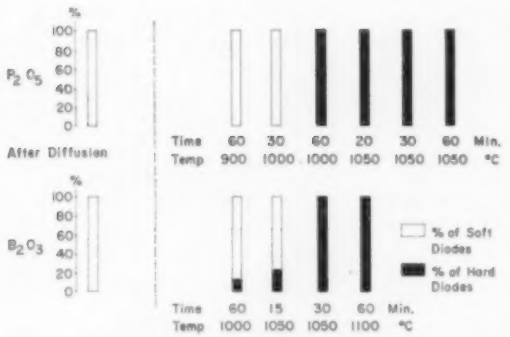

FIG. 8. Temperature and time dependence of P_2O_5 and B_2O_3 gettering.

has the advantage of using only one side of the slice for the gettering treatment, which leaves a highly doped layer on the silicon. It was tried on silicon slices of 150 μ thickness and also found effective. It works, however, only for a limited time at a high temperature (such as 1300°C) because the oxides tend to evaporate.

Sometimes it would be desirable to use a getter material that is not doping. Therefore a surface layer of PbO was tried for gettering. Results were promising, but the lead oxide glass could not be removed after gettering by any known etching treatment.

DISCUSSION OF RESULTS

The temperature dependence of gettering indicates that the diffusion of the precipitated metals to the surface is not the rate limiting factor, since the diffusion constant of all metals which were found to soften junctions is in the range of 10^{-6} to 10^{-5} cm^2/sec, and varies little with temperature.[8] Two other processes could cause the temperature threshold. One is the vacancy diffusion as already mentioned. The other is the temperature dependence of the chemical reactions on the surface, which lead to trapping of the metal atoms. The second possibility is suggested by the fact that the dependence of phosphorus oxide gettering on temperature is not the same as that of boron oxide gettering (Fig. 8).

Silicon dioxide itself has no effect on precipitates. This is plausible because of the strong bond between oxygen and silicon, which prevents formation of compounds with other elements. It was observed that gettering occurred only as long as the oxide glass on the surface was liquid. This can be understood by considering that there is always some oxidation of the silicon going on. As soon as the coating solidifies, a very thin layer of silicon dioxide will grow on the surface of the silicon and prevent further gettering.

No detailed investigation has been made on the oxide gettering effect on lifetime. There should be, however, an improvement of lifetime. This was verified by a few experiments on transistors which showed a considerable increase in amplification after gettering treatment.

CONCLUSIONS

Softness of characteristics with current proportional to V^n was found to be a reversible phenomenon. It can be induced by diffusion and precipitation of certain metals in silicon. These metals can be removed or prevented by a surface layer of either boron oxide or phosphorus pentoxide on at least one side of a silicon slice. Figure 9 shows three different methods of producing

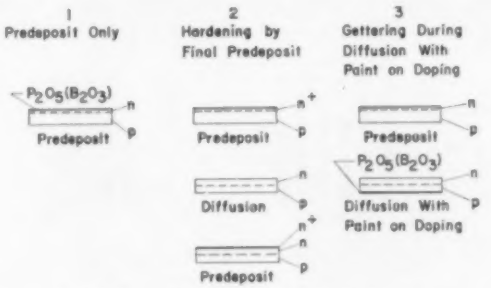

FIG. 9. Procedures for obtaining hard junctions.

hard junctions. Method 1 consists of a predeposit step only. Gettering and doping is done with the same surface layer. Method 2, which is important for deep junctions, consists of predeposition, diffusion and another predeposition. Finally, in method 3, a slice which has been predeposited on one side can be diffused while the other side is coated with paint-on doping.

Gettering is very easily achieved for all those devices which require a heavily doped surface layer. These can be degenerate layers on diodes for ohmic contacts or emitters of diffused transistors. The diffusion of this layer, which is usually the last step, can be designed to include the gettering effect.

ACKNOWLEDGMENTS

We would like to acknowledge the cooperation of Dr. Hans Wagner who designed some of the experimental apparatus, and Charles Stephens who made many of the electrical measurements. We also are indebted to B. McDonald, N. Zetterquist, and M. Lichtenstein for carrying out the diffusions.

[8] F. M. Smits, Ergeb. exak. Naturw. **31**, 167 (1959).

Letters to the Editor

On the Temperature of an Object Irradiated with Electrons

S. YAMAGUCHI
The Institute of Physical & Chemical Research, 31 Kamifuji (Hongo), Tokyo, Japan
(Received May 2, 1960)

INVAR (Ni, 36%), Curie temperature known to be 120°C, was employed in order to study the temperature elevation of an object caused by electron bombardment. Powder of Invar (size, about one micron) was prepared by filing an ingot of it. These particles were attracted to the sharp edge of a razor blade of hard steel, of which the remanence was known to be about 10 000 gauss. In this way the specimen of Invar was kept at saturation induction. As seen in Fig. 1, an electron beam grazed the magnetized particles of Invar to give rise to an electron diffraction pattern. The wavelength and the current of the incident electrons used in the present study were 0.0299 A and 0.1 mA, respectively. The electrons grazing the specimen were subjected to the Lorentz effect given by the induction of the specimen. A temperature dependence of this effect was observed as follows.[1]

A diffraction pattern of the specimen was *first* photographed. Here was avoided, as carefully as possible, preheating the specimen

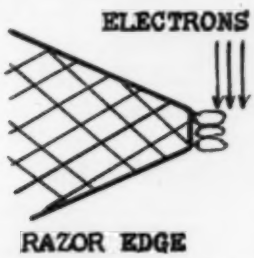

FIG. 1. Arrangement for the electron diffraction at the Invar particles.

with the incident electrons. The minimum exposure time for photographing the diffraction pattern was only 0.5 sec. *Secondly*, the diffraction pattern from the warmer specimen, which had been preheated for 2 min without interruption, was superposed upon the initial pattern from the cool specimen. In these processes, the wavelength and the intensity of the incident electrons as well as the position of the photographic plate were kept fixed. A double diagram obtained in this way from the cool and the hot specimen is shown in Fig. 2. This figure shows *eccentricity* among the diffraction rings. This implies that the Lorentz effect of the specimen on the electrons depends on the temperature of the specimen. The ring eccentricity ΔZ measurable in Fig. 2 makes it possible to calculate the difference ΔB between the induction of the specimen at the higher temperature and that at the lower temperature. That is

$$\Delta B \simeq \frac{h}{eL\lambda l}\cdot\Delta Z, \qquad (1)$$

where h means Planck's constant (6.6×10^{-27} erg sec); e, the electron charge (1.6×10^{-20} emu); L, the camera length (495 mm); λ, the wavelength of the electrons (0.0299 A); and l, the magnetic path traveled by the electrons. In Fig. 2 we measure $\Delta Z = 0.04$ cm. Therefore, we obtain

$$\Delta B \simeq 4000 \text{ gauss}$$

according to Eq. (1), where we assume $l \simeq 3\ \mu$.[2]

It is plausible that the temperature of the specimen, when irradiated with the electronsunder the present conditions (irradiation time, 2 min), exceeds 120°C (i.e., the Curie temperature of itself) and so it becomes paramagnetic. If this is the case, the value of ΔB measured here (4000 gauss) should be equal to the difference between B_s and B_r.

$$\Delta B \simeq B_s - B_r,$$

where B_s means the saturation induction of Invar (about 15 000 gauss at room temperature) and B_r, the remanence of the razor edge (about 10 000 gauss). This difference (5000 gauss) agrees approximately with the observed value of ΔB (4000 gauss).

During the present diffraction processes, some particles of Invar which had been attached to the razor edge left it after they had been irradiated two or three minutes with the rather intense beam of electrons. This is explained by the Invar particles, becoming paramagnetic as the result of the temperature elevation over the Curie temperature, so that their weight was now able to pull them off. In the diffraction pattern of Fig. 2 there are the weak rings corresponding to Fe_3O_4. This ferromagnetic inclusion, with the comparatively high Curie point (575°C), could play a role in making the Invar particles remain adhered to the razor edge after the temperature of these particles arrived at the Curie point

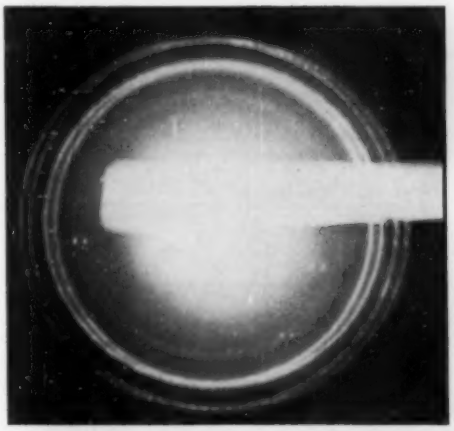

FIG. 2. A double diagram composed of the diffraction rings from the cold and the hot Invar specimen. Ring eccentricity is remarkable. Wavelength: 0.0299 A. Camera length: 495 mm. Positive enlarged about four times.

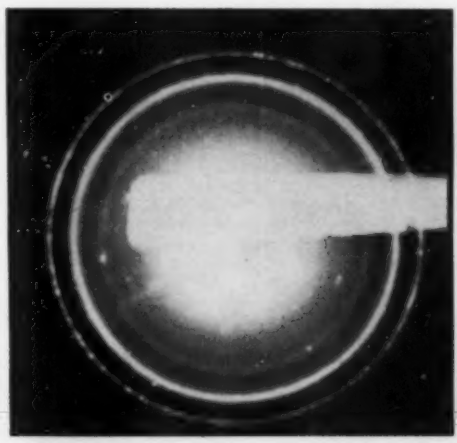

FIG. 3. A double diagram from the specimen at the different temperatures over its Curie point (120°C). There is no ring eccentricity.

(120°C). It is not plausible that the temperature of the specimen attained 500°C under the conditions of the experiment.

Figure 3 is a double diagram obtained from the specimen irradiated for two minutes with the electrons and from that irradiated for four minutes. In this double diagram there are concentric all the diffraction rings seen in Fig. 2. This implies that the specimen irradiated longer than two minutes under the present conditions exceeds the Curie point and so becomes paramagnetic.

[1] S. Yamaguchi, J. Appl. Phys. **30**, 1619 (1959).
[2] This l value is roughly estimated according to the process described in the previous report,[1] for the value of the induction at the razor edge (10 000 gauss) is known.

Determination of Dose Rates from Beta Transmission Currents

ARTHUR BRADLEY
Radiation Research Corporation, 1114 First Avenue, New York 21, New York
(Received May 16, 1960)

WORK in progress in this Laboratory involving electrostatic nuclear batteries[1] and radiation effects on solid dielectrics[2] has frequently required calculations of absorbed dose rates from experimental measurements of beta transmission currents. Using the approximation that beta absorption is an exponential function of sample thickness, the relationship can be reduced to a simple function of the characteristics of the beta emission and the area of the irradiated sample.

In a typical experimental setup, a thin dielectric is sandwiched between two electrodes, one of which is also a source of beta particles. The current measured in an external circuit connecting the electrodes is dependent upon the decomposition rate of the radioisotope, the geometry, the absorption losses, and distortion of the beta energy spectrum by space charge effects in the dielectric.[3] The dose rate to the sample could be computed, with difficulty, from these same factors, but fortunately it is possible to calculate it directly from the external circuit current.

The symbols employed are as follows:

I_β	beta transmission current (experimental) in micromicroamperes
I_β^0	beta current extrapolated to zero sample thickness
E_{av}	average beta energy (in Mev)
μ	mass absorption coefficient (cm²/g)
x	thickness of sample (g/cm²)
a	area of sample being irradiated (cm²)
R	dose rate in sample (rads/sec) (1 rad = 100ergs/g).

The beam power to which the sample is exposed is $10^{-6}I_\beta^0 E_{av}$, and that which it absorbs is $10^{-6}I_\beta^0 E_{av}(1-e^{-\mu x})$. A relationship between I_β and I_β^0 has been developed.[3] It may be expressed in the form of Eq. (1).

$$I_\beta^0 = (\mu x I_\beta)/(1-e^{-\mu x}). \tag{1}$$

The beam power absorbed is therefore equal to $10^{-6}\mu x I_\beta E_{av}$ (in watts).

To obtain the dose rate in rads, this must be divided by the weight of sample irradiated, and a numerical factor introduced to convert watts to ergs/sec, as in Eq. (2).

$$R = \frac{10^{-6}\mu x I_\beta E_{av}\cdot 10^7}{xa\cdot 10^2} = \frac{\mu I_\beta E_{av}}{10a}. \tag{2}$$

A typical I_β measurement in either a nuclear battery or an induced conductivity measurement would be 10^{-11} amp/cm². Using Eq. (2), the dose rate to a dielectric sample transmitting such a beta current ($I_\beta/a = 10$) has been calculated for several representative isotopes. The value of μ taken in each case is most accurate for materials of atomic weight close to aluminum.[4] This would generally include all dielectrics not containing an appreciable fraction of hydrogen. The electron-stopping power of hydrogen is significantly higher than all the remaining elements,[5] with the consequence that the same incident beam power can be expected to give a somewhat higher dose rate.

Because of the approximately reciprocal relationship between μ and E, the dose rate function of the beta transmission current is nearly independent of the isotope (Table I). It is not unreasonable that a high-curie source of weak emission and a low-curie source of strong emission—both resulting in the same residual beta current—would deliver about the same radiation dose to an absorber. Equation (2) may be expected to fail at higher sample thicknesses, where the assumptions behind the expression for I_β^0 [Eq. (1)] become invalid.[3]

TABLE I. Approximate dose rate (R) for $I_\beta/a = 10$, calculated for various radioisotopes from Eq. (2).

Isotope	μ, cm²/g	E_{av}, Mev	R, rads/sec
Pm^{147}	94	0.065	6.1
Kr^{85}	26	0.23	6.0
Sr^{90a}	30	0.2	6.0
Y^{90}	7.0	0.90	6.3
Pr^{144b}	4.9	1.2	5.9

[a] If the radioactive source is a mixture of two isotopes, in theory both should be considered independently. Depending on the absorber thickness, the Sr^{90}/Y^{90} contribution to I_β may vary from 0 to 0.5. Fortunately, the variation in R with emission energy is small and any error introduced by considering the equilibrium mixture exclusively Y^{90} would be negligible for this purpose.
[b] High-energy daughter of Ce^{144}. The presence of the latter isotope may be neglected, as in footnote a.

[1] J. H. Coleman, Nucleonics **11**, No. 12, 42 (1953).
[2] A. Bradley, A. P. Pinkerton, and S. Grand, Insulation **5**, No. 11, 27 (1959).
[3] B. Gross, A. Bradley, and A. P. Pinkerton, J. Appl. Phys. **31**, 1035 (1960).
[4] R. D. Evans, *The Atomic Nucleus* (McGraw-Hill Book Company, Inc., New York, 1955), p. 628.
[5] L. V. Spencer, *Energy Dissipation by Fast Electrons*, Natl. Bur. Standards (U. S.) Monograph 1, September, 1959.

Oscillations in Germanium with an Applied Pulsed Electric Field

M. CARDONA AND W. RUPPEL
Laboratories RCA Ltd., Zurich, Switzerland
(Received June 20, 1960)

CURRENT oscillations at room temperature in semiconductor crystals under the action of an electric field have been reported for transistor structures[1] and for uniform crystals in the presence of a magnetic field.[2] For the oscillations in uniform crystals, amplitude, frequency, and waveform depend in a complicated way on the magnitude and relative orientation of the electric and magnetic fields, the surface treatment of the sample, and the nature of the contacts. In this letter, oscillations occurring in uniformly doped samples, also in the absence of a magnetic field, are reported.

The oscillations were observed in 3 p-type germanium single crystals. Their resistivities were 23, 14, and 4.2 ohm cm. Their dimensions were 8, 4, and 2 mm. No oscillations were observed in n-type samples and in highly extrinsic p-type samples. The samples were etched with CP_4, and a tin soldered contact was made at one of their ends. A metal point contact was placed on the opposite end of each sample. Both platinum and Nikrothal wire[3] were used for the point contact, but apparently the metal used is not critical, provided the contact is rectifying.

The experimental setup was similar to the one used by Ivanov and Ryvkin.[2] A pulsed electric field was used to prevent heating of the sample by the high currents required to produce oscillations.

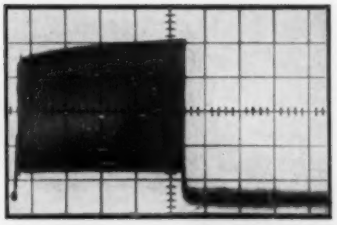

FIG. 1. Oscillations in p-type Ge during application of a pulse. No magnetic field. Horizontal scale: 5 μsec/div. Vertical scale: 4 ma/div.

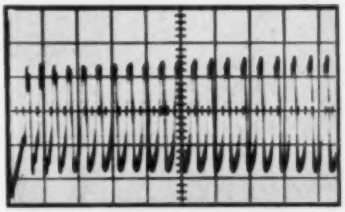

FIG. 2. Beginning of the oscillations in Fig. 1, enlarged. Horizontal scale: 1 μsec/div. Vertical scale: 4 ma/div.

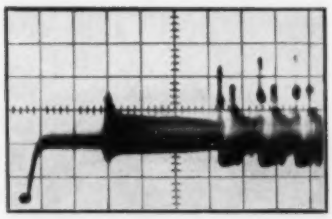

FIG. 3. Oscillations in a transverse magnetic field of 10 000 gauss. Horizontal scale: 2 μsec/div. Vertical scale: 4 ma/div.

The observations were made across a load resistor of 50 ohms in series with the sample. The circuit had no reactive components to which the oscillations could be attributed.

The large distance (8 mm) between the contacts and the absence of a collector junction ruled out the possibility of oscillations similar to those reported for transistors.[1] Furthermore, no negative resistance was observed.

Figure 1 shows a typical state of oscillation without magnetic field of the 14 ohm cm germanium sample. The amplitude of the current pulse was 10 ma. The duration of the pulse was 25 μsec with a repetition rate of 40/sec. Figure 2 shows the same oscillations on an expanded time scale.

The amplitude of the oscillations increased with increasing applied voltage. A minimum voltage of about 30 v was required to produce oscillations. The oscillations were coherent for any of the repeating pulses. This is shown by the figures, which were all taken with an exposure time of 10 sec.

The frequency of the oscillations varied within wide limits. Depending on the position of the contact, two types of oscillations were observed. One type had a frequency around 5 kc and the other around 5 Mc/sec. While for the low frequency oscillations the modulation of the applied pulse was about 10%, the modulation for the high-frequency oscillations was up to 80%.

When the ratio of the pulse width to the repetition time exceeded a certain value, the sample warmed up and the amplitude of the oscillations decreased. The heating of the sample seemed to affect more the high-frequency oscillations than the low-frequency oscillations.

A longitudinal magnetic field up to 10^4 gauss did not substantially alter the oscillations. Under the action of a transverse magnetic field, the oscillations either disappeared or were strongly distorted. An example of distorted oscillations in a transverse magnetic field is shown in Fig. 3.

Oscillations were only observed with a rectifying contact biased in the forward direction. The injection of minority carriers seemed to be necessary for the production of oscillations. Since almost the entire voltage drop occurs at the point contact, the oscillations probably originate in the immediate vicinity of the contact.

[1] H. Schenkel and H. Statz, Proc. IRE **44**, 360 (1956); M. C. Kidd, W. Hasenberg, and W. M. Webster, RCA Rev. **16**, 16 (1955).
[2] Yu. L. Ivanov and S. M. Ryvkin, Soviet Phys.-Tech. Phys. **3**, 722 (1958).
[3] Made by A. B. Kanthal, Sweden.

Direct Replica Technique for Copper

J. O. STIEGLER AND T. S. NOGGLE
Solid State Division, Oak Ridge National Laboratory, Oak Ridge, Tennessee*
(Received July 18, 1960)

HIGH resolution replica techniques for the electron microscope examination of metal surfaces usually employ evaporated films which must subsequently be stripped from the metal surfaces for examination in the microscope. The most critical stage in this technique is the stripping operation, in which acid attack is usually used to undermine and free the replica. In addition to extensive etching of the surface, this method is extremely erratic in the ease with which it frees the replicas. Frequently the gas evolved in the etching process breaks the film into unusable fragments. The system described in this note relates primarily to a stripping technique for preshadowed carbon replicas of copper surfaces which overcomes the disadvantages of acid stripping and introduces some unique advantages.

This method involves the dissolution of the thin oxide layer normally present on copper surfaces in a dilute aqueous solution of ethylenediamine (~0.1%).[1] Ethylenediamine attacks only the oxide film and not the copper surface, resulting in an essentially nondestructive replica technique. The stripping action is rather slow, and experience has shown that it can be speeded up considerably by exposing the replicated surface to the fumes of concentrated nitric acid prior to immersion in ethylenediamine. After this treatment the replicas immediately float free on the ethylenediamine solution. They can then be easily transferred to distilled water baths for washing and picked up on specimen grids in the usual manner. Using this technique replicas consistently may be stripped intact from areas several centimeters in mean dimension.

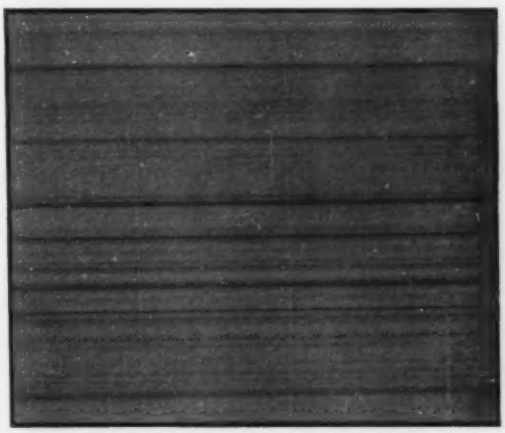

FIG. 1. Slip lines on single crystal copper specimen deformed in tension to 10% elongation. 12 000 ×.

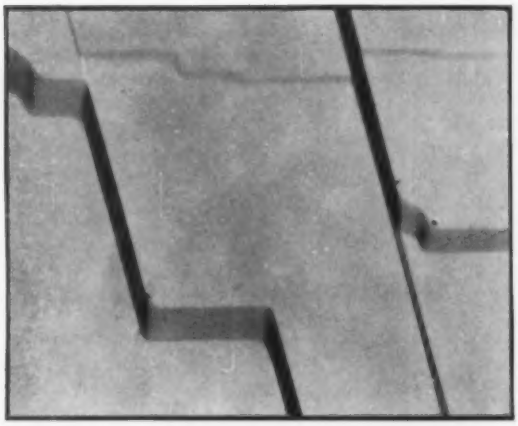

FIG. 2. Slip lines on irradiated single crystal copper specimen deformed in tension to 2% elongation. The deformation was concentrated in one region of the specimen; the local deformation level is 5 to 10 times greater, i.e., 10–20% elongation. Irradiated to $\sim 10^{19}$ nvt fast. 6000 ×.

Exposure to nitric acid fumes is an essential step in obtaining rapid, reproducible stripping. The carbon film appears to act as a permeable membrane to the oxidizing constituents in the nitric acid fumes allowing the formation of a thicker, more easily dissolved oxide layer under the replica. In general the thinner carbon films are removed more rapidly and reliably; difficulty is often encountered in removing carbon films thicker than about 500 A.

Platinum preshadowed carbon replicas have been employed in these studies. In no case has there been any evidence of a loss of shadowing material or of any change in the shadow arising from the exposure to the nitric acid fumes.

This technique is being employed in a study of the effect of reactor irradiation on the deformation of copper. Figures 1 and 2 illustrate the striking changes that occur as a result of the irradiation. Figure 3 is an example showing the possibility of repeated replication of the same surface. In this case the general roughening of the surface and frequent coarse pitting produced by two preceding replications are apparent; nevertheless, the original slip

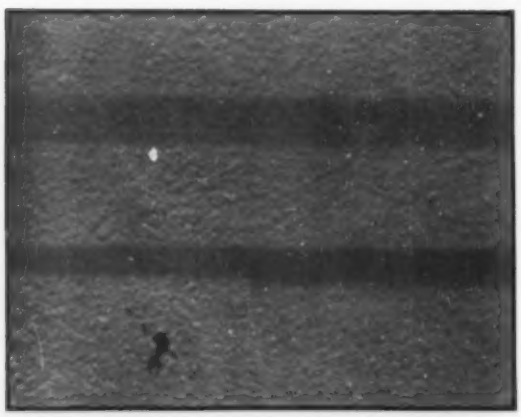

FIG. 3. Slip lines on irradiated single crystal copper specimen deformed in tension. The specimen was deformed to 5% elongation, electropolished, strained an additional 2%, and the surface replicated twice. It was then given an additional 1% elongation and replicated again. This micrograph is from the final replica and illustrates the effect of previous replications on the surface. Irradiated to $\sim 10^{19}$ nvt fast. 6500 ×.

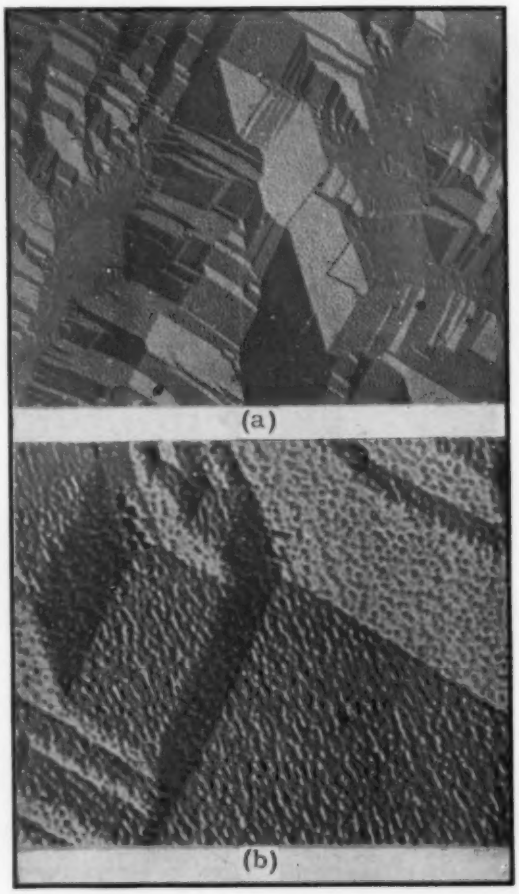

FIG. 4. (100) surface of a copper single crystal produced by anodic dissolution in a copper sulfate solution at a low current density. a: 8000 ×. b: 35 000 ×.

lines are still well defined and, in addition, may be differentiated from those introduced by the last strain increment since the slipped surface of the original lines has been slightly roughened as a result of the prior replication. Figures 4(a) and 4(b) are micrographs of a considerably rougher surface produced by anodic dissolution of a copper single crystal in a copper sulfate solution at low current density ($\sim 5\ \mu amp/cm^2$).[3] These micrographs clearly show the high quality of the replica produced by this technique for both low and high magnification studies.

No difficulty has been encountered in stripping carbon replicas from surfaces showing the range of roughness pictured here. The technique is rapid, reliable, and reproducible. Further, it is possible to replicate a surface several times without destroying the gross features and to distinguish changes in the structure occurring between replications. Possibly this technique may be extended to systems forming similar surface oxide films which are readily soluble in ethylenediamine or other strong complexing agents.

* Oak Ridge National Laboratory is operated by Union Carbide Corporation for the U. S. Atomic Energy Commission.

[1] For a discussion of the reaction of copper with aqueous ethylenediamine see L. H. Jenkins, ORNL-2829, (August 31, 1959), p. 88; also L. H. Jenkins, J. Electrochem. Soc. **107**, 371 (1960).

[2] Specimen kindly furnished by L. H. Jenkins, ORNL Solid State Division.

Generation of Millimeter Waves by the Electron Beam of a Microtron*

E. BRANNEN, H. FROELICH, AND T. W. W. STEWART
Department of Physics, University of Western Ontario, University College, London, England
(Received July 20, 1960)

AS first pointed out by Kaufman and Coleman,[1] the microtron is a source of a highly bunched electron beam. This property can be utilized to excite electromagnetic waves at frequencies which are harmonics of the fundamental frequency of the rf power used to accelerate the electrons. Applying the harmodotron scheme of Coleman *et al.*[2,3] we have generated 8-mm power at the milliwatt level and are at present extending the measurements to the 4-mm region.

The microtron used here was a conventional type with a homogeneous magnetic field and rf power at 10.83 cm. The third orbit (1.5 Mev) was extracted[4] and the beam focused by quadrupole magnetic lenses and injected into a tunable high-order mode cylindrical copper cavity. The peak current entering the cavity was approximately 0.7 ma. Typical powers generated were 0.5 mw in the TM_{018} and TM_{026} modes corresponding to a wavelength of 8.33 mm, in good agreement with theoretical values. Although the cavity was designed for optimum operation in these modes, power was detected at wavelengths as low as 6.77 mm but this was outside the calibration range of the instruments used. Many different high-order modes were identified consistent with the expected operation of the cavity. Future work at lower wavelengths will include comparison with the dielectric tube resonator and Cerenkov radiator.

The conventional microtron is limited in current output and a four-sector race track microtron (4–12 Mev) with beam injection has been designed and is being completed.

It is a pleasure to acknowledge in this work the continued support and cooperation of Dr. R. I. Primich of the Defence Research and Telecommunications Establishment, Ottawa.

* The research for this paper was supported by a grant from the National Research Council, and the Defence Research Board of Canada.
[1] I. Kaufman and P. D. Coleman, J. Appl. Phys. **27**, 1250 (1956).
[2] P. D. Coleman and M. D. Sirkis, J. Appl. Phys. **26**, 1385 (1955).
[3] R. H. Pantell, P. D. Coleman, and R. C. Becker, I R E Trans. on Electron Devices **ED-5**, 3, 167 (1958).
[4] E. Brannen and H. I. S. Ferguson, Rev. Sci. Instr. **27**, 833 (1956).

Research Reports

This column will announce the availability of reports describing research in the fields of physics represented in the Journal of Applied Physics. The supplies of copies of most reports are strictly limited and are rarely reprinted when the initial printing is exhausted.

An announcement for this column should be fewer than 150 words in length and should provide information on the content, length, price and address from which the report can be obtained. The announcement should be accompanied by a copy of the report, which will be reviewed to determine whether the report is of sufficient interest and relevance to warrant an announcement.

X Ray Literature List

A 20-page list of references spanning the years from 1930 to 1960, giving authors and publication names, article titles and publication dates for 376 papers on x ray analysis subjects, is available gratis from Philips Electronic Instruments, 750 South Fulton Avenue, Mount Vernon, New York.

Subjects covered in recent years include: Tooth Structure; Atomic and Automotive Problems; Biological Studies; High Temperature Work; Boiler Scale Analysis; Diamond Tools; Smelting; Properties of Garnets; Photographic Processes; Oil Contaminants; Pharmaceutical Research; Gasoline Additives; Clinical Pathology; Aerosols; Catalysts; Cement; and many others in chemical and metallurgical fields.

Books Reviewed

Prompt, noncritical reviews appear in this column. Critical reviews of many of the books described here will appear in Physics Today, The Review of Scientific Instruments, *or* American Journal of Physics.

Cryophysics. K. MENDELSSOHN. Pp. 170+xii. Interscience Publishers, Inc., New York, 1960. Price $4.50 (paperbound $2.50).

A brief comprehensive survey of low temperature physics written at a level suitable for graduate and advanced undergraduate students. The subjects include: methods of cooling, thermometry, specific heats, magnetism, electrical and thermal conduction, superconductivity, and liquid helium.

Molecular Structure (The Physical Approach). J. C. BRAND AND J. C. SPEAKMAN. Pp. 254+xxxvii. St. Martin's Press, Inc., New York. Edward Arnold & Company, London, 1960. Price $8.00.

This book gives a general account of the application of physical methods to the analysis of molecular structure, written at a level suited to honors students of physical chemistry, or to research workers in other branches of chemistry. It concentrates on principles rather than practice, explaining in greater detail those passages which need a very clear understanding of the nature of the molecule.

Plasma Dynamics. F. H. CLAUSER. Pp. 286+71. Addison-Wesley Publishing Company, Inc., Reading, Massachusetts, 1960. Price $12.50.

This volume is based on an international symposium on plasma dynamics held at Woods Hole, Massachusetts, during the week of June 9–13, 1958, under the sponsorship of the National Academy of Sciences and the Office of Scientific Research, Air Research and Development Command. While the subject is one of growing interest to many types of scientists, this book should be of particular value to thermonuclear physicists, missile and space engineers, astrophysicists, and electronics engineers.

The subject of the book is the science dealing with the interaction of deformable conducting materials (particularly conducting fields) and the electromagnetic field. It has been variously called plasma dynamics, magnetohydrodynamics, hydromagnetics, magnetoaerodynamics, and Hg-dynamics.

Fluid Mechanics. Vol. 6 of *Course of Theoretical Physics.* L. D. LANDAU AND E. M. LIFSHITZ. Pp. 529. Pergamon Press, New York; Addison-Wesley Publishing Company, Reading, Massachusetts, 1959. Price $14.50.

Since this volume describes fluid mechanics as a branch of theoretical physics, it differs considerably from other textbooks on the same subject. The authors have tried to develop as fully as possible all matters of physical interest, and to do so in such a way as to give the clearest possible picture of the phenomena and their interrelation. Consequently, they discuss neither approximate methods of calculation in fluid mechanics, nor empirical theories devoid of physical significance. On the other hand, some topics not usually found in textbooks on the subject are treated, such as the theory of heat transfer and diffusion in fluids; acoustics; the theory of combustion; the dynamics of superfluids; and relativistic fluid dynamics.

While it has not been possible for authors to incorporate in this English-language edition all new results in the field which have taken place since the Russian edition was published, they have added to the contents of the original edition one new chapter, that on the general theory of hydrodynamic fluctuations.

Books Received

Integraltafeln zur Quantenchemie. Vol. 4, no. 8. DR. H. PREUSS. Pp. 146. Springer-Verlag, Berlin, 1960. Vierter Band VIII, DM 45.

Announcements

The American Institute of Physics announces that *The Physics of Fluids* will be published monthly, instead of bimonthly, effective with Volume IV (1961). The journal is devoted to reporting the results of research on the structure, statistical mechanics, and general physics of gases, liquids, plasmas, and other fluids. As before, the journal will continue to offer papers on certain basic aspects of physics of fluids bordering geophysics, astrophysics, and related fields.

Subscription prices for 1961 will, of course, reflect the greater costs of monthly publication. The American Physical Society in lieu rate will be $5.50 domestic, $6.50 foreign, while the general member rate (to members of A.I.P. member societies) will be $11.00 domestic, $12.00 foreign. The nonmember rate will be $15.00 domestic, $17.00 foreign. For further information, write to the Institute.

New Editor, *Journal of Applied Physics*

On September 15, 1960, Dr. J. H. Crawford, Jr., became editor of the *Journal of Applied Physics*, replacing Dr. J. A. Krumhansl. Ethel C. McMillan will continue in the position of Assistant Editor. All comments and contributions should be addressed to the Journal's new office:

Dr. J. H. Crawford, Editor
Journal of Applied Physics
Solid State Division
Oak Ridge National Laboratory
Oak Ridge, Tennessee.

Cover Photograph

Dislocations having a Burgers vector in the basal plane and lying in this plane have been studied in graphite by the use of thin foil transmission electron microscopy. The dislocations are dissociated into ribbons consisting of two partials separated by a stacking fault. As shown by the cover photograph, the hexagonal networks contain extended and contracted nodes. The presence of two types of stacking faults gives rise to singularities which have been analyzed in terms of experimentally determined Burgers vectors. The dislocations and even the networks have been found to be very mobile along the basal plane. For further information, see "Electron Optical Study of Basal Dislocations in Graphite," by S. Amelinckx and P. Delavignette, which will appear in the November issue of the Journal of Applied Physics.

Proceedings of the Electron Microscope Society of America

The Annual Meeting of the Electron Microscope Society of America was held at Marquette University, Milwaukee, Wisconsin, on August 29, 30, and 31, 1960. Titles and abstracts of the papers are given below.

PROGRAM

Session AI, Inorganic and Polymetric Materials

A1. Electron Microscopy of Asbestiform Minerals. SANFORD B. NEWMAN, *National Bureau of Standards, Washington 25, D. C.*—Natural and synthetic chrysotiles and crocidolite were examined at high magnifications using a phosphotungstic acid negative staining technique.[1] Phosphotungstic acid (PTA) appears to improve resolution of chrysotile in the electron microscope. There is some indication that the PTA enters the central tubes of the fibers though the pathways are obscure. In the crocidolite fibers transverse dark bands are observed. These apparently are not affected by the PTA. The use of dark field electron microscopy and adjustment of beam-specimen orientation demonstrates the dependence of the bands on diffraction contrast. Some of the banding appears helical in form and may be related to structures observed in other asbestos fibers.

[1] S. Brenner and R. W. Horne, Biochim. Biophys. Acta **34**, 103 (1959).

A2. Electron Microscope Studies of Crystalline Structures Precipitated from Dilute Polyamide Solutions. V. F. HOLLAND, *Research Center, The Chemstrand Corporation, Decatur, Alabama.*—Thin platelets have been produced from dilute solutions of several polyamides. Many of these platelets resemble "single crystals" observed in linear polyethylene. Selected area electron diffraction measurements were made on these "crystals," and the results are discussed in relationship to the question of chain orientation and crystal structure.

A3. Morphology of Axially Compressed Nylon 66. FRANKLIN R. ANDERSON* AND D. A. ZAUKELIES, *Chemstrand Research Center, Inc., Durham, North Carolina.*—Axial compression of oriented nylon 66 produces localized deformation bands which lie at an angle of approximately 45° to the axis of orientation. These bands appear to be similar to Lüder's lines which occur in metals. Cold fracture and ion-bombardment etching were used to expose the internal form of the bands for study in the electron microscope.

A4. Structure of Polytetrafluoroethylene Latex Particles. J. H. HERSCHLEB, *Minnesota Mining and Manufacturing Company, St. Paul, Minnesota.*—Particles of "Teflon 30" polytetrafluoroethylene latex have been studied in the electron microscope by direct transmission and by replica techniques. Their structure is as unique among latex particles of various polymers as are the physical properties of the bulk polymer. By direct transmission marked changes in morphology can be observed as the beam intensity is increased. These changes are probably the result of degradation due to high-energy irradiation and heating taking place in a high vacuum. Cross-linking and changes in crystal structure also may occur. Electron micrographs taken in an RCA EMU-3 at 100 kv and 8000× with a beam intensity about 1/50th of normal, followed by others of the same field taken at the normal intensity, show the changes in structure produced by the electron beam. Two-step replicas of the particles show striations running the length of the particles, i.e., 1300 A to 5200 A and occurring at intervals of about 300 A. These structures are similar to those revealed by C. W. Bunn[1] and co-workers in their study of the bulk polymer obtained from a different type of polymerization process. They are also similar to the transmission micrographs of heavily chrome shadowed particles published by Grimaud[2] and co-workers.

[1] C. W. Bunn, A. J. Cobbold, and R. P. Palmer, J. Polymer Sci. **28**, 365–376 (1958).
[2] E. Grimaud, J. Sanlaville, and M. Troussier, J. Polymer Sci. **31**, 525–527 (1958).

A5. Subsurface Fatigue Characteristics of Pyroceram Bearings. S. HARRELL AND E. V. ZARETSKY, *National Aeronautics and Space Administration, Cleveland, Ohio.*—Rolling contact fatigue tests using half-inch Pyroceram balls in the NASA five-ball fatigue tester showed under optical microscopy that Pyroceram exhibited fatigue characteristics similar to those of steel. While steel bearings failed instantaneously after spalls developed, the total failure time for Pyroceram balls was five times that of the spalling time. Therefore, it was felt that Pyroceram would be an excellent research tool to help to understand the mechanism of failure of bearings. Electron micrographs are being made of unrun, partly run, and failed balls to study crack propagation and microstructural changes occurring in Pyroceram balls. Surfaces, fatigue-affected zones, and the centers of the balls are under examination. The Pyroceram is vibratory polished and then etched with HF (5 ml), HCl (5 ml), and H_2O (45 ml).

A6. Irradiation of Thin Evaporated Films of Uranium Dioxide.† T. K. BIERLEIN AND B. MASTEL,* *Hanford Laboratories Operation, General Electric Company, Richland, Washington.*—Damage sustained in approximately 100 A thick films of evaporated uranium dioxide after irradiation up to 4×10^{19} nvt (thermal) has been studied by electron microscopy and diffraction. At low exposures individual fission fragment tracks with widths of approximately 100 A and partial lengths up to 4 μ are disclosed. After exposures to 4×10^{17} nvt in an air environment, the original uniform film reverts to a heterog • eneous film from which isolated flocculent growths of uranium dioxide emanate. After an exposure of 2×10^{19} nvt, the heterogeneous film gives no electron diffraction pattern, but additional exposure to 4×10^{19} nvt causes the pattern to reappear. If irradiation is conducted in a vacuum environment, however, the film remains homogeneous to higher exposures and finally forms rounded isolated filaments. Examination of such films by electron diffraction discloses no change in interplanar spacing within experimental error.

† Work performed under contract for the U. S. Atomic Energy Commission.

A7. Dislocations in Graphite Single Crystals. ROGER BACON* AND R. SPRAGUE, *Research Laboratory, National Carbon Company,† Cleveland, Ohio.*—Techniques have been developed to permit direct observation in the electron microscope of dislocations in natural graphite single crystals. The crystals were cleaved in such a way as to produce very small amounts of mechanical deformation. Well-defined dislocation lines were observed lying in the (0001) basal planes. A jerky motion of

dislocations along a (0001) slip plane frequently was observed as the result of stresses induced by beam heating. Dislocation motion was seen to be impeded by interaction with other dislocations or with a foreign particle. Very regular dislocation networks were observed with spacings varying from about 4000 to 15 000 A. Frequent splitting of dislocations into partials separated by a distance of 1000 to 2000 A indicates a very low stacking fault energy for graphite. Electron micrographs illustrating all these phenomena will be shown.

† Division of Union Carbide Corporation.

A8. Striated Images of Single Crystals and Associated Forbidden Reflections. L. W. LABAW, *National Institutes of Health, Bethesda, Maryland.*—Striated images of single crystals can be (1) out-of-focus interference patterns, can result (2) from Bragg reflections, or from both (1) and (2).[1] In (1), the striations are related to the molecular plane spacings, while in (2), to the repeating unit in the lattice. In some organic crystals the striations from (1) can be photographed without those from (2) by using high-beam currents accompanied by rapid deterioration of the selected-area diffraction patterns. The striations from (2) can be photographed at focus without those from (1) before the diffraction patterns deteriorate using low-beam currents. For crystal structures in which the repeating unit differs from the molecular plane spacing, forbidden reflections are present in the diffraction patterns whenever striations resulting from (2) are on the crystal images; these both disappear on further bombardment and are associated with extinction contours. Illustrations will include crystals of indanthrone, indanthrene olive *T*, and two forms of phthalocyanine.

[1] J. M. Cowley, Acta Cryst. **12**, 367 (1959).

Session BI, Intracellular Morphology

B1. Intracellular Morphology of Polylysine Treated *Escherichia coli*. D. E. SLAGEL* AND M. A. STAHMANN, *Department of Biochemistry, University of Wisconsin, Madison 6, Wisconsin.*—Burger and Stahmann[1] showed that polylysine inhibited respiration of *E. coli* and was bacteriostatic. Electrophoretic experiments carried out by Katchalski *et al.*[2] indicated that the lysine residues of polylysine which were adsorbed when the net charge was brought to zero were much greater than the number of negative charges initially present on the bacterial surface. Electron micrographs of ultrathin sections of *E. coli* were obtained using a modification of Kellenberger's[3] technique in which the epoxy resin, Araldite, replaced Vestopal W. Electron micrographs of untreated cells showed a cell wall, granular cytoplasm, and a central nuclear vacuole. A striking morphological difference in cells incubated for 10 min with polylysine was the appearance of vacuoles around the periphery of the cell just inside the cytoplasmic membrane. These vacuoles seem to contain deoxyribonucleic acid which was drawn to the cell surface by electrostatic attraction to the positively charged polylysine. This may be the cause of the apparent increase in net negative charge.

[1] Burger and Stahmann, Arch. Biochem. Biophys. **39**, 27 (1952).
[2] Katchalski, Biochowski-Slomnitzki, and Volcani, Biochem. J. (London) **55**, 671 (1953).
[3] Kellenberger, Ryter, and Sechaud, J. Biophys. Biochem. Cytol. **4**, 671 (1958).

B2. Electron Microscope Observations on Fragmenting Aerobic Actinomycetes. O. F. EDWARDS* AND MARGARET HOTCHKISS, *Department of Microbiology and Keeneland Foundation Electron Microscope Laboratory, Lexington, Kentucky.*—The recent difficulties in the taxonomy of the actinomycetes have led to a re-examination of the details of structure of members of this family. The aerobic actinomycetes include some organisms which do not show marked tendencies to break into fragments. Electron microscope observations on representatives of the nonfragmenting group were reported earlier. Organisms of both groups are filamentous, show true branching, and contain small, round electron-dense structures which resemble the "metaphosphate bodies" of certain bacteria. Electron microscope observations on organisms of the fragmenting group also reveal some differences between the two groups of organisms. Organisms of the fragmenting group possess protoplasm of much greater electron density, which masks the interior structures. Thus the hyphae of the fragmenting group exhibit a uniform density. These hyphae readily break into oidia-like structures of irregular shape and size.

B3. Electron Microscopic Observations of the Reaction to Injury of Renal Tubules. BENJAMIN F. TRUMP* AND DAVID T. JANIGAN, *Department of Anatomy, University of Washington, Seattle 5, Washington, and Department of Pathology and Oncology, University of Kansas, Kansas City, Kansas.*—Alterations of renal tubular ultrastructure in response to injury have been studied in the rat and in human renal biopsy material. Swelling of the tubular epithelium, a well-known response to injury, appears to be divisible into at least 3 types: (1) swelling of mitochondria with dilatation of endoplasmic reticulum, observed after administration of nephrotoxins such as $HgCl_2$ or Thorotrast; (2) massive swelling of lysosomes with eventual rupture and confluence, producing the vacuolated appearance of the proximal tubular cytoplasm observed after the parenteral administration of sucrose; and (3) cisternal dilatation of the potentially extracellular spaces between the deeply infolded basilar cell membranes, observed after procedures such as renal vein ligation or rapid I.V. fluid administration, which produce rapid increases of the renal interstitial pressure. In the distal tubules, the double lamellae formed by the infoldings of the basilar plasma membrane become disorganized and fragmented following $HgCl_2$ administration or ureteral ligation. This disorganization eventually leads to the formation of concentric lamellar wrappings around organelles such as mitochondria. The apical poles of the proximal tubular cells react to injury by forming irregular cytoplasmic protrusions into the lumens. This can be induced by I.V. administration of hypertonic glucose and also has been observed in humans with glomerulonephritis. In the human, hyaline droplets appear as $\sim 0.2\ \mu$ masses of dense material which lie within membrane-limited vesicular structures $\sim 1\ \mu$ in diameter; they do not appear to be derived from mitochondria but instead from smaller pinocytotic vesicles containing similar appearing material, located near the base of the microvilli.

B4. Electron Microscopic Study on the Transitional Epithelium of the Toad Bladder. JAE KWON CHOI, *Department of Anatomy, University of Washington, Seattle 5, Washington.*—The transitional epithelium of the toad bladder consists of one or two layers of epithelial cells of several types which display well-developed desmosomal intercellular attachments. Between some of the desmosomes are wide intercellular spaces in which migratory cells can sometimes be seen. The most common type of cell in the epithelium has dense granules (PAS positive) just beneath the luminal surface. A second type is sack-like with constricted necks and abundant mitochondria. A third type consists of occasional mucous cells. Migratory cells identified as plasma cells and as macrophages are found in the epithelium in the lamina propria and in the muscle layer.

B5. Cardiac Desmosomes of the Toad. PHILIP GRIMLEY, *The Division of Laboratories and Research, New York State Department of Health, Albany.*—The fine structure of desmosomes and intercalated disks in the toad heart is discussed. A definite relationship between the dense components of these structures and the dense region of the *Z* band is demonstrated. The dense region of the *Z* band characteristically widens at its approach to the plasma membrane and often terminates beneath it in a distinct discoidal plaque. Cardiac desmosomes appear to be structures which result from the intimate apposition of plaques of *Z*-band material. These desmosomes retain the *Z*-band function as sites of attachment for myofilaments. Rotation of a desmosome and splitting of filaments from the adjacent sarcomere results in the formation of a simple steplike intercalated disk. Intermediate stages in this process are illustrated. Complex disks present in the toad probably represent the alignment of groups of simple disks produced by contractile forces. Other morphologic features of toad cardiac cells include a prominent *N* band.

B6. Some Observations on the Properties of the Planarian Parenchyma. KNUD JØRGEN PEDERSEN, *Department of Anatomy and Department of Pathology, University of Washington, Seattle 5, Washington.*—Electron microscopical, histochemical, and *in vivo* dissociation methods have been applied to the study of the parenchyma (mesenchyme, connective tissue) in two planarian species. Two cell types belong to the parenchyma proper: the "free" neoblast and the "fixed" parenchyma cell. The "fixed" parenchyma cells penetrate and bind together all structures between the epidermis and gastrodermis. They are very large and provided with many processes. They exhibit a strong PAS reaction and contain neutral mucopolysaccharides. In electron micrographs the cytoplasm appears very pale and contains few, small mitochondria and Golgi material. Many vesicles and lipid droplets of varying size are observed. The cells do not form a syncytium. No ground substance is present, and the extracellular space is extremely small, limited to the narrow space between two opposing cell membranes. In this space, nonetheless, are often found connective tissue filaments similar to those occurring in the subepidermal basement membrane. The "fixed" parenchyma cells are very flexible and probably play an important role in transport processes.

B7. Electron Microscopy of the Developing Skin of Anuran Larvae. C. ROLAND LEESON* AND LAWRENCE T. THREADGOLD, *Department of Anatomy, Dalhousie University, Halifax, Nova Scotia.*—The differentiation of skin has been studied in tails of tadpoles of *Rana pipiens* varying in length from 3 mm to 24 mm. Points under investigation have included the cytogenesis of component cells and the nature and differentiation of the contact between cells and of the basement lamella. There are distinct cytological differences between cells of the apical and basal layers of the two-layered epidermis. The basal cells contain considerable endoplasmic reticulum and numerous tonofilaments. Some of the latter are associated with desmosomes which appear first in the 8-mm stage and become more numerous in succeeding stages. In the early stages, the epidermis rests upon a simple basement membrane, but later there is increasing complexity at the dermo-epidermal junction, resulting finally in the appearance of a typical basement lamella in the 24-mm stage. Theories concerning the origin of the component fibrillae will be discussed.

B8. Structure of Photoreceptor Inner Segments in the Newt, *Triturus viridescens viridescens.* ANITA HENDRICKSON, *Department of Anatomy, University of Washington, Seattle 5, Washington.*—Retinae of adult newts were fixed in acrolein followed by OsO_4 at 20°C, or in OsO_4 at 4°C, and embedded in epoxy resins. Four types of photoreceptors are present in the newt retina: rods, two types of single cones, and double cones. There are striking differences in form, orientation, and density of the mitochondrial ellipsoids of the inner segment. In the rods, the mitochondria are very dense and highly irregular in form with circularly or longitudinally arranged cristae. A small PSA+ paraboloid is present deep to the ellipsoid. One type of single cone contains typical mitochondria rich in cristae with little associated PAS+ material. The second type of single cone has less dense, irregular mitochondria, often with short sparse cristae. A large PAS+ paraboloid is always associated with these mitochondria. The double cone is composed of both single cone types lying side by side.

B9. Electron Microscopy of Denatured and Renatured Collagen. ROBERT V. RICE* AND MORTON D. MASER, *Mellon Institute, Pittsburgh 13, Pennsylvania.*—The demonstration[1] of the return of asymmetric rods in cooled solutions of previously heated collagen has been extended. Measurement of length distributions of calf-skin collagen rods present in solutions which had been heated and then slowly cooled show that relatively long rods first reappear between 34–27°C. When cooled to this range from 70° in 5.5 hr, the mean length is about 1800 A. In the range 27–20°C, the mean length increases to about 2600 A. Upon further cooling to 3°C the mean length does not appreciably change in 24 hr. The study has been extended also to solutions of collagen from other sources and to commercial gelatin. Gelatin prepared from all of these sources shows asymmetrical rods when cooled. The results of this work, including electron micrographs, will be presented and discussed.

[1] R. V. Rice, Science **131**, 1319 (1960). Abstract of paper presented at National Academy of Sciences, April 25, 1960.

B10. Studies of Earthworm Cuticle Collagen. MORTON D. MASER* AND ROBERT V. RICE, *Mellon Institute, Pittsburgh 13, Pennsylvania.*—A component soluble in dilute acetic acid has been extracted from *Lumbricus terrestris* cuticle. This component contains collagen on the basis of its high hydroxyproline content, its sedimentation characteristics, and its appearance in the electron microscope. When examined by the Hall mica replica technique, the outstanding feature of the soluble component is its extremely asymmetric particles, of about 15-A diam and lengths up to 2 μ. Other characteristics of the soluble collagen and of the collagen fibrils will be discussed.

Symposium SI, Structure of Teeth and Bone

S1. X-Ray and Electron Diffraction Studies of Bone Dentin and Enamel. FREDERICK G. E. PAUTARD, *The University of Leeds, Leeds, England.*

S2. Fine Structure of Developing Pariatal Bone. ZELMA MOLINAR, *Department of Anatomy, University of Chicago, Chicago, Illinois.*

S3. Electron Microscopy of the Dentinogenesis. MARIA USSING NYLEN, *National Institute of Dental Research, National Institutes of Health, Bethesda, Maryland.*

S4. Electron Microscopy of the Human Amelogenesis. ERIK RÖNNHOLM, *Karolinska Institutet, Stockholm 60, Sweden.*

S5. Morphological Aspects of the Mechanism of Calcification. DAVID B. SCOTT, *National Institute of Dental Research, National Institutes of Health, Bethesda 14, Maryland.*

Session AII, Thin Metal Films

A9. Recent Developments in Techniques for Transmission through Thin Crystals. G. THOMAS AND M. C. HUFFSTUTLER, JR.,* *Department of Metallurgy, University of California, Berkeley.*—Techniques which have proved to be reproducible for preparing thin foils of Mg, MgO, and Mo will be described. In making Mg and Mo sections the starting point is sheet up to 200 μ thick which is electropolished by the window method. In the case of Mg the electrolyte used is 20% perchloric acid: 80% ethyl alcohol polishing at 10–12 v and 0.2 amp/cm². In the case of Mo the electrolyte is 870 cc H_2SO_4+30 cc H_2O and the conditions are: polishing at 12–20 v and 0.3–0.5 amp. A jet polishing method has been developed for making sections of MgO only 1000 A thick using hot orthophosphoric acid. A tilting stage has been devised for use with the Hitachi E. M. (type H.U.-10). Tilting of the specimen is a necessary requirement for obtaining contrast and determining Burgers vectors of dislocations.

A10. Dislocation Arrangements in Layer Structures. F. W. C. BOSWELL,† *Physical Metallurgy Division, Mines Branch, Department of Mines and Technical Surveys, Ottawa, Canada.*—Specimens of graphite and molybdenite (MoS_2) have been prepared by cleavage and examined by transmission electron microscopy. Dislocations lying in the basal planes have been observed, and in some instances the dislocations have been seen to glide in these planes. In many cases the dislocations are clearly dissociated into partials. In general the dislocations observed in a particular field lie on basal planes at different levels in the crystal. Interactions occur between dislocations on closely spaced planes and also between dislocations in the same plane. These latter can interact according to

$$a[100]+a[010]\rightarrow a[110]$$

to form segments of a third dislocation. Such interactions lead to the formation of extensive hexagonal nets, and these have been observed in both materials. In these nets alternate extended and contracted nodes usually can be seen. From this it is concluded that the dislocations dissociate into partials according to

$$a[100]\rightarrow \frac{a}{3}[2\bar{1}0]+\frac{a}{3}[1\bar{1}0].$$

Rotational moiré fringes have been observed. These may arise from the relative rotation of two parts of the crystal separated by a hexagonal network of dislocations in the screw orientation. It is possible that these boundaries result from deformation during cleavage.

† Paper to be read by E. Smith.

A11. Preparation of Thin Films from Ordinary Tensile Specimens for Transmission Electron Microscopy.† P. R. STRUTT, *The Franklin Institute Laboratories, Philadelphia 3, Pennsylvania.*—Various techniques are described for the preparation of thin films from ordinary tensile specimens, thus facilitating the examination of dislocation configurations within the bulk specimens. The description includes several new features, such as an electrolytic slitting wheel. The preparation of a film is divided into three stages, and alternative procedures are described for each stage. All the procedures are electrolytic so as to avoid introducing mechanical strains. Initially, sections are cut out from the bulk specimen; if desired, the section may be cut parallel to a desired crystallographic plane. The section is then electrolytically planed down to a uniform thin sheet; a minimum thickness of 10–20 thousandths of an inch may be obtained. The final stage is the preparation of the electron transparent area from the "planed down" thin sheet.

† This research was supported by the Office of Scientific Research.

A12. Apparatus for the Deformation of Foils at Elevated Temperatures in an Electron Microscope.† B. H. KEAR, *The Franklin Institute Laboratories, Philadelphia 3, Pennsylvania.*—A micro-tensile machine has been constructed that enables thin foils to be deformed plastically at elevated temperatures while under observation in the Philips EM 100-B electron microscope. The device has been tested up to temperatures of ~600°C. Practically no contamination of the specimen occurs at elevated temperatures, so the specimen may be examined for considerable periods of time. A preliminary study has been made of the plastic deformation of aluminum foils at 350°C, and interesting differences in slip behavior have been observed compared with room temperature deformation. In its present form, the device also should find application in studying creep and slow-cycle fatigue at elevated temperatures in the electron microscope.

† This research was supported by the Office of Naval Research.

A13. Observations on Operating Frank-Read Sources.† H. G. F. WILSDORF, *The Franklin Institute Laboratories, Philadelphia 3, Pennsylvania.*—A number of mechanisms have been proposed to account for the origin and multiplication of glide dislocations. A technique which makes it possible directly to observe dislocations and their behavior has been applied to the study of dislocation sources. Thin metal foils have been elongated in the electron microscope, and it was seen that often glide dislocations were emitted from grain and twin boundaries as well as subboundaries. Also, stress concentrations near precipitates initiated the production of dislocations, and observations concerning the action of prismatic loops under stresses will be included. The emphasis of the discussion, however, will be on the experimental evidence for the operation of Frank-Read sources.

† This research was supported by the U. S. Atomic Energy Commission.

A14. Defects Observed by Transmission Electron Microscopy in Neutron Irradiated Copper.† I. G. GREENFIELD* AND H. G. F. WILSDORF, *The Franklin Institute Laboratories, Philadelphia 3, Pennsylvania.*—Radiation damage in high-purity single crystals of copper was investigated by means of a transmission electron microscopical technique. The samples were irradiated with a dose of 5×10^{17} nvt (total fast neutron flux) at a temperature of about 70°C. After thinning to electron transparency, the samples were viewed in the electron microscope. The irradiated copper was found to contain many dark spots of a density about 3×10^{16}/cm³. These spots were identified as prismatic loops with diameters ranging from 50 A to 250 A. The effect of the irradiation-produced defects on the movement of glide dislocations also could be observed. Several single crystals were deformed in tension and then thinned down. The glide dislocations were found to be heavily kinked in a manner similar to that found in irradiated nickel.[1] In addition, prismatic dislocations were found to be swept out by the action of moving dislocations.

† This research was supported by the U. S. Atomic Energy Commission.
[1] H. G. F. Wilsdorf, Phys. Rev. Letters **3**, 170 (1959).

A15. Transmission Studies of Phase Transformations in Cu-Al Alloys. G. THOMAS AND M. C. HUFFSTUTLER, JR.,* *Department of Metallurgy, University of California, Berkeley.*—Current work on dynamics of the eutectoid and martensitic transformations in Cu-11% Al alloys will be reported. The use of the transmission techniques and heating stages makes it possible to determine orientation preferences and to investigate the transformation kinetics by ciné-film recording techniques.

A16. Transmission Electron Metallography on Permanent Magnets. KLAUS J. KRONENBERG, *Indiana Steel Products*

Division, Indiana General Corporation, Valparaiso, Indiana.—Samples of brittle permanent magnet materials have been produced which allow transmission electron microscopy. The peculiar precipitation structure of Alnico V found earlier by replicating techniques has been confirmed by transmission electron micrographs of the material proper. The two phases of Alnico V have been identified and analyzed by transmission electron diffraction. Relations between magnetic properties and the mosaic structure are being established.

A17. Direct Observation of Dislocations and Stacking Faults in Evaporated Silver Films.† V. A. PHILLIPS AND J. A. HUGO, *Metallurgy and Ceramics Research Department, General Electric Research Laboratory, Schenectady, New York.*—A ciné film has been made showing dislocation motion and stacking fault formation produced in monocrystalline silver films by electron beam stressing. Among the effects observable are the widening of stacking faults by movement of Shockley partial dislocations, interaction of simple stacking faults to form complex faults, and the interaction of dislocations and faults. Holes act as barriers to stacking fault widening and act as pinning points for partial dislocations.

† This film will be introduced by A. M. Turkalo.

A18. Precipitation of Carbon from Solution in α Iron. E. SMITH, *Department of Mines and Technical Surveys, Mines Branch, Ottawa, Canada.*—Iron sheet up to 0.005 in. thick is saturated with carbon at 720°C. Samples cut from the sheet are quenched from 720°C and given various aging treatments to precipitate the carbon. The sheet is then thinned electrolytically and the foil examined by transmission in the electron microscope. Initially, carbon precipitates as fine feathery particles along the dislocations. The particles coarsen with further aging. If enough carbon is present, precipitation also occurs within the iron matrix in the form of feathery platelets lying in {100} planes. These grow on further aging, and one particle may grow along all three {100} planes. The particles do not appear to be cementite or epsilon carbide. Cementite forms after a few hours at 200°C as bundles of rods growing along ⟨111⟩ directions in {110} planes. The problems of nucleation of the initial carbide and the cementite will be discussed.

A19. Dislocation Movements in Alpha Brass. F. W. C. BOSWELL† AND F. WEINBERG, *Physical Metallurgy Division, Mines Branch, Department of Mines and Technical Surveys, Ottawa, Canada.*—Annealed foils of alpha brass (70 wt % copper, 30 wt % zinc) were deformed a few percent, electrolytically polished to a thickness of approximately 1000 A, and examined in a Siemens Elmiskop I using 100-kv and double-condenser illumination. After waiting periods of up to several minutes, dislocations were observed to move in some regions. These movements were recorded by photographing the fluorescent screen of the electron microscope, using a 16-mm movie camera with a 2-in., *f*/1.6 lens. Since alpha brass has a relatively low stacking fault energy, a total dislocation can dissociate readily into two partials separated by a region of stacking fault. The ciné film shows typical examples of the movements of total and partial dislocations and the associated stacking faults. Examples of the interactions of dislocations with one another, with grain boundaries, and with other obstacles in the lattice are also depicted. Nucleation of dislocations near the edge of the foil and at regions of stress concentration due to dislocation pile-up at grain boundaries can be noted.

† This paper to be read by E. Smith.

Special Session on Techniques

T1. Alternate Speed Motor Drive for Porter Blum Microtome. ZANE PRICE* AND YOSHIMI NISHI, *The Nina Anderton Laboratory for Electron Microscopy, Department of Infectious Diseases, School of Medicine, University of California, Los Angeles.*—An electric motor drive has been designed for the Porter Blum microtome which enables the operator to regulate the cutting speed to fit cutting requirements. The drive motor is mounted on a separate stand to prevent vibration carry-over to the microtome and operates through a drive shaft that is separated from the motor and microtome by rubber universal joints. Cutting speed is regulated by an auto transformer connected by a microswitch to the motor. The drive also contains a higher speed bypass so that the tissue is more rapidly returned for the cutting stroke.

T2. Staining of Thin Sections with Chromyl Chloride. STANLEY BULLIVANT* AND JOHN HOTCHIN, *The Division of Laboratories and Research, New York State Department of Health, Albany, New York.*—Chromyl chloride is a red liquid which vaporizes easily at room temperature. Thin sections are stained by exposing them to the vapor. Examples of the effect of chromyl chloride on thin sections of helium fixed pancreas and osmium fixed pancreas, cardiac muscle, gastric mucosa, and tissue culture cells containing virus will be shown. Apart from the expected enhancement of contrast in membranes, chromyl chloride treatment leads to the selective removal of some components such as mucous and zymogen granules and the core material of virus particles.

T3. Preparation of Amoeba Proteus for Electron Microscopy by the *in Aqua* Freezing Method. EUBERT J. DANIEL, *Orthopedic Research Laboratory, Department of Orthopedic Surgery, Massachusetts General Hospital, Harvard University, Boston, Massachusetts.*—Streaming, monopodal amoebae were placed, encased within individual water droplets, upon specially prepared depression foils. The cells were observed microscopically and sketches made at leisure. At the appropriate moment the foil and amoebae were plunged into liquid propane cooled to −175°C by liquid nitrogen. The preparation was rapidly transferred to liquid nitrogen and stored in capsules until processed. Processing consisted of *in vacuo* dehydration at −35 to −40°C for 24 hr, followed by *in vacuo* application of heat (100°C) for 24 hr. The preparation was cooled and the desired fixatives or histochemical stains admitted into the vacuum chamber. Final preparation consisted of staining the individual cells with 2% alcoholic platinic tetrabromide, double embedding in celloidin-methacrylate plastic, and orientation for selected area sectioning. This method is suitable for the study of highly hydrated tissues and individual cells down to 10 μ in size. Damage by formation of large ice crystals was entirely absent.

T4. Practical Method for Estimating Specimen Thickness in the Electron Microscope. JOHN H. REISNER, *Radio Corporation of America, Camden, New Jersey.*—The ratio of current in the beam incident upon a specimen to current in the unscattered beam passing through the specimen is a reliable measure of mass thickness. These currents can be transferred to the viewing chamber for measurement by using an intermediate lens to image the objective crossover upon the object plane of the projector, as in producing the spot for selected area diffraction. Direct measurement of current is possible using a retractable electrode to intercept the crossover image. However, light from this image on the viewing screen is

proportional to beam current, so that the ratio of currents can be determined from the ratio of two photometric measurements. Calibration curves are derived from measurement of ratios for specimens of known composition and mass thickness, e.g., sections measured by color. Thickness measurements apply to areas as small as the incident beam cross section.

T5. Reusable Multiple Objective Aperture for the Electron Microscope. F. F. MOREHEAD, *American Viscose Corporation, Marcus Hook, Pennsylvania.*—A platinum multiple objective aperture is described for the Siemens electron microscope. Without changing the standard aperture carrier, 25–30 usable holes are available.

T6. X-Y Coordinate Method for the Location of Microareas in Electron Microscope Specimens. HARRY U. RHOADS* AND A. H. WEBER, *Department of Physics, Saint Louis University, Saint Louis 3, Missouri.*—In research applications of the electron microscope, it is necessary quite often to view the same microarea repeatedly. Hence, the problem of location and relocation of a minute structure (microarea), the details of which are resolved only by the electron microscope, arises. An accurate method for the location and relocation of specific surface structures and relocation of specific structures and microareas upon the viewing screen of the electron microscope by plotting X-Y coordinates, of a "point" within the area, referred to established index marks, will be described. The method is presented in detail (20-step procedure). The application of the technique to the specific problem of correlation of structural features of a thin metallic film, deposited upon a glass surface with those of the substrate, is described in detail.

T7. Vacuum Chamber for the Deposition of Carbon and Shadow Casting of Metals. H. C. VACHER, H. C. BURNETT,* AND R. H. DUFF, *National Bureau of Standards, Washington 25, D. C.*—There was need for a versatile small-volume vacuum chamber that could be used in the preparation of electron microscope replicas. The design was a cube having interchangeable ports on five sides, the sixth being adaptable to different evacuating units. Lucite was used for windows and insulators, O-rings for temporary vacuum seals, and epoxy adhesive for permanent vacuum seals. The port opposite the one adapted to the evacuating unit is used for a specimen stage rotatable to any position with respect to four ports, one used for shadow casting, one for carbon deposition, and the other two for windows. The carbon rods are held in removable "pin vises," one having a sliding fit so that the contact pressure is the weight of the pin vise when in the vertical position. The evacuation period for attaining a chamber pressure of less than 10^{-4} mm mercury is approximately 7 min.

T8. Simple Water Vapor Trap for Metallic Evaporators. BOLIVAR J. LLOYD, JR.,* AND H. KAHLER, *Laboratory of Physiology, National Cancer Institute, National Institutes of Health, Bethesda 14, Maryland.*—For eight years we have used a simple water vapor trap in our RCA-EMV-1 metallic evaporator which reduces the pumping down time to 5 to 10% of the usual requirement. The method is to chill a metal rod or block to the temperature of liquid nitrogen by suspending it in a 1-liter Dewar flask by a woven wire. The chilled block is then hung in the evaporator, which is quickly closed for pump down. A 1¼-in. brass rod, 3 in. long, has sufficient thermal capacity and surface area to trap the water vapor (and possibly some oil vapor) for a period of over an hour. The cold block should be held in the evaporator opposite to the filament and may be shielded from direct radiation by an opaque plate. The pressure drops to a value for evaporation in 20 min or less, depending on the size of the bell jar.

T9. New Shadowing Materials for Electron Microscopy. A. P. Murphy* AND J. F. GOODMAN, *Procter and Gamble Company, Miami Valley Laboratories, Cincinnati, Ohio.*—At high resolution many of the fine structural details of specimens shadowed with platinum are obscured by the metal crystallites. It has been found that evaporated films of osmium dioxide have a small grain size and show high contrast. Use of evaporated osmium dioxide has eliminated many of the disadvantages experienced with platinum. In contrast to the crystalline electron diffraction patterns given by evaporated platinum films, patterns from evaporated osmium dioxide consist of strong broad halos. The films are thus "amorphous" in the sense that carbon is "amorphous," but electrons are scattered strongly, and hence thin films form an image of high contrast. Examples are given of test specimens on carbon films shadowed with platinum and compared with specimens shadowed with osmium dioxide to illustrate the improvement.

T10. Low Noise Shadow-Casting with Molybdenum. L. BACHMANN,†A. S. BRILL,* AND B. M. SIEGEL, *Department of Engineering Physics, Cornell University, Ithaca, New York.*—The limiting factor in resolving the dimensions of shadow-cast organic macromolecules is the graininess of the metallic film. The method of C. E. Hall,[1] in which platinum is the shadowing material and freshly cleaved mica is the substrate, has until now provided the least granularity. We will demonstrate a substantial reduction in noise from a shadow-casting technique employing molybdenum.

† Physikalisches Chemisches Institut, University of Innsbruck, Innsbruck, Austria.

[1] C. E. Hall, Proc. Natl. Acad. Sci. U. S. **42**, 801 (1956).

Symposium SII, Theory and Applications of Electron Diffraction

S6. General Introduction. VICTOR HICKS, *Allen Bradley Company, Milwaukee, Wisconsin.*—A narrow beam of monoenergetic electrons, when passed through or across crystalline material, will be scattered by the atoms in that material, resulting in an electron diffraction pattern in the form of arcs or circles concentric about the beam, or in an orderly array of spots. Such patterns may yield information concerning the spatial arrangements of the scattering atoms, permitting the identification of solid elements or compounds or the determination of their structures. The patterns and analyzing procedures are similar to those in the x-ray case, except that the lower penetration and more efficient scattering associated with electrons makes practical the study of much thinner layers and smaller crystals with electrons. Some important applications are: identification of minor phases in alloys and products of surface reactions, orientations of polar molecules on surfaces and of metallic crystals in electroplating, the continuous recording of rapid reactions in solids, and mapping of electron densities in crystals.

S7. Instrumentation. JOHN H. REISNER, *Radio Corporation of America, Camden, New Jersey.*—The versatility of the electron microscope as a diffraction apparatus is not adequately appreciated

by most diffractionists, while at the same time the inherent versatility of the instrument often is not fully available to those who do appreciate it. The unique ability of the electron microscope to do Selected Area Diffraction will be discussed primarily from the standpoint of its use in crystallography. Instrumental factors influencing resolving power, symmetry of beam, and distribution of intensity will be discussed and related to such phenomena as line broadening, intensities, orientation, and refraction. Concurrently, manipulative problems such as beam adjustment, calibration, aperturing, flatness of field, orientation of Gaussian and diffraction images, and orientation of specimens will be covered. A short background sketch of the optics of selected area diffraction will be provided as a basis for understanding its special problems. Mention will be made of diffracted beam (selected angle) microscopy.

S8. Dynamic and Kinematic Theories of Electron Diffraction. HARRY M. BENDLER, *Research Laboratories, General Motors Corporation, Warren, Michigan.*—If the amplitude of the wave scattered by a crystal in an arbitrary direction is determined by summing the amplitudes of the waves scattered by the individual atoms in that direction, the kinematic theory may be applied. The vibration polygon phase amplitude diagram used in the elementary treatment of the optics of the diffraction grating is an example of the application of kinematic theory. If, however, the nature of the wave field within the crystal and the effect of boundary conditions at the entrance and exit faces of the crystal are considered, the solution for the diffracted intensities lies in the domain of the dynamic theory. Which theory will be required for the interpretation of the diffracted intensities in a given instance will depend on the thickness of the crystal and the reflection excited. The contrast effects observed in electron micrographs of thin crystals often may be described in a general way by the kinematic theory while a detailed analysis of the intensities requires the application of the dynamic theory. The fine structure observed in high-resolution diffraction patterns also may represent dynamic effects. In this case certain of the Fourier amplitudes of the crystal potential may be estimated from the geometry of the spot group. The basic assumptions of the kinematic and dynamic theories will be given, the range of validity of each estimated, and examples of their application outlined.

S9. Electron Diffraction Intensities. R. A. BONHAM,† *Naval Research Laboratory, Washington 25, D. C.*—The electron microscopist needs a knowledge of electron diffraction phenomena mostly for identification purposes, for interpretation of the structure and texture of specimens, and for interpretation of special features of the micrographs. A review of the different effects, governing the diffraction intensities, shows that a complete interpretation depends on a reliable theory of diffraction phenomena, on a knowledge of the physical constants of the instrument used for the observation, and, last but not least, on some information about the chemical composition of the specimen. The relevant theories have been presented in the preceding paper. Recent investigations have shown that, even for very thin specimens, the diffraction intensities, calculated on the basis of kinematic concepts alone, may have to be corrected, particularly in cases where the inelastic cross section is of the same order of magnitude as the elastic one. Such corrections may be needed also where the dynamic approach is based on the propagation of electron waves in a constant threefold periodic potential field alone. The influence of lattice imperfections on diffraction intensities has been clarified considerably since the advent of high-resolution instruments.

† On leave 1960–1961 from Indiana University, Bloomington, Indiana.

S10. Diffraction by Gas Molecules. L. S. BARTELL, *Department of Chemistry, Iowa State University, Ames, Iowa.*—In the last ten years electron diffraction has advanced from a qualitative, subjective method for determining structural parameters of molecules to a rigorous, objective method yielding parameters improved in accuracy and significance by perhaps tenfold. The experimental and theoretical developments responsible for this advance will be discussed along with an evaluation of the current status of electron diffraction as a research tool. Results of recent work will be used to illustrate the utility of the method.

Session BII, Virology

B11. Electron Micrographs of Macrophages Observed in Bone Marrow of Human Leukemia.† JOSEPH R. GOODMAN,* MORRIS GOLDMAN, MAMIE BENNETT, NAOMI WARDLOW, AND JOHN LOWE, *Veterans Administration Hospital, Long Beach, California, and Biochemistry Department, School of Medicine, University of Southern California, Los Angeles, California.*—Bone marrow aspirations from leukemic patients have been studied with thin-section techniques. Occasionally cells are observed to have a variety of inclusion body like structures in the cytoplasm. These cells are macrophages that contain mainly injested erythrocytes and their degradation products. These are compared to erythrocytes injested by circulating leukocytes in vitro. Alternate thin and thick sections are used in comparing and identifying areas of density on the electron microscope with cytochemically stained areas on the light microscope. The appearance of particles within these inclusions is contrasted to known virus inclusions.

† This work was supported by a U. S. Public Health Service grant.

B12. Structure of Measles Inclusions in the Hela Cell. JUTARO T. TAWARA, JOSEPH R. GOODMAN, DAVID T. IMAGAWA, AND JOHN M. ADAMS, *Departments of Pediatrics and Infectious Diseases, School of Medicine, University of California, Los Angeles; Veterans Administration Hospital, Long Beach, California; and Okayama University, Japan.*—Studies were undertaken to examine the fine structure of cellular inclusion bodies

produced by measles virus. Cytoplasmic inclusion bodies are seen as an array of linear structures similar to those described earlier in the nuclear inclusions. In some areas the dense particles are aligned in a geometric manner. The identity of the inclusion bodies on the electron micrographs was established by staining corresponding sections with hematoxylin and eosin. HeLa cells were inoculated with Edmonston strain of measles virus and harvested at various intervals for fixation. The cells were embedded in methacrylate, and adjacent thick and thin sections were mounted for light and electron microscopic study. The thick section was treated with acetone and xylol to remove methacrylate and then was stained with hematoxylin and eosin. The thin sections are processed for the electron microscope.

B13. Interaction between Vaccinia Virus and L Cells. K. O. SMITH* AND D. G. SHARP, *Department of Bacteriology and Immunology, School of Medicine, University of North Carolina Chapel Hill, North Carolina.*—The *L*-cell-vaccinia virus model was selected for studying virus-cell interaction because of its technical simplicity and the precision with which both cells and vaccinia particles can be counted. The sensitivity of the virus counting procedure is such as to permit quantitation at levels of one particle per cell. Rapid inoculation of cells has permitted measurements of virus-cell interaction within a very short period after contact. Observations during this period revealed a high percentage of virus attachment, followed by a rapid elution of approximately 60% of the adsorbed virus. About one-third of the adsorbed virus lost its morphological identity within 1 hr after inoculation. A small amount of virus remained cell-associated and morphologically identifiable until replication began. Growth studies suggest that several particles take part in the infection of a single cell and that there are several sites of replication within the cell.

B14. Staining of *L* Cells and Infection with Vaccinia Virus.† LEON ZEBROWSKI, *Instytut Weterynarii W Pulawach, Poland* (introduction by D. G. Sharp).—Normal *L* cells are stained by Brilliant Cresyl Blue. In logarithmic growth phase 96 to 97% take the stain, and in stationary phase 88% will stain. In cultures heavily infected with vaccinia virus the fraction of stained cells drops as low as 10%. Close correlation will be shown to exist between the fraction of unstained cells and the fraction of cells on or in which virus particles can be seen with the electron microscope. In cultures which have received various amounts of virus and identical incubation time the number of unstained cells is related to the yield of virus particles as counted by electron microscopy (sedimentation method). Cultures inoculated with virus show parallel increase, with time, in both unstained cells and virus particle yield.

† This work was done at the School of Medicine, University of North Carolina, Department of Bacteriology and Immunology, Chapel Hill, North Carolina, while holding Rockefeller Foundation Fellowship.

B15. Method for Achieving Rapid, Efficient Adsorption of Vaccinia Virus to Tissue Culture Cells. D. G. SHARP* AND K. O. SMITH, *Department of Bacteriology & Immunology School of Medicine, University of North Carolina, Chapel Hill, North Carolina.*—Large viruses such as vaccinia diffuse slowly and attach to tissue culture cells even more slowly. Much attached virus elutes, and accurate determination of the period of contact necessary to cause infection is difficult. Cells can be brought, however, into contact with virus by centrifugal force either by sedimenting virus upon cells in monolayer or by sedimenting virus particles, then producing a cell monolayer over the virus covered surface. Either of these procedures enables the experimenter to determine accurately the moment of virus-cell contact and the duration of this contact. Results, expressed as number of virus particles counted by the electron microscope, show 50% or more of the inoculum can be adsorbed to the *L* cells in 5 min without using large numbers of cells. These methods are being used to study the eclipse phase and subsequent growth of virus in these cells.

B16. Some Ultrastructural Aspects of Human Renal Clear Cell Adenocarcinoma. FRANCIS J. LUIBEL,* EMIL SANDERS, AND NANCY ARNOLD, *Department of Pathology, Southwestern Medical School, Dallas, Texas.*—Renal clear cell adenocarcinoma in the human was studied by means of electron microscopy and histochemistry. Observations were made on fresh osmium fixed and formalin fixed surgical specimens. The tissues studied included normal kidney, renal clear cell adenocarcinoma, and metastatic clear cell adenocarcinoma involving the lung and thyroid. Histochemical studies were carried out in an attempt to ascertain the nature of various cytoplasmic constituents of the neoplastic cells. These studies indicate that a major portion of the "clear substance" of the neoplastic cells is glycogen. A finely granular cytoplasmic component of the neoplastic cells observed in the nondiastase incubated specimens with the electron microscope was seen to disappear largely in the diastase incubated tissue. Lipid droplets observed within the tumor cells were also studied by histochemical means. Certain observations on the histogenesis of these tumors are discussed.

B17. Identification of Viruses by Ferritin-Conjugated Antibody. RICHARD A. RIFKIND,*† COUNCILMAN MORGAN, AND HARRY M. ROSE, *Department of Microbiology, Columbia University College of Physicians and Surgeons, New York, New York.*—Conjugation of ferritin (an iron-containing protein) with antibody globulin by reaction with *m*-xylene diisocyanate[1] should provide reagents which permit sites of antigen-antibody interaction to be visualized by electron microscopy in a manner analogous to the immuno-fluorescent technique of light microscopy. The specificity of such a conjugate was demonstrated in the tanned erythrocyte hemagglutinin system, employing bovine serum albumin and ferritin-anti-BSA, whereby immunologically specific ferritin deposition on erythrocytic stromata was seen in the electron microscope. Ferritin-anti-influenza virus globulin (strains PR8 and Lee) was reacted with homologous and heterologous virus emerging from infected cells of the chicken embryo chorioallantoic membrane. Thin sections revealed type-specific tagging of the homologous strain which was blocked by prior exposure to unconjugated antiserum. Likewise, ferritin-anti-vaccinia virus globulin showed specific tagging of extracellular vaccinia virus in HeLa cell cultures. These results indicate that specific identification of antigenically distinct viral particles can be made by electron microscopy.

† Fellow of the National Foundation.
[1] S. J. Singer, Nature **183**, 1523 (1959).

B18. Electron Microscopic Evidence for the Existence of the Human Mammary Tumor Inciter (Virus).† R. E. SMITH, *Department of Anatomy, Indiana Medical Center,* EDWIN E. PONTIUS, *Surgical Pathologist, Methodist Hospital,* AND R. BOHA, *Indiana Medical School, Indianapolis, Indiana.*—Studies of ultrathin and thick sections of various human mammary tumors strongly suggest the existence of an inciter. A total of twenty-two benign fibroadenomata, medullary, papillary, and scirrhous carcinomata were diagnosed by frozen-section examination, and small pieces were placed into appropriate fixative within a limit of 5 min after surgical excision. In some carcinomata, light microscopy has shown numerous cytoplasmic inclusions which are deeply basophilic, a few acidophilic. The over-all morphology of these inclusions is quite uniform, although there is variation in size. Such inclusions are found in animal and human tumors of known viral etiology. Electron microscopy demonstrates the presence of osmiophilic inclusion bodies in the cytoplasm of some cells in medullary, papillary, and a few scirrhous carcinomata. Our investigations not only present evidence for the existence of such inclusions, but point out that they differ in morphology,

and suggest their involvement in a conjected inciter cycle. Slides will be shown, demonstrating the presence of dense pleomorphic osmiophilic inclusions which seem to become round or oval. These oval cytoplasmic inclusions resemble bodies which have been termed Initial Bodies; later they contain denser granules observed best in profile—nucleoid containing inclusions. Intermediate bodies appear to form from Initial Bodies by developing out of the ground structure a finely reticular fibril inclusion. These inclusions are defined as "replicating forms" and may or may not break up, but their fibrils "knit" with small nucleoid-like bodies to form a single body or a mass of virus-like particles. The virus-like particles are individually in the order of 200 mμ in diameter and are apparently embedded in a matrix. The ellipitical center of the virus-like particle is separated from the rest of its contents by a less dense zone. The ellipitical center is the size of nucleoids found in inclusions. This information will be discussed in light of known viral infections, histochemical studies, and clinical observations.

† This research was supported by the Indiana Elks Cancer Fund.

B19. Electron Microscopic Studies of Chicken Renal Adenocarcinoma.† LEON DMOCHOWSKI, CLIFFORD E. GREY,* BEN R. BURMESTER, AND WILLARD G. WALTER, *Section of Virology and Electron Microscopy, The University of Texas M. D. Anderson Hospital and Tumor Institute; Department of Microbiology, Baylor University College of Medicine, Texas Medical Center, Houston, Texas; and U. S. Department of Agriculture, Regional Poultry Research Laboratory, Animal Husbandry and Research Division, East Lansing, Michigan.*—A study of primary (induced by myeloblastosis virus) and transplanted renal adenocarcinoma in chicken has established the presence of a large number of characteristic particles, similar to the particles observed in myeloblastosis and other forms of the chicken leukosis complex. Particles ranging in size from 600 A to 1400 A were observed chiefly in intercellular spaces of the cells forming the wall of the tubules and in the lumen of the tubules. Occasionally particles of more uniform size (800 A) were present within the cells, in inclusion-like bodies which appeared of mitochondrial origin, or scattered in the cytoplasm. In numerous cells, particles were observed being extruded through the cell membrane into the lumen of tubules and also being formed by the cellular membranes at the end of microvilli extending into the lumen. Frequently, densely osmiophilic, finely granular aggregations of the cytoplasm have been observed with virus particles appearing to develop within these aggregates. Particles present in the transplanted tumors were morphologically identical with the particles found in the primary tumors, and their mode of development followed the same pattern. In some areas, cell changes appeared slight or nonexistent; in other areas, various stages of cell degeneration were observed. No changes in the nuclei were seen.

† These studies have been supported in part by a U. S. Public Health Service grant and by an American Cancer Society grant.

B20. Electron Microscope Study of Tissues from Animals Infected with Polyoma Virus.† LEON DMOCHOWSKI,* CLIFFORD E. GREY, BERNICE E. EDDY, AND SARAH E. STEWART, *Section of Virology and Electron Microscopy, The University of Texas M. D. Anderson Hospital and Tumor Institute; Department of Microbiology, Baylor University College of Medicine, Texas Medical Center, Houston, Texas; and Division of Biologic Standards and National Cancer Institute, National Institutes of Health, Bethesda, Maryland.*—Studies were carried out on kidneys and tumors of mice, rats, and hamsters infected, when newborn, with polyoma virus. Characteristic particles (270 A in diameter) were observed in great numbers in sections of cells from kidneys with inflammatory and proliferative changes from mice, rats, and hamsters. Similar particles also were observed, in smaller numbers, in the cells of kidney tumors of mice, rats, and hamsters. Changes observed in the tumor cells will be described. Characteristic particles appeared chiefly in the nucleus, occasionally in the cytoplasm and outside the tumor cells. Occasionally, "crystalline" orderly arrays of the particles were seen in the nuclei of tumor cells. In the cytoplasm of tumor cells, inclusion-like bodies also were observed with virus particles in orderly arrays. These bodies appear to be formed within the cytoplasm. In sections of some tumorous kidney tubules, particles were observed in the nucleus of every cell forming the wall of the tubule. Occasionally, in a tumor cell with a ruptured nuclear membrane, particles were found scattered throughout the cytoplasm.

† These studies have been supported in part by a U. S. Public Health Service grant and by an American Cancer Society grant.

Session AIII, Electron Diffraction and Instrumentation

A20. Observation of Surface Microstructure on Metal Single Crystals by Reflection Electron Diffraction and Electron Microscopy. P. B. SEWELL, *Division of Applied Chemistry, National Research Council, Ottawa, Canada.*—Surfaces parallel to low index planes on tungsten single crystals have been prepared by electrolytic polishing and etching in 0.375 N sodium hydroxide. An attempt has been made to correlate fine structure in reflection electron diffraction patterns and surface structure observed with the aid of platinum-carbon replicas. For short periods of etching, fine structure in diffraction patterns is very diffuse because of limited development of etch facets. However, as facets increase in size, fine structure in the form of tailed diffraction maxima and multiple spots is clearly resolved. Diffraction patterns from the etched (001) surface indicate that (011) and (112) type facets are developed, but electron micrographs reveal only etch pits bounded by (011) facets. Information regarding surface microstructure not clearly resolved by replica techniques may be obtained by observing the shape of diffraction maxima from electropolished and lightly etched surfaces. Diffraction patterns from electropolished (001) and (011) surfaces illustrate these effects.

A21. Electron Diffraction and Microscope Study of Thin Oxide Films on Single Crystals of α Iron. E. G. BREWER,* P. B. SEWELL, AND M. COHEN, *Division of Applied Chemistry, National Research Council, Ottawa, Canada.*—Oxide films of mean thickness between 15 A and 120 A, prepared on electropolished surfaces of iron single crystals, have been studied by reflection electron diffraction and with the aid of platinum-carbon replicas. The oxide is identified in all cases as either γ Fe_2O_3 or Fe_3O_4 and its epitaxial relationship with the substrate determined. The films are then stripped from the iron by the iodine/methanol method and examined by transmission diffraction and microscopy. No change in composition or orientation of the oxide is found as a result of stripping. Large oxide nuclei which are not detected by reflection diffraction are observed in the films by electron microscopy. The size and distribution of such nuclei vary with the orientation of the substrate grain. Particles of the order of 20 A are resolved in a continuous oxide film stripped from a (001) iron surface, being in good agreement with the mean particle size estimated from the half-widths of diffraction maxima.

A22. Pfefferkorn and Electron Diffraction Studies of Iron Sulfide Crystal Growth. F. J. RADD,* F. G. ROWE, AND D. H. OERTLE, *Continental Oil Company, Ponca City, Oklahoma.*—This paper shows the crystal growth kinetics and preferred nucleation of iron sulfide (Fe_9S_8) upon Westinghouse Puron highly pure iron and upon steel. There is no uniform layer development. The electron diffraction patterns indicate that the early crystal lattice spacings are replaced by the normal spacings after about 1 hr. Aqueous hydrogen sulfide solutions were used at room temperature to cultivate the iron sulfide (Kansite) crystals. Our studies demonstrate the effectiveness of the Pfefferkorn electron microscopy technique to the growth of sulfides.

A23. Design Parameters for the Telefocus Grid Cap. JOHN W. COLEMAN, *Radio Corporation of America, Camden, New Jersey.*—High-intensity electron beams of small angular aperture and diameter are of increasing interest in microscopy and x-ray microanalysis. Standard guns at standard potentials can be made to yield such beams if the cathode field is modified. A relatively simple means to this end is the use of a substitute grid cap of the "telefocus" type.[1–3] This investigation concerns the design parameters for such a high-efficiency focusing grid cap. For ease of use, the results are presented as (a) intensity—geometry curves, (b) geometry—optical property curves, (c) geometry—bias curves. The three sets of curves constitute sufficient information from which a cap geometry may be deduced to give a beam of desired characteristics. General rules for design are given.

[1] K. H. Steigerwald, Optik **5**, 469 (1949).
[2] J. W. Coleman, Phys. Rev. **90**, 368 (1955).
[3] F. W. Braucks, Optik **15**, 242 (1958).

A24. Voltage Reference Sources for Electron Microscope Power Supplies. ROBERT L. LIBBEY, *Radio Corporation of America, Camden, New Jersey.*—Attainment of highest resolving power in the electron microscope requires very stable voltage and current supplies. These supplies, which are generally high-grain feedback electronic regulators, are stabilized by referencing their output to a source of constant potential. Such so-called reference voltages are commonly obtained from batteries, glow discharge regulator tubes, or semiconductors. Voltage reference sources are discussed with a view to the requirements imposed by the microscope and in relation to the influence of associated circuit elements. Comparisons of characteristics such as short and long-time stability, temperature dependence, life, and cost are given.

A25. Improved Pointed Filaments of Tungsten, Rhenium, and Tantalum for High-Resolution Electron Microscopy and Electron Diffraction.† H. FERNÁNDEZ-MORÁN, *Mixter Laboratories for Electron Microscopy, Massachusetts General Hospital, Boston.*—Tungsten, rhenium, and tantalum pointed filaments of modified Müller-type with a tip radius of 1 to 10 μ have been used with the double condenser system of the Siemens Elmiskop I to provide extremely intense, parallel illumination for electron microscopy and electron diffraction at 40 to 100 kv. Microbeams of 0.3- to 3-μ diam readily obtained with this arrangement give images of adequate brightness at the highest electron-optical magnifications (80 000 to 160 000×) even when the condenser lens is defocused or condenser apertures of 50 to 100 μ are introduced. Under these conditions marked enhancement of the contrast in thin sections and improved resolution in thin specimens have been observed regularly. The reduced divergence of the incident electron beam is particularly suitable for achieving higher resolution of periodic structures, including dark- and bright-field images of moiré patterns, and in general for high-resolution dark-field studies. The improved tungsten filaments have a useful lifetime of 20 to 40 hr, and substantially higher figures can be expected with appropriate selection of wire type and material. Pointed filaments of rhenium wire are easier to make, and rhenium has the additional advantage of being more resistant than tungsten to the deleterious water cycle effect and to work function change by oxygen absorption. The welding and electrolytical etching techniques used for reproducible preparation of the pointed filaments are described. The critical positioning of the filament tip within the different types of cathode shields for optimum utilization of the T-F emission is discussed. Representative micrographs and motion picture sequences taken at high electron-optical magnifications will be shown to illustrate the unique advantages of the pointed filaments.

† The valuable assistance of Mrs. G. Magnusson and Mr. F. Rosebury of the Research Laboratory of Electronics, Massachusetts Institute of Technology, Cambridge, in the development of the filaments is gratefully acknowledged. This work was supported by a U. S. Atomic Energy Commission contract and by a grant from the National Institutes of Health.

A26. Single-Crystals of Graphite and of Mica as Specimen Supports for Electron Microscopy.† H. FERNÁNDEZ-MORÁN, *Mixter Laboratories for Electron Microscopy, Massachusetts General Hospital, Boston.*—Coherent single-crystal films of mica and of synthetic graphite, about 50 to 500 A thick and with several square millimeters of useful area, have been prepared by a simple and reproducible cleavage method. This technique, which can be applied to many other crystalline materials, involves stripping off surface layers by pseudo-replication, followed by careful dissolving of the plastic backing, and spreading on liquid surfaces to select the crystalline lamellae of adequate thickness through correlation with their characteristic interference colors. The single-crystal films can be picked up directly on the specimen grids and are exceedingly thin and uniform over wide areas, being completely transparent to the electron beam at 60 to 100 kv. Compared with the usual polycrystalline carbon or plastic specimen films, these lamellae prepared from the synthetic graphite single-crystals made by Raytheon Company, and from mica, have the following significant advantages: (a) they are very thin, flat, and smooth and thus suitable as substrates for high-resolution shadow casting; (b) exhibit exceptional stability under electron bombardment because of their low thermal expansion coefficient and great heat resistance; (c) by virtue of their high degree of thermal and electrical anisotropy the graphite single crystals are particularly suitable for low-temperature electron microscopy, since favorable conditions for heat transfer and protection of appropriately oriented specimens are provided; (d) these films are considered to be impermeable to gases and liquids even at high temperatures and represent, therefore, effective specimen supports for electron microscopy of liquids in chambers of special design; (e) they are ideal substrates for moiré experiments and in general for electron-optical studies requiring single-crystal lamellae. Representative examples of these applications will be given, and the preparation technique demonstrated.

† We wish to thank Dr. T. H. Johnson and his associates of the Research Division, Raytheon Manufacturing Company, Waltham, Massachusetts, for kindly providing the samples of synthetic graphite. This work has been supported by a U. S. Atomic Energy Commission contract and by a grant from the National Institutes of Health.

A27. Direct Study of Ice Crystals and of Hydrated Systems by Low-Temperature Electron Microscopy.† H. FERNÁNDEZ-MORÁN, *Mixter Laboratories for Electron Microscopy, Massachusetts General Hospital, Boston.*—During continuation of previous investigations,[1] direct studies of ice crystal structure and growth have been carried out by recording electron micrographs and electron diffraction patterns of submicroscopic ice crystals which have been cooled (−130°C to −90°C) with a modified liquid nitrogen stage during observation with a microbeam of very low intensity. Through oriented deposition of ice crystals on single-crystal films of graphite, mica, and heavy metals, characteristic moiré patterns were observed which are considered to be related to the lattice structure of the ice crystals. By using a rapidly shifting electron microbeam of high intensity obtained with improved pointed filaments,

characteristic changes in the moiré patterns and other irradiation effects induced in the ice crystals at low temperatures have been recorded in motion picture sequences. It also has been possible to perform preliminary, direct electron microscope observations of certain liquids and of partially hydrated biological systems (bacteria, fibrous proteins, and other macromolecular components) at various temperatures by sandwiching them between single-crystal films of graphite or mica in microchambers of special design. Potentialities and inherent artifact sources of these techniques will be discussed.

† We wish to thank Mr. C. Percy and Mr. J. I. Quateman of the Bell and Howell Company, Chicago, Illinois, for their valuable help in the adaptation of the motion picture equipment for electron microscopy. The able technical assistance of Mr. F. Merk and Mr. E. Shmid in the course of this work is gratefully acknowledged. This work was supported by a U. S. Atomic Energy Commission contract and by grants from the National Institutes of Health.

[1] Ann. N. Y. Acad. Sci. **85**, 689 (1960).

Session BIII, Viruses and Related Topics

B21. Observations on Avian-Type Virus Particles in Various Tissues of "Normal" Chicks. R. F. ZEIGEL, *National Cancer Institute, Bethesda, Maryland.*—Pancreatic tissue from eight chicks of various ages picked at random from a "normal" colony were examined by electron microscopy. Six of the eight chick pancreases examined proved positive for virus particle content. Various other tissues (i.e., kidney, liver, spleen, small intestine, heart, and lung) were examined in several cases where virus particles could be demonstrated in association with the pancreas. The particles were demonstrated in relatively small amounts in the intercellular spaces and in small intracellular vacuoles. Particles rarely were observed in formative states in all tissues except the pancreas. Large quantities of particles frequently were demonstrated in the acinar-lumina. Various stages of particle formation by budding from the plasma membrane also were observed. The implications of these observations will be discussed.

B22. Growth Cycle of Vaccinia Virus in Earle's *L* Strain Cells and Fine Structure Changes Associated with Virus Multiplication in Stationary and Suspension Cultures. S. DALES*† AND L. SIMINOVITCH, *Ontario Cancer Institute, Toronto, Canada.*—Early events in the cycle of infection of vaccinia virus in *L* cells were studied by adding virus at very high multiplicities (~300:1) to cells in suspension. One hour after virus was added particles were present on the cell membrane and in the cytoplasm. Within 2 hr areas of fibrous material, presumably at the sites of virus disintegration, were evident in the cytoplasm. Changes occurring over a longer period were studied by infecting suspension cultures with lower virus-cell multiplicities (~5:1). Immature virus was first observed 4 hr after infection and mature forms 6 hr after infection. About 24–30 hr after adding virus large numbers of mature and immature particles of vaccinia were present throughout the cytoplasm. At this late stage of infection extensive "tubes" were observed in the cytoplasm whose walls consisted of many layers of very flat vesicles arranged concentrically. The fine structure of giant cells, formed in stationary cultures infected with vaccinia, also will be described.

† Present address: The Rockefeller Institute, New York, New York.

B23. Ferritin in the Human Intestinal Epithelium. ROBERTA S. HARTMAN,* RICHARD E. HARTMAN, AND MARCEL E. CONRAD, JR., *Department of Molecular Biology and Department of Hematology, Walter Reed Army Institute of Research, Washington, D. C.*—Iron absorption in the human now can be studied by direct examination of intestinal mucosa secured by an intraluminal biopsy instrument. Electron microscopy is indicated for that portion of the study concerned with the possible role of ferritin in regulating iron absorption. As absorption is known to be related to the iron stores, we are interested in studying the possibility of a relationship between iron stores and the *apparent* amount of ferritin in the absorptive cells. In preparation for such a study, normal specimens were examined to determine the usual site(s) of ferritin depots. In most of the cells the apical region was seen to contain several profiles of ferritin-containing bodies, the basic nature and origin of which are unknown. These slightly resembled large Golgi granules but have not been seen within the Golgi area. In a few instances small clusters of ferritin molecules were seen in the cytoplasmic matrix.

B24. Electron Microscope Studies of Pigment Cells in the Goldfish, *Carassius auratus L.* YUTAKA MISHIMA, FREDERICK F. SCHAUB, JR., AND ALDEN V. LOUD, *Department of Dermatology, Wayne State University, and Detroit Institute of Cancer Research, Detroit, Michigan.*—Thin sections of black pigmented goldfish scales normally show melanocytes, melanophores, and lipophores only in the dermis. Melanophores are characterized by dense melanin granules, 400–500 mμ, uniformly distributed in cytoplasm containing few mitochondria and membranous vesicles. Dendritic extensions of these cells frequently are seen. Lipophores contain many large vesicles filled with amorphous, possibly lipoid, substance, mitochondria with predominantly tubular cristae, and abundant small vesicles, 40–50 mμ, often showing high density. In xanthic goldfish only the lipophore type of pigment cell has been observed. Following subcutaneous injection with hydroquinone, a treatment which leads to the destruction of melanophores, nondendritic forms of melanophores were seen, and cells containing dense granules were found in the epidermis. No pigment cells have been observed penetrating the basement membrane of the epidermis, a membrane 700–800 mμ thick with a compact zone of 70–80 mμ on its epidermal side. Distinct tonofibrils are seen extending from regions of attachment between cells of the basal layer of the goldfish epidermis.

B25. Normal and Psoriatic Epidermis. WILLIAM G. BANFIELD* AND DARLENE C. BRINDLEY, *Laboratory of Pathology, National Cancer Institute, Bethesda, Maryland.*—In normal abdominal epidermis very dense granules 50 A in diameter are found only in the basal layer. They have the appearance of ferritin and in suitable preparations contain four smaller dense granules as does ferritin. Such granules have not been seen in psoriatic epidermis. Among the changes in psoriasis there is intercellular edema and defects in keratohyalin and keratin formation. The keratohyalin granules are few, small, and more regular than in normal epidermis. They develop a membrane and some persist into the keratinized layer. Often in the lower layers of the corneum the condensed cells contain compacted cytoplasmic elements. In one case of severe exfoliative psoriasis some of the cells in the Malpighian layer contain many bodies similar to those described by Charles *et al.*[1] in normal skin as "unknown bodies."

[1] A. Charles and F. G. Smiddy, J. Invest. Dermatol. **29**, 327 (1957).

B26. Electron Microscope Study of *Anaplasma marginale* in Deer. MIODRAG RISTIC* AND A. M. WATRACH, *Department of Pathology and Hygiene, College of Veterinary Medicine, and Electron Microscope Laboratory, University of Illinois, Urbana, Illinois.*—Erythrocytes of the deer with acute anaplasmosis have been studied in sections and shadow-cast preparations. The organism of *Anaplasma marginale* consisted of 1 to 8

initial bodies embedded in an apparently homogenous matrix. The latter was demarcated from the erythrocyte by a well-defined membrane of approximately 10 mμ in diameter and was enclosed in a double membrane. The internal structure of this body consisted of one central and a few peripheral, dense aggregates of finely granular material embedded in an electron lucid substance. Preliminary observations suggest that the initial body may reproduce by binary fission.

Symposium SIII, Recent Advances in Electron Metallography

S11. Examination of Thin Foils by Transmission Electron Microscopy. E. SMITH* AND F. W. C. BOSWELL, *Physical Metallurgy Division, Mines Branch, Department of Mines and Technical Surveys, Ottawa, Canada.*—A brief description of the preparation of thin foils will be given, followed by a review of some results obtained on various metals at the Mines Branch Laboratory with results of other workers described to give a more complete account of recent work in this field. Some results will be described on the configuration of dislocations in strained α brass, austenitic stainless steel, aluminum, and iron showing the different arrangements of dislocations after plastic deformation of these metals and the formation of dislocation networks on recovery. Precipitation in an aluminum-silver alloy and in low carbon iron will be described, showing two different modes of precipitation. Deformation twins have been observed in tin and in α iron and will be discussed briefly. An example will be shown of recent work on mechanical deformation of metals inside the electron microscope.

S12. Progress in Electron Metallography of Steels. GEORGE E. PELLISSIER, *Applied Research Laboratory, U. S. Steel Corporation, Monroeville, Pennsylvania.*—In the urgent technological effort to develop stronger, tougher, and more heat-resistant alloys, an understanding of the relationships between their microstructure and mechanical behavior has become a problem of dominant interest and importance. As further insight is gained into these relationships, more emphasis is being placed on the development of means for obtaining microstructures having desirable mechanical properties. To create new structures intelligently and systematically, and to devise methods for controlling known structures, considerable knowledge of the mechanisms of formation of different types of structures is needed. Furthermore, the effects of chemical composition, and of various thermal and mechanical treatments, on structure must be determined. And finally, the influence of actual, complex service conditions on structure needs to be studied to aid in evaluating both the particular service conditions and the reactions of different structures to those conditions. Clearly, all of these efforts entail a great deal of structural investigation. One of the most powerful tools available to the metallurgist for this work is the electron microscope, particularly when used conjointly with electron diffraction and microprobe x-ray analysis. The electron microscope is especially useful in steel research and development because the most important microstructures in modern steels are extremely fine and complex; their components cannot be resolved, identified, and measured with a light microscope. Some of the more important recent applications include investigations of the mechanisms of martensite tempering and bainite formation. In conjunction with electron diffraction, the electron microscope has been used extensively to identify minute metal carbide and nitride particles and to study their precipitation behavior in a variety of alloy steels. Some progress has been made in correlating features of steel microstructures, and their dimensions, with strength and toughness. Electron metallography still has not achieved widespread application in steel development, however, and the reasons for this will be discussed. Several examples of its potentialities and usefulness in this field will be presented.

S13. Light Metals and Alloys. D. L. ROBINSON, *Alcoa Research Laboratories, Aluminum Company of America, New Kensington, Pennsylvania.*—The discussion will be concerned with a general review of recent contributions and applications of electron microscopy to the study of light metals and alloys, with particular emphasis on aluminum. The relationship between the microstructure and resistance to corrosion of aluminum-magnesium alloys will be discussed. Also, recent developments in hot stage transmission electron microscopy at Alcoa Research Laboratories will be described. A very simple but effective hot stage for the Philips 100B electron microscope and some of the more interesting results obtained with this device will be described and illustrated. These will include the various stages of polygonization and recrystallization of a work-hardened aluminum-magnesium alloy and the distribution and annealing out of dislocation networks during the recovery process.

S14. Electron Metallographic Studies of Stainless Steels and Heat-Resistant Alloys. W. C. BIGELOW, *Department of Chemical and Metallurgical Engineering, The University of Michigan, Ann Arbor, Michigan.*—One of the most important and difficult metallurgical problems of the present time is that of providing alloys capable of withstanding the increasing stresses, elevated temperatures, and corrosive atmospheres encountered in the nuclear reactors, jet aircraft engines, and industrial processing equipment of our advancing technology. A variety of stainless steels and "superalloys" have been developed to date which can provide several thousand hours of service under stresses of the order of 25 000 psi at temperatures up to 1600°F. These alloys usually have relatively complex compositions so that conditions encountered in service and during various metallurgical fabrication procedures frequently produce submicroscopic changes in their microstructures which markedly influence their physical and metallurgical properties. Electron metallographic techniques are therefore

invaluable in providing the information necessary for understanding and controlling the properties of these alloys and for designing new alloys with improved properties. Recent electron metallographic studies of the stainless steels and heat-resistant alloys will be reviewed, and illustrations of typical results obtained in these studies will be shown.

S15. Application of Electron Microscopy to the Study of Metal Oxidation. WILLIAM E. BOGGS, *Applied Research Laboratory, U. S. Steel Corporation, Monroeville, Pennsylvania.*—A large amount of experimental work on the oxidation of metals is reported in the technical literature. Until fairly recently, the experimental work has been limited to quantitative measurements of the rate of thickening of oxide films. The kinetic data obtained by these means generally have provided certain mathematical relationships between the oxide film thickness and time, resulting in the development of several theories of the mechanisms of oxide film formation. However, a deficiency in experimental information on oxidation has become apparent in recent years as the precision of the kinetic data has improved. In attempting to overcome this deficiency, many investigators have employed electron diffraction to determine the crystal structure of oxide films, but few investigators have utilized electron microscopy to study the growth of oxide films starting from a very early stage of formation. The electron microscope can provide valuable information about the growth of oxide films that is not available by other techniques. In the author's laboratory this instrument was used to compliment a study of the kinetics of the oxidation of tin. It has been possible to correlate the kinetic data with observations concerning the mode of formation of the oxide films and arrive at certain conclusions concerning the mechanisms of oxidation which were not apparent from the kinetic data alone. Under all oxidizing conditions investigated, the oxide which is formed is α SnO. It nucleates at numerous sites on the tin surface and spreads laterally until the metal is essentially completely covered. For oxygen pressures of 1 mm Hg and above, the oxide nuclei developed into microscopic, wheel-shaped "growth centers." Segments of the rims of some of these grow outward as spikes in a spiral pattern and develop into oxide platelets. However, at oxygen pressures below 1 mm, the oxide grows from nuclei in a dendritic manner. When the surface of the tin becomes 60 to 80% covered by oxide, the oxidation rate begins to decrease, conforming to a direct logarithmic rate law. As this occurs, cavities are seen to develop at the oxide metal interface. It is believed that the growth of these cavities under the oxide causes the conformance to the direct logarithmic rate law. The cavities are first detected at the junctions of growth laminae or microtwins within the oxide platelets and enlarge with time until they may reduce the area of contact between the oxide and metal by one-third. The reasons for their growth appear to be rather complicated, since it has been found that they continue to grow even in a vacuum.

S16. ASTM Subcommittee on Electron Metallography. MAXWELL D. TEAGUE, *Engineering Division, Chrysler Corporation, Detroit 31, Michigan.*—Subcommittee XI of Committee E-4 of the American Society for Testing Materials has been actively engaged for a number of years in studying techniques and promoting the dissemination of information in the field of electron metallography. The past activities and the future plans of this Subcommittee will be reviewed briefly.

Session BIV, Fine Structure and Function

B27. The Golgi Complex in Living Cells.† GEORGE G. ROSE, *Tissue Culture Laboratory, Arabia Temple Crippled Childrens Clinic, Hermann Hospital, Houston 25, Texas.*—The primary purpose of this report is to add data to our knowledge of the Gogli complex by illustrating secretory cycles in living cells. A 400-ft 16-mm time-lapse motion picture film will be presented to show osteoblasts from embryo chick bone tissue cultures. Within these osteoblasts very prominent Golgi bodies may be observed as phase-dark juxtanuclear forms. From within these forms phase-white droplets are observed to emerge and to pass into the cytoplasm. In addition to this, cytochemical and vital dye techniques will be described which provide corroborating evidence to link this structure to the Golgi complex analyzed by electron microscopists and biochemists.

† This work was supported in part by a grant-in-aid from the American Cancer Society, Inc.; a grant-in-aid from the Orthopaedic Research and Education Foundation; and by a U. S. Army Medical Research and Development Command, Department of the Army, contract, administered by C. M. Pomerat.

B28. Ultrastructural Changes Attending Certain Common Mitochondrial Response or Behavioral Patterns. K. M. RICHTER* AND H. R. COLLINS, *Department of Anatomy, University of Oklahoma Medical Center, Oklahoma City, Oklahoma.*—Classical cytologic literature on mitochondrial changes during diverse normal, differential, experimental, and pathologic circumstances indicates collectively that there are at least four basic types of mitochondrial responses or behavioral patterns per se in a morphologically descriptive sense: (1) mitochondrial fusion, (2) mitochondrial dispersion (fragmentation, division, separation), (3) mitochondrial vesiculation, and (4) no change (i.e., maintenance of a given status quo). Because of the widespread occurrence of these response patterns or behavioral patterns, they must be regarded as essential cellular expressions and necessary to many facets of general cellular biology and to many special aspects of cytophysiology, cytochemistry, energy transformations, transfer, etc. Such mitochondrial response patterns warrant critical consideration. Observations will be presented bearing on the transformations and redispositions of mitochondrical membranes, cristae, and matrical components attending mitochondrial fusion, dispersion, and vesiculation phenomena during the course of flagellate sperm differentiation in the Notonectid, Buenoa.

B29. Fine Structure of the Z Band in Mammalian Skeletal Muscle. MICHAEL K. REEDY, *Department of Anatomy, University of Washington, Seattle 5, Washington.*—Rat diaphragm, fixed in collidine buffered osmium tetroxide, em-

bedded in epoxy resin, stained with heavy metals either before embedding or after sectioning, has been examined with the electron microscope. Published micrographs by other workers show two features also noted in this material: in cross sections, the Z band presents a crosshatched appearance, while longitudinal sections occasionally show Z bands having a dense zigzag structure. The fine myofilaments in one segment of the I band have been observed to be complexly connected through the Z band to fine myofilaments in the next segment of that I band. Various three-dimensional models of the Z band will be presented and their conformity to the evidence explored. The number, distribution, and arrangement of the Z-band filaments with reference to the I-band filaments will be discussed.

B30. Fine Structure of the Sperm Tail of the Domestic Fowl (*Gallus domesticus*). TOSHIO NAGANO, *Department of Anatomy, University of Washington, Seattle 5, Washington.*—The rooster sperm tail has one central pair of filaments and nine pairs disposed circumferentially. One filament of each peripheral pair is much denser than the other. The denser filaments are referred to as "dense filaments" and the partners are termed "light filaments." In cross section, the dense filament is seen as a circle filled with dense material. In addition, the dense filament is associated with both "arms" and "spokes" as noted by Afzelius for sea-urchin sperm. The light filament appears as a half-moon tubule bounded by a membrane of about 5 mμ in thickness. The light filament is attached to the dense filament along the concave face. The diameter of the dense filament is about 25 mμ, and the light filament is slightly smaller. The two central filaments appear as uniform tubules of the same diameter as the light filament. The two central filaments also have tenuous connections.

B31. Limiting Layers of the Seminiferous Tubule in the Albino Rat. JOST BRÖKELMANN, *Department of Anatomy, University of Washington, Seattle 5, Washington.*—In the rat the seminiferous tubule is surrounded by two cell layers, together about 1 μ thick, an interlamellar layer, and an adventitial layer. The fine structure of these layers, their basement membranes, and adjacent connective tissue will be described. The interlamellar layer, 0.3–0.5 μ thick, has extremely flat nuclei. Most of the cytoplasm is filled with a feltwork of filaments about 50 A in diameter. Adjacent cells overlap slightly; desmosomes are present. Pinocytotic vesicles are found in interlamellar and adventitial cells. The adventitial layer resembles an endothelium. In the cytoplasm straight filaments about 50 A thick occur in bundles. The cells overlap considerably; no desmosomes were observed. Four basement membranes are found: along the seminal epithelium, on both sides of the interlamellar layer, and on the inside of the adventitial layer. The connective tissue between basement membranes shows collagenous bundles embedded in a wickerwork of filaments approximately 50 A in diameter.

B32. Fine Structure of the Developing Trachea. T. S. LEESON, *Department of Anatomy, University of Toronto, Toronto 5, Canada.*—The appearances of the normal trachea as seen with the electron microscope now are well established.[1] This investigation was undertaken to study the trachea at varying stages of development, particularly with regard to the ciliated cells. By 28 days' gestation (i.e., at least 2 days before birth) the rabbit trachea has a mucosa with fully developed cilia. At 16, 18, 20, and 22 days, the tracheal mucosa is multilayered and no cilia are present. At 24 days, some cells have many cilia, but the mucosa generally is multilayered and with few ciliated cells. At this time, some cells contain granules with a dense center, these being located near the lumen. The hyaline cartilage, too, is of great interest. Its matrix contains microfibrils which are not collagenous.

[1] Brettschneider, Anat. Anz. **105**, 194–204 (1958).

B33. Electron Microscopic Studies of the Pineal (*Epiphysis Cerebri*) of the Adult Rat.† R. E. SMITH, *Department of Anatomy, Indiana University Medical Center, Indianapolis 7, Indiana.*—Ultrastructural studies of the adult male and female pineal gland indicate that it definitely meets the criteria for physiologic activity. At least two cell types can be distinguished, parenchymal and neuroglia. Electron microscopy reveals considerable difference between the two cell types. The parenchymal cells average 8 to 10 μ in diameter; their polymorphic nuclei are light in density and often heavily infolded. The nucleus may possess more than one nucleolus. The nucleoli are conspicuous because of their high electron density. Parenchymal cells have abundant cytoplasm; however, there appears to be no well-organized endoplasmic reticulum. The Golgi apparatus of each cell may be located either close to the nucleus or free in the cytoplasm. Mitochondria are numerous and often are concentrated in and around the Golgi. The neuroglia cells of the pineal are more epithelioidal, and their nuclei are less fusiform than are the pituicytes of the neurohypophysis. They have less cytoplasm than the parenchymal cells, and their nuclei are more electron dense. Preliminary studies indicate the presence of three types of secretory materials: masses of light density, electron dense masses of varying size similar to such masses found in the neurohypophysis, and small granules averaging 75 mμ in diameter. Composite masses of "secretory-like" material heretofore not reported appear to be formed in the gland and found free in the sinusoids. These findings will be discussed in light of their suggested physiological association to the pituitary.

† This research was supported by the Indiana Elks Cancer Fund.

B34. Ultrastructural Changes in the Endometrium of the Pseudopregnant Rat Accompanying Induced Decidual Cell Formation. WILLIAM P. JOLLIE,* *Department of Anatomy (Section of Histology-Embryology)*, AND SERGIO A. BENCOSME, *Department of Pathology, Queen's University, Kingston, Ontario, Canada.*—Eighteen mature, nulliparous rats were rendered pseudopregnant by electrical stimulation of the uterine cervex during vaginal estrus. In 12 of these, 4 days after stimulation, the antimesometrial endometrium was traumatized to produce massive decidua. These animals were killed at daily intervals from 1 to 5 days following traumatization; and the antimesometrial decidua was compared with the same region from the uteri of 6 nontraumatized, pseudopregnant rats. In the latter, stromal cells resemble fibroblasts. The Golgi material is localized; and a small amount of fine fibrillar material is evident in the cytoplasm. As decidua is formed, endoplasmic reticulum and fatty and hyaline droplets become more abundant. The Golgi apparatus becomes extensively ramified. There is an increase in fibrillar material, and its cytoplasmic disposition is often precisely localized. Other regions in the cytoplasm appear filled with a finely tubular, RNP-free reticulum. Possible relationships between this reticulum, the endoplasmic reticulum, and the fibrillar material are discussed.

B35. Fine Structural Alterations in the Rat Heart Following a Magnesium-Deficient Regime and Cold Stress.† RAJENDRA K. MISHRA,* LAWRENCE HERMAN, AND PATRICK J. FITZGERALD, *Department of Pathology, State University of New York, Downstate Medical Center, Brooklyn, New York.*—Female Sprague-Dawley rats were submitted to the following experimental conditions: restriction to a magnesium-deficient regime, cold stress, and a combination of the two. Magnesium deprivation, which is known to produce visible cardiac necrosis, was followed by prominent vacuolation of the sarcosomes and widening of the sarcoplasmic reticulum. Cold stress alone occasionally may produce fine structural alterations in the

sarcosomes and the sarcoplasmic reticulum. Cold stress superimposed on the deficient regime aggravated the cardiotoxic effects of magnesium deprivation. This manifested itself in gross calcification. At the electron microscope level intracellular calcification was found in the sarcosomes and certain cells of the exudate. In addition, myofibrillar dissolution and occasionally changes in the intercalated disks were observed. These findings will be discussed in relation to the protective role of magnesium against cardiac necrosis in general.

† This investigation was supported by U. S. Public Health Service grant.

B36. Fine Structure and Function in Cardiac Muscle Membranes. STANLEY C. SCHEYER, *Department of Anatomy, University of Washington, Seattle 5, Washington.*—The isolated perfused frog heart and the rat atrium both have been used extensively in cardiac electrophysiological studies. An attempt has been made to correlate electrical changes in the cell and cell membrane to morphological changes as observed with the electron microscope. Isolated preparations of both rat atrial and frog ventricular tissues were perfused with varying physiological solutions (normal, hypertonic, high Na^+, saturated chloroform, and digitalis). Changes in electrical events were monitored with micro-electrode recordings while simultaneous tissue biopsies were taken for study with the electron microscope. Preliminary results show morphological changes in the sarcoplasmic reticulum, interstitial spaces, sarcolemmatic structure, and relationships which can be related to the electro-physiological data.

B37. Electron Microscopic and X-Ray Diffraction Observations on Centrifuged Human Red Cell Ghosts. CHARLES D. ADAMS, *Department of Anatomy, University of Washington, Seattle 5, Washington.*—Human red cells were hemolyzed by mixing a sample of blood with 125 volumes of distilled water at 4°C. After 24 hr, the ghosts were collected by centrifugation (3000×G) at 4°. Aliquots of packed ghosts were frozen at −58° and then centrifuged at 25 000 G at +4° for 1 hr. The resulting volume reduction from the packed ghosts was greater than 90%. The ghosts were fixed in potassium permanganate and embedded in Epon. Tightly packed, flattened unit membranes were observed, which had a high degree of order and gave analyzable x-ray diffraction data indicating a spacing of 200 A. Many large myeloid figures were seen. The remarkable extent of the uninterrupted membranes seen was apparently the result of fusion of the membranes of many red cells. The membrane ultrastructure was morphologically identical to that seen in red blood cells and ghosts prepared by distilled water or freezing and thawing hemolysis alone.

Session AIV, Metallurgical Studies

A28. Electron Metallography of Tungsten Wires, Rods, and Powders. CHARLES F. TUFTS, *General Telephone and Electronics Laboratories, Inc., Bayside, New York.*—The carbon replica technique has been adapted and used extensively in these laboratories to study tungsten wires, rods, and powders. Experimental details are given for specimen preparation using platinum preshadowing in conjunction with Parlodion-carbon and direct carbon replication. Advantages of rotating the specimen during carbon deposition are discussed. This technique permits examination of excessively rough surfaces such as those produced by fracture or by pits formed during prolonged etching. The replicas are three-dimensional and permit stereo methods to be used effectively. In the powder work, complete aggregate geometry is revealed, giving the technique a distinct advantage over methods that employ only silhouette images. In addition, elements of surface geography in the 10- to 100-A size range are resolved. Illustrations show cold-worked, annealed, and recrystallized structures in wires and rods; also large grains of powder in the 30- to 40-μ size range.

A29. Investigation of Fatigue in Copper by Electron Microscopy. HARRY M. BENDLER,* *Research Laboratories, General Motors Corporation, Warren, Michigan,* AND W. A. WOOD, *Ballieu Laboratory, University of Melbourne, Victoria, Australia.*—Cylindrical rods, 0.25 in. in diameter, of OFHC copper have been fatigued by alternating torsion.[1] The rods are exercised at different amplitudes and for different fractions of their fatigue life at each amplitude. After exercising, the rods are silver-plated to preserve the surface structure, and a narrow flat is ground and polished on the surface parallel to the axis of the rod. Preshadowed positive carbon replicas are made of this surface. Electron micrographs of these specimens show examples of the progressive alteration of the crystal structure at successive stages of their fatigue life together with the formation and growth of fissures or fatigue cracks.

[1] W. A. Wood, Phil. Mag. **3**, 692 (1958).

A30. Study of Oxidation, Oxidation-Reduction, and the Thermal Etching of Iron Whisker Surfaces by Electron Microscopy.† J. V. LAUKONIS,* *General Motors Corporation,* AND R. V. COLEMAN, *University of Illinois, Urbana.*—Oxidation products, reduction of products, and the thermal etching single-crystal iron whisker surfaces have been studied by electron microscopy. The surfaces were WO_3-preshadowed and direct carbon replicated using the methods of Scott.[1] Three stages of oxidation will be illustrated. Variations in replication technique and the use of stereo electron microscopy will be discussed from the viewpoint of how they permit a more complete study of surface topography. Rearrangement surfaces which are the result of hydrogen reduction of oxidation products on iron surfaces will be shown. The dependence of such rearrangements on the crystallographic orientation of the surface which was oxidized will be discussed briefly. Several examples of unusual iron surface dendrites which are the result of thermal etching will be shown.

† Supported in part by the U. S. Atomic Energy Commission.

[1] R. L. Scott, J. Electron Micros. (Japan) **8**, 31 (1960).

A31. Electron Microscopic Studies of the Diffusion Zone of Nickel Coated Titanium-8 Manganese Alloy. JOHN F. DANOVICH, *Aeronautical Materials Laboratory, Naval Air Materiel Center, Philadelphia 12, Pennsylvania.*—The interface of nickel coated Ti-8 Mn alloy has been studied using the electron microscope to investigate factors leading to the improvement in adhesion and resistance to wear. Techniques of surface preparation of the titanium alloy and heat treatment after plating are major factors in producing adherent and wear-resistant nickel coatings. Electron micrographs of the interface show differences in diffusion zones and their effect on the coating and wear resistance. Electron diffraction was employed to identify the composition of the diffusion zone.

A32. Use of Thermionic Emission Microscopy and Cinematic Recording for Rate Studies of High-Temperature Transformations in Metals. S. R. ROUZE* AND W. L. GRUBE *Research Laboratories, General Motors Corporation, Warren, Michigan.*—In rate studies of high-temperature transformations in metals with the thermionic emission electron microscope, it is necessary that adequate time-resolved records of these transformations be obtained as they occur. In many

instances, the rate of transformation is such that cinematic methods are required. This in turn introduces the additional problem of recording faint, fluorescent-screen images at cinematic speeds. The current method being used to obtain adequate records in rate studies of high-temperature transformations will be discussed. In addition, the advantages of using simultaneous cinematic recording of both time and the event will be emphasized. The utility of the method employed will be illustrated with 16-mm motion picture films.

A33. Improved Method for Separating Nonmetallic Phases from Specimens. CHARLES F. TUFTS, *General Telephone and Electronics Laboratories, Inc., Bayside, New York.*—An improved cell which utilizes electrolytic action to remove formed films and deposits from metal surfaces, and to isolate and collect particles of nonmetallic phases, is discussed. This cell employs saturated KCl solution as the electrolyte. During operation, purified and dried gases are used to protect the specimen from chemical change and contamination. Provisions are made for washing the specimen either with liquids or gases with the specimen protected from contact with air. Isolated films and particles can be examined by electron diffraction, electron microscopy, x-ray spectroscopy, emission spectroscopy, light microscopy, and x-ray diffraction. The principal advantage of this technique is that the specimen is protected from chemical attack, thus reducing materially the possibilities of chemical and structural changes.

A34. Convenient Method of Calibrating Selected Area Electron Diffraction Patterns. G. N. MANIAR* AND W. C. BIGELOW, *Department of Chemical and Metallurgical Engineering, The University of Michigan, Ann Arbor, Michigan.*—The problem of determining accurately the instrument constant in selected area electron diffraction work often can be solved by depositing fine droplets of a solution of an appropriate crystalline material on the specimen just before it is placed in the electron microscope. The droplets evaporate rapidly in the vacuum of the microscope, forming very fine crystalline particles which serve as the necessary calibration standard. Droplets of suitable sizes can be formed conveniently by means of inexpensive, commercially available nebulizers.

A35. Method of Mounting Specimens for Ion Bombardment Etching. RONALD L. SCOTT, *Research Laboratories, General Motors Corporation, Warren, Michigan.*—Standard metallographic mounts used in photomicrography and electron metallography possess inherent deficiencies when specimens are to be polished electrolytically and/or etched by ion bombardment or electrolysis. To circumvent some of these difficulties a new mounting technique has been devised. The mount is comprised of two layers, one of which is an insulator, the other a metal conductor.

Session BV, Intracellular Morphology

B38. Some Electron Microscopic Observations on the Structure and Differentiation of the Indirect Flight Muscles of the Fruit Fly, *Drosophila melanogaster*. S. A. SHAFIQ, *Department of Anatomy, University of Washington, Seattle 5, Washington.*—Fibrils of the muscle cells of adult flies consist of thick and thin myofilaments. Their I bands are very short compared to the A bands except in the terminal parts of the fibers (i.e., near the myotendinal junctions) where the I bands are longer. The mitochondria in these regions are much fewer and smaller than in the rest of the fiber. The M bands have discrete granules which show up well after staining. The sarcoplasmic reticulum is poorly developed. The nerve fibers and tracheoles deeply project into the muscle cells. The myoblasts which give rise to the dorsal flight muscles form a mass of discrete cells in the early pupa. Each cell has a few small mitochondria and a compact endoplasmic reticulum bearing Palade granules. Later the myoblasts fuse to form syncytia, their endoplasmic reticulae become dispersed, and fibrils begin to appear. Various stages of fibrogenesis will be described.

B39. Structure and Fate of the Notochord in the Larva of the Ascidian *Boltenia villosa* (Stimpson). RICHARD A. CLONEY, *Department of Anatomy, University of Washington, Seattle 5, Washington.*—The notochord of the fully developed larva is composed of a series of about forty cells, an axial core of fluid, and an outer acellular sheath. The notochordal cells do not form a syncytium as claimed for other species by N. J. Berrill (1947) but retain their individuality as first recognized by A. O. Kowalevsky (1866) in the larva of *Phallusia mammillata*. Details of the endoplasmic reticulum, Golgi apparatus, mitochondria, yolk granules, and nuclei are described. The acellular sheath of the notochord is PAS positive and contains fibers which extend around the notochord at right angles to the major axis of the tail. The axial core of fluid first arises during development as intercellular vacuoles. During the early stages of metamorphosis the notochordal cells and fluid move out of the ruptured proximal end of the sheath into the posterior region of the trunk.

B40. Studies of the Thermal Destruction of Spores of *Bacillus coagulans*. JOHN W. HUNNELL, RUBIN BORASKY,* AND Z. JOHN ORDAL, *Electron Microscope Laboratory and Department of Food Technology, University of Illinois, Urbana.*—The bacterial endospore possesses unique properties of resistance to thermal destruction and chemical composition. For this study, spores of *Bacillus coagulans* 8038 were produced under various conditions for the study of structure and function with respect to heat resistance. The spore harvests were cleaned by treatments with lysozyme and repeated washings. For morphological studies, ultrathin sections were made from osmium fixed spores. Unheated spores showed the typical internal structures of a layered spore coat, a cortex of low density, and a core which is in general diffuse except for shapes of low density, ascribed to nucleic acids. Spores were heated and samples taken during the lethal heat treatment. The survivor curves from the heat treatment showed an increased heat resistance with an increased sporulation temperature. The effects of thermal death were observed both in shadowed specimens and in ultrathin sections. The cortical area appeared to be affected first. After loss of the cortex, the core showed a general breakdown. Only the spore coat remained after a prolonged heat treatment.

B41. Biochemical and Cytological Studies of Developing Soybean Cotyledons. R. F. BILS,* *Department of Botony and Electron Microscope Laboratories, University of Illinois, Urbana,* AND R. W. HOWELL, *U. S. Regional Soybean Laboratory, Urbana, Illinois.*—Developing soybean cotyledons, from 15 days after flowering to maturity, were studied whole and in section. A rapid increase in lipid percentage to about 20% occurs from 18 to 36 days after flowering. Percentage of total protein increases slowly from 25 to 40%. However, large protein globules (3–4 μ in diameter) increase rapidly in number from 26 to 30 days. It is proposed that this globular protein be designated as storage protein to distinguish it from the initial metabolic protein. Although no starch is found in the mature

soybean, a small amount exists from 18 up to 57 days after flowering. During the period studied, cytological observations will be correlated with the biochemical changes taking place.

B42. Electron Microscope Study of the Ice Phase in Rapidly Frozen Muscle Fibers.† LEO J. MENZ* AND B. J. LUYET, *American Foundation for Biological Research, Madison, Wisconsin.*—Pieces about 5 mm long of single muscle fibers, teased from frog skeletal muscle, were frozen by abrupt immersion in isopentane at −60° or −150°C, or in supercooled propane at −190°, then dehydrated by vacuum sublimation, embedded in methacrylate, sectioned, stained with phosphotungstic acid, and examined. At all cooling velocities a network of ice had been formed which disturbed the orderly arrangement of the myofilaments, compressing them into bundles. The size of the masses of ice constituting the network varied from a few microns in the center of the fibers to some 100 A near their periphery. In some cases, at the very edge of the fibers, the formation of crystalline ice might have been prevented, as the myofilaments appeared normal and undisturbed.

† Supported by a grant from Oscar Mayer and Company.

B43. Effect of Hypertonic Solutions of Sodium, Potassium, and Magnesium Chloride upon the Submicroscopic Structure of *Amoeba proteus*. EUBERT J. DANIEL,† *Department of Anatomy, University of Chicago, Chicago, Illinois.*—*Amoeba proteus*[1,2] was exposed for a maximum of 18 hr to 0.5% solutions of NaCl, KCl, and $MgCl_2$. At intervals, single cells were removed and prepared for electron microscopy by *in aqua* freeze-drying. Examination of sections revealed considerable alterations in the structural phase of the cytoplasm and nucleus. Immersion in NaCl and KCl resulted in granularity of the structural phase and watery vacuolization, both consistent with the pinocytosis, rehydration, and increase in intracellular Brownian motion observed under the light microscope. Exposure to $MgCl_2$ resulted in a condensation of the structural phase and the formation of a hydrated layer of marginal cytoplasm. This was consistent with the increased cell refractility and absence of Brownian motion observed under the light microscope. NaCl and $MgCl_2$-induced alterations were not lethal. KCl produced irreversible structural alterations.

† Present address: Orthopedic Research Laboratories, Department of Orthopedic Surgery, Massachusetts General Hospital, Boston, Massachusetts.

[1] D. M. Prescott and P. W. James, Exptl. Cell Research **8**, 256 (1955).
[2] D. M. Prescott and P. W. James, Compt. rend. trav. lab. Carlsberg **30**, 1 (1956).

B44. Comparison of the Submicroscopic Organization of *Amoeba proteus* Prepared by the Osmium Tetraoxide and Freeze-Drying Methods. EUBERT J. DANIEL, *Orthopedic Research Laboratory, Department of Orthopedic Surgery, Massachusetts General Hospital, Harvard University, Boston, Massachusetts.*—Amoebae prepared by the osmium tetraoxide method[1] were characterized by (1) changes in cellular dimensions during preparation; (2) absence of the outer layer of the cell wall and an outward displacement of the plasmalemma, especially along the margins of active pseudopods; (3) presence of swollen cellular organelles; (4) presence of a dispersed, granular cytoplasm and nucleoplasm. The characteristic features of cells prepared by the freeze-drying method[2] were (1) retention of cellular dimensions during preparation; (2) preservation of the outer layer of the cell wall and retention of the spacial relations of plasmalemma and adjacent cytoplasm; (3) slight changes in cell organelle size; (4) presence of a nongranular cellular organization composed of a structural phase enclosing compartments 300 A–800 A in diameter, resembling those theoretically postulated as existing in cellular systems.[3] The fine structure in the frozen-dried amoebae was related more easily to the known physical and colloidal features of amoeboid cells than was that exhibited in specimens prepared by the osmium tetraoxide method.

[1] G. Palade, J. Exptl. Med. **95**, 285 (1952).
[2] I. Gersh, J. Biophys. Biochem. Cytol. **4**, 37, Suppl. (1956).
[3] O. L. Sponsler and J. D. Bath, *The Structure of Protoplasm* (1942).

B45. Some Observations on Spermiogenesis of a Fire-Brat *Thermobia domestica*—a Cytochemical Phase, and Electron Microscope Study. S. R. BAWA,† *Department of Anatomy, Cornell University Medical College, and Department of Zoology, Columbia University, New York, New York.*—To date, the spermiogenesis of two Thysanurans (a group of primitive insects), *Lepisma domestica* and *Pterobius maritimus*, has been studied with the light microscope using classical techniques. However, there are conflicting reports on the morphology of the sperm with particular reference to the acrosome, centriole, and the mitochondrial nebenkern. The small size of the sperm has led to confusion in the correct interpretation of these organell. Results of the present study indicate that the orientation of the components of the mature spermatozoon of *Thermobia domestica* is unique in two respects—the centriole is at the anterior end of the nucleus while the acrosome is at the posterior end of the nucleus. The identification of this body as the acrosome is strengthened by the observation that it is PAS positive and that it arises in connection with a typical acroblast which results from partial fusion of dictyosomes. These latter are of the common cuplike form showing the usual ultrastructure and, as indicated by cytochemical tests, have appreciable concentrations of lipids and rather basic proteins plus some neutral polysaccharides groups; there is no detectable nucleic acid in the dictyosomes. The mitochondrial history is of the usual insect type. The complete loss of mitochondria in the later stages of spermiogenesis (reported in *Lepisma*) does not occur in *Thermobia*. Preliminary electron microscope studies reveal further that the sperm of *Thermobia* is atypical in having a well-developed fibrous sheath around the axial filament of the tail. The sperm tail seems to run adjacent to the elongated nucleus. It is important to recall that the cilia, flagella, and sperm tails of amphibia and invertebrates have been reported to lack the fibrous sheath wrapping. The physiological significance of this sheath will be discussed.

† Population Council Research Fellow, 1960–1961; Boese Post-Doctoral Fellow, 1959–1960.

B46. Toxoplasma Cysts in Mouse Brain. T. WANKO,* L. JACOBS, AND J. S. REMINGTON, *Ophthalmology Branch, National Institute of Neurological Diseases and Blindness, and Laboratory of Parasitic Diseases, National Institute of Allergy and Infectious Diseases, National Institutes of Health, Bethesda 14, Maryland.*—White, weanling mice of the NIH "general purpose strain" were infected subcutaneously with 0.25 ml of a 1:10 dilution of mouse brain homogenate containing cysts of the Beverley strain of *Toxoplasma gondii*. Blocks from the cerebral cortex were fixed 17, 60, and 210 days after innoculation in 2% osmium and embedded in both methacrylate and araldite. The protozoa in a cyst are encapsulated by an opaque layer wherein vesicular and membranous structures are resolved. Within the cyst, the space between the cell boundaries of the individual organisms is filled with a homogenous material which is in continuity with the capsule and of similar opacity. These protozoa closely resemble the proliferative forms present in peritoneal exudate of mice acutely infected with a virulent strain of toxoplasma. They contain a nucleus with nucleolus; mitochrondria; Golgi complex; endoplasmic reticulum; toxonemata, emanating from the conoid; a submembranous fibrillar apparatus; and vacuoles.

B47. Preliminary Report on the Ecological Study of *Endamoeba gingivalis*. OWEN KELLER, JANE H. MATHER, GRACE R. BAIRD, AND FRANK J. ORLAND, *Zoller Dental Clinic, University of Chicago, Chicago, Illinois.*—A long-range study of

oral microorganisms and their interrelationship has been under way for some time at the Zoller Clinic. The protozoan *Endamoeba gingivalis* (Gros) often is found in the immediate environment of certain teeth in man. With some difficulty, cultures have been isolated and propagated. This small *Endamoeba* and accompanying bacteria from these cultures have been fixed and stained in buffered osmic tetroxide, embedded in methacrylate, sectioned, and studied under the electron microscope. Nutritional studies of the amoeba and bacteria are being conducted, while our electron microscopy laboratory is comparing the structural similarities of *Endamoeba gingivalis* with the more widely known *Amoeba proteus*. As the project progresses, tissues from patients harboring the amoeba as well as from germ-free animals inoculated with the cultures, will be studied utilizing the electron microscope for definitive observations.

Index of Authors of Contributed Papers

Adams, C. D.—B37
Adams, J. M.—B12
Anderson, F. R.—A3
Arnold, N.—B16
Bachmann, L.—T10
Bacon, R.—A7
Baird, G. R.—B47
Banfield, W. G.—B25
Bawa, S. R.—B45
Bencosme, S. A.—B34
Bendler, H. M.—A29
Bennett, M.—B11
Bierlein, T. K.—A6
Bigelow, W. C.—A34
Bils, R. F.—B41
Boha, R.—B18
Borasky, R.—B40
Boswell, F. W. C.—A10, A19
Brewer, E. G.—A21
Brill, A. S.—T10
Brindley, D. C.—B25
Brökelmann, J.—B31
Bullivant, S.—T2
Burmester, B. R.—B19
Burnett, H. C.—T7
Choi, J. K.—B4
Cloney, R. A.—B39
Cohen, M.—A21
Coleman, J. W.—A23
Coleman, R. V.—A30
Collins, H. R.—B28
Conrad, M. E., Jr.—B23
Dales, S.—B22
Daniel, E. J.—B43, B44, T3
Danovich, J. F.—A31
Dmochowski, L.—B19, B20
Duff, R. H.—T7
Eddy, B. E.—B20
Edwards, O. F.—B2
Fernández-Morán, H.—A25, A26, A27
Fitzgerald, P. J.—B35
Goldman, M.—B11
Goodman, J. F.—T9
Goodman, J. R.—B11, B12
Greenfield, I. G.—A14
Grey, C. E.—B19, B20
Grimley, P.—B5
Grube, W. L.—A32
Harrell, S.—A5
Hartman, R. E.—B23
Hartman, R. S.—B23
Hendrickson, A.—B8
Herman, L.—B35
Herschleb, J. H.—A4
Holland, V. F.—A2
Hotchin, J.—T2
Hotchkiss, M.—B2
Howell, R. W.—B41
Huffstutler, M. C., Jr.—A9, A15
Hugo, J. A.—A17
Hunnell, J. W.—B40
Imagawa, D. T.—B12
Jacobs, L.—B46
Janigan, D. T.—B3
Jollie, W. P.—B34
Kahler, H.—T8
Kear, B. H.—A12
Keller, O.—B47
Kronenberg, K. J.—A16
Labaw, L. W.—A8
Laukonis, J. V.—A30
Leeson, C. R.—B7
Leeson, T. S.—B32
Libbey, R. L.—A24
Lloyd, B. J., Jr.—T8
Loud, A. V.—B24
Lowe, J.—B11
Luibel, F. J.—B16
Luyet, B. J.—B42
Maniar, G. N.—A34
Maser, M. D.—B9, B10
Mastel, B.—A6
Mather, J. H.—B47
Menz, L. J.—B42
Mishima, Y.—B24
Mishra, R. K.—B35
Morehead, F. F.—T5
Morgan, C.—B17
Murphy, A. P.—T9
Nagano, T.—B30
Newman, S. B.—A1
Nishi, Y.—T1
Oertle, D. H.—A22
Ordal, Z. J.—B40
Orland, F. J.—B47
Pedersen, K. J.—B6
Phillips, V. A.—A17
Pontius, E. E.—B18
Price, Z.—T1
Radd, F. J.—A22
Reedy, M. K.—B29
Reisner, J. H.—T4
Remington, J. S.—B46
Rhoads, H. U.—T6
Rice, R. V.—B9, B10
Richter, K. M.—B28
Rifkind, R. A.—B17
Ristic, M.—B26
Rose, G. G.—B27
Rose, H. M.—B17
Rouze, S. R.—A32
Rowe, F. G.—A22
Sanders, E.—B16
Schaub, F. F, Jr..—B24
Scheyer, S. C.—B36
Scott, R. L.—A35
Sewell, P. B.—A20, A21
Shafiq, S. A.—B38
Sharp, D. G.—B13, B15
Siegel, B. M.—T10
Siminovitch, L.—B22
Slagel, D. E.—B1
Smith, E.—A18
Smith, K. O.—B13, B15
Smith, R. E.—B18, B33
Sprague, R.—A7
Stahmann, M. A.—B1
Stewart, S. E.—B20
Strutt, P. R.—A11
Tawara, J. T.—B12
Thomas, G.—A9, A15
Threadgold, L. T.—B7
Trump, B. F.—B3
Tufts, C. F.—A28, A33
Vacher, H. C.—T7
Walter, W. G.—B19
Wanko, T.—B46
Wardlow, N.—B11
Watrach, A. M.—B26
Weber, A. H.—T6
Weinberg, F.—A19
Wilsdorf, H. G. F.—A13, A14
Wood, W. A.—A29
Zaretsky, E. V.—A5
Zaukelies, D. A.—A3
Zebrowski, L.—B14
Zeigel, R. F.—B21

Index of Invited Symposia Speakers

Bartell, L. S.—S10
Bendler, H. M.—S8
Bigelow, W. C.—S14
Boggs, W. E.—S15
Bonham, R. A.—S9
Boswell, F. W. C.—S11
Hicks, V.—S6
Molinar, Z.—S2
Nylen, M. U.—S3
Pautard, F. G. E.—S1
Pellissier, G. E.—S12
Reisner, J. H.—S7
Robinson, D. L.—S13
Rönnholm, E.—S4
Scott, D. B.—S5
Smith, E.—S11
Teague, M. D.—S16

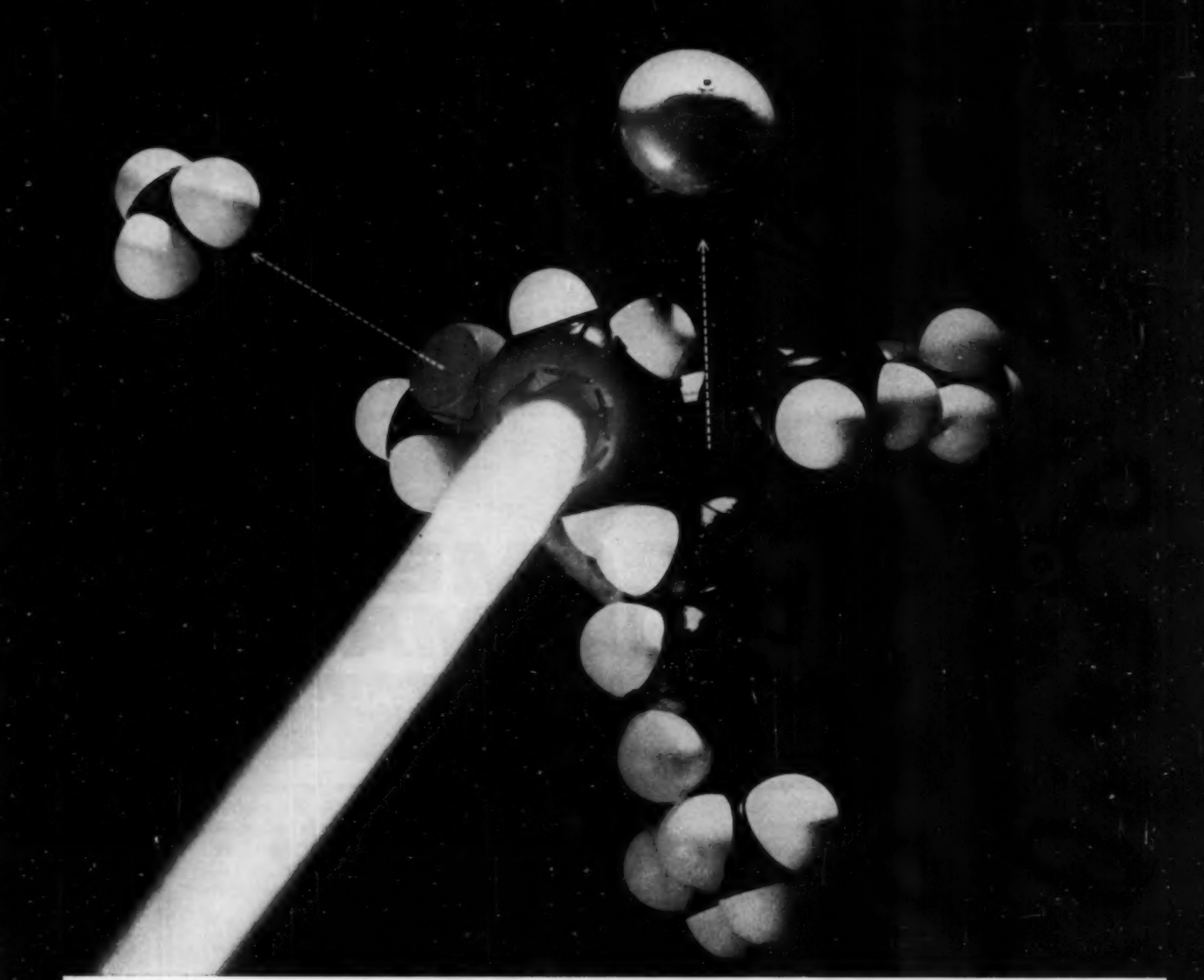

When Victoria blue leuconitrile absorbs light, it may decompose by one of the two modes indicated in the model above.

Organic molecules excited by light

Light energy can excite organic molecules, sometimes inducing color changes. Organic molecules can be treated as if they were independent molecules (even in the liquid and solid phases). The effect of small changes in their structure can be studied. Organic materials therefore offer a fruitful realm for investigating photoprocesses—the interactions of light and matter. Some of these photoprocesses have attracted our attention for their image-storing potential.

Several areas of organic photochemistry are now under study by a group of IBM scientists. A quantum of light absorbed by an organic molecule may interact with it to produce any of the following over-all effects: (1) transfer of the excitation energy to other molecules or to other parts of the same molecule; (2) re-emission of light of different wave lengths and time constants; (3) conversion of the light energy to heat; (4) decomposition of the organic molecule.

Researchers at IBM are striving to advance our understanding of the mechanisms of these molecular reactions. One study, for example, has probed the principles that govern decomposition by light of Victoria blue leuconitrile molecules, which exhibit all four of these reactions under photoexcitation. One of the possible modes of decomposition leads to color formation.

Clarifying the mechanisms of photochemical reactions in the liquid and solid states will add to our understanding of the interactions of energy with matter. It may lead to the development of new photoprocessing techniques.

IBM.RESEARCH

Investigate the many career opportunities available in exciting new fields at IBM. International Business Machines Corporation; Dept. 579W, 590 Madison Avenue, New York 22, New York

unequalled for **SELECTIVITY**

RANGE 0.2 TO 35 MICRONS

A highly versatile instrument which can be used for the ultraviolet, visible and infrared regions simply by interchanging prisms, cams and λ scales. High spectral purity, isolation of narrow wave-lengths, highest resolution and negligible scattered radiation are inherent characteristics. Available for automatic or manual operation.

Farrand Double

SPECTROMETER· MONOCHROMATOR

Technical data available on request
Specify Bulletin No. 805AP

FARRAND OPTICAL CO., INC.
BRONX BLVD. AND EAST 238th STREET • NEW YORK 70, N. Y.

CHEMISTS
PHYSICISTS

Rapid and steady growth has created new openings in Melpar's Physical Sciences Laboratory for several experienced solid state chemists or physicists. Must be skilled in both theoretical and applied techniques, involving the selection, synthesis, application and testing of a wide variety of materials. Broad areas of interest include infrared, electroluminescence, semiconductors, nonlinear amplifiers, thermoelectricity, electro-chemistry, and fabrication of microcircuits.

Send complete resume to: **Professional Employment Supervisor**

MELPAR, INC.

A Subsidiary of Westinghouse Air Brake Co.

3343 Arlington Boulevard, Falls Church, Va.
In Historic Fairfax County. *(10 MILES FROM WASHINGTON, D.C.)*

SOLID STATE SCIENTIST

High Temperature Materials, Inc., Extends An Opportunity to Carry Out Original Work In Solid State Areas of Unusual Promise

HTM is an expanding, well-regarded organization with a growing reputation in the research, development and manufacture of revolutionary materials. At the present time we are implementing a challenging new program that is directed toward understanding and exploiting the many and varied solid state properties of pyrolytic graphite, pyrolytic carbide, boron nitride, and other vapor phase process materials.

To direct this important activity we are seeking a solid state scientist of unusual competence whose principal responsibilities will be measuring the solid state properties of vapor phase process materials and utilizing these measurements in the design and development of new solid state devices.

Applicants for this senior position should possess a Ph.D. in Physics or Electrical Engineering and a minimum of 2–3 years' experience in theoretical and experimental solid state studies under the direction of a scientist with an established reputation in the field.

Inquiries may be directed in complete professional confidence to:

Dr. Daniel Schiff,
Director of Research & Development

H T M

HIGH TEMPERATURE MATERIALS, INC.

130 Lincoln Street, Brighton 35, Mass.

now from Librascope:

NARROW-BAND INTERFERENCE FILTERS

... with a new approach to side-band problems

Recent achievements at Librascope's Applied Research Center make it possible for you to now order high-precision, multilayer, narrow-band interference filters... custom-made to your specified wavelength, side-band requirement, and detector's spectral characteristics. Greater than 70% transmission and a half bandwidth of approximately 1% at specified peak wavelength. Delivery from stock: set of 8 filters uniformly distributed over visible spectrum ... as well as mercury and sodium lines. Send your requirements for quotation today.

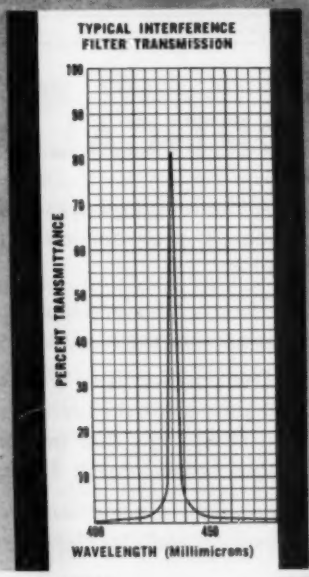

BURBANK BRANCH
LIBRASCOPE DIVISION
GENERAL PRECISION, INC.
100 East Tujunga • Burbank, Calif.

GP

Wanted: A Ph.D. who cannot tell whether he is an E.E. or Solid State Physicist !

...A broadly imaginative and knowledgeable man who will feel the pioneering challenge of **A NEW CLASS** *of* **GLASS-CERAMIC MATERIALS**

Our applied research group requires the services of an imaginative and knowledgeable man to participate in the planning and carrying out of a program to exploit a class of materials with unusual properties. Most of these materials are dielectrics, although some have interesting electronic properties. The approach is new.

THE MAN NEEDED will act both as a consultant to others in the group and carry out his own original research. The consultation requires a background in the physics of solids and good familiarity with measurements of the electrical properties of solids. He will carry out an original program in this general area and will also advise on possible use of these materials in prototype devices..

A PH.D. DEGREE is a minimum requirement. Experience is desirable and can extend the immediate assigned responsibilities but is not required. Fundamental knowledge and imagination are the prime considerations. The position is open at the Owens-Illinois Technical Center in Toledo, Ohio, a modern, well-equipped research facility. Toledo is a community of 350,000 with many delightful residential sections, fine schools and a well-rated university. The community has excellent recreational and cultural facilities. You can drive via turnpike to Chicago or Pittsburgh in 4½ hours: to Ann Arbor (U of M) or Detroit by expressway in 1½ hours.

WHO WE ARE. Owens-Illinois manufactures Duraglas containers, Libbey table glassware, Kimble scientific and electronic glassware, and construction glass products. We are a leading manufacturer of corrugated boxes, closures, and blown plastic containers. We have 58 plants and mills and more than 35,000 employees.

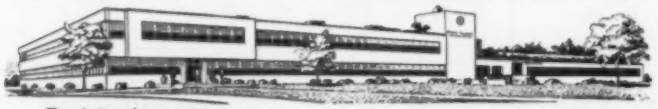

For interview, contact:
Harold F. Zink
Owens-Illinois Technical Center
1700 N. Westwood Ave., Toledo 1, Ohio

MAKERS OF (O) PRODUCTS

OWENS-ILLINOIS
GENERAL OFFICES · TOLEDO 1, OHIO

OPTICAL MASER RESEARCH

A challenging opportunity exists for a man who can take charge of a research program on light amplification and related fluorescence studies.

The man we are looking for is a physicist, physical chemist, or a microwave engineer with a Ph.D degree or equivalent experience.

The position is in a new field of interest for Corning Glass Works, a 108-year-old firm recognized for its pioneering research achievements. The company's new modern laboratories are situated in the beautiful Finger Lakes region of New York State.

For full information, write to Mr. James L. Knapp, Staff Manager, Research and Development Division.

CORNING GLASS WORKS
Corning, New York

SOLID STATE PHYSICISTS ●

Expanding long-range programs require that Battelle add solid state physicists, physical chemists and electrical engineers to its professional staff.

The programs now under way cover a wide variety of interesting problems. Included are studies in thin films, "noise," transistors, rectifiers, thermoelectric energy conversion, semiconductor materials, and related topics.

The following openings are available:

- **Ph.D. in physics or physical electronics (preferably with 2 to 5 years experience) for theoretical solid state research.**
- **B.S. to Ph.D. level with experience in transistor materials and their applications to solid state devices.**
- **Recent graduate B.S. or M.S. with degree in physics or electrical engineering, to work with experienced scientists on application of solid state devices.**
- **M.S. or Ph.D. in physics or physical chemistry with an avid interest and experience in thin films and their applications to electronics.**

These positions offer unusual opportunities to work and study with outstanding scientists and technologists in an organization where initiative and creative enthusiasm is encouraged and appreciated.

For further details, application form and descriptive brochure, write to:

L. G. Hill

Battelle Memorial Institute

505 King Avenue Columbus 1, Ohio

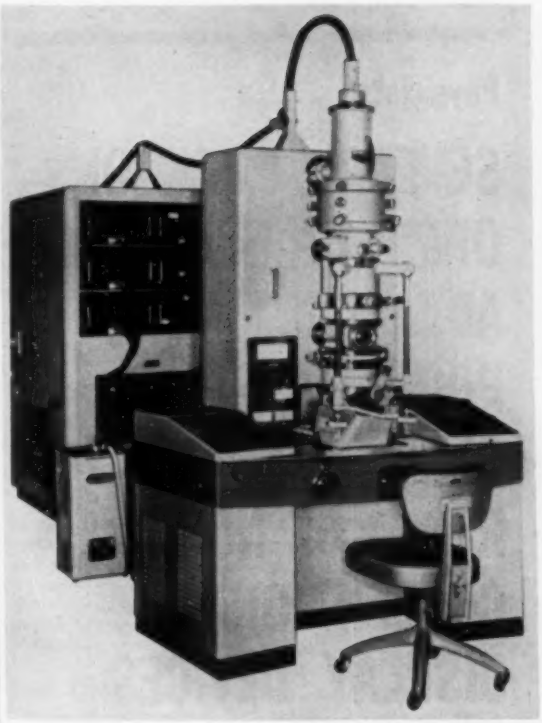

the new HITACHI HU-11

Hitachi's guaranteed 8–10 Angstrom Unit resolution allows you to probe the very basic structure of matter—making full use of the HU-11's 250,000x direct magnification.

The basic Hitachi HU-11, without accessories, serves as a highly efficient electron diffraction apparatus for use with opaque or transparent specimens. With such accessories as a low temperature stage, a high temperature stage, a reflection microscopy attachment and a X-Ray shadow camera, the Hitachi HU-11 allows investigations into every field of research.

ERB & GRAY SCIENTIFIC, Inc.

Exclusive Hitachi Distributors for the U.S.

854 Figueroa St., Los Angeles 17, Calif.
501 5th Ave., New York 17, N. Y.

Physicists:

SEVERAL POSITIONS OPEN IN NEW ADVANCED PROJECTS OPERATION FOR R & D OF NON-CONVENTIONAL DISPLAY DEVICES

Although details cannot be published here, one of the activities of this new group will concern development of an entire family of unusual information recording, storage and display systems.

Key Posts to be Filled in These Areas:

Electron Optics
Light Optics
Vacuum Technology Development
Gettering
Thermionic Emission
Tube Development
Display System Analysis
Circuit Analysis
Organic Material Analysis
Synthesis & Application of Organic Materials to Electronic Components

For more information, write informally or forward your resume in confidence to Mr. James F. Leete, Dept. 37-MJ. Your inquiry will receive prompt review and an early reply.

CATHODE RAY TUBE DEPARTMENT

GENERAL ELECTRIC

Electronics Park — Syracuse, New York

TADANAC BRAND

Special Research Grade

ANTIMONY

TADANAC Brand Special Research Grade antimony is primarily developed for production of intermetallic compounds such as indium and aluminum antimonides. No individual impurity exceeds 0.1 ppm. and shipments can be made from sections of zone refined bars. These bars contain large crystals and have a very low oxygen content.

Other TADANAC Brand high purity metals or compounds include Special Research Grade indium and tin, High Purity Grade bismuth, cadmium, indium, lead, silver, tin, zinc, and indium antimonide. Send for our brochure on TADANAC Brand High Purity Metals.

COMINCO

THE CONSOLIDATED MINING AND SMELTING COMPANY OF CANADA LIMITED
215 ST. JAMES ST. W., MONTREAL 1, QUEBEC, CANADA · PHONE AVenue 8-3103

0161

OPTICAL SYSTEMS DESIGNERS

Are invited to investigate an outstanding career opportunity in the rapidly growing West Coast research laboratory of

The
PERKIN-ELMER
Corporation

Please submit a complete resume to

5670 E. Washington Blvd.
Los Angeles 22, Calif.

NEWS from the NRC Vacuum MICRONICLE*

New 6″ vacuum pump —70% more speed— no loss of reliability

Upgraded performance is but half the story on the new NRC Model H6-1500. Compared with its predecessor it assures: *Speed* — 1500 l/s, up 70%. *Forepressure Tolerance* — 700 microns, up 275%. *Backstreaming* — less than 0.03 mg/-cm²/min, down 40%. *Height* — 18½″, down 34%. *Blank-off* — as low as 10^{-10} mm Hg in trapped UHV system.

The other half is the way it can do all this without carefully regulated power and water supplies, oversized backing pumps, delicate pump oils, or frequent maintenance. Stainless steel body — 4-stage fractionating jet assembly (securely anchored yet demountable in 15 sec.) — easily removable, long-lived "cast-in" heater — silver soldered cooling coils — all keep operating and maintenance costs low. Original cost is low, only $495.

*Send for FREE periodical containing details on H6-1500 and other news about high vacuums. Dept. P-10 160 Charlemont St., Newton 61, Mass.

NRC EQUIPMENT CORPORATION

A Subsidiary of National Research Corporation

NRC-17

SENIOR PHYSICIST

Advanced Memory Department of our Research Division offers an unusual opportunity for a physicist or engineer (Ph.D. desirable) to lead experimental and theoretical studies in new information storage media and techniques. Background in information storage or in solid state materials (ferroelectrics, scotophors, energy sensors, semiconductors or optical devices) essential. Company sponsored projects are underway in these areas and others may be initiated and directed by this man. Job environment emphasizes individual achievement.

AMPEX CORPORATION

World Leader in Magnetic Recording

Send resumes to:
Skipwith W. Athey
Director, Research Lab.
934 Charter Street
Redwood City, California

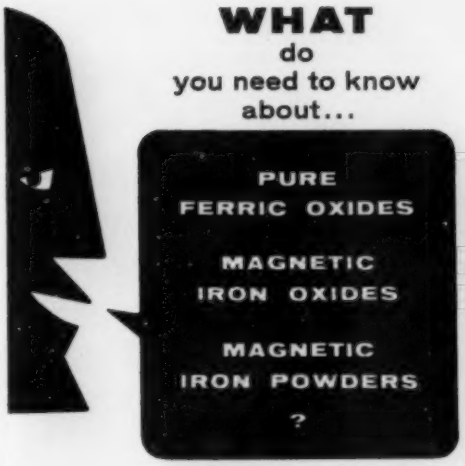

Since final quality of your production of ferrites, electronic cores, and magnetic recording media depends on proper use of 3 specialized groups of magnetic materials . . . you'll find it mighty helpful to have all the latest, authoritative technical data describing the physical and chemical characteristics of each. This information is available to you just for the asking. Meanwhile, here are highlights of each product group.

PURE FERRIC OXIDES—For the production of ferrite bodies, we manufacture a complete range of high purity ferric oxide powders. These are available in both the spheroidal and acicular shapes, with average particle diameters from 0.2 to 0.8 microns. Impurities such as soluble salts, silica, alumina and calcium are at a minimum.

MAGNETIC IRON OXIDES—For magnetic recording—audio, video, instrumentation etc.—we produce a group of special magnetic oxides with a range of controlled magnetic properties. Both the black ferroso-ferric and brown gamma ferric oxides are available.

MAGNETIC IRON POWDERS—For the fabrication of magnetic cores in high-frequency, tele-communication, and other magnetic applications, we make a series of high purity iron powders.

If you have problems involving any of these materials, please let us go to work for you. We maintain fully equipped laboratories for the development of new and better inorganic materials. Write . . . stating your problem . . . to C. K. Williams & Co., Dept. 38, 640 N. 13th St., Easton, Penna.

WILLIAMS
COLORS & PIGMENTS

C. K. WILLIAMS & CO.
E. ST. LOUIS, ILL. • EASTON, PA. • EMERYVILLE, CAL.

MEASUREMENT OF LINEAR DIMENSIONAL CHANGES WITH GAERTNER OPTICAL INSTRUMENTS

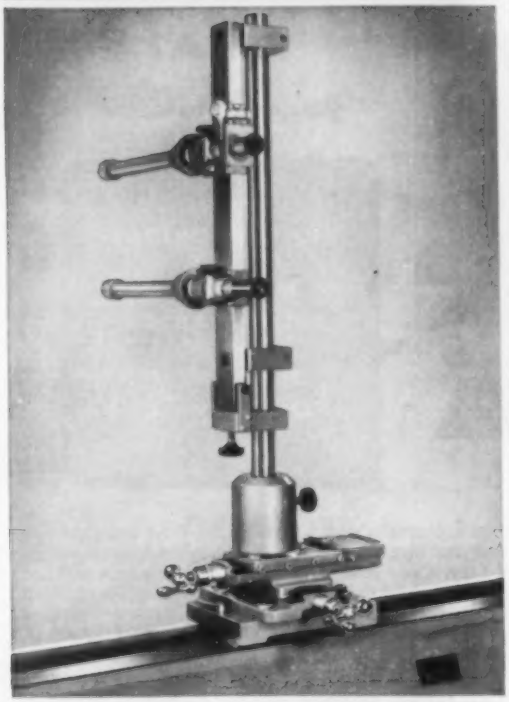

Instrument shown permits measurement of specimens 2" to 12" long. Total range of measurement .080", reading to .00002". Has relay lenses for 8" working distance. Adjustment in 3 axes. Mounted on lathe bed type bench for use with multiple specimen setups.

For measurement of dimensional changes of specimen materials caused by creep, tensile test, or environmental conditions

Gaertner Measuring Instruments feature variable working distances to meet individual situations. Specimens may be oriented horizontally or vertically, and practically any specimen length can be accommodated. Consistent repeatable readings to .00002" are possible.

Gaertner offers a wide range of precision scientific optical and measuring instruments to scientists in all fields. Our services include modifications of these instruments to meet unusual needs, complete design and manufacture of special instruments and optical systems, and manufacture of assemblies and instruments from customer sketches and drawings.

Write or phone and put this experience to work for you.

Gaertner
SCIENTIFIC CORPORATION
1246 Wrightwood Ave., Chicago 14, Illinois • BU 1-5335

SENIOR PHYSICIST

Magnetics department of our Research Division offers an unusual opportunity for a physicist or engineer (Ph.D. desirable) to participate in and lead experimental and theoretical studies in various aspects of magnetism and magnetic materials. Company sponsored projects are underway on thin films, fine particles, magneto-optics and allied areas. Job environment emphasizes individual achievement.

AMPEX CORPORATION
World Leader in Magnetic Recording

Send resumes to:
Donald F. Eldridge
Head, Magnetics Department
934 Charter Street
Redwood City, California

NOW!
Easy Demonstration of basic Gas Laws
CENCO Kinetic Theory Apparatus

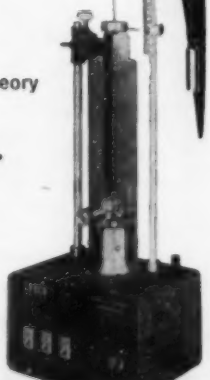

Permits quantitative determination of the most fundamental principles of gas mechanics. Adapted from a design by H.F Meiners of Rensselaer Polytechnic Institute. Plot p-V and p-T curves-measure molecular diameters, verify the fundamental gas laws and Van der Waals Corrections.

No. 77722 without stroboscope, **$295.00**

cenco®

CENTRAL SCIENTIFIC CO.
A Subsidiary of Cenco Instruments Corporation
1718-A Irving Park Road • Chicago 13, Illinois
Branches and Warehouses—Mountainside, N. J.
Boston • Birmingham • Santa Clara • Los Angeles • Tulsa
Houston • Toronto • Montreal • Vancouver • Ottawa

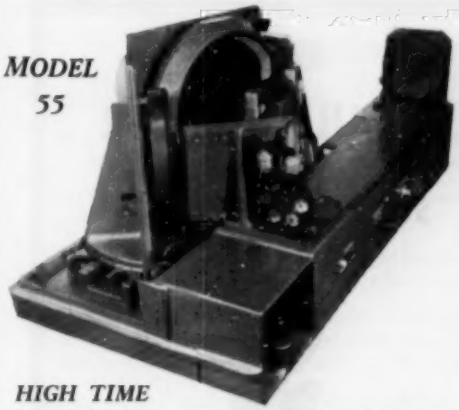

MODEL 55

HIGH TIME RESOLUTION STREAK SPECTROGRAPH

A research instrument for investigation of transient luminous sources emitting radiations in the visible or ultraviolet spectrum. Provides a two dimensional time versus wavelength record on 35mm film. Spectral ranges 3050 to 4350 A° with 45 A°/mm dispersion, and 4200 to 6000 A° with 60 A°/mm dispersion. Relative aperture F/2.0. Resolvable time interval is 10^{-7} seconds.

Send for descriptive literature

Tropel, Inc., 52 West Ave., Fairport, N.Y.

NEW *micro* SIZE!

CENCO®

LAB-JACK

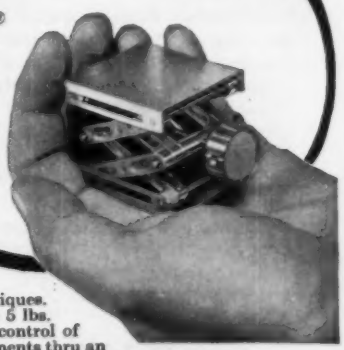

Excellent for micro techniques. Supports up to 5 lbs. with precision control of vertical adjustments thru an elevation of more than 3". 3x3" stainless top and bottom auxiliary plates for quick attachment. Model 19066 each $19.50.

CENCO the most complete line of scientific instruments and laboratory supplies in the world.

cenco®

CENTRAL SCIENTIFIC CO.
1718-A Irving Park Road • Chicago 13, Illinois
Branches and Warehouses — Mountainside, N. J. Boston • Birmingham • Santa Clara • Los Angeles • Tulsa Houston • Toronto • Montreal • Vancouver • Ottawa

TIFFEN OPTICAL FACILITIES FOR SCIENCE AND INDUSTRY

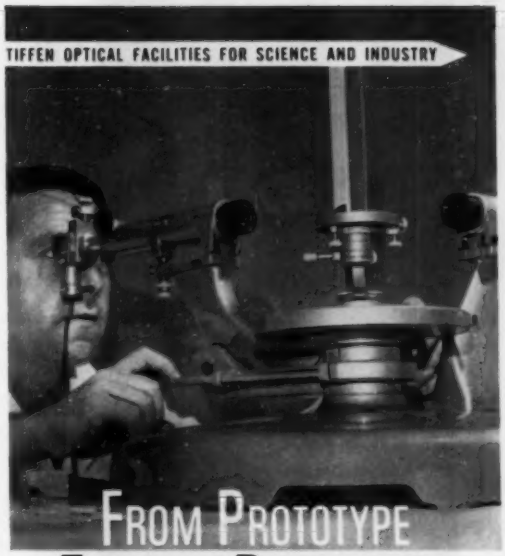

FROM PROTOTYPE THROUGH PRODUCTION

For over a decade, government agencies, industrial firms and photo studios have turned to TIFFEN for precision optical accessories. Now, TIFFEN offers their specialized knowledge, experience and expanded facilities to all industry employing optics in their product. TIFFEN's major facilities are partially described below:

BLANCHARDS . . . flat grinding to .00005". Diamond wheel shaping to .0001". ***EDGING*** . . . to less than .001", to 20" dia. Bevels and odd shapes ground. ***DRILLING*** . . . dia. 010" to 12", concentric to within .0005", on glass, ceramics, silicon, germanium, etc. ***GRINDING & POLISHING*** . . . 1mm. dia. to 24" dia., within 1/10 wavelength in flatness, under 2 seconds arc in parallel. Roof prisms to 2 seconds of arc accuracy. ***COATING*** . . . high vacuum deposition of all types of material, partial coatings for beam splitters and metallic neutral density filters. ***COLOR LABORATORY*** . . . includes Densichron, Beckman Du Spectrophotometer, Weston Foot Lambert Meter. ***FILTERS*** . . . laminated glass equal in environmental tests to solid glass, with superior color control, resolution to 100 lines per mm. ***MACHINING*** . . . multi-spindle automatic to 4", secondary machines to 10" capacity. ***TOOL ROOM*** . . . 23" swing lathes, grinders, millers. All tools and jigs manufactured internally.

Special problems? Write, call or visit: **TIFFEN OPTICAL CO.**, 71 Jane St., Roslyn Hgts., L. I., N. Y.
West Coast Rep.: CRAIG CORP., 3410 So. La Cienega Blvd., Los Angeles 16, Cal.

TIFFEN DELIVERS THE GOODS!

a vacuum pump as dynamically balanced as . . .

Engineered to give you years of vibration-free, superior operation, Stokes Series H Microvac pumps are the most advanced in their class. Exceptionally compact, Stokes pumps take up 50% less floor space than conventional vacuum pumps.

Learn all the reasons why Stokes offers you more pumping performance per dollar. Simply write: Vacuum Equipment Division, F. J. STOKES CORPORATION, 5500 TABOR ROAD, PHILA. 20, PA.

STOKES

SEND TODAY
for your free
Vacuum Slide Calculator!

EPLAB

PYRHELIOMETER
For the Measurement of SOLAR RADIATION

Eppley Pyrheliometers are used for solar radiation measurements at ninety-eight weather stations in the continental United States, Canada, Alaska, Greenland, Iceland, Caribbean Sea, and the Pacific Ocean. Sixty-two of these stations are under the direction of the United States Weather Bureau.

The Eppley Pyrheliometer was adopted as standard equipment by the Weather Bureau after considerable experimentation. It was found to be the best instrument so far tested by the Bureau.

Used in conjunction with a suitable recorder, the Eppley Pyrheliometer will provide an accurate and reliable record of total solar and sky radiation on a horizontal surface.

Bulletin No. 2 On Request

THE EPPLEY LABORATORY, INC.
Scientific Instruments
6 Sheffield Ave.
Newport, Rhode Island, U.S.A.

PETROLEUM PRODUCTION RESEARCH

Vacancies for men of initiative and imagination exist at the Gulf Research Center.

M.S. or Ph.D. Engineer or Physicist to study combustion phenomena as related to the recovery of crude oil. A solid background in mathematics is essential.

M.S. or Ph.D. Engineer or Physical Chemist to apply modern concepts in surface chemistry to the problems of oil recovery.

M.S. or Ph.D. Engineer or Physicist interested in a combination of experimental and theoretical work having as its object the design, construction and operation of scaled models of complex oil field processes.

M.S. or Ph.D. Engineer, Physicist or Applied Mathematician to work on long-range programs in the general fields of fluid flow and properties of porous media. The aim is to help build a body of information which may ultimately assist in the design of radically new schemes for oil recovery.

- *Modern facilities located near Pittsburgh.*
- *Liberal publication policy.* • *Salaries open.*

Reply to:

Gulf Research & Development Company
Attn: Employment Manager
P. O. Drawer 2038
Pittsburgh 30, Pennsylvania

Off-Press in January, 1961 . . .

RETRIEVAL GUIDE TO THERMOPHYSICAL PROPERTIES RESEARCH LITERATURE

Edited by Y. S. Touloukian
Thermophysical Properties Research Center
Purdue University

Ten thousand scientific and technical research papers have been coded as to property, substance, subject, language, physical state, etc. and the information stored on magnetic tapes of a computer at Purdue University. The thermophysical properties of 14,500 substances are reported. This work represents the print out of a special computer program and will provide the engineer, scientist, or reference librarian with quick access to the world literature on the following seven thermophysical properties: thermal conductivity, thermal diffusivity, diffusion coefficient, specific heat, viscosity, emissivity and Prandtl number.

Volume I, *The Three Book Set*, (10,000 bibliographic references), $120.00

McGRAW-HILL BOOK COMPANY, Inc.
330 West 42nd Street **New York 36, N.Y.**

INDEX TO ADVERTISERS

Name	*Page*
AMPEX CORPORATION	xxiii, xxiv
BATTELLE MEMORIAL INSTITUTE	xxi
BECKMAN & WHITLEY, INC.	Cover 2
Manufacturers of high-speed research cameras—both framing and sweeping-image type; specialized meteorological instruments; heat-flow transducers; and explosive-actuated mechanisms.	
BELL TELEPHONE LABORATORIES	v
CENTRAL RESEARCH LABS.	xiii
CENTRAL SCIENTIFIC CO.	xxiv, xxv
Manufacturers of Cenco physical apparatus and instruments to meet all requirements of University, College and High School Physics Laboratories. Specializing in high vacuum pumps and development of instruments and apparatus for various sciences.	
CONSOLIDATED MINING & SMELTING CO.	xxii
CORNELL-DUBILIER ELECTRIC CORP.	xxx
Primarily interested in the design and manufacture of special type capacitors for thermonuclear work along the lines of the enclosed illustrations. These special fast discharge low inductance capacitors, operating in voltages up to 160 KV, have extensive use in the advanced study of high temperature and high current fields.	
CORNING GLASS WORKS	xx
EPPLEY LABORATORY, INC.	xxvi
ERB & GRAY SCIENTIFIC, INC.	xxi
ERIE RESISTOR CORPORATION	xv
FARRAND OPTICAL CO.	xviii
GAERTNER SCIENTIFIC CORP.	xxiv
Spectroscopes, spectrometers, spectrographs, spectrophotometers, heliostats, measuring microscopes, comparators, cathetometers, reading telescopes, interferometers, chronographs, dividing machines, etc.	
GENERAL ELECTRIC Cathode Ray Tube Dept.	xxii
GENERAL MOTORS Delco Radio Div.	vi
GENERAL RADIO CO.	Cover 3
Manufacturers of electronic measuring instruments; vacuum-tube voltmeters, amplifiers, and oscillators; wave analyzers, noise meters and analyzers, stroboscopes, laboratory standards of capacitance; inductance and frequency; impedance bridges, decade resistors and condensers, air condenser and variable inductors; rheostats, variacs, transformers; other laboratory accessories.	
GULF RESEARCH & DEVELOPMENT CO.	xxvii
HAMNER ELECTRONICS CO., INC.	x
HARVEY-WELLS ELECTRONICS, INC.	iv
HIGH TEMPERATURE MATERIALS, INC.	xix
I. B. M. CORPORATION	iii, xvii
KEITHLEY INSTRUMENTS, INC.	vii
Vacuum tube electrometers, microammeters, kilovoltmeters, static detectors, meg-meg-ohm-meters, high gain dc amplifiers, dc vacuum tube voltmeters, high input impedance ac isolation amplifiers.	
LOCKHEED MISSILES & SPACE DIV.	ix
LOS ALAMOS SCIENTIFIC LAB.	xi
LIBRASCOPE DIV. OF GENERAL PRECISION, INC.	xix

INDEX—*Continued*

Name *Page*

McGRAW-HILL BOOK CO., INC. xiv, xxvii

MELPAR, INC. xviii

NRC EQUIPMENT CORP. xxiii

Manufacturers of standard and special high vacuum components, equipment, and systems including mechanical booster, and diffusion pumps; gauges; valves; seals; connectors; melting and heat-treating furnaces; coaters; impregnators; gas in metal analyzers; driers and freeze driers; altitude chambers; and leak detectors.

OWENS-ILLINOIS xx

PERKIN-ELMER CORP. xxii

RAMO-WOOLDRIDGE LABS. .... Cover 4

Research, development, and manufacture in the field of electronic systems for commercial and military applications, and in the field of guided missiles.

STOKES CORP., F. J. xxvi

Mechanical and oil vapor pumps; vacuum valves, gauges and other components; vacuum furnaces, metalizers, processing systems and other special high vacuum equipment.

STROMBERG-CARLSON
Div. of General Dynamics xii

SYLVANIA ELECTRIC
PRODUCTS, INC. viii

TIFFEN OPTICAL CO. xxv

TROPEL, INC. xxv

WELCH SCIENTIFIC CO., W. M. ... xvi

Manufacturers of high-vacuum pumps, both mechanical and diffusion; vacuum gauges; electrical measuring instruments; physics equipment; and other items for the physical and chemical laboratories.

WILLIAMS & CO., C. K. xxiii

Soviet Physics—SOLID STATE

Monthly. A cover to cover translation of the USSR Academy of Sciences journal, "Fizika Tverdogo Tela."

Soviet Physics—TECHNICAL PHYSICS

Monthly. A cover to cover translation of the USSR Academy of Sciences journal, "Zhurnal Tekhnicheskoi Fiziki."

Soviet Physics—CRYSTALLOGRAPHY

Bimonthly. A cover to cover translation of the USSR Academy of Sciences journal, "Kristallografiya."

Please address orders and inquiries to the publisher:

AMERICAN INSTITUTE OF PHYSICS
335 East 45th Street, New York 17, N. Y.

POSITIONS OPEN

LUBRICANTS

RESEARCH AND DEVELOPMENT

We have a challenging opportunity for a research specialist in the field of boundary lubrication.

Applicant should have at least five years' experience and demonstrated ability in the development of EP lubricants.

Rare opportunity for top talent to advance, or to initially assume position on management level with progressive, research-minded, and fast-growing company.

Location—Connecticut coast. Commuting distance—New York City.

Write in detail. Box 1060-B, Journal of Applied Physics, 335 East 45th St., New York 17, N. Y.

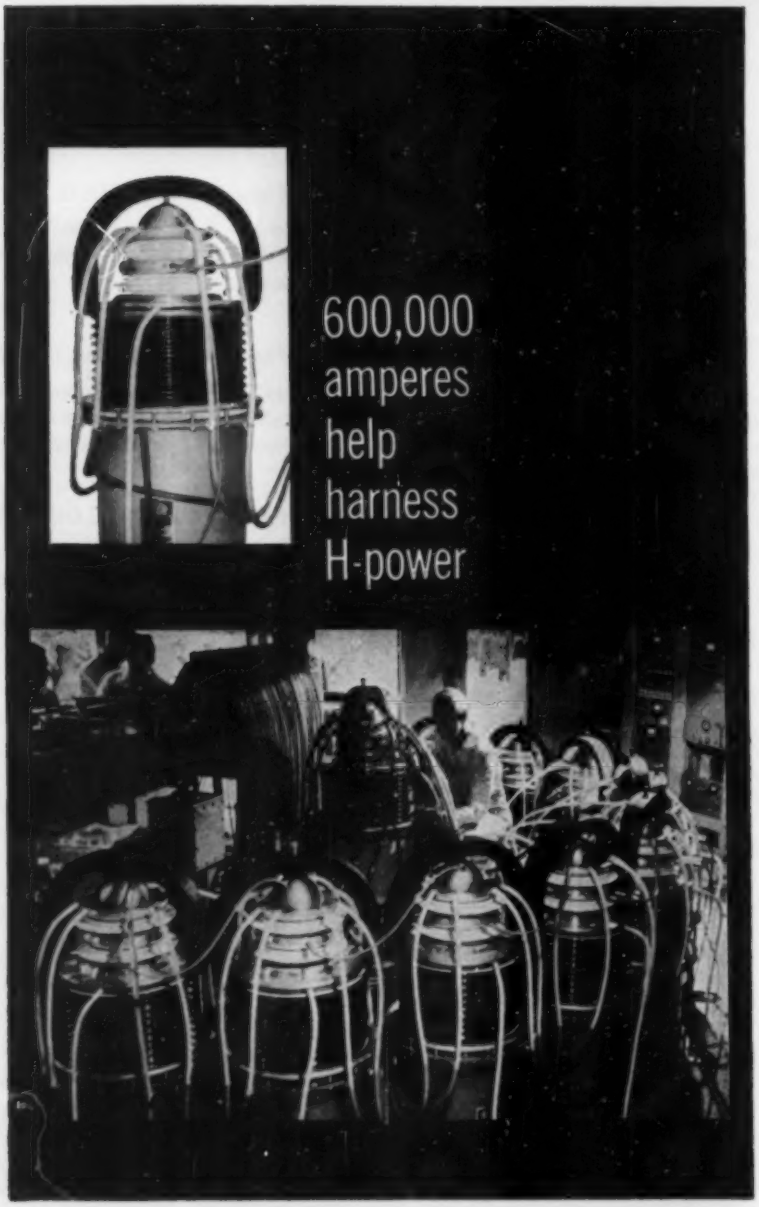

At the historic Geneva Atoms-For-Peace Conference, Los Alamos scientists unveiled **Scylla**—a fusion device used to heat a plasma of ionized heavy hydrogen particles millions of degrees by blasting it with a 600,000-ampere thunderbolt.

Surrounding the heart of this thermonuclear machine is a bank of low-inductance, energy-storage capacitors...each rated at 100,000 volts, each capable of a 20,000 megawatt peak surge.

This unique installation, like others of its type, is the result of long experience in capacitor specialization. If adherence to rigid specifications is a 'must' on your project—call us in to help with creative engineering. We invite inquiries for a single energy-storage capacitor or a complete energy-storage system including capacitors, racks, interconnecting lines, protective devices and charging power supply.

For further technical information, write for Bulletin No. 191 to Cornell-Dubilier Electric Corporation, New Bedford, Mass.

CDE

CORNELL-DUBILIER ELECTRONICS DIVISION
FEDERAL PACIFIC ELECTRIC COMPANY

New STROBOTAC®

helps develop improved mid-range speaker

its bright white light and short duration flash permit detailed study of operation of electromechanical devices.

1531-A STROBOTAC $260

- ★ direct reading range 110 to 25,000 rpm; useful to several hundred-thousand rpm
- ★ ±1% accuracy
- ★ short flash (0.8 to 3.0 μsec) eliminates blur
- ★ 70 times brighter than previous model
- ★ unique carrying case doubles as adjustable stand

How Well Does A Speaker Speak? Engineers at Acoustic Research, Inc., use stroboscopic techniques to get the answer. With the new Type 1531-A Strobotac, investigations are now possible over the full audio frequency range.

First, they apply finely chopped strands of rayon flock to a line of glue on the surface of a dome radiator diaphragm. Then, with the speaker excited at a given frequency, the behavior of the free ends of the cemented strands is observed under stroboscopic light. This technique clearly reveals all diaphragm movement, including nodal points and any breakup that may occur.

Investigations such as these led the way to the development of a corrective guard ring that produces uniform energy dispersion and a flatter frequency response.

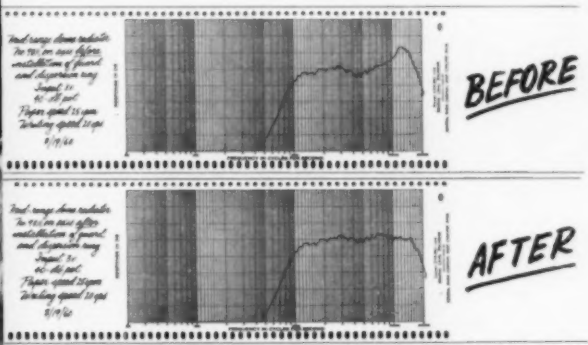

"Before and after" frequency-response recordings made with a G-R 1304 Beat-Frequency Generator and 1521-A Graphic-Level Recorder, the perfect team for audio-response recordings. Note the flatter characteristic of the improved mid-range reproducer. The link coupling between the instruments enables the Recorder to plot response data logarithmically and automatically from 20c to 20 kc. Price for this complete system is $1765.

Write For Complete Information

GENERAL RADIO COMPANY

WEST CONCORD, MASSACHUSETTS

NEW YORK, WOrth 4-2722
NEW JERSEY, Ridgefield, WHitney 3-3140

CHICAGO
Oak Park
Village 8-9400

PHILADELPHIA
Abington
HAncock 4-7419

WASHINGTON, D.C.
Silver Spring
JUniper 5-1088

SAN FRANCISCO
Los Altos
WHitecliff 8-8233

LOS ANGELES
Los Angeles
HOllywood 9-6201

IN CANADA
Toronto
CHerry 6-2171

автоматический перевод

вычислительные машины

способствуют исследова-

нию языков

AUTOMATIC TRANSLATION
INDEXING
ABSTRACTING

To formulate rules for automatic language translation is a subtle and complex task. Yet, significant progress is being made. During the past several years large amounts of Russian text have been translated and analyzed at Ramo-Wooldridge's Intellectronics Laboratories using several types of existing general purpose electronic computers.

Many hundreds of syntactic and semantic rules are used to remove ambiguities otherwise present in word-for-word translation. The considerable improvements that have been effected during the progress of this work indicate that it may be possible within the next year or so to produce, for the first time, machine translation of sufficient accuracy and at sufficiently low cost to justify practical application. Electronic computers are also invaluable for other language research activities at Ramo-Wooldridge.

Techniques for automatic indexing, automatic abstracting, and other aspects of communicating scientific information are also being investigated. Research and development at the Intellectronics Laboratories will eventually lead to electronic machines capable of carrying on self-directed programs of research and analysis and "learning" by their own experiences.

The accelerating pace at which these "communication of knowledge" problems are growing in importance has created challenging career opportunities in new fields of scientific endeavor.

For a copy of our career brochure, "An Introduction to Ramo-Wooldridge," write to Technical Staff Development.

RAMO-WOOLDRIDGE
a division of *Thompson Ramo Wooldridge Inc.*
8433 FALLBROOK AVENUE, CANOGA PARK, CALIFORNIA